

Sebastiano Ferraris

**Image Computing Tools for the  
Investigation of the Neurological Effects  
of Preterm Birth and Corticosteroid  
Administration**

University College London  
Medical Physics and Biomedical Engineering

A dissertation submitted in partial fulfilment  
of the requirements for the degree of  
**Doctor of Philosophy**  
of  
**University College London.**

Centre for Medical image computing  
Translational Imaging Group

March 23, 2019



I, Sebastiano Ferraris, confirm that the work presented in this thesis is my own.  
Where information has been derived from other sources, I confirm that this has  
been indicated in the thesis.



## Abstract

In this thesis we present a range of computational tools for medical imaging purposes within two main research projects. The first one is a methodological project oriented towards the improvement of the performance of a numerical computation utilised in diffeomorphic image registration. The second research project is a pre-clinical study aimed at the investigation of the effects of antenatal corticosteroids in a preterm rabbit animal model.

In the first part we addressed the problem of integrating stationary velocity fields. This mathematical challenge had originated with early studies in fluid dynamics and had been subsequently mathematically formalised in the Lie group theory. Given a tangent velocity field defined in the tridimensional space as input, the goal is to compute the position of the particles to which the velocity field is applied. This computation, also called numerical Lie exponential, is a fundamental component of several medical image registration algorithm based on diffeomorphisms, i.e. bijective differentiable maps with differentiable inverse. It is as well a widely utilised tool in computational anatomy to quantify the differences between two anatomical shapes measuring the parameters of the transformation that belongs to a metric vector space.

The resulting new class of algorithms introduced in this thesis was created combining the known scaling and squaring algorithm with a class of numerical integrators aimed to solve systems of ordinary differential equations called exponential integrators. The introduced scaling and squaring based approximated exponential integrator algorithm have improved the computational time and accuracy respect to the state-of-the-art methods.

The second part of the research is a pre-clinical trial carried forward in collaboration with the Department of Development and Regeneration, Woman and Child Cluster at the KU Leuven University. The clinical research question is related to the understanding of the possible negative effects of administering antenatal corticosteroids for preterm birth. To tackle this problem we designed and started a pre-clinical study using a New Zealand perinatal rabbit model.

In this part of the research I was involved in the research team to provide the tools to automatise the data analysis and to eliminate the time consuming and non reproducible manual segmentation step. The main result of this collaboration is the creation of the first multi-modal multi-atlas for the newborn rabbit brain. This is embedded in a segmentation propagation and label fusion algorithm at the core of the proposed open-sourced automatic pipeline, having as input the native scanner format and as output the main MRI readouts, such as volume, fractional anisotropy and mean diffusivity.



## Impact statement

The main contributions of this thesis are two computational tools for medical image analysis. The first one is a new method to integrate stationary velocity fields arising in diffeomorphic image registration, and the second one is a pipeline to automatise the pre-clinical magnetic resonance images data analysis of the newborn rabbit brain model. This last includes a multi-modal multi-atlas based segmentation method.

The consequent findings on the methodological side have improved the accuracy and computational time in integrating vector fields modelling the transformation between anatomies. On the pre-clinical side, the produced data analysis pipeline provided new insights in understanding the effects of antenatal corticosteroids administration and therefore could lead to reduce complications in the preterm birth treatment.

The development of the computational tools have provided relevant research results, such as the first vector field integration algorithms based on a combination of the scaling and squaring method and the exponential integrators, and the first multi-modal multi-atlas for the automatic parcellation of the newborn rabbit brain. This animal model is currently widely used in neurodevelopmental studies due to its likeness to human perinatal myelination. In the pre-clinical research environment, the proposed multi-atlas replaced weeks of manual workload with a reproducible automatic segmentation method.

Part of the thesis is also aimed at reporting the limitations and drawbacks encountered during the research, and to suggest a range of improvements in the methodologies employed as well as in the data acquisition. This part could prove to be useful in reducing the amount of trials and errors for other research groups and therefore to reduce the number of animals employed in subsequent studies.

The code produced during the research had been open-sourced and maintained in a collaborative environment, thereby making solutions available to other groups addressing similar questions, and potentially contribution to accelerated output of research findings.

As most relevant results are published on international journals and deal with problem shared by any biomedical and bioengineering research group addressing the investigation of pathologies in a newborn rabbit model, the impact affects other research groups outside University College London and Katolische Universitat Leuven, where the research had been carried forward.

In the final part of the thesis, eight possible research projects are described as future work for which the reported results and the provided tools can constitute a possible starting point.

## Publications

- |                   |  |
|-------------------|--|
| Methodological    | <ul style="list-style-type: none"> <li>– <b>Ferraris S*</b> and van der Merwe J*, Van Der Veecken L, Prados F, Iglesias JE, Melbourne A, Lorenzi M, Modat M, Gsell W, Deprest J and Vercauteren T <i>A magnetic resonance multi-atlas for the neonatal rabbit brain</i>. NeuroImage Volume 179, 1 October 2018, Pages 187–198, Elsevier [doi] [code].</li> <li>– <b>Ferraris S</b>, Lorenzi M, Daga P, Modat M, and Vercauteren T. <i>Accurate Small Deformation Exponential Approximant to Integrate Large Velocity Fields: Application to Image Registration</i>. In Proceedings of the IEEE CVPR Workshops, pp. 17-24, 2016 [paper] [code].</li> <li>– Iglesias JE, Lorenzi M, <b>Ferraris S</b>, Peter L, Modat M, Stevens A, Fischl B, Vercauteren T: <i>Model-based refinement of nonlinear registrations in 3D histology reconstruction</i>, MICCAI 2018 [paper].</li> <li>– Ebner M, Modat M, <b>Ferraris S</b>, Ourselin S, and Vercauteren T. <i>Forward-Backward Splitting in Deformable Image Registration: A Demons Approach</i>. In 2018 IEEE 15th International Symposium on Biomedical Imaging 2018. Washington, D.C.: IEEE [paper].</li> <li>– Iglesias JE, <b>Ferraris S</b>, Modat M, Gsell W, Deprest J, van der Merwe JL, Vercauteren T: <i>Template-free estimation of intracranial volume: a preterm birth animal model study</i>. MICCAI Workshop: Fetal and Infant Image Analysis, 2017 [paper].</li> </ul> |
| Clinical          | <ul style="list-style-type: none"> <li>– van der Merwe J, van der Veecken L, <b>Ferraris S</b>, Gsell W, Himmelreich U, Toelen J, Ourselin S, Melbourne A, Vercauteren T, and Deprest J. <i>Early neuropathological and neurobehavioral consequences of preterm birth in a rabbit model</i>. Scientific reports 9, no. 1 (2019): 3506.</li> </ul>  |
| Software          | <ul style="list-style-type: none"> <li>– <b>Ferraris S</b>, Shakir DI, Van Der Merwe J, Gsell W, Deprest J and Vercauteren T. <i>Bruker2nifti: Magnetic Resonance Images converter from Bruker ParaVision to Nifti format</i> Journal of Open Source Software 2017. [code].</li> <li>– A detailed list providing the open source software produced during the PhD is presented in Section 7.2.2.</li> </ul>  |
| Technical reports | <ul style="list-style-type: none"> <li>– <b>Ferraris S</b>, Mendelson A, Ballesio G, and Vercauteren T. <i>Counting sub-multisets of fixed cardinality</i>. arXiv:1511.06142 math.CO, 2015 [manuscript] [code].</li> </ul>   |

Award – Best young scientist poster award *High Resolution MR Multi-Modal Multi-Atlas Brain for the Neonatal Rabbit*. First Workshop on Assistive Technology for Fetal Therapy and Surgery, Leuven Belgium, 12 December 2017.

## Acknowledgments

The first thanks goes to the Engineering and Physical Sciences Research Council, the Wellcome Trust and the University College London for the support provided throughout the master and the doctoral study. I have a great debt of gratitude towards these institutions and their funders.

I am very grateful to my supervisors Tom Vercauteren, Marc Modat, and Jan Deprest for their trust and guidance. A challenging feedback who greatly improved this work had been provided by Gary Zhang and Maria Deprez during the viva, to whom I have a debt of gratitude.

This thesis is the outcome of three years of intense collaboration with members of the GIFT-Surg research project and with the researchers involved at KU Leuven. My thanks go in particular to Johannes Van Der Merwe. With his hard work and open mind, the multidisciplinary work has always been smooth, fruitful and productive. Fundamental was the support of Willy Gsell for sharing his experience and for the scanner setup advice. This work would have not been possible without the guidance and help I received from Ferran Prados, Sjored Vos, Andrew Melbourne, Tom Doel, Dzhoshkun Shakir, Juan-Eugenio Iglesias, Roberto Annunziata, Francois Chadebecq, Matteo Mancini, Loic Peter, Michael Ebner, Rosalind Pratt, Natalie Suff, Wenqi Li and Carole Sudre.

I am very grateful to the rowing fellows at the GIFT-Surg Project, with whom I started this journey: Michael Ebner, Luis Herrera, Efthymios Maneas, Marcel Tella, and Guotai Wang.

Indispensable was the contribution of Rebecca Holmes, Katie Konyn, Liz Zuzikova, Alexandra Ferrell and Denise Beales for their passion and efficiency in scientific, communication and finance management.

Finally, the amendments of the thesis had been made while working full time at the core banking company Thought Machine. I benefited from the support of Mike Cripps and colleagues who encouraged me in moving forward with this work.

# Contents

<b>1</b>	<b>Introduction</b>	<b>27</b>
1.1	Background . . . . .	27
1.2	Research challenges . . . . .	29
1.2.1	Diffeomorphic image registration . . . . .	29
1.2.2	Antenatal corticosteroids pre-clinical trial . . . . .	31
1.3	Methodological contributions . . . . .	33
1.4	Thesis organisation . . . . .	35
<b>2</b>	<b>Preterm birth and corticosteroid administration: an overview</b>	<b>39</b>
2.1	Epidemiology . . . . .	40
2.2	Public attention and social costs . . . . .	42
2.3	Etiology, pathogenesis and long term consequences . . . . .	44
2.4	Preventions, treatments and therapies . . . . .	45
2.5	Clinical question . . . . .	47
<b>3</b>	<b>Rabbit brain animal model: experiment design and dataset acquisition</b>	<b>55</b>
3.1	Why rabbit . . . . .	56
3.2	Pre-clinical study . . . . .	58
3.2.1	Multimodal design . . . . .	59
3.3	Design selection for the MRI acquisitions . . . . .	60
3.3.1	In vivo and ex vivo protocols . . . . .	60
3.3.2	Longitudinal and cross-sectional design . . . . .	63
3.3.3	High resolution MRI readouts and areas of interest . . . . .	63
3.4	Protocols . . . . .	64
3.4.1	<i>Ex vivo</i> acquisition protocol . . . . .	64
3.4.2	<i>In vivo</i> acquisition protocol . . . . .	65
3.5	Appendix: protocol development . . . . .	66

<b>4</b>	<b>Diffeomorphic image registration and integration of stationary velocity fields</b>	<b>77</b>
4.1	Motivations . . . . .	78
4.1.1	Segmentation propagation and label fusion . . . . .	79
4.1.2	Morphometry in the tangent space . . . . .	80
4.2	Image registration principles . . . . .	81
4.2.1	Rigid, affine and deformable registration . . . . .	81
4.2.2	Possible classifications in the literature . . . . .	85
4.2.3	The challenge of validation . . . . .	87
4.3	Diffeomorphisms: a biologically sound deformation model . . . . .	88
4.3.1	Motivations . . . . .	88
4.3.2	Stationary and time-varying velocity fields . . . . .	89
4.3.3	LDDMM and Demonology . . . . .	90
4.3.4	Splitting strategy for the cost function optimisation . . . . .	91
4.4	Integration of stationary velocity fields . . . . .	92
4.4.1	Mathematical background . . . . .	92
4.4.2	SVF in the diffeomorphic image registration scheme . . . . .	94
4.4.3	Classical numerical integrators . . . . .	96
4.4.4	Scaling and squaring method and its generalisation . . . . .	97
4.4.5	The composition of stationary velocity fields . . . . .	99
4.4.6	Combining generalised scaling and squaring and exponential integrators . . . . .	101
4.4.7	Resulting algorithms . . . . .	105
4.5	Benchmarking . . . . .	106
4.5.1	Rigid body transformations . . . . .	106
4.5.2	General linear group . . . . .	108
4.5.3	Homographies . . . . .	112
4.5.4	Gaussian velocity vector fields . . . . .	114
4.5.5	BrainWeb dataset . . . . .	114
4.5.6	ADNI dataset . . . . .	117
4.5.7	Inverse consistency . . . . .	118
4.5.8	Benchmarking with NiftyReg . . . . .	119
4.6	Open-source software: calie . . . . .	122
4.7	Conclusions and limitations . . . . .	122
<b>5</b>	<b>A multi-atlas for the neonatal rabbit brain</b>	<b>131</b>
5.1	MR imaging as biomarker . . . . .	132
5.1.1	MRI readouts . . . . .	132
5.1.2	Image segmentation challenge . . . . .	133

5.2	Image segmentation method for the newborn rabbit . . . . .	134
5.2.1	Currently available rabbit atlases . . . . .	135
5.3	Multi-atlas for the neonatal rabbit brain . . . . .	136
5.3.1	Materials and methods . . . . .	137
5.3.2	Segmentation pipeline and proposed stereotaxic orientation . .	138
5.3.3	Manual segmentation and taxonomy . . . . .	142
5.3.4	Automatic segmentation algorithm . . . . .	146
5.3.5	Probabilistic atlas creation . . . . .	147
5.3.6	Results . . . . .	147
5.3.7	Validation . . . . .	149
5.3.8	<i>In vivo</i> experiments . . . . .	153
5.4	Parameters benchmarking: multi-modal versus uni-modal . . . . .	155
5.5	Conclusions . . . . .	156
5.6	Appendix: Newborn Rabbit Brain Taxonomy . . . . .	157
<b>6</b>	<b>Newborn rabbit brain data analysis</b>	<b>169</b>
6.1	Pre-clinical trial data analysis aims . . . . .	169
6.2	Bruker2nifti and NiLabels . . . . .	170
6.3	Data collection pipeline . . . . .	173
6.4	Exploratory Data analysis . . . . .	175
6.4.1	Statistical model: from theory to practice . . . . .	175
6.4.2	Full brain volume differences: are the results due to chance? . .	177
6.4.3	Region-wise volume outcome . . . . .	180
6.4.4	Region-wise fractional anisotropy . . . . .	181
6.4.5	Region-wise mean diffusivity . . . . .	181
6.5	Conclusions . . . . .	183
<b>7</b>	<b>Conclusions and future work</b>	<b>189</b>
7.1	Contributions . . . . .	190
7.1.1	Pre-clinical contributions . . . . .	190
7.1.2	Methodological contributions and limitations . . . . .	190
7.1.3	Open source software contributions and limitations . . . . .	191
7.2	Future work . . . . .	191
7.2.1	Further methods on the exponential integrators . . . . .	191
7.2.2	Open source code maintenance and improvements . . . . .	192
7.2.3	A NiLearn-inspired investigation for the fMRI rabbit brain analysis . . . . .	194
7.2.4	Longitudinal design . . . . .	194
7.2.5	4D multi-modal multi-atlas for the rabbit brain . . . . .	195

7.2.6	Extending the range of biomarkers . . . . .	197
7.2.7	Histology-MRI multi atlas for the rabbit brain . . . . .	197
7.2.8	A rabbit tracker for automatic unbiased neurobehavioural as- essment . . . . .	198

# List of Figures

30-1	<b>Schematic overview of the infinite dimensional Lie group and Lie algebra of diffeomorphisms.</b> The infinite dimensional Lie group of diffeomorphisms over $\Omega$ , indicated with $\text{Diff}(\Omega)$ is represented with a grey surface. To each diffeomorphic transformation $\phi$ corresponds an element $\mathbf{u}$ in the infinite dimensional tangent vector space, the Lie algebra $V(\Omega)$ . The correspondence between Lie group and Lie algebra and vice versa are the Lie logarithm and the Lie exponential respectively. . . . .	30
32-1	<b>Stationary velocity field and corresponding integral curves of a rotation.</b> A sagittal slice of a human brain MRI (left), a tangent vector field generated by a rotation of 30 degrees respect to the centre (centre) and the result of the rotation applied to the first image (left). The integral curve of the tangent vector field, in blue, represent the position where each voxel after the transformation parametrised by the SVF, in red. . . . .	32
33-1	<b>Axial slice of the newborn rabbit brain manually segmented with the corresponding taxonomy.</b> The multi-modal multi-atlas proposed in this section allows to create an automatic parcellation of the newborn rabbit brain, as the one shown above. Further details of the method and the complete taxonomy are provided in Chapter 5. . . . .	33
41-1	<b>Fetal growth from 20 to 40 gestational week.</b> Any childbirth between the 24 <sup>th</sup> and the 37 <sup>th</sup> week is considered preterm. According to the severity different treatments may be required. For high risks of preterm and very preterm birth (between 24 <sup>th</sup> and the 37 <sup>th</sup> gestational week) administration of antenatal corticosteroids (ACS) and tocolytics is customary: the positive impact of the treatment on the lungs growth is believed to compensate for possible brain insults caused by ACS. To balance risks and benefit of administering ACS for late preterms, in particular between the 25 <sup>th</sup> and the 35 <sup>th</sup> gestational week, it is crucial to quantify the possible negative effects of ACS administration. Fetuses images courtesy of <a href="http://hopkinsmedicine.org">hopkinsmedicine.org</a> . . . . .	41

42-1	<b>Estimated preterm birth rate by country for the year 2010.</b> PTB appears to equally affect low and high income countries. Image from [BCO <sup>+</sup> 12]. . . . . .	42
43-1	<b>Observed and maximum potential PTB rates of survival and survival without profound impairment.</b> (a) presents the relation between gestational age, divided by weight and sex, versus the observed rate of survival and the maximum potential rate (upper bound for the maximum potential percentage of infants with a favourable outcome). (b) the proportions of survivors without profound impairments after intensive care. Image from [TPL <sup>+</sup> 08]. . . . . .	43
56-1	<b>Adult rabbit brain and skull.</b> Screenshots from the Dept. of Medical science Heritage College of Osteopathic Medicine, Ohio university ( <a href="http://www.ohio.edu">www.ohio.edu</a> , last access 21-05-18). Right column, the adult rabbit brain atlas, Munoz et al. [MMA <sup>+</sup> 13] in a single surface (top) and divided in anatomical regions (bottom). The comparison shows the location of the brain in the skull and its 3D shape. . . . . .	56
57-1	<b>Study design timeline.</b> (T) normal control or term, cesarean birth after 31 days of gestation. (PT) preterm model, cesarean birth after 28 days of gestation. (LPT) late preterm, cesarean birth after 30 days and (LPT+) late preterm with antenatal corticosteroid administration. Harvesting is performed for the each datasets at the 32 <sup>nd</sup> day to produce equivalent development day. Image acquisition is scheduled afterwards and performed according to scanner availability within one week. . . . . .	57
60-1	<b>Multimodal design.</b> The study started in May 2016, and ongoing at the moment of writing this thesis involves three approaches: histology, neurobehavioural assessment and High resolution MR imaging. Numerical quantifications of the three approaches will be compared to provide a better understanding of the functional and structural effects of preterm birth and corticosteroids administration. . . . . .	60
61-2	<b>Axial, sagittal and coronal view of subject 0802, <i>in vivo</i> protocol.</b> The only applied pre-processing is region of interest extraction, reorientation and a bias field correction. Resolution (0.234375, 0.187500, 0.234375) mm for (128, 128, 128) voxels grid. The acquisition protocol is described in Section 3.4. . . . . .	61

61-3	<b>Axial, sagittal and coronal of subject 1702, <i>ex vivo</i> protocol.</b> As for fig. 59-2, the only applied pre-processing are region of interest extraction, reorientation and a bias field correction. Resolution is (0.077920, 0.077920, 0.077920) mm for (385, 385, 385) voxels grid. The acquisition protocol is described in Section 3.4. . . . .	61
62-4	<b>Axial, sagittal and coronal of the main direction of the DTI, subject 0802, <i>in vivo</i> protocol.</b> Applied pre-processing is region of interest extraction, reorientation, tensor fitting, multiplication of the main direction times the fractional anisotropy map. Colour code: red R/L, blue A/P green S/I. In the sagittal section, parts of the cerebellar hemispheres are not present due to the reduced field of view of the <i>in vivo</i> acquisition. . . . .	62
62-5	<b>Axial, sagittal and coronal of the main direction of the DTI, subject 1305, <i>ex vivo</i> protocol.</b> Same pre-processing steps of Figure 59-4. . .	62
67-1	<b><i>Ex skull</i> acquisition.</b> Artefacts created by this option are: (A) flattening of the olfactory bulbs, (B) disruption of optic tracts, (C) cortex disruption, and (D) percolation of gadolinium along the pipe. Subject 0104. . . . .	67
68-2	<b><i>Open skull</i> acquisition.</b> Midway between <i>in skull</i> and <i>ex skull</i> protocols. A syringe needle is introduced through an opening in the skull to introduce gadolinium-based fluid. Internal anatomies definition is comparable to an <i>ex skull</i> acquisition. . . . .	68
69-1	<b>3D rendering of an <i>ex skull</i> acquisition. Top:</b> superior (left) and inferior (right) view. Anterior side points north. <b>Bottom:</b> lateral view. As in Figure 67-1: flattening of the olfactory bulbs (A), disruption of optic tracts (B), cortex disruption (C), percolation of gadolinium along the pipe (D). . . . .	69
70-2	<b>Motion artefact of the <math>b = 0</math>.</b> First time-point of the DWI in the <i>ex vivo</i> acquisition protocol. Coronal section, subject 4302. . . . .	70
70-3	<b>Syringe to keep the head steady during the 10h acquisition.</b> This setting, proposed and implemented by Johannes van der Merwe in KU Leuven solved the motion artefacts encountered with Falcon pipes. . . . .	70
71-1	<b>Example of low dose of gadolinium and phase wrap-around artefact.</b> Coronal section, subject 4507. . . . .	71
72-2	<b>Ghosting and <i>fencing</i> artefacts in sagittal section.</b> Loose RF-coil for the T1 modality, can result in a peculiar artefact, here called <i>fencing</i> , as well as in ghosting artefact. . . . .	72
72-3	<b>Comparison between T1 and <math>b = 0</math>.</b> The presence of air bubble in the perfusion fluid results in a <i>black hole</i> in the T1 and in a deformation in the $b = 0$ providing a representative example of susceptibility artefact. Coronal section, subject 1805. . . . .	72

73-4	<b>Example of perivascular spaces enlargement due to high pressure in the trans-cardiac perfusion.</b> Subject 1505. . . . .	73
84-1	<b>Schematic view of the registration algorithm.</b> The archetypal deformable image registration is made of two inputs (fixed and moving images) an output transformation $\hat{S}$ and 5 main components: resampling, cost function, optimisation, stopping criteria, and a deformation model to which the estimated transformation output belongs. Human brain coronal sections shown are MRI scans with inverted contrast from the ADNI database [JBF <sup>+</sup> 08].	84
90-1	<b>Some landmarks in the evolution of diffeomorphic image registration algorithms</b> with Demons approach, started in 1998 and the Large Deformation Diffeomorphic Metric Mapping approach, started in 2005. For a complete perspective of the landscape of image registration algorithms in medical imaging we refer to Sotiras et al. [SDP13b]. . . . .	90
95-1	<b>Schematic view of the diffeomorphic registration algorithm.</b> The archetypal deformable image registration based on diffeomorphisms is made of two inputs (fixed and moving images) an output transformation in the tangent space $\hat{\mathbf{u}}$ and, as in the more general case, 5 main components: resampling, cost function, optimisation, stopping criteria, and a deformation model. In this case the deformation model of diffeomorphisms parametrised with stationary velocity fields, and the exponential function plays a pivotal role. . . . .	95
99-1	<b>Scaling and composing scheme, as a generalisation of the scaling and squaring.</b> The input stationary velocity field $\mathbf{u}$ is scaled by a factor of $N$ . Then a selected numerical integrator is applied, and its result, indicated with $\widehat{\exp}(\mathbf{u}/N)$ , is iteratively composed by itself $N$ -times. When $\widehat{\exp}(\mathbf{u}/N)$ is approximated with $\text{Id} + \mathbf{u}/N$ and the iterative composition is computed with the squared composition, then the algorithm is the classical scaling and squaring proposed by Arsigny et al. [ACPA06]. When the iterative composition is performed sequentially backward, it is equivalent to the Euler method. . . . .	99
109-1	<b>Computational time versus error for 50 SVF generated by rotations.</b> The proposed methods are indicated with * and are compared with a selection of the classical methods. Methods are compared for different steps (or discretisation of the interval $[0, 1]$ ). Each point represents a different number of steps in the list $[1, 2, 3, 4, 5, 6, 7, 8, 9, 10, 15, 20, 25, 30, 40]$ . . . . .	109

110-1	<b>Possible classification of the elements of the general linear group.</b> From left to right, top to bottom: unstable node, stable node, saddle, unstable spiral, stable spiral and circles. . . . .	110
111-2	<b>Computational time versus error for 50 SVF generated by linear transformations.</b> As Figure 108-1 with SVF generated by elements of the general linear algebra. For this dataset, the difference between the two asymptotes is less prominent than the previous case. . . . .	111
112-1	<b>Computational time versus error for 50 SVF generated by homographies.</b> As Figure 110-2 with SVF generated by elements of the homography algebra. In this non-linear case, the proposed methods beats the state of the art and the two asymptotes in the convergence are almost overlapping . . . . .	112
115-1	<b>Computational time versus error for 50 randomly generated SVF smoothed with a Gaussian filter.</b> This is the most non-linear dataset of the one selected. Unlike the previous cases, it is not possible to estimate a ground truth, therefore the <code>rk4</code> method for 7 steps is chosen as benchmark. As before, the proposed method <code>gss_aei</code> has the best comparative performance. The other proposed method <code>euler_aei</code> does not seem to reach convergence, even after 30 steps. . . . .	115
116-2	<b>Computational time versus error for 19 SVFs generated with a cross-sectional experiment with the BrainWeb dataset.</b> This case is very similar to the one previously proposed, where the SVFs had been generated with Gaussian filter smoothing random vector fields. The proposed <code>gss_ei</code> improve the scaling and squaring at each step, if compared to the selected benchmarking method. . . . .	116
117-1	<b>Computational time versus error for 10 SVFs generated with a longitudinal experiment with the ADNI dataset.</b> This case is very similar to the previous ones, where the proposed methods are improving the state-of-the-art methods, and showing that the findings are consistent across different datasets. . . . .	117
118-1	<b>Inverse consistency for the ADNI generated SVF.</b> For an high enough number of steps the inverse consistency is almost the same for all methods in log-scale. The proposed methods beats the state of the art for a number of steps between 5 and 10. . . . .	118

121-1	<b>Steps versus Cost function value.</b> With three parametrisation of NiftyReg applied to the 10 subjects from the ADNI dataset presented in the previous section, this graph compares the cost function values respect to the timepoints. The diffeomorphic registration methods reaches an higher value for the function to be maximised from the first step. The slope is higher as well for the first 50 steps. The proposed method does not differ significantly respect to the state-of-the-art, in particular for the initial range of steps. . . . .	121
136-1	<b>Sample selection and distribution.</b> Brain and body weight of all subjects prepared for the study: 8 pre-term (7 males / 3 females) and 4 term (3 males / 4 females). Of the initial 17 subjects (10 pre-term, 7 term), 5 have been discarded due to image artefacts. Cross-hair shows the mean, blue ellipsoids the covariance and gray rectangle shows the 25 <sup>th</sup> and 75 <sup>th</sup> percentiles. . . . .	136
139-1	<b>Comparison between adult rat and rabbit skeletons and skulls.</b> Comparison between the adult rat and rabbit skeletons. Note the difference in latent posture and head position resulting in skull attitude differentiation. Inspired by <a href="https://www.behance.net/">https://www.behance.net/</a> and <a href="http://bcrc.bio.umass.edu/">http://bcrc.bio.umass.edu/</a> . Last access March 23, 2019. . . . .	139
139-2	<b>Comparison between adult rat and rabbit skulls.</b> Comparison between the adult rat and rabbit skull. Note the shape difference of the frontal and parietal skull shape. Inspired by <a href="http://www.skullsite.co.uk/">http://www.skullsite.co.uk/</a> . . . . .	139
140-3	<b>Rat and rabbit brain compared.</b> Representation of the newborn rat and rabbit brain. 3D representative sketches (top) and mid-sagittal section (bottom). Inspired by <a href="http://www.medicinafetalbarcelona.org/rabbitbrainatlas/">http://www.medicinafetalbarcelona.org/rabbitbrainatlas/</a> and <a href="http://www.skullsite.co.uk/Rat/comrat.htm">http://www.skullsite.co.uk/Rat/comrat.htm</a> . . . . .	140
140-4	<b>Proposed stereotaxic orientation for the MR imaged newborn rabbit brain.</b> In the mid-sagittal section, the bicommissural plane forms a 45° angle with the horizontal plane. The full line represents the bicommissural plane and the dashed line the horizontal plane. Centers of the anterior and posterior commissure are highlighted in the coronal and the axial sections. . . . .	140
142-5	<b>3D brain surface rendering.</b> Segmentation of 6 selected coronal slices of the right hemisphere are shown with the remaining labels in transparency. Corresponding slices are delineated over the T1 modality with the corresponding nomenclature in Figure 138-6. . . . .	142

143-6	<b>Delineation of anatomical regions over the T1 modality.</b> Progressive coronal sections, anterior to posterior. Only the segmentation outline is delineated for visualization purposes. Region of interest surrounding the brain is visible in the image, to show the border delineation between the brain and the skull. See Table 138-1 for the abbreviation and nomenclatures. Detailed taxonomy table is proposed in the additional material. . . . .	143
144-1	<b>3D brain surface rendering.</b> The first row emphasises a selection of subcortical regions (corona radiata in pink, corpus callosum in purple and subcortical white matter in blue) and of fibertracts (anterior and posterior commissure in yellow, and optic tracts in orange). The second row highlights the regions that are believed to be affected by pre-term birth. Superior view: corpus callosum (purple), hippocampus left and right (pink), thalami (red), caudate nuclei (blue) and cerebellar hemispheres (green). Inferior view: optic tracts (orange), internal capsula left and right (brown). The third row points out the right hemisphere cortex. Superior view: olfactory bulb (aquamarine blue), anterior (red), frontal (green) and occipital (khaki). Inferior view: piriform (yellow), entorhinal (brown) and amygdala (turquoise), the hippocampi (left and right in pink) and the basal forebrain (blue). . . . .	144
145-2	<b>Software scheme.</b> Visualisation of the segmentation procedure, involving atlas propagation, label fusion and elective manual adjustments. For the creation of our multi-atlas the whole procedure with the manual adjustments had been performed three times. . . . .	145
148-1	<b>Probabilistic atlas and probabilistic segmentation of 4 selected regions.</b> Coronal sections at the origin of the coordinate system for each of the 12 subjects of the multi-atlas. Each subject is shown with the manual segmentation of parietal cortex (green), hippocampi (pink), caudate nuclei (purple) and basal forebrain (blue). On the right side, the probabilistic atlas as average of the 12 subjects on the left, with the voxel-wise probabilistic labels shown in the space of the atlas for each of the mentioned regions. . . .	148
151-1	<b>Visual comparison of the inter-rater variability and automatic method in the segmentation of the left hippocampus.</b> Comparison between automatic method in red, rater <sub>1</sub> in yellow (expert) and rater <sub>2</sub> in turquoise (non expert) for the segmentation of hippocampi, in an axial slice. Regions of intersection between borders are rater <sub>1</sub> $\cap$ auto in orange, rater <sub>2</sub> $\cap$ auto in purple, rater <sub>1</sub> $\cap$ rater <sub>2</sub> in green and rater <sub>1</sub> $\cap$ rater <sub>2</sub> $\cap$ auto in white. . . .	151

152-1	<b>Intra-rater test-retest.</b> Box plot comparing two different manual adjustments of the same initial segmentation ( <i>adj1</i> , <i>adj2</i> ) and the automatic initialization ( <i>auto</i> ) measured with inverted Dice's score (1 - Dice's score), covariance distance (CovDist), symmetric Hausdorff distance (HD) and normalized symmetric contour distance (NSCD). Only the regions with 1 - Dice's score smaller than 1 have been considered (48 regions out of 89). The very low inverted Dice's scores (or very high Dice's score) proves that few manual interventions were required to obtain a visually optimal results, and that consecutive manual interventions on the same subject were performed consistently.	152
153-1	<b>Leave one out cross validation for the selected macro-regions.</b> Each point in the boxplot corresponds to the error at the given macro-region and for the given scoring system between the manual ground truth and the propagation of one of remaining 11 subjects. Differences between segmentations are scored with 1 - Dice score, covariance distance, Hausdorff distance and normalized symmetric contour distance, and the last three measures are plotted in log-scale. The correspondence between the x-axis and the macro-regions labels is reported in Table 146-1.	153
154-1	<b>In vivo experiment.</b> The result of the automatic algorithm tested on an <i>in vivo</i> acquisition. The subject, left in the original orientation, is provided with a visually good segmentation. In this setting, the multi-modal approach was not feasible due to the too low resolution of the diffusion weighted image.	154
155-1	<b>Leave-one-out parametrisation benchmarking.</b> Comparison between majority voting (MV), STAPLE and STEPS with a range of parametrisations. STEPS_K_N represents the STEPS method for $K = 5, 7, 10$ size of the kernel and $N = 5, 7$ number of layers.	155
170-1	<b>Bruker2nifti converter interface.</b> Code documentation can be found at the git-hub page provided in the publication [FSM <sup>+</sup> 17].	170
172-1	<b>Data folder structure.</b> From the root folder, each subfolder group is named <i>phase</i> (00_raw_data_zipped, 01_raw_data_unzipped_TMP ...), <i>study</i> (ACS, PTB ...) and <i>category</i> (ex_vivo01, ex_skull ...). Nomenclatures for <i>study</i> and <i>category</i> are the same for each <i>phase</i> .	172
174-1	<b>Schematic representation of the full data analysis pipeline.</b> Pipeline is divided in 10 phases. Developed and open sourced underpinning tools are <i>bruker2nifti</i> , <i>NiLabels</i> and <i>SpotANeonatalRabbit</i> . The central column represents the stages of the pipeline, named in blue on the right, the left column the data input and software and the lower right object the output location.	174

176-1	<b>Brain volume per subject.</b> Preliminary results for the on-going study shows different distributions in the brain volumes for term (T), pre-term (PT), late pre-term (LPT) and late pre-term with administration of corticosteroids (LPT+). Numbers are not providing statistically significant conclusions, although visually the group with the lowest brain volume appears to be the one of the fourth group. . . . .	176
177-1	<b>Chance model for the median volume to compare the rabbit full brain volume of term and pre-term.</b> The difference of the median between group T and group PT observed in Figure 176-1 is significant respect to the chance model of median of the bootstrapped volumes, for a Pearson correlation coefficient of 2.3. . . . .	177
178-2	<b>Chance models for the median volume for the four selected groups.</b> Figure 177-1 was providing only one of the possible six comparison between the boxplots shown in Figure 176-1. In this figure all the possible six models comparisons are shown. The highest difference is reported for late pre-term (LPT) and late pre-term with steroids (LPT+) with a Pearson index of 3.9. The median of the volumes for the pre-term and late pre-term with steroids are not statistically different, with a Pearson index of 0.6. . . . .	178
179-3	<b>Brain volumes Pearson correlation coefficients for the four selected groups.</b> Pearson correlation coefficients reported in Figure 177-2 are summarised in this graph. This representation will turn out to be relevant to compare the sub-volumes of the analysed rabbit brains. . . . .	179
180-1	<b>Brain volumes per subjects per regions.</b> As Figure 176-1, here we show the volumes of the regions that are believed to be affected by gestational age.	180
182-2	<b>Region-wise brain volumes Pearson correlation coefficients for the four selected groups.</b> Pearson correlation coefficients for the volumes of 9 selected regions. This graph provides a quick overview of the significance of the differences between the boxes of the boxplots for the region volumes shown in Figure 180-1. . . . .	182
183-1	<b>Fractional anisotropy (FA) for the 9 selected regions.</b> From this preliminary investigation, no sharp visual difference can be visually identified between the boxes of each region. . . . .	183
184-2	<b>Region-wise Fractional Anisotropy Pearson correlation coefficients for the four selected groups.</b> Pearson correlation coefficients for the volumes of 9 selected regions. This graph provides a quick overview of the significance of the differences between the boxes of the boxplots shown in Figure 181-1. . . . .	184

185-3	<b>Mean diffusivity (MD) for selected 9 regions.</b>	In contrast to what happens for the volume, and on a similar trend of the fractional anisotropy, MD does not appear to differentiate between groups. . . . .	185
186-4	<b>Region-wise Mean Diffusivity Pearson correlation coefficients for the four selected groups.</b>	Pearson correlation coefficients for the volumes of 9 selected regions. This graph provides a quick overview of the significance of the differences between the boxes of the boxplots shown in Figure 181-3.	186
196-1	<b>Comparison between an 8 weeks old rabbit (subject 12503) and 1 day old rabbit (subject 1305) acquired with <i>ex vivo</i> protocol.</b>	Newborn rabbit is shown as contour of the brain segmentation. Both subjects are oriented in stereotaxic coordinates (see Section 5.3.2 for details). . . .	196
196-2	<b>3D rendering of the newborn (1d) and adult (8w) brain tissue segmentation.</b>	Subjects and orientation are the same as in Figure 195-1. Left: superior view. Top right: lateral view. Bottom right: frontal view. .	196
198-1	<b>Allen mouse atlas, coronal section.</b>	A screenshot of a coronal section from the online Allen, [LHA+07] mouse histological atlas. This result was achieved annotating the histological sections of a mouse, and made quickly available in an interactive web interface. Combining the 3D MRI annotation, as shown in Figure 138-6 and the histological data acquired in this project, would produce a 3D atlas with histological resolution. Researches in this direction are presented in [PIY+18]. . . . .	198

# List of Tables

120-1	<b>Computational time in seconds of standard, diffeomorphic and diffeomorphic with approximated exponential integrators.</b> The same ADNI dataset presented in the previous section is employed to benchmark the non-rigid (Default) parametrisation, the Diffeomorphic and the diffeomorphic with Approximated Exponential Integrators (Diffeomorphic aei) in NiftyReg. Blue colours is employed when the proposed diffeomorphic aei is faster than the diffeomorphic method. The * indicate the cases when convergence occurred before the maximum number of 400 iterations. . . . .	120
141-1	<b>Delineated regions in the proposed new-born rabbit brain taxonomy.</b> For symmetric structures, we follow- -ed the convention left/right odd/even. An extended hierarchical taxonomy is provided in the supplementary material B of our paper [FvdMVDV <sup>+</sup> 18]. . . . .	141
147-1	<b>Macro-regions grouping.</b> For validation purposes, the 89 regions were grouped in to 16 macro-regions. The proposed grouping was constructed by keeping regions of similar importance or anatomy or quality together, in this order of preference. . . . .	147
151-1	<b>Quantification of the inter-rater variability and automatic method in the segmentation of left hippocampus.</b> Rater <sub>1</sub> (expert) and rater <sub>2</sub> (non expert) manually segmented the left hippocampus of an unlabeled and randomly selected subject. Resulting segmentations are compared with the automatic one. Differences are assessed with Dice's score, covariance distance (CovDist), symmetric Hausdorff distance (HD) and normalized symmetric contour distance (NSCD). .	151
160-0	<b>Newborn rabbit brain hierarchical taxonomy,</b> with abbreviation and numbering including the 89 regions proposed in the multi-atlas. . . . .	160



# Chapter 1

## Introduction

### Contents

---

<b>1.1</b>	<b>Background . . . . .</b>	<b>27</b>
<b>1.2</b>	<b>Research challenges . . . . .</b>	<b>29</b>
1.2.1	Diffeomorphic image registration . . . . .	29
1.2.2	Antenatal corticosteroids pre-clinical trial . . . . .	31
<b>1.3</b>	<b>Methodological contributions . . . . .</b>	<b>33</b>
<b>1.4</b>	<b>Thesis organisation . . . . .</b>	<b>35</b>

---

The two main research threads motivating this study are the integration of stationary velocity fields, as employed in diffeomorphic image registration, and the investigation of potential negative effects of administering antenatal corticosteroids, as part of the preterm birth treatment.

These two areas are introduced from the broader perspective of the collaboration between the clinical and the engineering domain, and this chapter briefly introduces the engineering tools here developed, with particular emphasis to their clinical motivations and subsequent challenges.

### 1.1 Background

Medical imaging is a wide, varied and multidisciplinary field, borrowing knowledge from several domains of science. Rather than remaining at the core of a single theoretical framework or a methodology, it customarily orbits around an instance of a clinical problem.

The role of the biomedical engineer working in the clinical environment is to provide technical support with algorithms development, software implementation and

in building reliable tools. Prompted by a practical goal, the boundaries between scientific domains such as mathematics, physics, mechanical engineering and computer science fade away to be recomposed in the final outcome: a tool aimed at tackling the initially given problem.

A most notable outcome of decades of experimentations and collaborations in this interdisciplinary domain is the Magnetic Resonance Imaging (MRI) technique. This ever-progressing radiological method created by advanced theoretical physics, carefully designed hardware and cutting edge software, is now widely utilised both in clinical practice and in clinical and pre-clinical research.

Processing and extending the images produced with an MR scanner is the subsequent domain of research. In the research presented in this thesis, a high resolution magnetic resonance imaging scanner for small animals in pre-clinical trials constitutes an important source of experimental data in understanding the effects of the administration of corticosteroids.

Compared to other investigation modalities aimed at the same goal, such as neurobehavioural assessments and histological studies, MRI has as well some advantages. MR images are digital representation of the anatomy, providing the possibility of using the magnetic properties of the tissue as a biomarkers to gain insights otherwise impossible to achieve. The preservation of the morphological structure of the tissue sample, not attainable with histology, attains a digital readouts that can be non-destructively analysed, and endlessly preserved, often automatically, with a wide range of reproducible methods.

The continuous technological advancements resulting in the increase of magnetic fields strength, the consequent increase of image resolution and the creation of new sequences had led to the need of facing new engineering challenges when analysing the subsequent images. The ubiquitous problems of image segmentation and registration are the main one, and they still require methodological and algorithmic advancements to improve their accuracy and decrease the computational time. Another challenge is the model selection and parameters optimisation, that must be tackled combining technologies and intuition in the perspective of the clinical or pre-clinical setting and aims [EB07].

In this thesis we tackle both a methodological and a clinical problem. The first one is the investigation of novel methods to improve accuracy and computational time in the widely utilised diffeomorphic image registration. In particular we provide a new class of methods to integrating stationary velocity fields (SVF) combining the known methods of *exponential integrators* [HO10] with the *scaling and squaring* method [ACPA06].

The second problem we address in this thesis is the development of a pipeline for the MRI data analysis resulting from a pre-clinical study aimed at investigating

the effects of antenatal corticosteroids on the newborn rabbit brain. This part of the study is carried forward in collaboration with the Department of Development and Regeneration, Woman and Child Cluster and the moSAIC Facility, Biomedical MRI, Department of Imaging and Pathology both located at the Katholieke Universiteit Leuven. The main outcome of this study is the first pipeline for the automatic analysis of the newborn rabbit brain based on the first multi-modal multi-atlas for the rabbit brain [FvdMVDV<sup>+</sup>18].

## 1.2 Research challenges

Even if apparently very different in nature, the underpinning problems motivating the two parts of the thesis are related by the need for engineering tools to automatise MRI data analysis as accurately and quickly as possible. These two parts, introduced in the previous section, are detailed below.

### 1.2.1 Diffeomorphic image registration

Medical image registration is a set of tools and techniques aimed to solving the problem of determining correspondences between two or more images. Its development is a challenging field that has seen the application of a growing number of mathematical theories in the research of customizations, improvements of precision and reduction of computational time. The range of applications of image registration in the medical domain extends to several domains, ranging from lung motion correction [MHM<sup>+</sup>11, MHSK], Alzheimer disease diagnoses [PCL<sup>+</sup>15, FF97, GWRNJ12], and image mosaicing [VPM<sup>+</sup>06, Sze94].

Image registration is as well utilised in computational anatomy to quantify the differences between two images [JDJG04, HOP08, Pen11, MP14]. Its main aim is to find the transformation minimising the differences between the two images and subsequently is to establish a metric on the space of transformations. A consistent mathematical framework provided with the sought metric, is the space of transformations parametrised with smooth tangent vector fields. In this setting, the employed transformations belong to the space of smooth mappings with smooth inverse (or diffeomorphisms) and their parametrisations belongs to an Euclidean space where the metric is well defined.

Other than providing a metric space in bijective correspondence with the transformations, diffeomorphisms provide as well a sound deformation model. Due to the smoothness of the transformation (and up to the resampling imposed by the digitalisation), the images belonging to the same orbit of the action of diffeomorphisms are invariant for their topological genus.

When the tangent vector field is time independent (also called stationary velocity field or SVF), the corresponding diffeomorphic algorithm is therefore based on the transformation between the time-independent tangent vector field (or the parametrisation), and the actual transformation (or the one parameter sub-group of diffeomorphisms, also called flow of diffeomorphisms).

In the Lie group theory language, the space of the transformations is called *Lie group* and the space of the parametrisation is the *Lie algebra*. As schematically represented in Figure 30-1, the transformation between the Lie group and the Lie algebra is called Lie logarithm and the inverse transformation is the Lie exponential, consisting of the numerical integration of the tangent vector field. Their names are after the finite and linear dimensional case, where for the matrix Lie group and matrix Lie algebras, the Lie logarithm and Lie exponential are computed with a closed form solution corresponding to the Taylor expansion series of the logarithm and exponential for matrices [HSSE09].

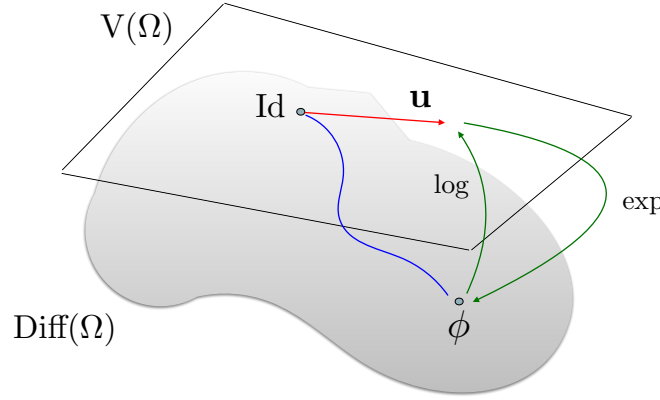


Figure 30-1: **Schematic overview of the infinite dimensional Lie group and Lie algebra of diffeomorphisms.** The infinite dimensional Lie group of diffeomorphisms over  $\Omega$ , indicated with  $\text{Diff}(\Omega)$  is represented with a grey surface. To each diffeomorphic transformation  $\phi$  corresponds an element  $u$  in the infinite dimensional tangent vector space, the Lie algebra  $V(\Omega)$ . The correspondence between Lie group and Lie algebra and vice versa are the Lie logarithm and the Lie exponential respectively.

The idea of decoupling the parametrisation and the actual transformation can be seen with a simple example based on a rotation of  $\pi/8$  radians respect to the centre of the image. Figure 31-1 shows a brain coronal slice from the Sythetic Brain-Web<sup>1</sup> dataset whose rotation is represented in the centre with its parametrisation (red arrows) and flow (blue integral curves). To each possible smooth vector field corresponds an element of the Lie algebra, represented in the figure above as a single vector of an infinite dimensional vector space, tangent to the Lie group of diffeomor-

<sup>1</sup><http://brainweb.bic.mni.mcgill.ca/brainweb/> last access March 23, 2019.

phisms, where the corresponding transformation lies. For brevity the Lie algebra is represented as a 2D plane and the Lie group as a 2D surface.

The Lie exponential is at the core of the SVF-based diffeomorphic registration framework (this will be seen in details in Chapter 4) and a fast and efficient numerical computation of the Lie exponential makes this approach possible. A milestone towards this direction is the phase flow method [YC06] or scaling and squaring method [ACPA06] for the integration of SVF.

Even if the core of the scaling and squaring method is still based on the Euler method, it is faster and more accurate than the Euler method itself due to the recursive squared composition performed when subdividing the trajectory to be integrated in sub-steps. The challenge of improving the accuracy and computational time of the numerical method remains an open field of research, and in this thesis we present the steps forwards made in addressing this problem.

### 1.2.2 Antenatal corticosteroids pre-clinical trial

Rather than investigating the effects of a new drug to be introduced in the market, the proposed pre-clinical trial investigates possible negative effects of the antenatal corticosteroids that are currently prescribed in the clinical practice. After the importance of enhancing the development of the preterm lungs, steroids are administered during pregnancy when the symptoms of a preterm birth are detected.

In the recent years, longitudinal clinical studies carried forward by Newnham [New01] and Huang [Hua11] have challenged the use of corticosteroids as potentially harmful for the cognitive abilities in adult life. Due to the impact and the wide range of confounding factors it is reasonable to consider impossible to prove or disprove this claim on a human cohort.

Moreover the preterm birth syndrome (PTB) is in most cases induced by a range of concomitant infections, potentially affecting the neurodevelopment of the affected subject. A statistical analysis on data collected from a wide range of clinical environments may not provide any insight in isolating the consequences of PTB from the consequences of the possible concomitant infection. It is also intrinsically difficult to sample preterm newborn in groups with the same or similar associated precursors, as the determining factor inducing PTB is often not diagnosed.

For this reason in the spring of 2015 a pre-clinical study had started at KU Leuven to assess the effects of steroids on a rabbit animal model. The rabbit is the small animal with the closest white matter maturation to human, and the cost and availability enable for large cohort study.

At the beginning of the study, the main challenge was to create a study design to optimally model the human case in order to provide useful insights for the clinical

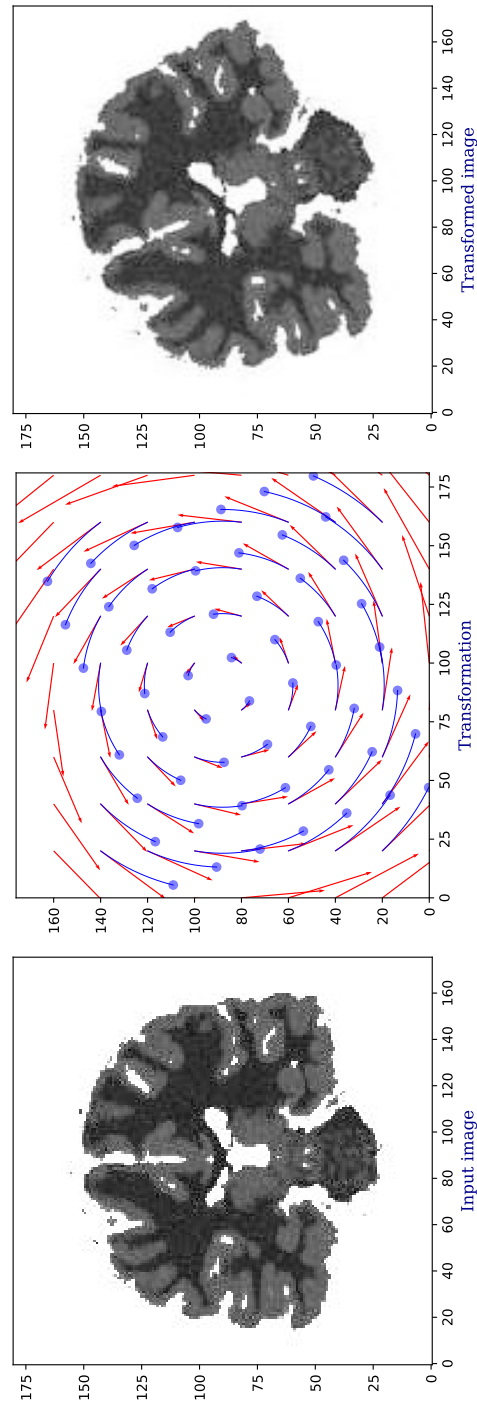


Figure 31-1: **Stationary velocity field and corresponding integral curves of a rotation.** A sagittal slice of a human brain MRI (left), a tangent vector field generated by a rotation of 30 degrees respect to the centre (centre) and the result of the rotation applied to the first image (left). The integral curve of the tangent vector field, in blue, represent the position where each voxel after the transformation parametrised by the SVF, in red.

case. The second challenge was the creation of an unbiased segmentation of the region of interests for the further MRI quantification, and for the automatic creation of a segmentation, such as the one shown in Figure 33-1.

Rats and mice for which annotated anatomies are available in literature, would have provided a less effective model respect to the rabbits in relation to the human myelination. The rabbit is not as widely studied and there are neither digital multi atlas for the newborn, nor newborn taxonomies. As a consequence, at the beginning of the study it had not been possible to have a method for the automatic segmentation for a region-wise investigation.

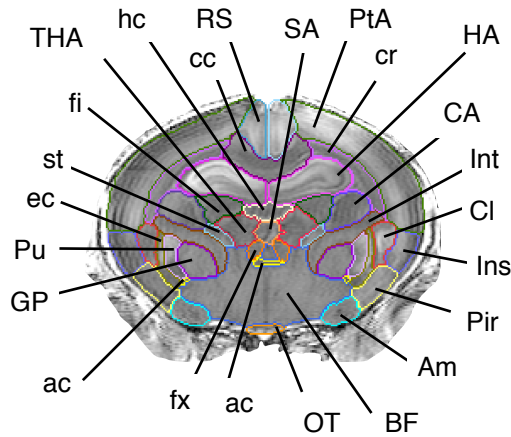


Figure 33-1: **Axial slice of the newborn rabbit brain manually segmented with the corresponding taxonomy.** The multi-modal multi-atlas proposed in this section allows to create an automatic parcellation of the newborn rabbit brain, as the one shown above. Further details of the method and the complete taxonomy are provided in Chapter 5.

The lack of this asset made impossible to create an unbiased and reproducible segmentation of the acquired images. The manual approach, the only option available at the beginning of the study, would have been impractical for a large dataset.

### 1.3 Methodological contributions

To improve accuracy and computational time of the numerical computation of the Lie exponential, for the first time the numerical integrator methods had been combined with the scaling and squaring algorithm to provide a novel method. This had been proved to constitute the state-of-the-art for the integration of tangent vector fields, and it had been integrated in the widely utilised framework NiftyReg [MRT<sup>+</sup>10]. The resulting method had been published in the conference paper [FLD<sup>+</sup>16] and a benchmarking against the previous method is proposed in Chapter 4.

Despite the improvements in the numerical computation of the Lie exponential, this constitute only a small component in the image registration framework. The main bottleneck of the registration algorithm is in the optimisation of the cost function and the improvements provided by the proposed method in the numerical computation of the Lie exponential had not provided a significant improvements in the overall method. A collaborative contribution had addressed the problem of the optimisation of the cost function, applying two forward backward splitting (FBS) methods (FISTA and iPiano) for the convex function optimisation [EMF+18].

In the pre-clinical study, image registration had been widely applied for the segmentation propagation and label fusion method in producing an automatic segmentation. Despite related to the main methodological contribution presented in this thesis, the proposed Lie exponential had not been applied in this context. Due to the need of pursuing the investigation of the effect of ACS with well established and well known methodologies, and after the relatively low improvement in the computational time of the novel integration method in the overall framework, in particular for large images, we had used instead the standard diffeomorphic method for the integration of stationary velocity fields implemented in NiftyReg. This is also motivated by the increase in computational time and by the fact that at this stage we had not implemented neuromorphological investigations based on the image transformations.

In pursuing the investigation of the effects of steroids in the neurdevelopment after preterm birth, a range of computational tools had been developed and open-sourced during the study. The first contribution of this part of the thesis is the creation of the first image converter from Bruker to nifti format, compatible with ParaVision version 5 and 6. This computational tool, despite being a basic component, was not publicly available at the moment of starting the study, and its lack would have made the research unfeasible [FSM+17].

The second main contribution, outcome of the main challenge, is the production of the first multi-modal multi-atlas for the neonatal rabbit brain, with a taxonomy and a stereotaxic orientation, proposed in Chapter 5. In the process of producing the multi-atlas, we present as well in this thesis a list of errors and the issues that we have had in developing setting up the protocol and preparing the acquisition.

The third contribution is the construction of the pipeline for the full data analysis investigation, going from the initial acquisition in Bruker format to the biomarkers readouts of volume, fractional anisotropy (FA) and mean diffusivity (MD), passing through the automatic segmentation method based on the proposed multi-atlas.

At the moment of writing this thesis, a new study with the adult rabbit model brain (week 8) is currently in progress. This is left as future work, although promising results in term of image quality and preliminary template creation.

The last contribution is the analysis of the data obtained with this pipeline, that is

intended to provide an insight about the effects of the administration of the antenatal corticosteroids on the main MRI biomarkers.

## 1.4 Thesis organisation

As the research carried forward in the last 3 years was devoted to address a methodological and a pre-clinical challenge, the thesis structure does not follow the usual broad subdivision in state-of-the-art, contributions, limitations and future work.

Each chapter of the thesis is intended as an independent unit, each one having its table of content, state-of-the-art, limitations, possible contribution, limitations and bibliography related to the proposed topic. All the sections remains connected by the same underpinning motivation exposed in this chapter and the hyper-references of images and equations across chapters are facilitated by the correspondence between their numbering with the page where they appear or where they are cited.

- Chapter 1** Thesis introduction, research challenges and subsequent contributions provided during the PhD studies. Number of words: 3042.
- Chapter 2** Here we present presents the clinical problem motivating the whole study. Pre-term birth is introduced with its epidemiology, social costs, etiology, known pathogenesis and therapies. Particular attention is given to the problem of confounding factors in the clinical setting, motivating the proposed pre-clinical study based on a rabbit animal model presented in the next chapter. The clinical question and the need for further investigation is expressed in the last section. Number of words: 3134.
- Chapter 3** In this chapter we introduce the experiment design and the dataset. With the design and the sample processing, we provide the acquisition protocol for the *in vivo* and *ex vivo* brain rabbit samples. Number of words: 3708
- Chapter 4** Two of the fundamental tools in medical image analysis are image segmentation and image registration. This chapter is devoted to the application of image registration as a tool for the automatic segmentation of the newborn rabbit brain images. The first contribution of this thesis is the methodological investigation to tackle the Lie exponential computation bottleneck when dealing with diffeomorphic image registration frameworks. Number of words: 13936
- Chapter 5** This chapter presents the second main contribution of the thesis: the first high resolution MR multi-modal multi-atlas for the Neonatal rabbit brain. This is

applied with a segmentation propagation and label fusion method to automatise the Newborn rabbit brain segmentation. Number of words: 7948

**Chapter 6** The automatic segmentation propagation method based on the multi-atlas introduced in the previous chapter is embedded in the pipeline applied to the data analysis. This chapter presents the data analysis pipeline and the third main contribution of the thesis: outcome of the analysis of the volume, FA and MD of the acquired dataset. Number of words: 4087

**Chapter 7** The final chapter is divided in two parts. The first part summarises the contributions and discusses the proposed methodologies to provide hints for future work. The second part explicitly lists a range of possible future work and directions. Number of words: 2998

Total number of words: 38853

## Chapter bibliography

- [ACPA06] Vincent Arsigny, Olivier Commowick, Xavier Pennec, and Nicholas Ayache. A log-euclidean framework for statistics on diffeomorphisms. In *Medical Image Computing and Computer-Assisted Intervention–MICCAI 2006*, pages 924–931. Springer, 2006.
- [EB07] Bradley J Erickson and Jan C Buckner. Imaging in clinical trials. *Cancer informatics*, 4:13, 2007.
- [EMF<sup>+</sup>18] Michael Ebner, Marc Modat, Sebastiano Ferraris, Sébastien Ourselin, and Tom Vercauteren. Forward-backward splitting in deformable image registration: A demons approach. In *Biomedical Imaging (ISBI 2018), 2018 IEEE 15th International Symposium on*, pages 1065–1069. IEEE, 2018.
- [FF97] Nick C Fox and Peter A Freeborough. Brain atrophy progression measured from registered serial mri: validation and application to alzheimer’s disease. *Journal of Magnetic Resonance Imaging*, 7(6):1069–1075, 1997.
- [FLD<sup>+</sup>16] Sebastiano Ferraris, Marco Lorenzi, Pankaj Daga, Marc Modat, and Tom Vercauteren. Accurate small deformation exponential approximant to integrate large velocity fields: Application to image registration. In *Proceedings of the IEEE Conference on Computer Vision and Pattern Recognition Workshops*, pages 17–24, 2016.

- [FSM<sup>+</sup>17] Sebastiano Ferraris, Dzhoshkun Ismail Shakir, Johannes Van Der Merwe, Willy Gsell, Jan Deprest, and Tom Vercauteren. Bruker2nifti: Magnetic Resonance Images converter from Bruker ParaVision to Nifti format. *The Journal of Open Source Software*, 2(16), Aug 2017.
- [FvdMVDV<sup>+</sup>18] Sebastiano Ferraris, Johannes van der Merwe, Lennart Van Der Veen, Ferran Prados, Juan-Eugenio Iglesias, Andrew Melbourne, Marco Lorenzi, Marc Modat, Willy Gsell, Jan Deprest, and Tom Vercauteren. A magnetic resonance multi-atlas for the neonatal rabbit brain. *NeuroImage*, 2018.
- [GWRNJ12] Serge Gauthier, Liyong Wu, Pedro Rosa-Neto, and Jianping Jia. Prevention strategies for alzheimer’s disease. *Translational neurodegeneration*, 1(1):1–4, 2012.
- [HO10] Marlis Hochbruck and Alexander Ostermann. Exponential integrators. *Acta Numer*, 19:209–286, 2010.
- [HOP08] Monica Hernandez, Salvador Olmos, and Xavier Pennec. Comparing algorithms for diffeomorphic registration: Stationary lddmm and diffeomorphic demons. In *2nd MICCAI workshop on mathematical foundations of computational anatomy*, pages 24–35, 2008.
- [HSSE09] Darryl D Holm, Tanya Schmah, Cristina Stoica, and David CP Ellis. *Geometric mechanics and symmetry: from finite to infinite dimensions*. Oxford University Press London, 2009.
- [Hua11] Li-Tung Huang. The link between perinatal glucocorticoids exposure and psychiatric disorders. *Pediatric research*, 69:19R–25R, 2011.
- [JDJG04] Sarang Joshi, Brad Davis, Matthieu Jomier, and Guido Gerig. Unbiased diffeomorphic atlas construction for computational anatomy. *NeuroImage*, 23:S151–S160, 2004.
- [MHM<sup>+</sup>11] JR McClelland, S Hughes, M Modat, A Qureshi, S Ahmad, DB Landau, S Ourselin, and DJ Hawkes. Inter-fraction variations in respiratory motion models. *Physics in medicine and biology*, 56(1):251, 2011.
- [MHSK] J. R. McClelland, D. J. Hawkes, T. Schaeffter, and A. P. King. Respiratory motion models: A review. *Medical Image Analysis*, 17(1):19–42, 2015/04/01.

- [MP14] Nina Miolane and Xavier Pennec. Statistics on Lie groups : a need to go beyond the pseudo-Riemannian framework. In *MaxEnt 2014*, Amboise, France, September 2014.
- [MRT<sup>+</sup>10] Marc Modat, Gerard R Ridgway, Zeike A Taylor, Manja Lehmann, Josephine Barnes, David J Hawkes, Nick C Fox, and Sébastien Ourselin. Fast free-form deformation using graphics processing units. *Computer methods and programs in biomedicine*, 98(3):278–284, 2010.
- [New01] John P Newnham. Is prenatal glucocorticoid administration another origin of adult disease? *Clinical and Experimental Pharmacology and Physiology*, 28(11):957–961, 2001.
- [PCL<sup>+</sup>15] Ferran Prados, Manuel Jorge Cardoso, Kelvin K Leung, David M Cash, Marc Modat, Nick C Fox, Claudia AM Wheeler-Kingshott, Sebastien Ourselin, Alzheimer’s Disease Neuroimaging Initiative, et al. Measuring brain atrophy with a generalized formulation of the boundary shift integral. *Neurobiology of aging*, 36:S81–S90, 2015.
- [Pen11] X Pennec. From riemannian geometry to computational anatomy. *Emerging Trends in Visual Computing, Statistical Computing on Manifolds: From Riemannian Geometry to Computational Anatomy*, 5416:347–386, 2011.
- [Sze94] Richard Szeliski. Image mosaicing for tele-reality applications. In *Applications of Computer Vision, 1994., Proceedings of the Second IEEE Workshop on*, pages 44–53. IEEE, 1994.
- [VPM<sup>+</sup>06] Tom Vercauteren, Aymeric Perchant, Grégoire Malandain, Xavier Pennec, and Nicholas Ayache. Robust mosaicing with correction of motion distortions and tissue deformations for in vivo fibered microscopy. *Medical image analysis*, 10(5):673–692, 2006.
- [YC06] Lexing Ying and Emmanuel J Candès. The phase flow method. *Journal of Computational Physics*, 220(1):184–215, 2006.

## Chapter 2

# Preterm birth and corticosteroid administration: an overview

### Contents

<b>2.1</b>	<b>Epidemiology . . . . .</b>	<b>40</b>
<b>2.2</b>	<b>Public attention and social costs . . . . .</b>	<b>42</b>
<b>2.3</b>	<b>Etiology, pathogenesis and long term consequences . . .</b>	<b>44</b>
<b>2.4</b>	<b>Preventions, treatments and therapies . . . . .</b>	<b>45</b>
<b>2.5</b>	<b>Clinical question . . . . .</b>	<b>47</b>

Most of the questions that are awaiting to be answered by medical researchers investigating spontaneous preterm delivery therapies are driven by the urge of improving the early treatment of this syndrome. Questions relate in particular to the prediction of the neurocognitive consequences of the praxis of administering corticosteroids as growth enhancer.

In this chapter, we briefly introduce the preterm births clinical background through a review of the main publications related to its epidemiology, social costs, etiology, pathogenesis, consequences and treatments. The main resource for this chapter is the recent literature about the current therapies involving the administration of corticosteroids, with particular attention towards the clinical needs and practices.

We address in particular the possible covariate of preterm birth, such as concomitant infections, maternal lifestyle, age and education, potentially affecting the neurological development of the newborn brain.

The main goal of this chapter is to provide the reader with a perspective upon the complexity of the problem, in particular upon the difficulties in drawing statistically significant conclusions from human cohort studies, as naturally biased by unquantifiable confounding factors. Emphasis on this problem is aimed at providing the

motivation for the pre-clinical study proposed in Chapter 3.

## 2.1 Epidemiology

For humans, the length of a normal pregnancy is expected to range between 37 and 42 weeks. Preterm birth (PTB) syndrome is the varied set of symptoms and medical conditions of a preterm child, delivered before the 37<sup>th</sup> gestational week.

Medical literature and the World Health Organisation agree with the PTB classification shown in Figure 40-1. *Extremely preterm* babies are born before 28 weeks or less of gestational age, *very preterm* between 28 and 32 and *moderate or late preterm* between 32 and 37. This classification reflects the severity of PTB, as related to gestational age at delivery. The 24<sup>th</sup> gestational week is the *viability threshold* [SDR<sup>+</sup>14]. This threshold was established after medical considerations as well as facing ethical dilemmas in respect to the extremely low survival expectation. The ethical side is considered by Behrman et al. [BB<sup>+</sup>07], and more recently by Doronjski and Stojanović [DS16].

The 2012 and 2013 publications by Blencowe et al. [BCO<sup>+</sup>12, BCC<sup>+</sup>13] examine the data about early labours in 184 countries between 1990 and 2010. After inclusion/exclusion criteria to limit the uncertainty and variations between countries, the research claims that PTB affects 11% of the overall births worldwide, ranging from 5% to 18%. The first of the two studies considers data collected from 41 countries and the proportion of the affected population splits into 5.2%(±0.1%) extremely preterm, 10.4%(±0.1%) very preterm and 84.3%(±0.2%) moderate or late preterm.

The impact PTB worldwide is summarised in Figure 42-1, from [BCO<sup>+</sup>12]. The same paper reports that the mortality rate is generally higher in low-income countries. In high-income countries, where intensive care is available, very preterm newborns are more likely to survive at the expense of suffering from severe medical conditions such as pulmonary distress syndrome and sepsis, potentially degenerating into cerebral palsy.

A study by Tyson et al. [TPL<sup>+</sup>08] based in the U.K. investigates the survival rate with intensive care treatment in a cohort of 3702 preterm infants born in 19 centres of the Neonatal Research Network. As reported in the paper and summarised in Figure 43-1, for 24 completed weeks gestational age and birth weight ranging between 501 and 600 grams, survival rate is 51%/41% (female/male). The observed survival rate decreases to 2%/3% (female/male) for 22 completed weeks gestational age and birth weight between 401 and 500 grams. Among the survivors of the first cited group, only 37%/24% (female/male) do not appear to have long-term complications, while for the second cited group the percentage decreases to 2%/2% (female/male).

Concurrent pathologies affecting mothers and potentially inducing PTB may fur-

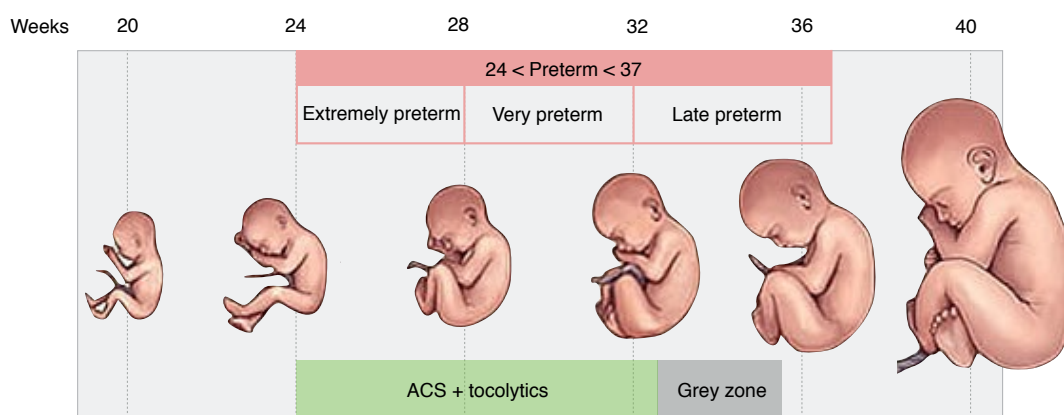


Figure 40-1: **Fetal growth from 20 to 40 gestational week.** Any childbirth between the 24<sup>th</sup> and the 37<sup>th</sup> week is considered preterm. According to the severity different treatments may be required. For high risks of preterm and very preterm birth (between 24<sup>th</sup> and the 37<sup>th</sup> gestational week) administration of antenatal corticosteroids (ACS) and tocolytics is customary: the positive impact of the treatment on the lungs growth is believed to compensate for possible brain insults caused by ACS. To balance risks and benefit of administering ACS for late preterms, in particular between the 25<sup>th</sup> and the 35<sup>th</sup> gestational week, it is crucial to quantify the possible negative effects of ACS administration. Fetuses images courtesy of [hopkinsmedicine.org](http://hopkinsmedicine.org).

ther affect the newborn health when compared to non-pathologically induced PTB at the same gestational age. It is therefore relevant to consider statistical correlations with other common causes of child mortality, such as HIV and malaria. Moreover early labour can be dependent on the specific therapy that the mother is undergoing at the time of preterm delivery. For example Lopez et al. [LFH<sup>+</sup>12], in a retrospective cohorts selected in Barcelona area (Spain), reported that highly active antiretroviral therapy (HAART) for HIV treatment can induce PTB, and risks of PTB is higher for both HIV HAART and non-HAART. According to the study of van der Broek [vdBJBN14] lead in Malawi, persistent malaria, mother's age below 20 and anemia increase the chances of PTB, while no relationship between HIV and PTB was found. For a cohort study in Tanzania, Zach et al. [ZGA<sup>+</sup>14] identified maternal age, maternal illiteracy, malaria, gastrointestinal parasites (*Entamoeba coli*), no low pregnancy weight gain, and HIV disease as PTB risks factors. Again in Tanzania, studying malaria pathogenetic mononuclear cell infiltration in a cohort of placentae, Mendez et al. [MOI<sup>+</sup>00] reported a correlation between *placental malaria* and PTB.

In the study by Liu et al. [LJC<sup>+</sup>12], where PTB is defined as a syndrome, authors did not discriminate between the consequence that caused the increase in the mortality rate and PTB itself. Therefore, if for one subject the cause of mortality is attributed to sepsis, the pathology was not classified as PTB-induced sepsis. The same study also emphasised a methodological limitation, estimating that in 2012 only

2.7% of deaths of children younger than 5 years worldwide were medically certified.

The claimed impossibility of collecting an informative or accurate enough medical report for each single case makes misdiagnosis and missed diagnosis a concerning source of bias. Moreover, what emerges from the mentioned epidemiological statistical studies is that the wide range of possible concomitant pathologies inducing PTB are intrinsically biased by the wide range of concomitant diseases and therapies. This makes difficult to establish with any degree of confidence a generalisable cause leading to PTB and to separate the consequences of PTB from its precursors.

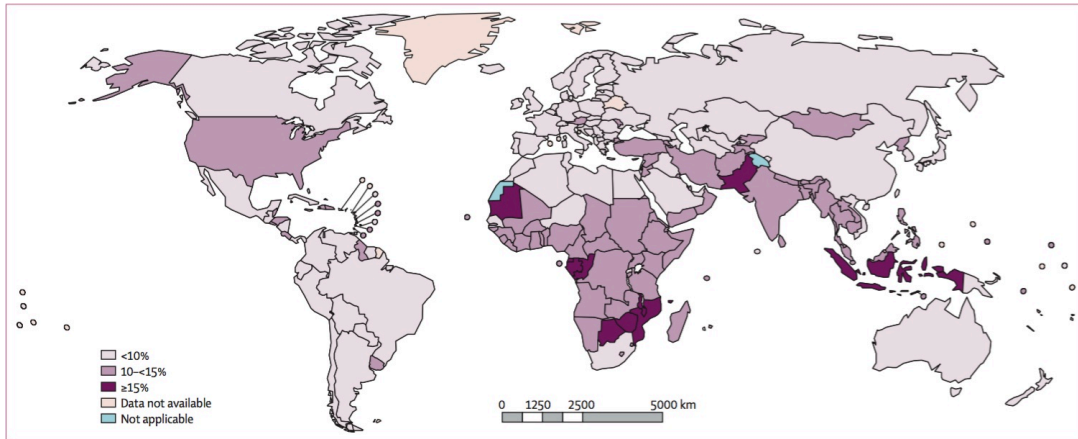


Figure 42-1: **Estimated preterm birth rate by country for the year 2010.** PTB appears to equally affect low and high income countries. Image from [BCO<sup>+</sup>12].

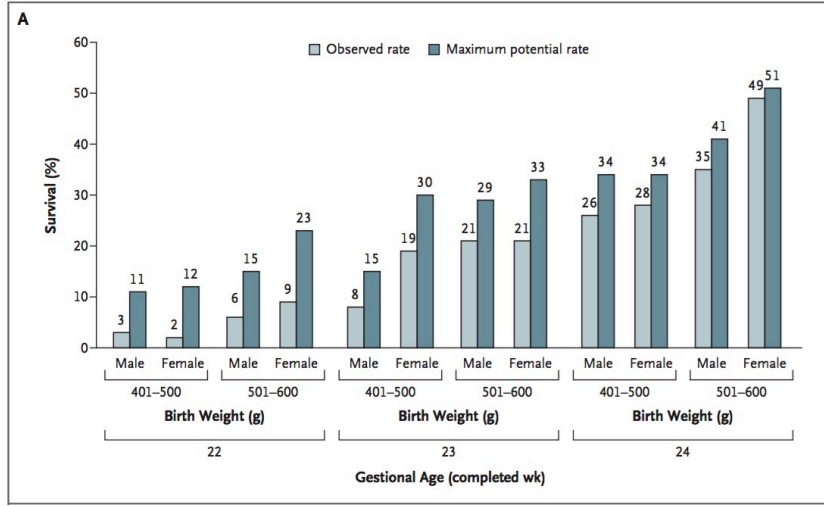
## 2.2 Public attention and social costs

Data published in recent years, as in the already cited [BCO<sup>+</sup>12] and in [HKML13], are raising the attention of private and public associations towards PTB. In the study about the incidence of PTB in the time lapse 1989–2004, proposed by VanderWeele [VLL12], preterm births in the U.S. has increased from 11.2% to 12.8% in this time-range. There are several active charities and foundations working to engage the public, support parents and to fund researches. It is worth mentioning Bliss ([www.bliss.org.uk](http://www.bliss.org.uk)), Borne ([www.borne.org.uk](http://www.borne.org.uk)) Tommy's ([www.tommys.org](http://www.tommys.org)) and the Bill and Melinda Gates Foundation ([www.gatesfoundation.org](http://www.gatesfoundation.org)), each raising several million pounds of donation per year.

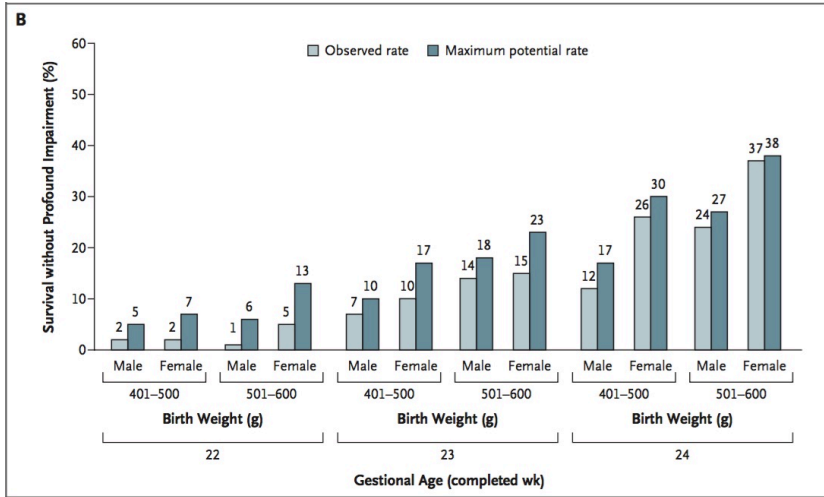
Regarding the financial impact, Petrou et al. in 2006 [PHB<sup>+</sup>06] reported that, in the U.K. for the first 12 months of life, the social costs of PTB is on average almost three times higher when compared to the term birth. If considering only the early interventional costs at birth for a cohort selected in Massachusetts, Clemens et al. [CBAW07] reported an overall increase of costs by two for the Late preterm and and

by seven for extremely and very preterm.

These two studies did not considered the healthcare and social costs related to the potential long term effect of PTB in teenage and adult life. In the study by Mangham et al. [MPD<sup>+</sup>09] reported the costs related to the first 18 years after birth of a cohort of PTB affected children in England and Wales. The average cost increase respect to the term child was estimated as £22885 for late preterm, £61781 for very preterm and £94740 for extremely preterm.



(a)



(b)

Figure 43-1: **Observed and maximum potential PTB rates of survival and survival without profound impairment.** (a) presents the relation between gestational age, divided by weight and sex, versus the observed rate of survival and the maximum potential rate (upper bound for the maximum potential percentage of infants with a favourable outcome). (b) the proportions of survivors without profound impairments after intensive care. Image from [TPL<sup>+</sup>08].

## 2.3 Etiology, pathogenesis and long term consequences

As previously reported, it is not possible to isolate a single cause of preterm birth. Multiple pathological processes including physiological and bacteriological conditions can lead to spontaneous preterm labour. According to Romeo et al. [RDF14], one third of PTB is caused by intra-amniotic infection and is induced by the consequent inflammatory process. As underlined by Goldenberg et al. [GCIR08], 30% of bacterial infections can reach the fetal circulation resulting in an inflammation response. The risks for long term complications for such cases are therefore not only a consequence of the PTB, whereas the PTB itself can be induced by the consequence of bacterial infections. Other risk factors for PTB are preterm prelabour rupture of membranes (PROM), preeclampsia or eclampsia, history of spontaneous or surgical abortion, maternal age and weight, genetic predisposition, multiple pregnancies and drug abuse.

Early labour can be as well medically induced, for example after maternal or fetal concomitant diseases. *Medically indicated PTB* is particularly relevant in the light of the findings of the already mentioned study by VanderWeele et al. [VLL12]. For the selected U.S. cohort, the paper reports that between 1989 and 2004 spontaneous rates of early labour declined by 21% (from 7.8% to 6.2% overall), while medically indicated early labour increased by 94% (from 3.4% to 6.6% overall), leading to an overall increase of the PTB.

The prediction of spontaneous preterm birth during pregnancy remains an open challenge. The majority of women experiencing preterm birth present with symptoms of cramping abdominal pain, or amniotic fluid or blood loss. Consequent investigations include biochemical analysis and ultrasound examination, other than well-being fetal assessment by fetal heart rate monitoring and uterine contractions assessment with cardiotocography. Examination of cervical dilation and cervical effacement are performed on ultrasound rather than with a speculum or digital examination to avoid iatrogenic increase of the risk of early labour. Other microscopy tests such as vaginal swabs and fetal fibronectin test (FFT) may be performed to help in the prediction of PTB. To assess the cervical changes, a standardised scoring system was introduced by Dr. Edward Bishop in 1964 and subsequently kept up-to date with the new technologies and advances in knowledge. A statistical comparison between this method and the analogous cervical score, introduced in 1982, was proposed by Newman et al. [NGI<sup>+</sup>08] in 2008.

The range of pathologies originating from PTB is believed to be mainly related to the newborn lungs underdevelopment at birth. In PTB cases, the observed lack of surfactant layer in the lungs can result in respiratory distress syndrome (RDS) [HWS<sup>+</sup>10], sepsis and consequent enterocolitis or meningitis [P<sup>+</sup>12]. In addition, in the last 5 weeks of normal gestation the brain rapidly develops one third of its final

weight. When premature, this important growth takes place outside the womb, where the newborn is exposed to potential risks. The resulting neurological consequences, including white matter injuries (WMIs) and intraventricular hemorrhages (IVHs), is termed *encephalopathy of prematurity* (EoP) [CEC<sup>+</sup>08, Vol09, IHW<sup>+</sup>99]. The already mentioned preterm prelabour rupture of membranes (PPROM) is strictly related to PTB, involving 40% of the PTB cases. The mortality for deliveries after PPRM is a direct consequence of the related PTB [MW96, Car06].

If some of the impairments can be detected at birth (Wood et al. [WMC<sup>+</sup>00]) and early childhood (Hack et al. [HF99]), PTB also impacts late childhood, teenage and adult life, causing learning difficulties (Saigal et al. 2003 [SdOW<sup>+</sup>03], Marlow et al. [MWBS05], Moster et al. [MLM08], Huddy et al. [HJH01] and Luu et al. [LMA<sup>+</sup>11]), ADHD (Rabie et al. [RBM<sup>+</sup>15]), general behavioural problems (Mathewson et al. [MCD<sup>+</sup>17], Hille et al. [HDOS<sup>+</sup>01]) as well as cardiovascular and metabolic disorders (Saigal et al. 2008 [SD08], Anderson et al. [ADG<sup>+</sup>03]).

Similarly to what happened in understanding the causes of PTB among a range of pathologies, isolating the consequences on a long term study is an open challenge. Non-PTB related factors can bias the outcomes of the neurobehavioural assessment of an adult born preterm respect to the control match. Moreover, biological factors leading to learning difficulties may not be detectable in the early stages of life.

For this reason neonatal magnetic resonance imaging (MRI) techniques have appeared to be a feasible and promising option in the understanding of neuropathologies related to EoP from an early stage of development (Woodward et al. [WAA<sup>+</sup>06], Melbourne et al. [MERB<sup>+</sup>13]).

Several clinical measures are available to try to minimise the adverse consequences of PTB. One in particular, main topic of the next section, is the administration of corticosteroids through the mother, designed to anticipate the development of the lungs and reduce the risk of respiratory distress.

## 2.4 Preventions, treatments and therapies

As reported by Behrman et al. [BB<sup>+</sup>07], screening for infections, adequate diet and improved lifestyle before conception can help in preventing PTB. After conception, when there is a risk of delivery between the viability threshold (24<sup>th</sup> gestational week) and when the fetus is expected to be fully developed (37<sup>th</sup> gestational week), a range of clinical procedures designed to postpone the birth and to limit the negative consequences can be applied. According to the pathogenesis, they can be antibiotics to reduce infections or tocolytic drugs to delay labour before significant cervical changes occur. Surgical cervical cerclage can be performed if there is a risk of cervical weakness when no infection, uterine contractions, bleeding or PROM are present. Again

Behrman et al. [BB<sup>+</sup>07] investigated the rate of success of these therapies: tocolytics in particular can be administered to buy time for the corticosteroids administration via intramuscular injection to the mother, whose effect requires usually one day of delay.

As reported by Roberts et al. [RD06], statistical evidence shows that antenatal corticosteroids (ACS) are safe for the mother and effective in reducing respiratory distress syndrome and intraventricular hemorrhage, leading to a significant reduction in rates of neonatal death. This reduces the rate of intensive care admissions and the overall risks of systemic infections. The decision of corticosteroid administration requires all the clinical aspects to be considered and may be offered between the starting of the 24<sup>th</sup> and late 34<sup>th</sup> week, or even considered for the 23<sup>rd</sup> week. It can be administered in a single course or in two subsequent courses.

Again Roberts et al. compares the use of ACS to a 1-week increase in gestational age. Nonetheless, since their introduction, its use in the clinical practice has raised questions related to the possible risks involved in the child brain development as collateral effect. The clinical trials described by Crowley et al. in [CCK90] exclude any increase of death rate given by corticosteroid, but does not address the issue of possible related brain damages or lungs benefits. In the already mentioned study by Marlow et al. [MWBS05] as well as in Wood et al. [WCG<sup>+</sup>05] it is hypothesized a correlation between cerebral palsy and antenatal corticosteroids, in particular when more than one course is applied. Such a correlation is very difficult to assess, given the impossibility of collecting a match sample with the same causing factors of PTB, gestational age, mother age and background, with and without the corticosteroids administration.

The Green Top guideline dedicated to the topic [Rob10] states:

*Evidence on the longer-term benefits and risks of a single course of antenatal corticosteroids shows no clear difference in adverse neurological or cognitive effects. There is still insufficient evidence on the longer-term benefits and risks of multiple courses of antenatal corticosteroids.*

In support of these hypothesis, the research study proposed by Newnham [New01] shows an association between multiple courses administration with delayed myelination of the central nervous system and altered blood pressure in a preclinical study. The article published in Nature by Huang et al. [Hua11] suggests an association between ACS and psychiatric disorders appearing in adult life, while the previously published long term studies by Smolders et al. [SdHNS<sup>+</sup>90] and Dessens et al. [DSdHK00] showed no clear adverse neurological or cognitive effects.

The need for further understanding of the effects of corticosteroids and PTB

introduces the clinical question motivating this thesis and presented in the next section.

## 2.5 Clinical question

Multiple studies showed clear benefits of corticosteroids administration in relation to PTB, both in decreasing the rate of mortality and in reducing the intensive care period. Nonetheless, given the confounding factors impacting the cognitive development of the premature subject, it appears very difficult to tell whether adverse long term neurological or cognitive effects originate from the antenatal corticosteroids (ACS) administration.

When ACS administration provides a crucial contribution for the survival rate, a complete understanding of possible negative effects in the later life is not a fundamental requirement. As schematically indicated in Figure 40-1, the region where a deeper understanding is required is with the late preterm period. Here the PTB condition is not life-threatening, nonetheless ACS may improve the general health condition. For these cases, the benefits may not be justified in the light of possible negative effect of ACS on the brain development.

From a collection of clinical data alone it is likely to be impossible to isolate the confounding factors and to differentiate the extent of the brain damage due to ACS and PTB. Even if clinically less frequent than its combination with other source of infection, an investigation on a *clean* delivery can provide the ideal ground to assess the consequences of early delivery unbiased by covariates. Therefore, this research investigates the consequences of iatrogenic PTB, with no occurrence of other pathologies.

The main aim of the ongoing study presented in this thesis is to provide a baseline explaining the presence and extent of possible brain damages caused by the steroids administration. In particular it is aimed at establishing, with reproducible and generalisable experiments, a decisional threshold where possible damages and benefits of corticosteroids are balanced.

The international research project led by Jan Deprest and Hannes Van Der Merwe at the Katholieke Universiteit Leuven, Biomedical Science Group and by Tom Vercauteren at the University College London, Translational Imaging Group, has as objective the prediction of the neurocognitive consequences of preterm birth and corticosteroids administration on a rabbit animal model. The animal experiments are carried out at the Centre for Surgical Technologies and histological experiments are carried out at the Laboratory of Experimental Gynaecology, both located at Leuven. Image analysis tools are developed at Translational Imaging group, University College London. This thesis is focused on the presentation of the computational tools

developed to investigate the readouts after having established the biomarkers.

## Chapter bibliography

- [ADG<sup>+</sup>03] Peter Anderson, Lex W Doyle, Victorian Infant Collaborative Study Group, et al. Neurobehavioral outcomes of school-age children born extremely low birth weight or very preterm in the 1990s. *jama*, 289(24):3264–3272, 2003.
- [BB<sup>+</sup>07] Richard E Behrman, Adrienne Stith Butler, et al. *Preterm birth: causes, consequences, and prevention*. National Academies Press, 2007.
- [BCC<sup>+</sup>13] Hannah Blencowe, Simon Cousens, Doris Chou, Mikkell Oestergaard, Lale Say, Ann-Beth Moller, Mary Kinney, and Joy Lawn. Born too soon: the global epidemiology of 15 million preterm births. *Reproductive health*, 10(1):1, 2013.
- [BCO<sup>+</sup>12] Hannah Blencowe, Simon Cousens, Mikkell Z Oestergaard, Doris Chou, Ann-Beth Moller, Rajesh Narwal, Alma Adler, Claudia Vera Garcia, Sarah Rohde, Lale Say, et al. National, regional, and worldwide estimates of preterm birth rates in the year 2010 with time trends since 1990 for selected countries: a systematic analysis and implications. *The Lancet*, 379(9832):2162–2172, 2012.
- [Car06] SG Carroll. Preterm prelabour rupture of membranes. *Green Top guideline*, 44, 2006.
- [CBAW07] Karen M Clements, Wanda D Barfield, M Femi Ayadi, and Nancy Wilber. Preterm birth–associated cost of early intervention services: An analysis by gestational age. *Pediatrics*, 119(4):e866–e874, 2007.
- [CCK90] Patricia Crowley, Iain Chalmers, and Marc Jen Kerse. The effects of corticosteroid administration before preterm delivery: an overview of the evidence from controlled trials. *BJOG: An International Journal of Obstetrics & Gynaecology*, 97(1):11–25, 1990.
- [CEC<sup>+</sup>08] Serena J Counsell, A David Edwards, Andrew TM Chew, Mustafa Anjari, Leigh E Dyet, Latha Srinivasan, James P Boardman, Joanna M Allsop, Joseph V Hajnal, Mary A Rutherford, et al. Specific relations between neurodevelopmental abilities and white matter microstructure in children born preterm. *Brain*, 131(12):3201–3208, 2008.

- [DS16] Aleksandra Doronjski and Vesna Stojanović. Ethical issues in the treatment of extremely low birth weight neonates. *Croatian medical journal*, 57(4):395, 2016.
- [DSdHK00] Arianne B Dessens, Hetty Smolders-de Haas, and Janna G Koppe. Twenty-year follow-up of antenatal corticosteroid treatment. *Pediatrics*, 105(6):e77–e77, 2000.
- [GCIR08] Robert L Goldenberg, Jennifer F Culhane, Jay D Iams, and Roberto Romero. Epidemiology and causes of preterm birth. *The lancet*, 371(9606):75–84, 2008.
- [HDOS<sup>+</sup>01] Elysée TM Hille, A Lya Den Ouden, Saroj Saigal, Dieter Wolke, Michael Lambert, Agnes Whitaker, Jennifer A Pinto-Martin, Lorraine Hoult, Renate Meyer, Judith F Feldman, et al. Behavioural problems in children who weigh 1000 g or less at birth in four countries. *The Lancet*, 357(9269):1641–1643, 2001.
- [HF99] Maureen Hack and Avroy A Fanaroff. Outcomes of children of extremely low birthweight and gestational age in the 1990’s. *Early human development*, 53(3):193–218, 1999.
- [HJH01] CLJ Huddy, A Johnson, and PL Hope. Educational and behavioural problems in babies of 32–35 weeks gestation. *Archives of Disease in Childhood-Fetal and Neonatal Edition*, 85(1):F23–F28, 2001.
- [HKML13] Christopher P Howson, Mary V Kinney, Lori McDougall, and Joy E Lawn. Born too soon: preterm birth matters. *Reproductive health*, 10(1):1, 2013.
- [Hua11] Li-Tung Huang. The link between perinatal glucocorticoids exposure and psychiatric disorders. *Pediatric research*, 69:19R–25R, 2011.
- [HWS<sup>+</sup>10] Judith U Hibbard, Isabelle Wilkins, Liping Sun, Kimberly Gregory, Shoshana Haberman, Matthew Hoffman, Michelle A Kominiarek, Uma Reddy, Jennifer Bailit, D Ware Branch, et al. Respiratory morbidity in late preterm births. *JAMA: the journal of the American Medical Association*, 304(4):419, 2010.
- [IHW<sup>+</sup>99] Terrie E Inder, Petra S Huppi, Simon Warfield, Ron Kikinis, Gary P Zientara, Patrick D Barnes, Ferenc Jolesz, and Joseph J Volpe. Periventricular white matter injury in the premature infant is followed by reduced cerebral cortical gray matter volume at term. *Annals of neurology*, 46(5):755–760, 1999.

- [LFH<sup>+</sup>12] Marta Lopez, Francesc Figueras, Sandra Hernandez, Montserrat Lonca, Raul Garcia, Montse Palacio, and Oriol Coll. Association of HIV infection with spontaneous and iatrogenic preterm delivery: effect of HAART. *AIDS*, 26(1):37–43, 2012.
- [LJC<sup>+</sup>12] Li Liu, Hope L Johnson, Simon Cousens, Jamie Perin, Susana Scott, Joy E Lawn, Igor Rudan, Harry Campbell, Richard Cibulskis, Mengying Li, et al. Global, regional, and national causes of child mortality: an updated systematic analysis for 2010 with time trends since 2000. *The Lancet*, 379(9832):2151–2161, 2012.
- [LMA<sup>+</sup>11] Thuy Mai Luu, Laura Ment, Walter Allan, Karen Schneider, and Betty R Vohr. Executive and memory function in adolescents born very preterm. *Pediatrics*, 127(3):e639–e646, 2011.
- [MCD<sup>+</sup>17] Karen J Mathewson, Cheryl HT Chow, Kathleen G Dobson, Eliza I Pope, Louis A Schmidt, and Ryan J Van Lieshout. Mental health of extremely low birth weight survivors: A systematic review and meta-analysis. *Psychological bulletin*, 143(4):347, 2017.
- [MERB<sup>+</sup>13] Andrew Melbourne, Zach Eaton-Rosen, Alan Bainbridge, Giles S Kendall, Manuel Jorge Cardoso, Nicola J Robertson, Neil Marlow, and Sebastien Ourselin. Measurement of myelin in the preterm brain: multi-compartment diffusion imaging and multi-component t2 relaxometry. In *International Conference on Medical Image Computing and Computer-Assisted Intervention*, pages 336–344. Springer, 2013.
- [MLM08] Dag Moster, Rolv Terje Lie, and Trond Markestad. Long-term medical and social consequences of preterm birth. *New England Journal of Medicine*, 359(3):262–273, 2008.
- [MOI<sup>+</sup>00] C Menendez, J Ordi, MR Ismail, PJ Ventura, JJ Aponte, E Kahigwa, F Font, and PL Alonso. The impact of placental malaria on gestational age and birth weight. *Journal of infectious diseases*, 181(5):1740–1745, 2000.
- [MPD<sup>+</sup>09] Lindsay J Mangham, Stavros Petrou, Lex W Doyle, Elizabeth S Draper, and Neil Marlow. The cost of preterm birth throughout childhood in England and Wales. *Pediatrics*, 123(2):e312–e327, 2009.
- [MW96] Gerald B Merenstein and Leonard E Weisman. Premature rupture of the membranes: neonatal consequences. In *Seminars in perinatology*, volume 20, 5, pages 375–380. Elsevier, 1996.

- [MWBS05] Neil Marlow, Dieter Wolke, Melanie A Bracewell, and Muthanna Samara. Neurologic and developmental disability at six years of age after extremely preterm birth. *New England Journal of Medicine*, 352(1):9–19, 2005.
- [New01] John P Newnham. Is prenatal glucocorticoid administration another origin of adult disease? *Clinical and Experimental Pharmacology and Physiology*, 28(11):957–961, 2001.
- [NGI<sup>+</sup>08] RB Newman, RL Goldenberg, JD Iams, PJ Meis, BM Mercer, AH Moawad, E Thom, M Miodovnik, SN Caritis, M Dombrowski, et al. Preterm prediction study: comparison of the cervical score and bishop score for prediction of spontaneous preterm delivery. *Obstetrics and gynecology*, 112(3):508, 2008.
- [P<sup>+</sup>12] Richard A Polin et al. Management of neonates with suspected or proven early-onset bacterial sepsis. *Pediatrics*, 129(5):1006–1015, 2012.
- [PHB<sup>+</sup>06] Stavros Petrou, Jane Henderson, Melanie Bracewell, Christine Hockley, Dieter Wolke, Neil Marlow, EPICure Study Group, et al. Pushing the boundaries of viability: the economic impact of extreme preterm birth. *Early human development*, 82(2):77–84, 2006.
- [RBM<sup>+</sup>15] NZ Rabie, TM Bird, EF Magann, RW Hall, and SS McKelvey. Adhd and developmental speech/language disorders in late preterm, early term and term infants. *Journal of Perinatology*, 35(8):660–664, 2015.
- [RD06] D Roberts and S Dalziel. Antenatal corticosteroids for accelerating fetal lung maturation for women at risk of preterm birth (review). *Cochrane Database Syst Rev*, 19:CD004454, 2006.
- [RDF14] Roberto Romero, Sudhansu K Dey, and Susan J Fisher. Preterm labor: one syndrome, many causes. *Science*, 345(6198):760–765, 2014.
- [Rob10] D Roberts. Antenatal corticosteroids to reduce neonatal morbidity and mortality. *Green Top guideline*, 7, 2010.
- [SD08] Saroj Saigal and Lex W Doyle. An overview of mortality and sequelae of preterm birth from infancy to adulthood. *The Lancet*, 371(9608):261–269, 2008.
- [SdHNS<sup>+</sup>90] H Smolders-de Haas, J Neuvel, B Schmand, JG Koppe, J Hoeks, et al. Physical development and medical history of children who were treated

- antenatally with corticosteroids to prevent respiratory distress syndrome: a 10-to 12-year follow-up. *Pediatrics*, 86(1):65–70, 1990.
- [SdOW<sup>+</sup>03] Saroj Saigal, Lya den Ouden, Dieter Wolke, Lorraine Hoult, Nigel Paneth, David L Streiner, Agnes Whitaker, and Jennifer Pinto-Martin. School-age outcomes in children who were extremely low birth weight from four international population-based cohorts. *Pediatrics*, 112(4):943–950, 2003.
- [SDR<sup>+</sup>14] A Soe, ALM David, AD Roberts, K Costeloe, The London School of Medicine, and Dentistry. Perinatal management of pregnant women at the threshold of infant viability (the obstetric perspective). *New England Journal of Medicine*, Scientific Impact Paper No. 41(16):1672–1681, February 2014.
- [TPL<sup>+</sup>08] Jon E Tyson, Nehal A Parikh, John Langer, Charles Green, and Rosemary D Higgins. Intensive care for extreme prematurity—moving beyond gestational age. *New England Journal of Medicine*, 358(16):1672–1681, 2008.
- [vdBJBN14] Nynke R van den Broek, Rachel Jean-Baptiste, and James P Neilson. Factors associated with preterm, early preterm and late preterm birth in Malawi. *PloS one*, 9(3):e90128, 2014.
- [VLL12] Tyler J VanderWeele, John D Lantos, and Diane S Lauderdale. Rising preterm birth rates, 1989–2004: changing demographics or changing obstetric practice? *Social science & medicine*, 74(2):196–201, 2012.
- [Vol09] Joseph J Volpe. Brain injury in premature infants: a complex amalgam of destructive and developmental disturbances. *The Lancet Neurology*, 8(1):110–124, 2009.
- [WAA<sup>+</sup>06] Lianne J Woodward, Peter J Anderson, Nicola C Austin, Kelly Howard, and Terrie E Inder. Neonatal mri to predict neurodevelopmental outcomes in preterm infants. *New England Journal of Medicine*, 355(7):685–694, 2006.
- [WCG<sup>+</sup>05] Nicholas S Wood, Kate Costeloe, Alan T Gibson, Enid M Hennessy, Neil Marlow, and Andrew R Wilkinson. The epicure study: associations and antecedents of neurological and developmental disability at 30 months of age following extremely preterm birth. *Archives of Disease in Childhood-Fetal and Neonatal Edition*, 90(2):F134–F140, 2005.

- [WMC<sup>+</sup>00] Nicholas S Wood, Neil Marlow, Kate Costeloe, Alan T Gibson, and Andrew R Wilkinson. Neurologic and developmental disability after extremely preterm birth. *New England Journal of Medicine*, 343(6):378–384, 2000.
- [ZGA<sup>+</sup>14] Rachel M Zack, Jenna Golan, Said Aboud, Gernard Msamanga, Donna Spiegelman, and Wafaie Fawzi. Risk factors for preterm birth among HIV-infected Tanzanian women: a prospective study. *Obstetrics and gynecology international*, 2014, 2014.



## Chapter 3

# Rabbit brain animal model: experiment design and dataset acquisition

### Contents

---

<b>3.1</b>	<b>Why rabbit . . . . .</b>	<b>56</b>
<b>3.2</b>	<b>Pre-clinical study . . . . .</b>	<b>58</b>
3.2.1	Multimodal design . . . . .	59
<b>3.3</b>	<b>Design selection for the MRI acquisitions . . . . .</b>	<b>60</b>
3.3.1	In vivo and ex vivo protocols . . . . .	60
3.3.2	Longitudinal and cross-sectional design . . . . .	63
3.3.3	High resolution MRI readouts and areas of interest . . . . .	63
<b>3.4</b>	<b>Protocols . . . . .</b>	<b>64</b>
3.4.1	<i>Ex vivo</i> acquisition protocol . . . . .	64
3.4.2	<i>In vivo</i> acquisition protocol . . . . .	65
<b>3.5</b>	<b>Appendix: protocol development . . . . .</b>	<b>66</b>

---

Driven by the clinical question presented in the previous chapter, we introduce the design of the subsequent pre-clinical study. To investigate the encephalopathy of prematurity (EoP) on a newborn rabbit animal model, three different strategies are implemented: histology, neurobehavioural assessment and high-resolution magnetic resonance images (HrMRI).

Histology and neurobehavioural assessment are performed by Johannes van der Merwe and Leenard Van Der Veerke at the Department of Development and Regeneration, Woman and Child Cluster, Group Biomedical Sciences, KU Leuven. Magnetic

Resonance Image acquisition by Johannes van der Merwe and Willy Gsell at the mo-SAIC facility, Biomedical MRI, Department of Imaging and Pathology, KU Leuven.

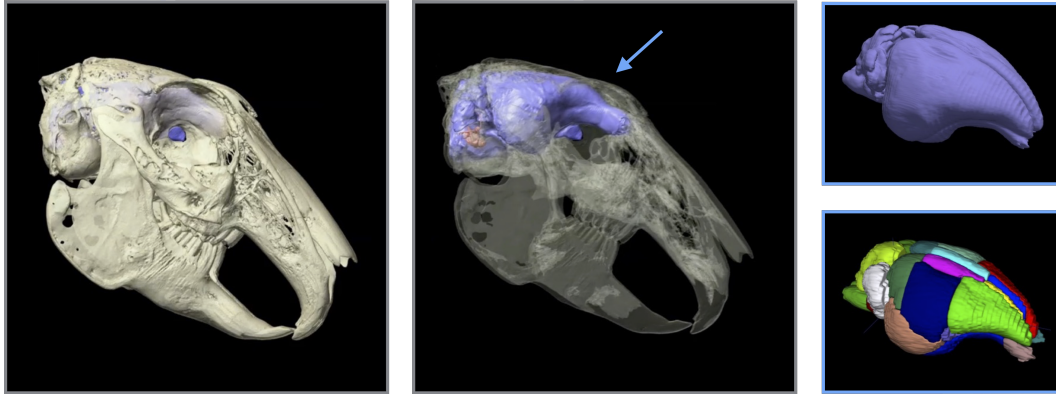


Figure 56-1: **Adult rabbit brain and skull.** Screenshots from the Dept. of Medical science Heritage College of Osteopathic Medicine, Ohio university ([www.ohio.edu](http://www.ohio.edu), last access 21-05-18). Right column, the adult rabbit brain atlas, Munoz et al. [MMAPB+13] in a single surface (top) and divided in anatomical regions (bottom). The comparison shows the location of the brain in the skull and its 3D shape.

## 3.1 Why rabbit

Animal models are a fundamental asset in the analysis of pathological neurodevelopmental processes. Commonly employed models divides in two categories: *small animals*, such as rodents and rabbits, and *large animals* such as sheep and non-human primates. While the second category usually has a higher translational value, in particular for non-human primates, their employability is limited by high costs, technical difficulties in implementing large studies in short times and ethical considerations. Small animals are best suited for high resolution scanner and provides statistical power at lower cost compared to large animals.

In respect to the preterm birth problem, on large animals Dieni et al. [DIY+04] and Inder et al. [INYR05] have investigated the effects of intrauterine inflammation and prematurity on a non-human primate model, underlying the similarities between premature baboon and premature human infants. In a subsequent study, again by Inder et al. [INK+05] histology and magnetic resonance acquisitions are compared to investigate the effects of very preterm and late preterm birth on baboons.

On a sheep animal model, De Matteo et al. [DMBS+10] characterised the consequence of PTB in term of body weight, size and rate of mortality. Nuygen et al. [NDMH+17] studied the effects from birth to adolescence of preterm sheeps, considering weight and rate of mortality.

Burd et al. [BBK12] reviewed a range of pre-clinical studies on small animals,

investigating the effect of intrauterine inflammation, closely related to PTB. Most of the reported studies are based on rodents (mice and rats) animal models. For example, Yang et al. [YHY<sup>+</sup>04] studied the possible improvements of selective dopamine receptor A68930 administered to perinatal hypoxia-induced rats. Ramani et al. [RvGK<sup>+</sup>13] investigated hypoxia after extreme PTB on a mouse animal model and Arteni et al. [AST<sup>+</sup>03] studied the memory impairments after neonatal cerebral hypoxia-ischaemia on the adult rat.

Rodents neurocognitive models are well established, despite their translation value seems to be limited, especially in view of their lissencephalic brain structure with low proportion of white matter. Moreover, rodents are not prenatal brain developers, being therefore less sensitive to PTB injuries if compared to humans.

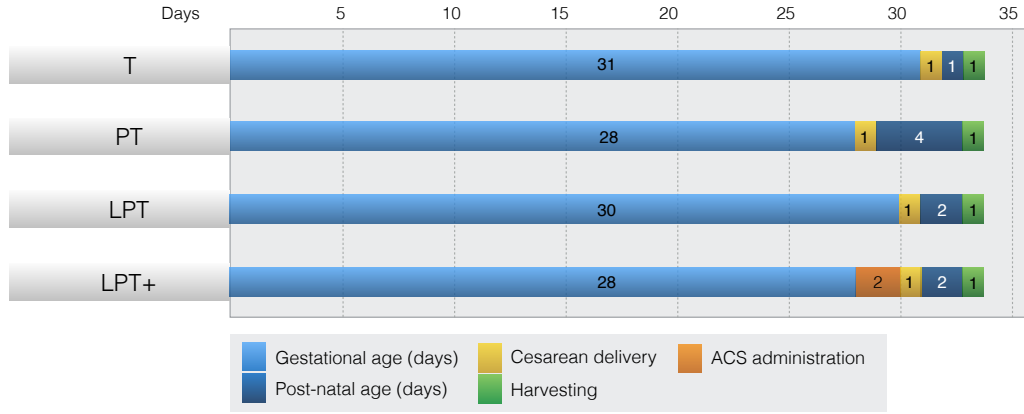


Figure 57-1: **Study design timeline.** (T) normal control or term, cesarean birth after 31 days of gestation. (PT) preterm model, cesarean birth after 28 days of gestation. (LPT) late preterm, cesarean birth after 30 days and (LPT+) late preterm with antenatal corticosteroid administration. Harvesting is performed for the each datasets at the 32<sup>nd</sup> day to produce equivalent development day. Image acquisition is scheduled afterwards and performed according to scanner availability within one week.

As an alternative, rabbits can provide a small animal model with white matter maturation, proportion and myelination process more similar to humans. According to Derrick et al. [DDJT07], the rabbit appears to be an optimal model for the investigation of preterm-related cerebral palsy, and to bridge the gap in translational research between small and large animals.

Although less numerous than the ones involving rodents, several studies are available in the scientific literature involving rabbits for the investigation of the effects of PTB. The two most relevant, and strongly related to the research that we propose in this thesis are Chua et al. [CCB<sup>+</sup>09] and Drobyshevsky et al. [DJL<sup>+</sup>14]. The first study investigates the induced intraventricular hemorrhage with ultrasound assessment, followed by neurobehavioral, histological, and diffusion tensor imaging

evaluation. The second one investigates the myelination defects with neurobehavioral assessment, electrophysiology and MRI.

In the investigation of functional and anatomical structure of the brain, a particularly important asset is the availability of an atlas and a taxonomy. Digital atlases, such as the one presented by Mazziotta et al. [MTE<sup>+</sup>01] for humans, are indispensable tools in every computational manipulation of the acquisitions. Most of the digital atlases available refers to the human anatomy, both for adults and developing subjects.

For the adult rabbit brain there are three adult brain atlases available. A digital atlas, shown in Figure 56-1, is proposed by Munoz et al [MMAPB<sup>+</sup>13]. The anatomical chart and taxonomy of the adult rabbit brain, provided by Mullhaupt et al. [MAS<sup>+</sup>15], without digital annotations. A DWI based study of the developing brain on four selected regions manually annotated, proposed by Lim et al. [LTC<sup>+</sup>15].

Before the contribution proposed in this thesis, there was no newborn atlas in literature. The digital newborn rabbit brain multi-atlas produced in this research is present in Chapter 5.

## 3.2 Pre-clinical study

To study the neurological effects of corticosteroids, preterm birth, and their combinations, we designed a study involving four datasets.

**T** - Term or normal control, delivery at 31 days of gestation.

**PT** - Pre-term, delivery at 28 days of gestation.

**LPT** - Late pre-term, delivery at 30 days of gestation.

**LPT+** - Antenatal corticosteroids administered at 28 gestational days followed by late pre-term delivery at 30 days of gestation.

As the gestational age of the chosen New Zealand rabbit is 31 days, we selected 28 gestational days in the rabbit to model human early preterm. With the 30 days model, we expect to model the equivalent of the grey zone for the humans represented in Figure 40-1.

The comparison between the four groups is expected to provide a wider understanding of the impact of PTB when not induced by other concomitant causes (non-infective and non-ischaemic prematurity), The proposed design enables to compare the term with the preterm as well as the late preterm and the late preterm with administration of corticosteroids.

As summarised in Figure 57-1, cesarean delivery is performed at 31, 30 and 28 gestational days for term, late-preterm and preterm. Late preterm are considered both with and without steroids. Pups are raised in an incubator after birth for 1 day for the first set, and for 2 days for the second and 4 days for the third and fourth set. MRI scans and harvesting for histology are performed one day after birth (postnatal PN +1d) for the term, and an equivalent postnatal age for the other three groups (PN +4d for early delivery and PN +2d for the late preterm delivery).

### 3.2.1 Multimodal design

To investigate the effects of PTB and ACS, the analysis of the rabbit brain is performed both on a structural and functional level.

For each of the proposed dataset, the comparison between histology and MRI is aimed at providing additional insights on the brain structure. A pre-clinical assessment of neurological, neuromotoric and neurobehavioral performance is aimed at providing the functional insights. The correlation between the three experimental settings will provide the relationship between the brain structure and neurological function.

In this study design, the alternative hypothesis is that preterm rabbits have a decreased neural density and oligodendrocyte counts, with lower apparent diffusion coefficient (ADC) and fractional anisotropy (FA) on MRI (especially for the areas of interest described in sec. 3.3.3) and inferior scores on the neurobehavioral assessments.

Even if each individual part of the research may provide useful insights on the investigated question, the overarching aim is to combine the outcomes from the three parts<sup>1</sup>, as schematically represented in Figure 59-1.

The three approaches considered can not be applied to the same subject, since

1. Both histology and MRI are performed *ex vivo*.
2. Histology and *ex vivo* MRI require incompatible fixation protocols (staining or gadolinium perfusion respectively).

Moreover, the *in vivo* MRI requiring anaesthetics, could induce long term effect invalidating further neurobehavioural assessments, or possible subsequent *ex vivo* examinations.

Knowing these limitations, the next section introduces the experimental setting and designs for the MRI study.

---

<sup>1</sup>The neurobehavioural assessments and the histological studies will provide to be an important part of the study, but the methodological challenges have not been addressed in this thesis. See the co-authored paper [vdMvdVF<sup>+</sup>19].

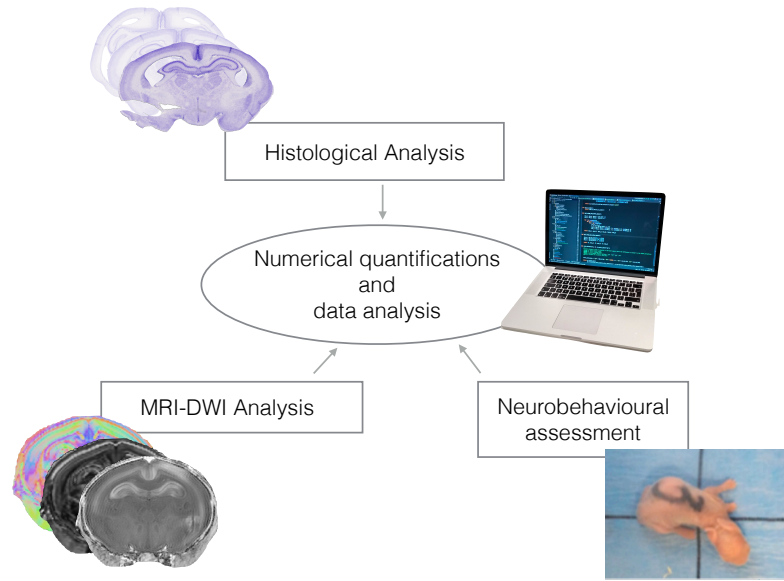


Figure 59-1: **Multimodal design.** The study started in May 2016, and ongoing at the moment of writing this thesis involves three approaches: histology, neurobehavioural assessment and High resolution MR imaging. Numerical quantifications of the three approaches will be compared to provide a better understanding of the functional and structural effects of preterm birth and corticosteroids administration.

## 3.3 Design selection for the MRI acquisitions

The main design question relates to the choice of *in vivo* or *ex vivo* protocol, and between longitudinal or cross-sectional design. Advantages and disadvantages of each approach are examined in the next Sections.

### 3.3.1 In vivo and ex vivo protocols

The *in vivo* protocol is the only option to develop longitudinal studies. Its drawbacks are the lower resolution and DWI directions, given the limited amount of scanning time, and the need for anaesthetics. The anaesthetic in particular may induce iatrogenic effects on the brain that are difficult to quantify, potentially adding a covariate in the statistical study. For these reasons, only 8 acquisitions in the pilot study had been based on the *in vivo* protocol as a feasibility test. Resulting *in vivo* and *ex vivo* protocols are reported in Section. 3.4.

Figure 59-2 shows the result of a T1 *in vivo* acquisition. Its resolution of (0.234375, 0.187500, 0.234375) mm is three times lower than the corresponding *ex vivo* resolution due to the scanning time constraints. For the *ex vivo*, shown in Figure 59-3, the resolution is (0.077920, 0.077920, 0.077920) mm, isotropic.

The impact of the choice of the protocol is even higher for the resulting DWI.

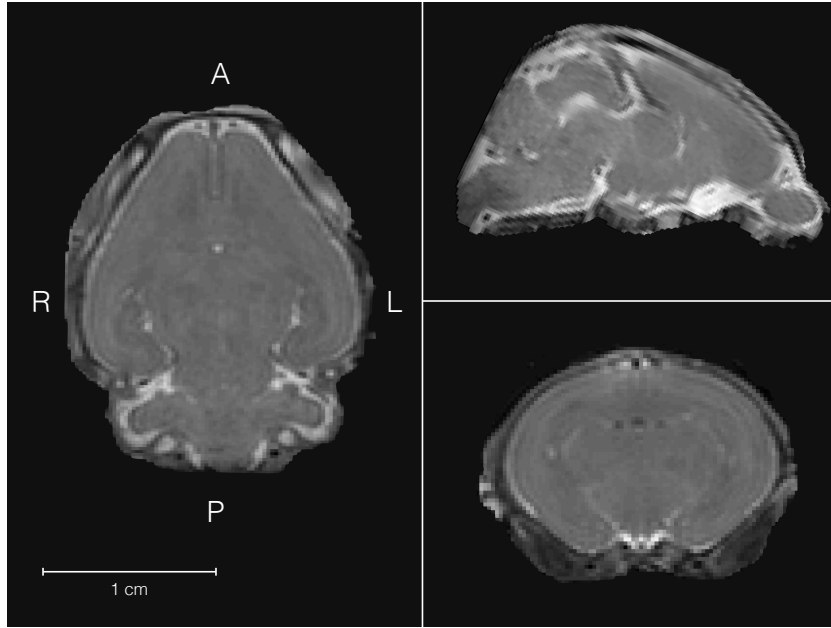


Figure 59-2: **Axial, sagittal and coronal view of subject 0802, *in vivo* protocol.** The only applied pre-processing is region of interest extraction, reorientation and a bias field correction. Resolution (0.234375, 0.187500, 0.234375) mm for (128, 128, 128) voxels grid. The acquisition protocol is described in Section 3.4.

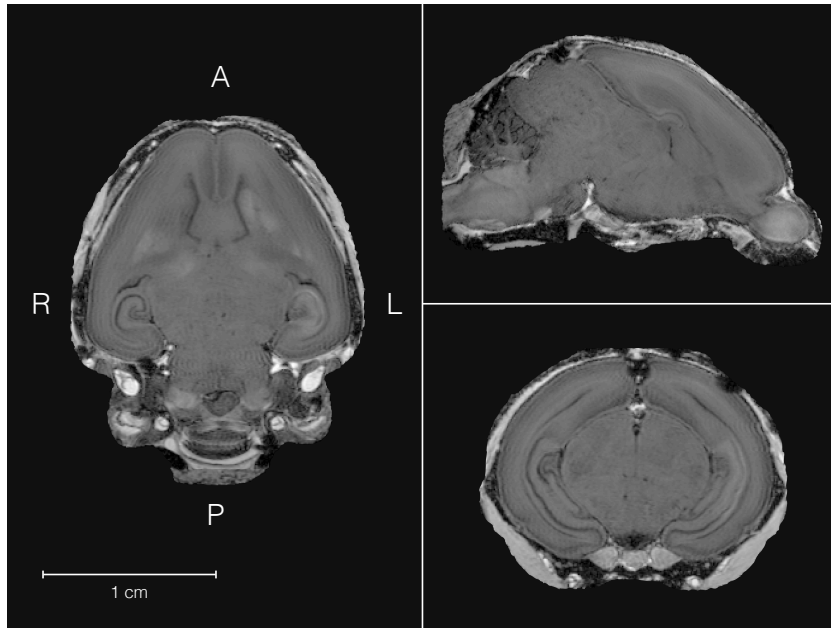


Figure 59-3: **Axial, sagittal and coronal of subject 1702, *ex vivo* protocol.** As for fig. 59-2, the only applied pre-processing are region of interest extraction, reorientation and a bias field correction. Resolution is (0.077920, 0.077920, 0.077920) mm for (385, 385, 385) voxels grid. The acquisition protocol is described in Section 3.4.

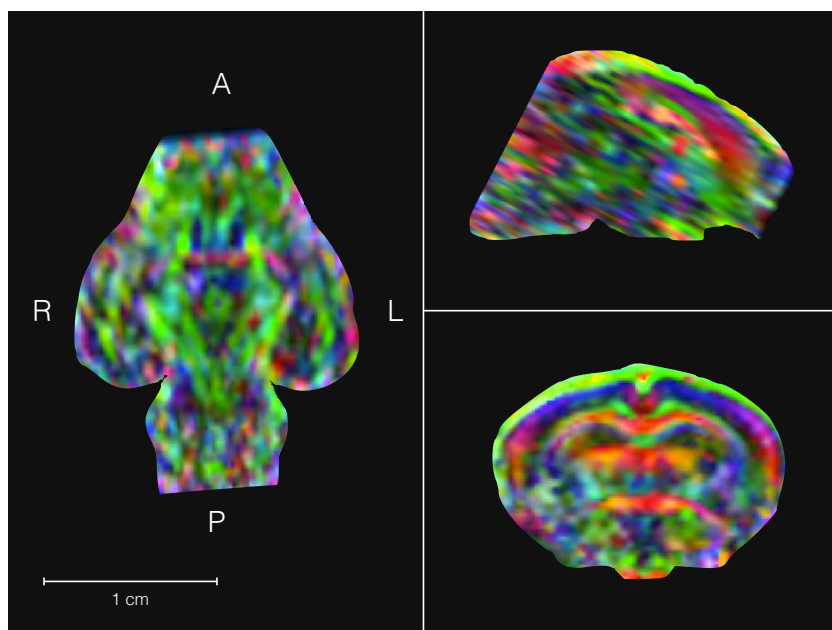


Figure 59-4: **Axial, sagittal and coronal of the main direction of the DTI, subject 0802, *in vivo* protocol.** Applied pre-processing is region of interest extraction, reorientation, tensor fitting, multiplication of the main direction times the fractional anisotropy map. Colour code: red R/L, blue A/P green S/I. In the sagittal section, parts of the cerebellar hemispheres are not present due to the reduced field of view of the *in vivo* acquisition.

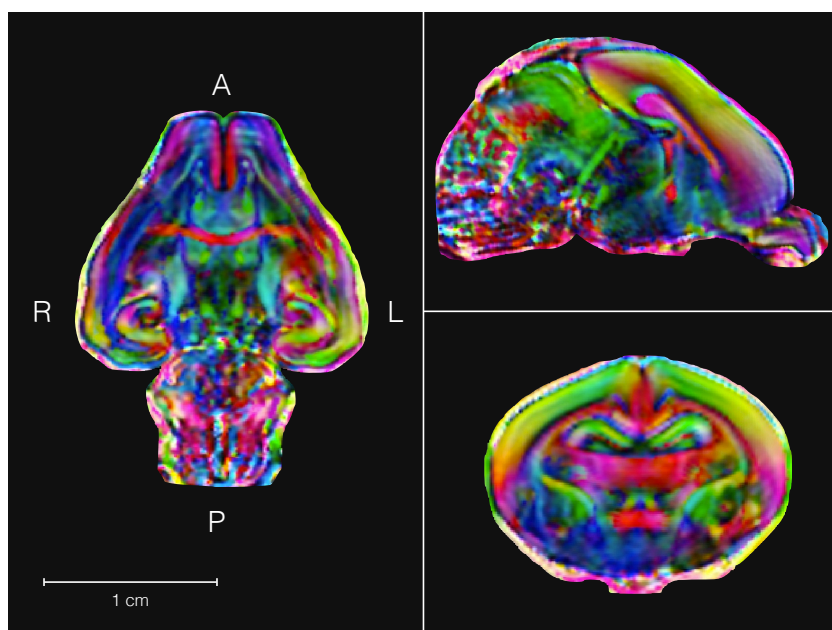


Figure 59-5: **Axial, sagittal and coronal of the main direction of the DTI, subject 1305, *ex vivo* protocol.** Same pre-processing steps of Figure 59-4.

Differences on the resolution of the diffusion tensor images can be visually assessed in Figure 59-4 and Figure 59-5.

### 3.3.2 Longitudinal and cross-sectional design

In a series of three articles, Kate Levin [Lev05a, Lev05b, Lev06] briefly introduces a range of possible statistical study design, with pros and cons in the clinical practice. Particular attention is given by the author to the issue of the influence of chance and bias affecting each model. The author addresses in particular the issue of chance and bias for each chosen design.

These publications had been particularly inspiring for the study here presented: in accordance with Levin a longitudinal study design is in theory the most appealing option to investigate the progression of the effects of an analogous case to the PTB and ACS we are concerned. The longitudinal model has the potential to unveil causal relationships between clinical practice and long term effects.

A cross-sectional design, where the evolution of the brain is considered at each point with statistics on a sampled dataset, does not allow to study the evolution of a single subject in its time progression.

If it was possible to acquire *in vivo* images with the same resolution as the *ex vivo*, the selected design would have been a sequence of *in vivo* acquisition followed by a final *ex vivo* and subsequent histological examination. This would have combined both the longitudinal and the cross-sectional design, dodging the limitation of the two methodologies.

Due to the challenges faced during the *in vivo* protocol, the poor consequent resolution, possible confounding factors after anaesthetic and the incompatibility of the MRI perfusion and histological perfusion, we considered for this phase of the study only the cross sectional study design at day 1 (1d). Multiple time-points such as the pre-adolescent model at the 8<sup>th</sup> week (8W) are at its initial phase at the moment of writing the thesis. This option is left as future work, and preliminary images are shown in Chapter 7.

### 3.3.3 High resolution MRI readouts and areas of interest

From the clinical literature introduced in Chapter 1 and the pre-clinical studies considered in this one, it emerged that there is a range of regions that can potentially be affected by the PTB and ACS [Vol09, DDJT07, DJL<sup>+</sup>14]. Regions that are particularly relevant in this context are:

1. Cerebellar hemisphere (CeH).
2. Thalamus (Th).

3. Hippocampi (Hc).
4. Internal capsule (IC).
5. Caudate nucleus (CN).
6. Corpus callosum (CC).
7. Prefrontal cortex, part of the frontal cortex (FCx).
8. Optic tracts (OT).

These regions are delineated in Figure 138-6 of Chapter 5 after introducing the multi-atlas.

The readouts selection and their quantification for these regions of interest for the four dataset defined in Figure 57-1 are the first goal after the acquisition.

The first phase is the creation of an automatic segmentation algorithm in the magnetic resonance images. This tool is introduced in Chapter 5.

Subsequent volumetric and diffusion weighted analysis, such as diffusion tensors biomarkers, such as fractional anisotropy (FA) and mean diffusivity (MD), are the main topic of Chapter 6.

## 3.4 Protocols

In this last section we provide the main outcome of the first part of the study: the *in vivo* and *ex vivo* MRI protocols. Further on the dataset and data analysis study is provided after the methodological parts, in Chapter 6.

In the light of the considerations exposed in this chapter in respect to the *in vivo* and *ex vivo*, and longitudinal and cross-sectional protocols, we carried forward the study according to the finalised MRI-DWI protocols described below.

### 3.4.1 *Ex vivo* acquisition protocol

MRI was performed on fixed brains placed in Falcon tubes and immersed in Fomblin (a chemically inert, or proton-free perfluoropolyether fluorocarbon). This is a common approach to mitigate magnetic susceptibility artefacts, as Fomblin produces no MRI signal but has a similar magnetic susceptibility to tissue. Scanner employed is a Bruker Biospec 9.4 Tesla small animal MR scanner (Bruker Biospin, Ettlingen, Germany; horizontal bore, 20 cm) equipped with actively shielded gradients (600 mT/m) utilising a rat brain surface receiver decoupled to a volume quadrature transmit coil (internal diameter of 72 mm). We acquired three different modalities:

▷ T1-weighted image acquisition:

First, high resolution three-dimensional MR images were acquired using a gradient-echo sequence (3D Flash) with Time of Echo (TE)/Time of Repetition (TR) 5.5/50 ms; flip angle 70 degrees; bandwidth 50 kHz; in plane acquisition matrix of  $256 \times 192 \times 128$ ; resolution  $78 \times 78 \times 86\mu\text{m}$ ; 4 averages; acquisition time 1 h 20 min.

▷ Diffusion-weighted images acquisition:

Afterwards, diffusion-weighted images (DWI) were acquired using a 3D segmented spin-echo version of the echo-planar imaging (SE-EPI) sequence with 8 segments; TR/TE: 280/24 ms; FOV: 30 x 25 x 25 mm; matrix:  $192 \times 160 \times 160$  conferring an isotropic spatial resolution of  $156\mu\text{m}$ ; 64 directions and 4 B values (0, 800, 1000, 1500)  $\text{s}/\text{mm}^2$ ; acquisition time 10 hrs.

▷ T2 mapping (Myelin density):

The MSME-T2 sequence, (based on the Carr Purcell Meiboom Gill (CPMG) sequence) was used for assessing the myelin density with TR: 4000 ms; array of 16 time-points ranging from 6 up to 96ms with increment of 6 ms; 4 averages; FOV:  $25 \times 25$  mm; matrix:  $240 \times 240$  conferring an in-plane resolution of  $104 \times 104\mu\text{m}$ ; 32 contiguous slices acquired in interleaved manner with 0.6 mm thickness; acquisition time 48 min.

### 3.4.2 *In vivo* acquisition protocol

MRI was performed on living animals under isoflurane anaesthesia using a Bruker Biospec 9.4 Tesla small animal MR scanner (Bruker Biospin, Ettlingen, Germany; horizontal bore, 20 cm) equipped with actively shielded gradients (600 mT/m) utilising a rat brain surface receiver decoupled to a volume quadrature transmit coil (internal diameter of 72 mm). No contrast agents had been injected.

▷ T1-weighted image acquisition:

Anatomical reference was obtained through a 3D T1 weighted RARE sequences (TR/TE: 42/1000 ms; RARE factor: 8; FOV:  $24 \times 30 \times 30$  mm; matrix:  $160 \times 192 \times 192$ ; acquisition time 19 min). Field homogeneity was corrected using fieldmap correction (MAPSHIM protocol, Bruker Paravision 5.1).

▷ Diffusion-weighted images acquisition:

Afterwards, diffusion-weighted images (DWI) were acquired using a spin-echo version of the echo-planar imaging (SE-EPI) sequence with 4 segments; TE/TR: 27/5000 ms; 2 averages; FOV:  $30 \times 30$  mm; matrix:  $192 \times 192$ ; 20 axial slices of 1mm thickness with a 0.2mm gap; 6 directions and 4 B values (100, 500, 1000, 1500  $\text{s}/\text{mm}^2$ ); acquisition time: 16 min.

▷ T2 mapping (Myelin density):

The Carr Purcell Meiboom Gill (CPMG) sequence was used for assessing the myelin density with TR: 3000 ms; array of 8 TEs ranging from 7.3 up to 58.1 ms with increment of 7.3 ms; FOV:  $30 \times 30$  mm, matrix:  $192 \times 192$  conferring an in-plane resolution of  $156 \times 156$   $\mu\text{m}$ ; 19 slices in interleaved manner with 1 mm thickness and 0.2 mm gap; acquisition time 7 min 12 s.

### 3.5 Appendix: protocol development

Methodological sections from the literature rarely present the difficulties inherent to the improvements of a suitable MR protocol. From the methodological sections appearing in the published works it is often difficult to glimpse the predominant approach leading to the final results. This approach is trials and errors.

When the studied system has a high complexity, either because there is no prior knowledge or because there are too many options available and no clear selection criteria or because the system is made of interacting smaller parts with unpredictable mutual influence, the only scientific option is to try and then discard and try again.

Although trials and errors are carried forward in the best possible approximation of controlled environment, unforeseeable events occur. During the study here presented, we had to deal with scanner parts breakdown (twice the receiving coil, twice the cooling system, once the motherboard short-circuited) cluster overheating (cooling system failure, twice) and coffee machine leaking (once)<sup>2</sup>.

This appendix contributes to the thesis showing some of the trial and error outcomes in the image acquisition process. This section would be hopefully informative to any researcher looking to set up similar studies.

#### *Ex skull experiments*

During the pilot study, some test acquisitions have been performed after skull stripping as proposed by Munoz et al. for the adult rabbit brain [MMA<sup>+</sup>PB<sup>+</sup>13]. This option provided better contrast, but it was discarded due to the introduction of significant tissue deformation in the manual skull stripping process, such as:

(A) Flattening of the olfactory bulbs.

(B) Disruption of optic tracts.

(C) Non-systematic cortex disruption.

---

<sup>2</sup>This last *per se* not particularly critical, if the water leak had not flooded on the cluster room right underneath.

(D) Percolation of gadolinium along the pipe.

These are shown in Figure 67-1 and Figure 68-1. The percolation of gadolinium can also happen in the *in skull* acquisition, albeit in this case the high concentration of magnetically susceptible fluid is not in direct contact with the brain, reducing the consequent high intensity bias on the tissue.

Other than the listed artefacts, removing the brain from the skull induces an overall shape deformation due to lack of the skull support. Furthermore, the absence of skull in the acquisition makes impossible any intra cranial volume estimation, and the brain volume assessment is heavily biased after the arbitrary choice of the chord resection line.

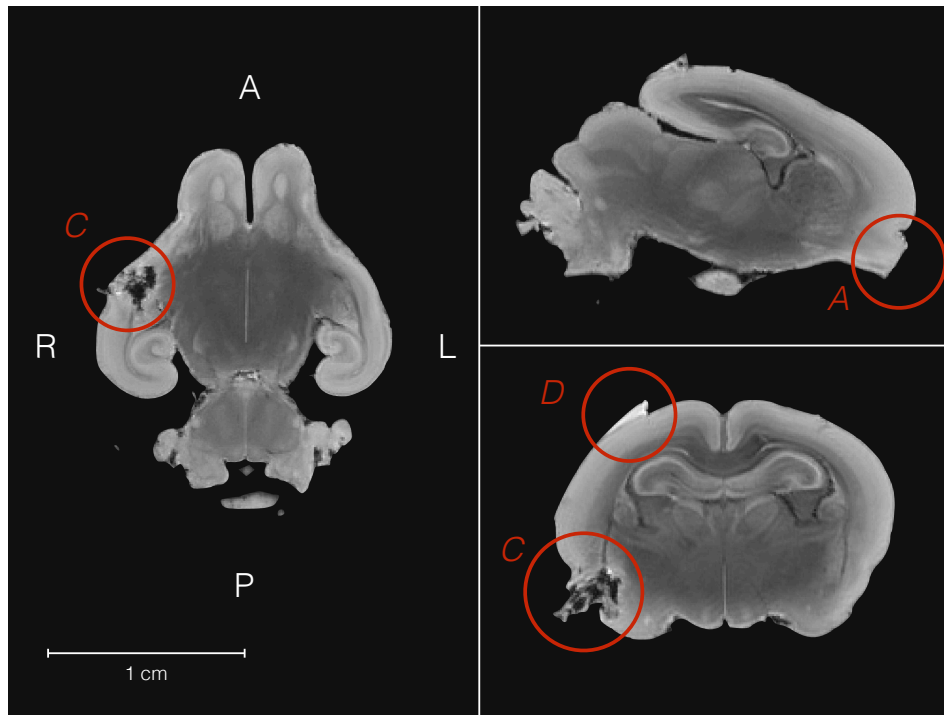


Figure 67-1: ***Ex skull* acquisition.** Artefacts created by this option are: (A) flattening of the olfactory bulbs, (B) disruption of optic tracts, (C) cortex disruption, and (D) percolation of gadolinium along the pipe. Subject 0104.

### ***Open skull* perfusion experiments**

Early experiments for the *in skull* acquisitions have been performed with an intracranial perfusion to improve the gadolinium absorption. In this setting, an additional dose of gadolinium-based fluid is injected through an opening in the skull. A subject acquired with this modality is shown in Figure 67-2.

The *open skull* option results in a better delineation of the internal structure, closer to the *ex skull* than to the *in skull* acquisition.

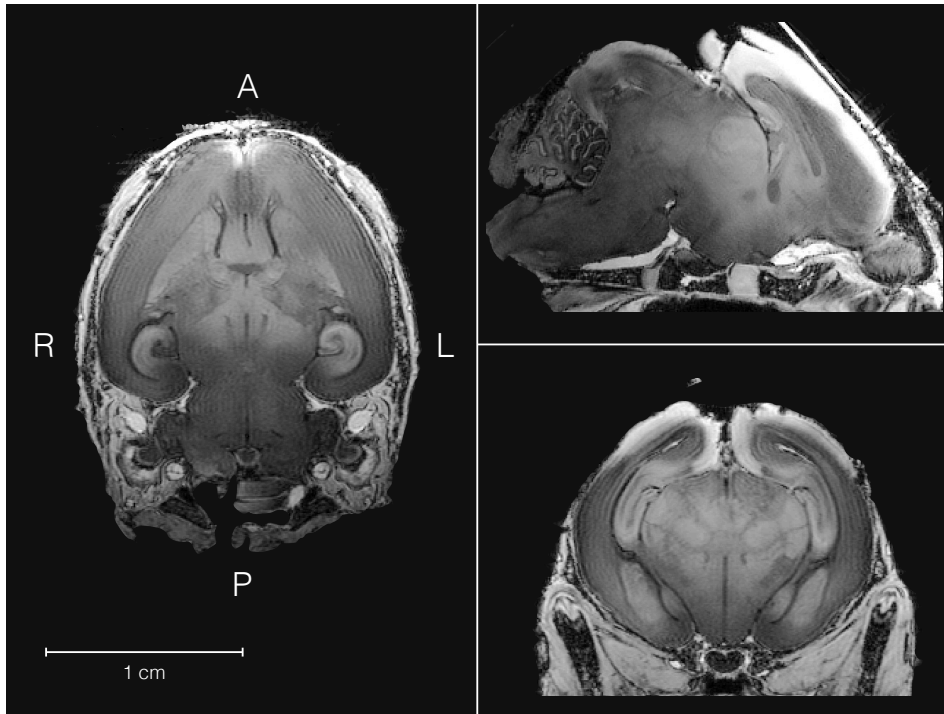


Figure 67-2: **Open skull acquisition.** Midway between *in skull* and *ex skull* protocols. A syringe needle is introduced through an opening in the skull to introduce gadolinium-based fluid. Internal anatomies definition is comparable to an *ex skull* acquisition.

As for the *ex skull*, the *open skull* protocol is too dependent upon the manual intervention and creates a systematic disruption of the skull and part of the cortex. Therefore, the intra cranial volume can not be estimated. Additionally the acquired images may present presents hyperintensities in the cortex region due to the uneven perfusion. Several bias field correction methods had been applied to try to compensate for this artefact with no success, as the phenomenon causing the hyperintensities has a different physical origin if compared to the bias field.

### Motion in *ex vivo*

The main cause of motion artefacts in *ex vivo* MRI is the long time in the scanner, combined with scanner vibration. Therefore, sample stability is crucial in obtaining optimal results. Sample drifting may result as well in a ghosting artefact, as the one shown in Figure 68-2.

To prevent similar artefacts, Falcon pipes for the *ex vivo* protocol had been replaced with a syringe. Here the sample is placed and kept steady by the piston and by small plastic base on the ventral side of the head, as shown in Figure 68-3.

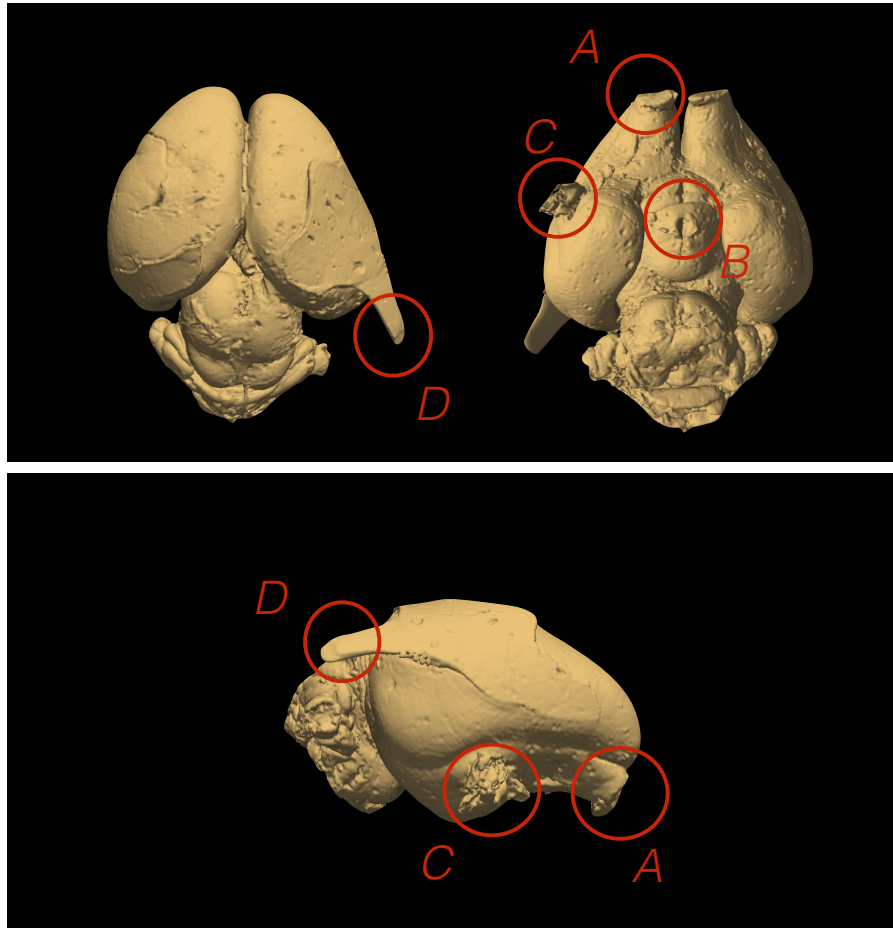


Figure 68-1: **3D rendering of an *ex skull* acquisition.** **Top:** superior (left) and inferior (right) view. Anterior side points north. **Bottom:** lateral view. As in Figure 67-1: flattening of the olfactory bulbs (A), disruption of optic tracts (B), cortex disruption (C), percolation of gadolinium along the pipe (D).

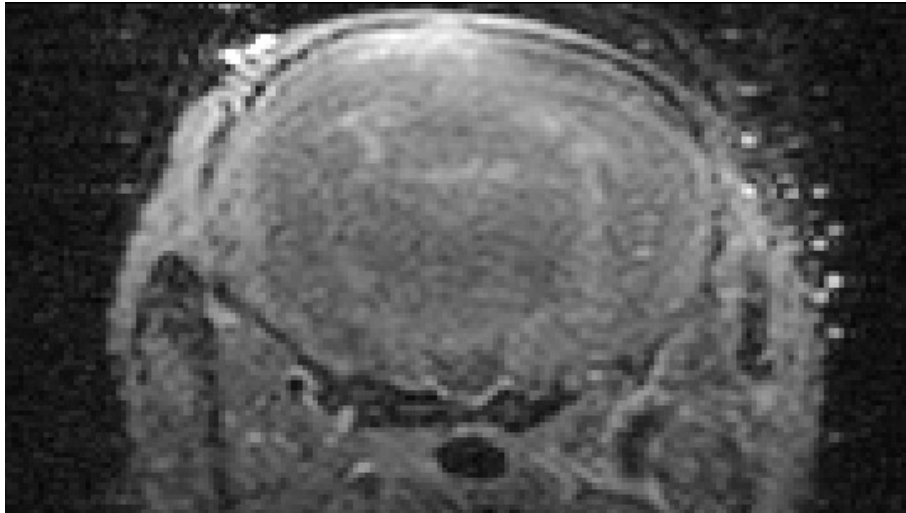


Figure 68-2: **Motion artefact of the  $b = 0$ .** First time-point of the DWI in the *ex vivo* acquisition protocol. Coronal section, subject 4302.

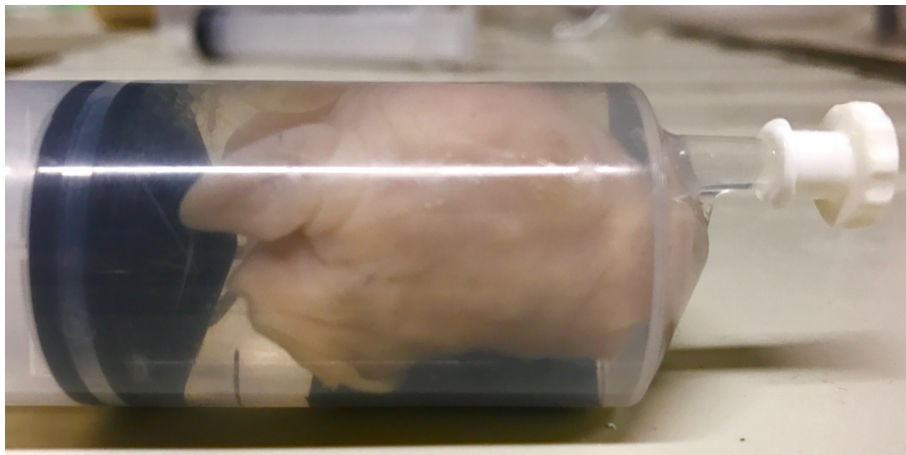


Figure 68-3: **Syringe to keep the head steady during the 10h acquisition.** This setting, proposed and implemented by Johannes van der Merwe in KU Leuven solved the motion artefacts encountered with Falcon pipes.

### Dosimetry, warping effect and RF coil positioning

For the first part of the study, the MRI fluid perfusion was based on Magnevist<sup>®</sup> (dimeglumine gadopentetate) contrast agent. Due to lack of supply, the second half of the study was carried forward with Dotarem (gadoterate meglumine). The dosimetry had to be re-tuned and the first results with the new contrast agent had very poor intensities contrast.



Figure 71-1: **Example of low dose of gadolinium and phase wrap-around artefact.** Coronal section, subject 4507.

Figure 71-1 shows an example where the gadolinium percentage in the perfusion fluid was too low providing poor contrast. The same figure also shows a warping or phase wrap-around artefact. This is caused by an aliasing the k-space caused by the fact that part of the sample was outside the field of view. Further on this artefact is provided by Pusey et al. [PYAL88].

Another artefact was caused by a defect in the support the RF-coil positioned above the sample. This had become loose during the scanning session, providing the results shown in Figure 71-2

### Susceptibility artefacts

The major artefact in the *in skull* protocol, not happening in the *ex skull*, is caused by air bubbles entrapped between the skull and the cortex during perfusion.

As can be seen in Figure 71-3, this results in a black hole effect for the T1 modality and a deformation in the DWI modality.

This problem was solved at preparation and perfusion time with a degasification

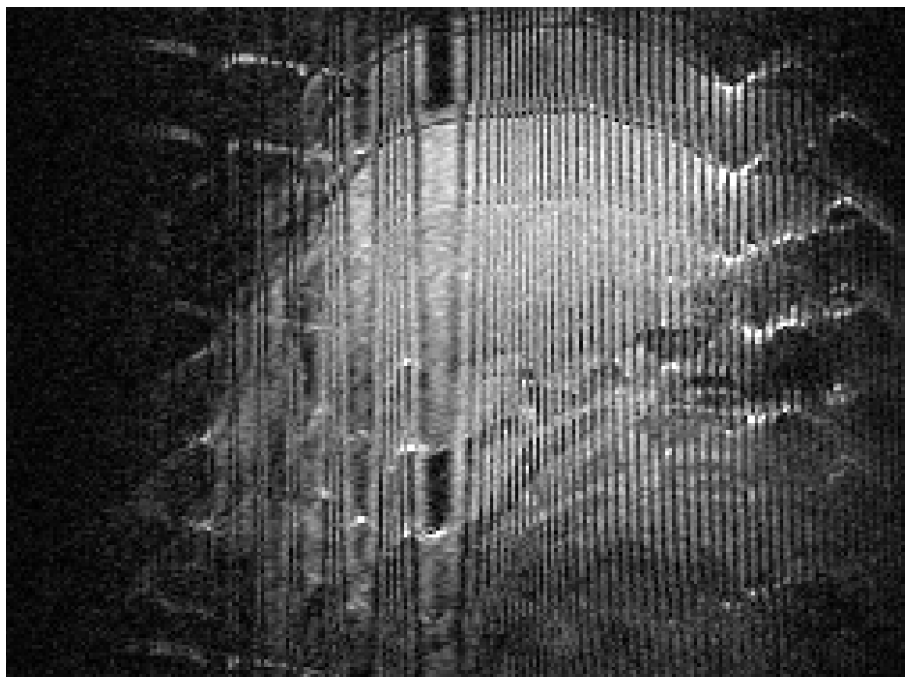


Figure 71-2: **Ghosting and *fencing* artefacts in sagittal section.** Loose RF-coil for the T1 modality, can result in a peculiar artefact, here called *fencing*, as well as in ghosting artefact.

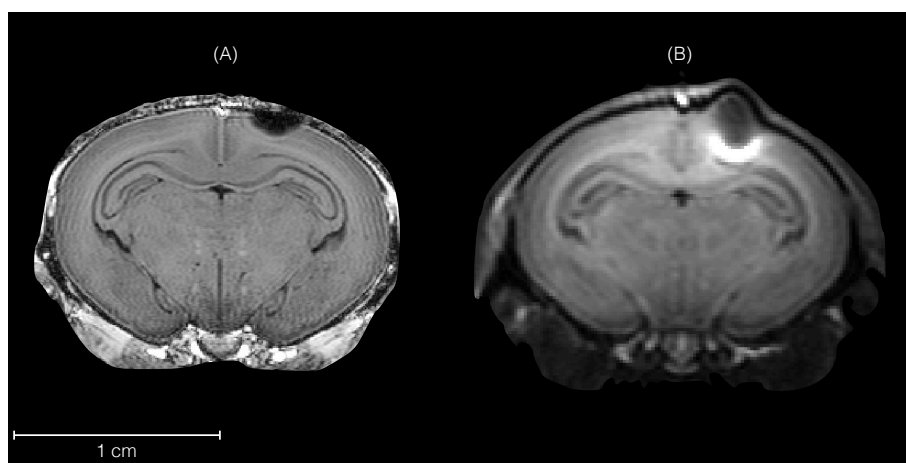


Figure 71-3: **Comparison between T1 and  $b = 0$ .** The presence of air bubble in the perfusion fluid results in a *black hole* in the T1 and in a deformation in the  $b = 0$  providing a representative example of susceptibility artefact. Coronal section, subject 1805.

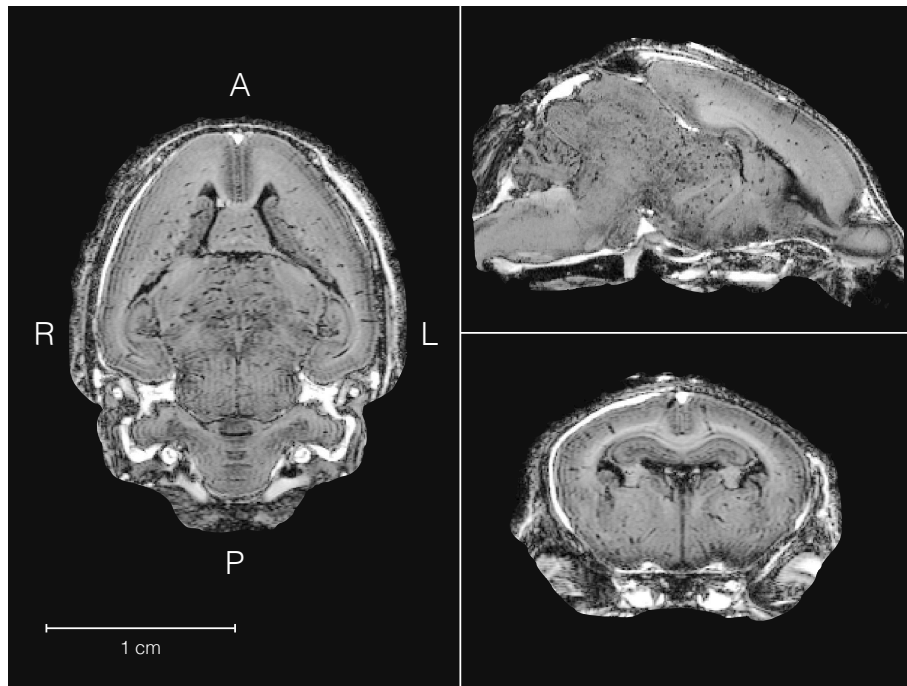


Figure 71-4: **Example of perivascular spaces enlargement due to high pressure in the trans-cardiac perfusion.** Subject 1505.

process in the perfusion fluid preparation and a subsequent sample manipulation to ensure the absence of air bubbles.

### Enlarged perivascular spaces

The pressure of the perfusion is another critical component. Low pressure will provide poor results due to too low intensity and high pressure will enlarge the vessels.

Resulting enlarged perivascular spaces are shown in Figure 71-4. This artefact was again solved after pressure tuning.

## Chapter bibliography

- [AST<sup>+</sup>03] Nice Sarmiento Arteni, Jennifer Salgueiro, Iraci Torres, Matilde Achaval, and Carlos Alexandre Netto. Neonatal cerebral hypoxia–ischemia causes lateralized memory impairments in the adult rat. *Brain research*, 973(2):171–178, 2003.
- [BBK12] Irina Burd, Bindu Balakrishnan, and Sujatha Kannan. Models of fetal brain injury, intrauterine inflammation, and preterm birth. *American journal of reproductive immunology*, 67(4):287–294, 2012.

- [CCB<sup>+</sup>09] Caroline O Chua, Halima Chahboune, Alex Braun, Krishna Dum-mula, Charles Edrick Chua, Jen Yu, Zoltan Ungvari, Ariel A Sherbany, Fahmeed Hyder, and Praveen Ballabh. Consequences of intraventricular hemorrhage in a rabbit pup model. *Stroke*, 40(10):3369–3377, 2009.
- [DDJT07] Matthew Derrick, Alexander Drobyshesky, Xinhai Ji, and Sidhartha Tan. A model of cerebral palsy from fetal hypoxia-ischemia. *Stroke*, 38(2):731–735, 2007.
- [DIY<sup>+</sup>04] Sandra Dieni, Terrie Inder, Bradley Yoder, Todd Briscoe, Emily Camm, Gary Egan, Derek Denton, and Sandra Rees. The pattern of cerebral injury in a primate model of preterm birth and neonatal intensive care. *Journal of Neuropathology & Experimental Neurology*, 63(12):1297–1309, 2004.
- [DJL<sup>+</sup>14] Alexander Drobyshesky, Rugang Jiang, Laixiang Lin, Matthew Derrick, Kehuan Luo, Stephen A Back, and Sidhartha Tan. Unmyelinated axon loss with postnatal hypertonia after fetal hypoxia. *Annals of neurology*, 75(4):533–541, 2014.
- [DMBS<sup>+</sup>10] Robert De Matteo, Natasha Blasch, Victoria Stokes, Peter Davis, and Richard Harding. Induced preterm birth in sheep: a suitable model for studying the developmental effects of moderately preterm birth. *Reproductive Sciences*, 17(8):724–733, 2010.
- [INK<sup>+</sup>05] Terrie Inder, Jeffrey Neil, Christopher Kroenke, Sandra Dieni, Bradley Yoder, and Sandra Rees. Investigation of cerebral development and injury in the prematurely born primate by magnetic resonance imaging and histopathology. *Developmental neuroscience*, 27(2-4):100–111, 2005.
- [INJR05] Terrie Inder, Jeffrey Neil, Bradley Yoder, and Sandra Rees. Patterns of cerebral injury in a primate model of preterm birth and neonatal intensive care. *Journal of child neurology*, 20(12):965–967, 2005.
- [Lev05a] Kate Ann Levin. Study design i. *Evidence-based dentistry*, 6(3):78, 2005.
- [Lev05b] Kate Ann Levin. Study design ii. issues of chance, bias, confounding and contamination. *Evidence-based dentistry*, 6(4):102, 2005.
- [Lev06] Kate Ann Levin. Study design iii: Cross-sectional studies. *Evidence-based dentistry*, 7(1):24, 2006.

- [LTC<sup>+</sup>15] Seong Yong Lim, Yeu-Sheng Tyan, Yi-Ping Chao, Fang-Yu Nien, and Jun-Cheng Weng. New insights into the developing rabbit brain using diffusion tensor tractography and generalized q-sampling mri. *PloS one*, 10(3):e0119932, 2015.
- [MAS<sup>+</sup>15] Désirée Müllhaupt, Heinz Augsburger, Andrea Schwarz, Gregor Fischer, Patrick Kircher, Jean-Michel Hatt, and Stefanie Ohlerth. Magnetic resonance imaging anatomy of the rabbit brain at 3 t. *Acta Veterinaria Scandinavica*, 57(1):1, 2015.
- [MMA<sup>+</sup>13] Emma Muñoz-Moreno, Ariadna Arbat-Plana, Dafnis Batalle, Guadalupe Soria, Miriam Illa, Alberto Prats-Galino, Elisenda Eixarch, and Eduard Gratacos. A magnetic resonance image based atlas of the rabbit brain for automatic parcellation. *PloS one*, 8(7):e67418, 2013.
- [MTE<sup>+</sup>01] John Mazziotta, Arthur Toga, Alan Evans, Peter Fox, Jack Lancaster, Karl Zilles, Roger Woods, Tomas Paus, Gregory Simpson, Bruce Pike, et al. A probabilistic atlas and reference system for the human brain: International consortium for brain mapping (icbm). *Philosophical Transactions of the Royal Society of London B: Biological Sciences*, 356(1412):1293–1322, 2001.
- [NDMH<sup>+</sup>17] Vivian B Nguyen, Robert De Matteo, Richard Harding, Aneta Stefanidis, Graeme R Polglase, and M Jane Black. Experimentally induced preterm birth in sheep following a clinical course of antenatal betamethasone: effects on growth and long-term survival. *Reproductive Sciences*, 24(8):1203–1213, 2017.
- [PYAL88] Elizabeth Pusey, Chun Yoon, Michael L Anselmo, and Robert B Lufkin. Aliasing artifacts in mr imaging. *Computerized medical imaging and graphics*, 12(4):219–224, 1988.
- [RvGK<sup>+</sup>13] Manimaran Ramani, Thomas van Groen, Inga Kadish, Arlene Bulger, and Namasivayam Ambalavanan. Neurodevelopmental impairment following neonatal hyperoxia in the mouse. *Neurobiology of disease*, 50:69–75, 2013.
- [vdMvdVF<sup>+</sup>19] Johannes van der Merwe, Lennart van der Veeken, Sebastiano Ferraris, Willy Gsell, Uwe Himmelreich, Jaan Toelen, Sebastien Ourselin, Andrew Melbourne, Tom Vercauteren, and Jan Deprest. early neuropathological and neurobehavioral consequences of preterm birth in a rabbit model. *Scientific reports*, 9(1):3506, 2019.

- [Vol09] Joseph J Volpe. Brain injury in premature infants: a complex amalgam of destructive and developmental disturbances. *The Lancet Neurology*, 8(1):110–124, 2009.
- [YHY<sup>+</sup>04] San-Nan Yang, Chung-Bin Huang, Chin-Hwa Yang, Ming-Chi Lai, Wu-Fu Chen, Chih-Lu Wang, Chia-Lu Wu, and Li-Tung Huang. Impaired SynGAP expression and long-term spatial learning and memory in hippocampal CA1 area from rats previously exposed to perinatal hypoxia-induced insults: beneficial effects of A68930. *Neuroscience letters*, 371(1):73–78, 2004.

## Chapter 4

# Diffeomorphic image registration and integration of stationary velocity fields

### Contents

---

<b>4.1</b>	<b>Motivations . . . . .</b>	<b>78</b>
4.1.1	Segmentation propagation and label fusion . . . . .	79
4.1.2	Morphometry in the tangent space . . . . .	80
<b>4.2</b>	<b>Image registration principles . . . . .</b>	<b>81</b>
4.2.1	Rigid, affine and deformable registration . . . . .	81
4.2.2	Possible classifications in the literature . . . . .	85
4.2.3	The challenge of validation . . . . .	87
<b>4.3</b>	<b>Diffeomorphisms: a biologically sound deformation model</b>	<b>88</b>
4.3.1	Motivations . . . . .	88
4.3.2	Stationary and time-varying velocity fields . . . . .	89
4.3.3	LDDMM and Demonology . . . . .	90
4.3.4	Splitting strategy for the cost function optimisation . . . . .	91
<b>4.4</b>	<b>Integration of stationary velocity fields . . . . .</b>	<b>92</b>
4.4.1	Mathematical background . . . . .	92
4.4.2	SVF in the diffeomorphic image registration scheme . . . . .	94
4.4.3	Classical numerical integrators . . . . .	96
4.4.4	Scaling and squaring method and its generalisation . . . . .	97
4.4.5	The composition of stationary velocity fields . . . . .	99
4.4.6	Combining generalised scaling and squaring and exponential integrators . . . . .	101

4.4.7	Resulting algorithms . . . . .	105
<b>4.5</b>	<b>Benchmarking . . . . .</b>	<b>106</b>
4.5.1	Rigid body transformations . . . . .	106
4.5.2	General linear group . . . . .	108
4.5.3	Homographies . . . . .	112
4.5.4	Gaussian velocity vector fields . . . . .	114
4.5.5	BrainWeb dataset . . . . .	114
4.5.6	ADNI dataset . . . . .	117
4.5.7	Inverse consistency . . . . .	118
4.5.8	Benchmarking with NiftyReg . . . . .	119
<b>4.6</b>	<b>Open-source software: calie . . . . .</b>	<b>122</b>
<b>4.7</b>	<b>Conclusions and limitations . . . . .</b>	<b>122</b>

---

In this chapter we introduce the underpinning theoretical framework of diffeomorphic image registration to present the related methodological contribution: the scaling and squaring based approximated exponential integration method, proposed in [FLD<sup>+</sup>16].

Before addressing the main topic, we introduce the principles of image registration, focusing in particular on the ever-lasting problem of the validation. We subsequently introduce the motivations behind the use of diffeomorphisms as deformation model. We propose a well a brief perspective on the historical evolution of the use of diffeomorphisms according to the two main families of relevant registration algorithms, the LDDMM and the Demons.

Diffeomorphic registrations will be applied in Chapter 5 for the automatic segmentation of the newborn rabbit brain via segmentation propagation and label fusion, being segmentation propagation the thread connecting the methodological and the pre-clinical study reported in this thesis.

## 4.1 Motivations

In the process of transforming medical images into clinically relevant results with a reproducible method, the first step is the identification and delineation of the regions of interests. This goal can be achieved with an image labelling or segmentation strategy.

One of the options to obtain a segmentation of a given image is with the *segmentation propagation and label fusion*, a methodology underpinned by a registration tool [BS15].

While labelled images can provide the most direct source of information, there is also a wide range of possible statistics that can be computed on the transformation themselves. In particular, when diffeomorphisms are employed, the study of these transformation (and of their parametrisation in the tangent fields in particular), opens the door to a branch of *computational anatomy* called *diffeomorphometry*.

Segmentation propagation and label fusion and diffeomorphometry are introduced below, as starting point for the proposed contributions.

#### 4.1.1 Segmentation propagation and label fusion

As it is known intuitively - and mathematically, thanks to Wolpert and Macready [WM97] - there is no single best algorithm if the problem is general enough. In the field of medical imaging in particular, due to the lack of a ground truth, even assessing the goodness of an algorithm to solve a specific problem is not straightforward.

Among the several approaches to segment an image, the one that motivates the study of the image registration method is the segmentation propagation and label fusion.

Given an image to be segmented and another image of an equivalent anatomy already segmented, the propagation method works as follows: the segmented image is aligned with the unsegmented one through a selected registration algorithm. Subsequently the obtained transformation is applied to the segmentation. The so obtained new segmentation provides an estimate of the target segmentation.

This method relies on the availability of an existing segmentation of a similar anatomy, and it strongly depends upon the quality of the selected registration method. This approach is particularly suited when dealing with magnetic resonance images, as for most of the anatomical regions and for vast majority of the species, there can be more than one reference image already segmented, called in this context *multi-atlas*, or there can be a probabilistic map providing the likelihood for a voxel of belonging to a particular class, called *probabilistic atlas*. Examples of multi-atlas publicly available on the web are (last access March 23, 2019):

▷ <http://www.loni.usc.edu/atlasses/>

▷ <http://www.thehumanbrain.info/mri>

When a multi-atlas is available, the information from the stack of the propagated segmentations from the sources to the target can be combined, or *fused*, in a final segmentation with a *label fusion* technique. Most common fusion methods are *Majority Voting* (MV), *Simultaneous Truth And Performance Level Estimation* (STAPLE) [WZW04] and *Similarity and Truth Estimation for Propagated Segmentations* (STEPS) [CLM<sup>+</sup>13].

Majority voting is the simplest label fusion method. When applied, the final label assigned at each voxel is the one that have appeared more often when propagating the segmentation of each subject in the multi-atlas. STAPLE estimates the value of the final label adding at the spatial distribution of the segmented structures a spatial homogeneity constraint within a probabilistic model optimized with an Expectation-Maximisation algorithm. STEPS extends STAPLE, considering a ranking strategy based on the local normalized cross correlation (LNCC) measure of similarity applied to the propagated anatomies on the new subject anatomy.

When a large dataset of manually annotated images is not available, segmentation propagation and label fusion with a multi-atlas is the state of the art method for image segmentation. For the task of segmenting adult human brains, where is it possible to rely on large datasets, the state-of-the-art automatic methods for image segmentation is through the training of a convolutional neural network (see for example [GLS<sup>+</sup>18] as the first open source tool specifically tuned for neuroanatomy).

### 4.1.2 Morphometry in the tangent space

Morphometry dates back to the work of the Scottish biology D’Archy Wentworth Thompson On growth and Form [T<sup>+</sup>42], whose aim is the quantification of the shape variability. The birth of computational anatomy happened after combining morphometry with the emerging computational tools to implement sophisticated transformation models *in silico*. In particular when the transformations considered are diffeomorphisms, the resulting branch of computational anatomy is called *diffeomorphometry*.

Diffeomorphometry have had as starting point the viscous models developed and employed in the branch of physics of hydrodynamics, as proposed by Vladimir Arnold [Arn66]. One of the milestone in the application of these models in the transformations between human shapes is the work of Christensen, Rabbitt and Miller [CRM96].

There are two fundamental peculiarities of the diffeomorphic model:

- ▷ Diffeomorphisms preserve the topological genus of a shape [Mun00].
- ▷ There is a bijective correspondence between a diffeomorphism of  $\mathbb{R}^D$  and its tangent velocity field belonging to an Hilbert space.

Therefore, diffeomorphisms are a sensible choice when the two anatomies to be registered are believed to be in the same orbit of the group of diffeomorphisms, or when there is the need of computing statistics on the transformation model.

Diffeomophometry had evolved until today, after the challenges posed by the ever increasing datasets of medical images. Two of the main trends in diffeomorphic image

registration, LDDMM and Diffeomorphic Demons are introduced in Section 4.3.3, with a short bibliographical survey.

Further elements on this topic are introduced in Section 4.3, after the next section about the general principles of image registration.

## 4.2 Image registration principles

Medical image registration is an open and active field of research. A recent overview on the state-of-the-art methods can be found in the paper by Viergever et al. [VMK+16], having as starting point the previous surveys of Sotiras et al. [SDP13a] and Maniz et al. [MV98].

This section is devoted towards an introduction of the salient aspects of image registration oriented to the goal of this chapter: introducing the diffeomorphic based methods and the exponential of stationary velocity fields.

### 4.2.1 Rigid, affine and deformable registration

Given a *fixed* (or target) image  $F$  and a *moving* (or source) image  $M$  that is required to match the target through a to-be-found spatial transformation, the image registration problem can be formulated as an optimisation problem. The unknown  $\hat{S}$ , element of a space of spatial transformations  $\mathbb{S}$  or *deformation model*, must minimise a cost function  $\xi$  representing a distance, or a regularised distance, between the fixed image and the moving image after the transformation  $S$ :

$$\hat{S} = \arg \min_{S \in \mathbb{S}} \xi(F, M, S) \quad (81-1)$$

In the *continuous framing*,  $M$  and  $F$  are maps from a compact subset of  $\mathbb{R}^D$ . In the *discrete framing*, the  $M$  and  $F$  are matrices embedded in the space according to their affine transformations.  $M$  resampled after the transformation of  $S$  in the grid of  $F$  is represented with the composition  $M \circ S$  and it is called *warped image*.

The cost function  $\xi$  is based on the choice of a metric or distance between the space of images  $\text{Sim}$  (typically sum of squared differences, normalised mutual information or Kullback-leibler distance, according to the underpinning biomedical need) and on a Tikhonov regularization  $\text{Reg}$ , consisting on a chosen metric or distance defined on the space of spatial transformations. The cost function  $\xi$  can be written as:

$$\xi(F, M, T) = \text{Sim}(F, M \circ T) + \lambda \text{Reg}(T) , \quad (81-2)$$

where  $\lambda$  is a positive real number weighting the regularisation.

## 4.2. IMAGE REGISTRATION PRINCIPLES

---

Two settings are possible: in the *forward* setting, the transformation  $S$  maps the domain of  $F$  into the one of  $M$ , and  $M \circ S$ , i.e. the warped image, is the function composition. In the *backward* setting, more widely used as more efficient to implement, the transformation maps the domain of the moving image  $M$  in the domain of the fixed  $F$  and the warped of the moving image is computed as  $M \circ S^{-1}$ .

The continuous and forward setting can be summarised with a commutative diagram [JD94], where  $\Omega_F$  and  $\Omega_M$  are the domains of  $F$  and  $M$  respectively:

$$\begin{array}{ccc}
 \Omega_F & \xrightarrow{S} & \Omega_M \\
 \downarrow F & \searrow M \circ S & \downarrow M \\
 \mathbb{R} & \xrightarrow{\text{Id}} & \mathbb{R}
 \end{array}$$

In the practice, the parts of the anatomy that are not relevant for the optimisation function can be left out of the process with a mask. This is equivalent to restrict the domain  $F$  and  $M$  in the continuous framing, that corresponds to set to *NaN* the unwanted values in the matrices of the discrete framing.

The class of methods based on the description here provided, usually called *intensity-based methods*, are not the only ones available. Rather than optimising the distances between the image intensities, a set of landmarks (such as points, lines or surfaces) can be associated to each image. The consequent optimisation problem is aimed at minimising the distance in the landmarks space. These methods are called *landmark-based methods*.

For both intensity-based and landmark-based algorithms the determining element that defines the nature of the registration is the choice of the deformation model  $\mathbb{S}$ . In the *rigid deformation model*,  $\mathbb{S}$  is bonded to the rotation and translations of the image space. Therefore, it is defined as the semidirect product of the special Euclidean Lie group  $\text{SE}(D)$  and the vector space of dimension  $D$ . The *affine deformation model* is based instead on the general linear group  $\text{GL}(D)$ .

Matrix representation of the rigid and affine deformation model is customarily expressed in homogeneous coordinates as:

$$S = \begin{pmatrix} G & \tau \\ 0 & 1 \end{pmatrix} \quad (82-1)$$

where  $G$  belongs to  $\text{SE}(D)$  for the rigid or to  $\text{GL}(D)$  for the affine registration and  $\tau$  is a column vector of dimension  $D$  representing the translation part. When  $D = 3$ ,  $G$  has dimension  $3 \times 3$  and  $S$  has 5 linearly independent variables.

Rigid registration algorithms are employed when the anatomies to be aligned are expected to be approximatively congruent. Affine, when the anatomies are expected to belong to the same orbit of the group of affine transformation.

Limiting the deformation model  $\mathcal{S}$  to a space of linear transformation, such as translations, rigid body transformations and affine transformations, leads to a registration algorithm adequate to deal with a wide range of practical cases.

More and less recent publications provide very accurate and efficient methods to solve numerically or even analytically vast majority of affine registration problems.

For example the paper by Arun et al. [AHB87] introduced a closed solution for the least square minimisation problem between clouds of points in the 3D space, solving the rigid landmark-based registration problem. For curves and surfaces based rigid registration, an optimisation-based method called *iterative closest point matching algorithm* was subsequently proposed by Besl and McCay [BM92]. The range of iterative algorithms aimed at reaching the approximated solution can be enhanced by two strategies: symmetrisation and block-matching. Joined in a single method by Modat et al. [MCD<sup>+</sup>14], the symmetrisation is aimed at reducing the bias introduced in the selection of the fixed respect to the moving image. The block matching reduced the impact of the initialisation in reaching the final solution and it is robust to outliers. Resulting algorithm with parallelised implementation is publicly available within NiftyReg<sup>1</sup>.

When the fixed and the moving images are not expected to align satisfactorily after an affine transformation, more elaborate deformation models are needed. Non-linear geometric distortions can be caused by imaging device or induced by the investigated biological phenomenon. In these cases the 5 degrees of freedom provided by the affine registration methods are not enough and models with a higher number of parameters must be considered. The registration methodology is in this case called *deformable* or *non-linear*.

The outcome of a deformable registration algorithm is typically a control point grid overlaying the Fixed image. The vector of the deformation matching the moving and the fixed image is defined at each control point.

A common computational approach to deal with the high dimensionality of the problem is to apply a pyramidal method. Proposed in medical imaging by Thevenaz et al. [TRU98], the pyramid method consists of starting the optimisation on a transformation where the resolution of the control point grid is lower than the Fixed image. Once the coarse grid search has reached convergence, the resolution is increased and a new search is initiated. This approach is studied to reduce the local minima at each pyramid step and to control at the same time the registration smoothness level.

---

<sup>1</sup><https://github.com/KCL-BMEIS/niftyreg>.

Most relevant books written on the topic of deformable registration, such as Goshtasby [GSST03], Hajnal [HH01] and Modersitzki [Mod04] state that the ideal non-linear image registration algorithm should be:

1. Adaptable: the same algorithm is expected to adapt to different measures of similarity so to work with different clinical settings.
2. Computable: the transformation parametrisation must have a reasonably low computational time.
3. Constrained: the deformation model must satisfy a range of selected constraints reflecting the biology of the modelled deformation.
4. Inverse consistent: the transformation between the anatomy A and B must be the inverse of the transformation between B and A.

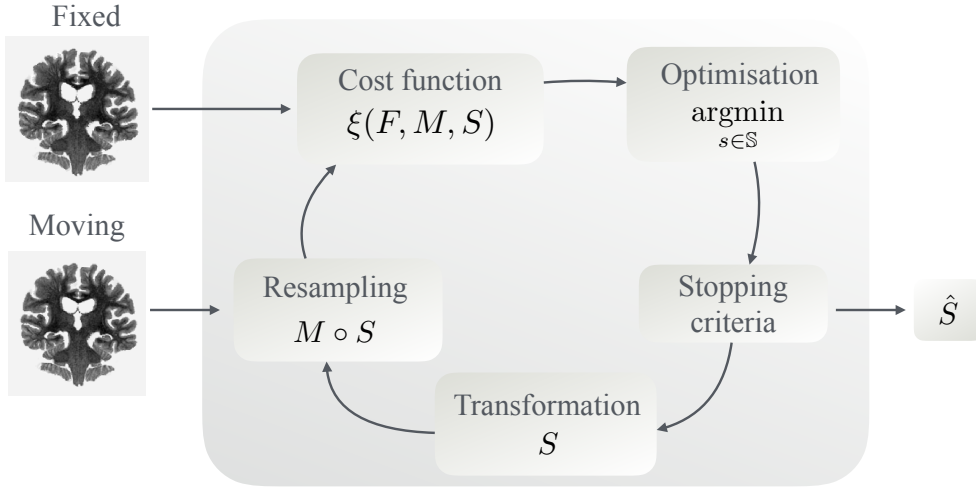


Figure 84-1: **Schematic view of the registration algorithm.** The archetypal deformable image registration is made of two inputs (fixed and moving images) an output transformation  $\hat{S}$  and 5 main components: resampling, cost function, optimisation, stopping criteria, and a deformation model to which the estimated transformation output belongs. Human brain coronal sections shown are MRI scans with inverted contrast from the ADNI database [JBF+08].

Figure 84-1 shows the prototypical linear and non-linear registration algorithm scheme, similar to the one proposed in the ITK software guide [ISNC03]. Given a fixed and a moving image, that can have 3 or more dimensions (if more than one time-point or modality is provided), the moving image is initially resampled with the initial estimate of the transformation (customarily the identity, or an initial affine alignment in some cases). The so obtained moving, the provided fixed image, and the

to-be-found transformation belonging to a defined set of transformations are taken as argument of the optimisation function (sometimes called *energy function*) whose minimum is expected to provide the transformation minimising the distance between the fixed and the transformed moving. As seen above, the energy function is usually a linear combination between a distance defined over the domain of the images and a regularisation term. The subsequent step is the optimisation of the cost function, usually a gradient descent method.

If a stopping criteria is reached, then the obtained transformation is returned as an estimate of the best transformation aligning the moving image over the fixed one. If the criteria is not matched, then the obtained transformation  $S$  is taken as input of a new cycle and re-sampled with the moving image, outcome of the previous cycle.

This broad generalisation of the prototypical registration algorithm, turns out to have a practical value. It provides within the same framework the range of variability of the various components: the range of the similarity measure, the range of regularisations and a range of deformation models. Moreover, it provides an overview on the possible bottlenecks hindering the efficiency of the algorithm. When the deformation model is expected to preserve the topology between anatomies - or, as introduced more formally before, the topological genus [Mun00] - then the infinite dimensional Lie group of the topology-preserving diffeomorphisms parametrised with stationary velocity fields appears to be a reasonable choice.

Before diving into this particular class of algorithms, we provide a section with a brief overview on the possible classifications of the relevant literature. We end the section addressing the issue of the validation in image registration, that will work as introduction for the validations proposed in Chapter 5.

#### 4.2.2 Possible classifications in the literature

The literature offers several possible registration algorithm classifications. Sotiras et al. [SDP13b] classified the registration algorithm according to the deformations models: physics-based, interpolation-based, knowledge-based and task specific constraints.

Oliveira and Tavares [OT14], updating the previous survey by Maintz and Viergever [MV98], admitted that a single classification criteria is not enough to reach a satisfactory perspective over the field. Therefore, they proposed a range of perspective to classify image registration algorithms: dimensionality, nature of the registration basis, nature of transformation, domain of transformation, interaction, optimisation procedure, modalities involved in the registration, subject and object.

In refraining from providing another classification that would eventually turn out to be an extenuating (both for the reader and the author) and fundamentally not use-

ful entomological undertaking, we propose instead in this section a very short list of selected papers and books constituting a possible pathway to a broader investigation, starting from the parts constituting the archetypal registration algorithm.

Referring again to Figure 84-1 the moving image is resampled with the initial transformation (the identity for the first iteration) and then the distance between images is computed using the selected cost function. If the stopping criteria is not reached (usually based on a tolerance of the cost function and on a lazy convergence criteria) the selected optimisation strategy is employed to find a new transformation to start again the iterative cycle.

If the transformation  $S$  can be expanded as a linear combination of a chosen basis functions (e.g. radial basis functions or thin-plate-splines), then the algorithm is classified as *parametric*. In this case, the sought transformation minimises the chosen distance in the space spanned by the basis.

If the transformation is not modelled with a linear combination of basis function (e.g. Gaussian smoothed vector fields or Stokes fluid obeying a system of ordinary or partial differential equations), then the resulting algorithms is called *non-parametric* [Mod04].

In parametric case the constraint imposed by the transformation model consists of the space generated by the basis function itself, and the transformation is a vector of linear coefficients of the basis. In the non-parametric case the constraint is not intrinsic of how the deformation model is described, but it is given by an external system of equations that an otherwise unconstrained deformation must satisfy.

Parametric and non-parametric approaches can be combined. In the method proposed by Rueckert et al. [RAH<sup>+</sup>06], the deformation model is constrained by an ordinary differential equation (ODE), which does not make the model parametric by definition, but it is at the same time expressed in term of the b-spline basis function, which does indeed make the model parametric.

Often, a good approach consists of combining sequentially two or more approaches, according to the addressed problem. The resulting pipeline can not strictly belong to any category. Moreover, boundaries of these classifications are admittedly loose. There are algorithms that may belong to different categories, while being very similar in practice, or that do not belong to any of the proposed categories, such as the Completely Useless Registration Tool (CURT) by Rohlfing et al. [Roh12] or the registration based on optimal mass transport theory by Haker et. al [HZTA04].

Validation and scoring of registration algorithms constitutes an important part of the medical imaging research. They can as well provide an indirect criteria of classification. In neuroimaging, Ferrarese et al. [FSFM14], Ou et al. [OAB<sup>+</sup>14] and Crum et al [CRJ<sup>+</sup>04] provided some contributions in this direction.

And on the topic of the image registration validation we move to the next section.

### 4.2.3 The challenge of validation

Each endeavour belonging to the medical domain must provide demonstrable validity according to the strictest criteria. Medical imaging is not exempt from this requirement, as it is not exempt from the intrinsic difficulties in validating a claim in the absence of a ground truth.

The whole registration methodology is based upon the selection of a distance between images. Yet, Rohlfing [Roh12] provided experimental evidence of the fact that measures such as image similarity and tissue overlap, even when used in combination, are independent from the measure of the accuracy of the transformations employed in the registration. This is problematic, as the stopping criteria in a registration algorithm, is intrinsically defined over an measure of image similarity.

The mentioned paper reinforced the need to call for a case by case validation strategy that is external to the registration algorithm itself, given that the convergence of the method is not *per se* a validation. A validation strategy, proposed before Rohlfing, can involve the construction of synthetic plausible transformations, to deform a dataset of patients real data images. The correspondence between the original and the deformed images is in this way the gold standard that the accurate and realistic registration algorithm should be able to recover [STCS<sup>+</sup>03].

Another strategy, as advocated by Rohlfing is to validate the registration algorithm, not on a distance defined on the space of images, but on an overlap measure on a segmentation provided within the anatomies, or with the distances between landmarks. Even if very direct pragmatic, this strategy is intrinsically biased by the lack of a ground truth in the image segmentation and landmarks delineation. Therefore, it is not possible to tell if the detected error based on these image features is due to imprecise segmentations and landmarks or due to the registration itself.

Several proposed registration methods have been incorporating an uncertainty term in a probabilistic framework for the on-line results improvements [HSJ<sup>+</sup>13, SWA<sup>+</sup>13], nonetheless no probabilistic validation framework for a general case had appeared so far in the literature. This is after the fact that generalising a validation strategy is probably not a feasible option, due to the nature of the optimisation problems, and each algorithm must be evaluated in respect to its specific goal and application. This is as well problematic, as the final goal may not have a dataset providing a gold standard.

For example in an hypothetical study of the morphometric variability of the brain in the Alzheimer disease, it is possible to consider the shrinkage of the hippocampi as a given fact, and use this fact to validate if the registration algorithm is accurately detecting this variability. Or, vice versa, it is possible to use a registration algorithm that is believed to be accurate, because validated on another unrelated dataset (with

the consequent risks involved in the parameters selection), to prove that the shrinkage of the hippocampi for the AD patients occurs, and to use this tool to quantify its extent.

These circular impasses in the validation are relatively frequent in medical imaging, and a way to solve these deadlocks is to recur to a ground truth from histology and resulting 2D manual measurements. This cross sectional comparison works only partially as intrinsically affected by error in the histological measurements, possible hidden confounding factors in the statistical bias selection and by the assumption of an chosen underpinning statistical distribution.

In the specific case of image registration, being an optimisation problem, it directly calls the already cited paper by Wolpert and Mcready [WM97] into play. The no free-lunch theorem mathematically showed that all algorithms have the same performance on a wide enough dataset. This analogous of the Goedel incompleteness theorem for optimisation, makes the validation of an algorithm acting on a specific dataset, let's say  $A$ , a fundamental need, no matter how the same algorithm had provided a good performance on a different dataset  $B$ .

Moreover, if on the dataset  $B$  a ground truth making the validation possible was available, a ground truth is not likely to be available on the dataset  $A$ , where we are typically more interested to apply the algorithm. This problem should lead to the challenge of defining a metric on the set of datasets to enable a quantification of the uncertainty in moving away from  $B$  to  $A$ .

The next section is devoted to the core of the chapter: the deformation model of diffeomorphisms.

### 4.3 Diffeomorphisms: a biologically sound deformation model

In the previous sections we have introduced the general principles of image registration. In this one and in the subsequent ones we focus the attention towards the diffeomorphic deformation model, starting from the motivation and from an historical perspective on how this model had influenced and changed the field.

#### 4.3.1 Motivations

A diffeomorphism on the closed subset  $\Omega$  of  $\mathbb{R}^D$ , is a differentiable and invertible function with differentiable inverse. The set of diffeomorphisms over  $\text{Diff}(\Omega)$  becomes an algebraic group with the operation of composition, over the structure of infinite dimensional manifold. As previously mentioned, the study of diffeomorphisms in physics originated in hydrodynamics, with the seminal paper by the Russian mathe-

matician Vladimir Arnold [Arn66], leading to subsequent works by the same author [Arn13], as well as notable works from other Russian and Russian-American mathematicians (Khesin [KW08], Marsden [MA70], Ebin [EM70]).

Fluid dynamics had been considered in medical image registration as providing the constraint on the possible deformable transformations to the ones that reflect the changes occurring in a fluid, compressible (diffeomorphisms) as well as incompressible (diffeomorphisms with Jacobian everywhere defined equals to 1, or volumorphisms). This model is believed to be the more realistic in generating a likely transformation of a biological shape.

It is implicit in the use of a model that the real causes leading to the modelled phenomenon can be different from the causes of the variability as described by the model. For example in the case of ventricular expansion in Alzheimer, where diffeomorphisms are widely used in the clinical research [BLR<sup>+</sup>17, LBC<sup>+</sup>17, TW16], the loss of white matter, happening through an erosive process, is modelled instead with a fluid shrinkage, as this is closer to how the effects of the disease is visually perceived, but it does not represent what is happening in the practice.

Two possible parametrisation are used to model diffeomorphisms in medical image registration, the stationary and the time-varying.

### 4.3.2 Stationary and time-varying velocity fields

According to the dependence of the time parameter employed in the ordinary differential equation (ODE) modelling the tangent vector field parametrising the deformable transformation, there are two types of model: if the vector field depends on time, then it is called varying velocity field model (TVVF). If the vector field employed to model the diffeomorphisms is time-independent then the tangent field is called stationary velocity field (SVF).

Transformations parametrised with time-varying (or non-stationary) velocity fields have appeared in medical imaging in the work by Grenander, Miller, Trouné, Pennec and colleagues, and plays a fundamental role in the field of *computational anatomy* [DGM98a, GM98, Mil04].

Using time-varying velocity fields to parametrise the deformations, that are not necessarily diffeomorphic, implies the need of solving a non-linear time varying ordinary differential equation at each control point of the grid deformation, at each iteration of the algorithm. A faster version of the algorithm, restricts the parametrisation to the diffeomorphisms, whose tangent vector field is a stationary velocity field (SVF). The consequent differential equation is a stationary ordinary differential equation (ODE). An introduction of SVF and TVVF had been proposed by Hernandez et al. [HPOG09], where in the same paper, a selection of SVF-based algorithms

are compared.

When considered with a multi-atlas, Diffeomorphic registration can be a component of a class of segmentation propagation algorithms. This will be described in Chapter 5 for the automatic segmentation of the brain rabbit. In the next subsection we introduce two common image registration families, and how they have evolved historically under the influence of the diffeomorphisms.

In Section 4.4 we will be focusing the attention over the SVF, detailing the consequent algorithm and one of the consequent bottleneck of choosing this deformation model for the parametrisation of the transformation.

#### 4.3.3 LDDMM and Demonology

In the historical evolution of the deformable registration approaches, we can identify two main trends that are relevant for the contributions proposed in the next sections. These are particularly interesting in respect to the evolution of the cost function optimisation method.

The two trends are shown in Figure 90-1. The LDDMM side is above the timeline and the Demons is below. The seven years gap between the fist Demons and the LDDMM is filled in 2007, where the introduction of stationary velocity fields had resulted in three almost equivalent papers published at the same time: the stationary LDDMM, the DARTEL and the diffeomorphic Demons.

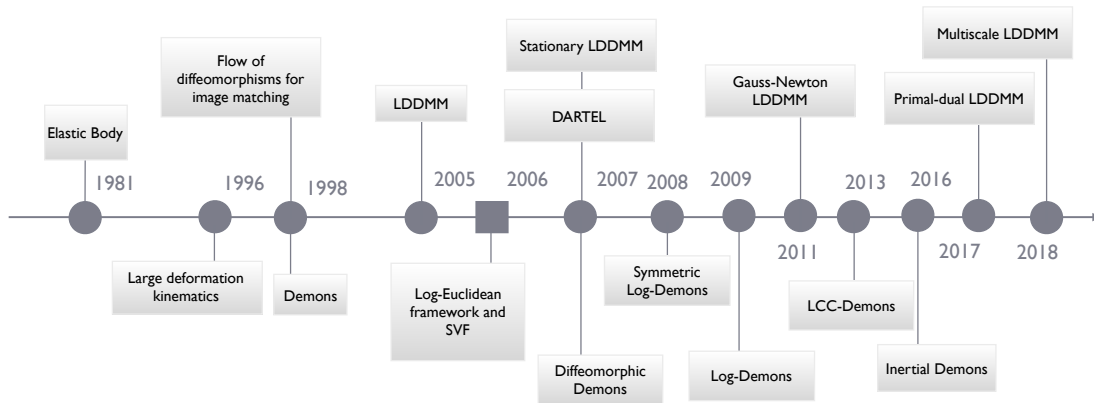


Figure 90-1: **Some landmarks in the evolution of diffeomorphic image registration algorithms** with Demons approach, started in 1998 and the Large Deformation Diffeomorphic Metric Mapping approach, started in 2005. For a complete perspective of the landscape of image registration algorithms in medical imaging we refer to Sotiras et al. [SDP13b].

The origin of the LDDMM algorithm can be traced back to the Elastic body algorithm by Broit et al. [Bro81] introducing the elastic mechanics in the modelling

of the deformation between images. Dupuis et al. [DGM98b] approached the deformation between images with a fluid dynamic model, whose evolution produced the successful LDDMM by Beg et al. [BMTY05]. A different approach, called Demons in analogy with the Maxwell Demon as proposed by Thirion et al. [Thi98], was an evolution of the kinematics deformations by Christensen et al. [CRM96]. Demons method was renewed by the introduction of the log-Euclidean framework and the scaling and squaring algorithm in medical imaging by Arsigny et al. [ACPA06] (and outside the field of medical imaging, by Ying and Candes [YC06]).

The log-Euclidean framework was applied to the Demons algorithm in Vercauteren et al. [VPPA07], with the log-Demons. The log-Euclidean framework was considered as well for an analogous stationary version of the LDDMM by Hernandez et al. [HBO07]. In between the two approaches Ashburner et al. proposed DARTEL [Ash07], where again diffeomorphisms are parametrised with SVF and integrated with the already mentioned scaling and squaring algorithm.

Subsequent notable evolutions on the LDDMM side have been the Gauss-Newton LDDMM, again proposed by Ashburner [AF11], the primal-dual LDDMM by Hernandez [Her17] and more recently the Multiscale LDDMM by Tan et al. [TQ18]. On the Demons side, the diffeomorphic Demons [VPPA07] was followed by the symmetric log-Demons and the log-Demons again by Vercauteren et al. [VPPA08, VPPA09]. It was initially based on the sum of squared difference as measure of similarity; therefore, in the subsequent research work by Tristán-Vega et al. [TVVSFAF08] other metrics were compared, such as the local normalised cross correlation and a newly introduced one called normalised mean squared difference. On the same trail, Lorenzi et al. [LAF<sup>+</sup>13] proposed again the log-Demon based on the local cross correlation. A further evolution of the log-Demons, based on the momentum method was then proposed by Santos-Ribeiro et al. [SRNM16]. Figure 90-1 reports a chronological representation of the selected bibliography.

#### 4.3.4 Splitting strategy for the cost function optimisation

In the diffeomorphic Demons, the splitting strategy underpinning the classical Demons is embedded in a mathematical formalisation, and the optimisation step is improved with a decoupled scheme.

Here we are presenting some details. The decoupled scheme works as follows: the cost function is written as:

$$\xi_{F,M}(S, T) = \text{Sim}(F, M, S) + \lambda \text{Dist}(S, T) + \text{Reg}(T) \quad (91-1)$$

where  $T$  is an auxiliary transformation of the deformation model  $\mathbb{S}$ ,  $\text{Sim}$  is a measure of similarity  $\text{Dist}$  is a metric (or a distance) between the sought transformation  $S$

and the auxiliary one and  $\text{Reg}$  is the regularisation term. In the first step of the decoupled optimisation,  $T$  is fixed and the cost function is optimised respect to  $S$ . In the second one,  $S$  is fixed to the one found in the previous step, and the cost function is optimised respect to  $T$ .

The classical Demons can be reformulated with the splitting cost function, considering the Gaussian filter on  $S$  as a strategy to optimise  $\lambda \text{Dist}(S, T) + \text{Reg}(T)$ . Gradient descent methods and conjugate descent methods have been implemented to minimise Equation 91-1 for several similarity measures and regularisations by Modat et al. [MRT<sup>+</sup>10].

The main bottleneck of image registration is the optimisation of the cost function. There is a wide multi-disciplinary research literature addressing the problem of optimisation. For the particular case of diffeomorphic image registration algorithms based on SVF there is a main second bottleneck: the Lie exponential map computation, to which the next section is devoted.

## 4.4 Integration of stationary velocity fields

In the previous sections we introduced the general image registration framework, we motivated the need for diffeomorphisms when dealing with medical imaging and we reviewed the literature for the two main families of medical image registration algorithms based on diffeomorphism.

Subsequently we addressed the optimisation problem, as the first bottleneck of image registration, and mentioned the second bottleneck when the stationary velocity field are employed as deformation model parametrisation. The first three sections of this chapter had been devoted to introduce the problem from the medical image registration perspective. Now we address the mathematical details of this second bottleneck, and how this interacts with the prototypical registration framework. We start introducing mathematical background and the state of the art methods for the integration of stationary velocity fields and we describe the proposed class of algorithms.

### 4.4.1 Mathematical background

The constraints imposed by the choice of diffeomorphisms as deformation model can be technically implemented through the parametrisation of the transformation in the space of stationary velocity fields (SVF). The spatial transformation parametrised by an SVF is computed integrating the vector field with a numerical method.

The ordinary differential equation (ODE) governing the parametrisation, that

recurs in several fields of science, is given by:

$$\left. \frac{d\phi_t(\mathbf{x})}{dt} \right|_{t=\tau} = \mathbf{v}(\phi_\tau(\mathbf{x})), \quad \phi_0 = \text{Id}, \quad t \in T \subseteq \mathbb{R}, \quad \mathbf{x} \in \Omega, \quad (92-1)$$

where  $T$  is a connected domain of the time parameter,  $\phi : T \times \Omega \rightarrow \Omega$  is the flow of diffeomorphisms that solves the equation and  $\mathbf{u} : \Omega \rightarrow \mathbb{R}^D$  is the stationary velocity field or tangent vector field<sup>2</sup>. The relevant case in diffeomorphic image registration is for  $\tau = 1$ , where the sought diffeomorphism  $\phi_1 : \Omega \rightarrow \Omega$  solves the ODE for the selected timepoint. Having a distinctive application, the solution at  $t = 1$  is often indicated with  $\phi = \phi_1$ .

The set of diffeomorphisms whose infinitesimal variation is given by  $\mathbf{v}$ , is acting over  $\Omega$  and it varies according to a time parameter  $t$ . This set, indicated by  $\{\phi_t\}_{t \in \mathbb{R}}$  defines a dynamical system or a *flow of diffeomorphisms*, and it satisfies the one-parameter subgroup property:  $\phi_0$  corresponds to the identity function over  $\Omega$  and  $\phi_t \circ \phi_s = \phi_{t+s}$ . For a range of examples and further theoretical notes, see Holm et al. [HSSE09], page 102 (still related to the imaging problem) as well as the first chapter of Arnold [Arn06] (related to dynamical systems and fluid dynamics).

In the practice, usually the vector field  $\mathbf{v}$  is represented in *Lagrangian coordinates* (also unhappily called *displacement coordinates*), where each affine vector is considered respect to its relative position in the space. The deformation  $\phi$  is usually represented in *Eulerian coordinates* (also unhappily *deformation coordinates*), where at each point of  $\Omega$  is associated the vector joining the origin and the final position of the particle starting at the point. The identity in Lagrangian coordinates is a vector field that at each point  $\mathbf{x} \in \Omega$  associates the zero vector. The identity in Eulerian coordinates is a vector field that at each point  $\mathbf{x} \in \Omega$  associates  $\mathbf{x}$ .

The solution of Equation 92-1 is called *Lie exponential*, in analogy with the fact that when  $\mathbf{v} = A$  is a linear vector field, the solution is provided by the matrix exponential of  $A$ . Any numerical method whose aim is to find an approximation is a *numerical integrator*. We refer again to Holmes [HSSE09] Chapter 5 for a range of examples.

The mathematical structure constituting the domain and image of the exp function are the infinite dimensional Lie algebra and Lie group of diffeomorphisms respectively. They are usually indicated with  $V(\Omega)$  and  $\text{Diff}(\Omega)$ , or with  $\mathfrak{g}$  and  $\mathbb{G}$  respectively. The scalar product and sum of the Lie algebra satisfies in fact the condition to be an algebra, and the composition between diffeomorphisms satisfy the condition of being a group for the Lie group. The trivial fact that both spaces are

---

<sup>2</sup>To simplify the notation, sometimes the above ODE is indicated with  $\frac{d\phi(\mathbf{x})}{dt} = \mathbf{v}(\phi(\mathbf{x}))$  or even with  $\frac{d\phi}{dt} = \mathbf{v}(\phi)$  or, using the Peano convention, with  $\dot{\mathbf{x}} = \mathbf{v}(\mathbf{x})$  for  $\tau = 0$ .

locally Euclidean, for a single chart, makes them Lie structures [Car92].

In mathematics, Lie theory studies the Lie groups, their tangent spaces and their mutual relationship. It usually deals with vector fields defined on more general manifolds than the one relevant to medical image registration. In fact, in medical image registration, the considered manifold is the simplest one, i.e.  $\mathbb{R}^D$ , and its tangent space at any point is  $\mathbb{R}^D$  itself. Therefore, there is no need to include in this discussion concepts that are relevant for the study of more convoluted cases, such as local charts, changes of coordinates maps and fibre bundles.

The main component is the Lie exponential, the map that associates to a tangent vector field the diffeomorphism solving Equation 92-1. In the literature, at the time-point  $t$ , the Lie exponential is indicated with:

$$\exp(t\mathbf{u}) = \phi_t \quad (94-1)$$

and the numerical approximation of the Lie exponential is indicated here with:

$$\widetilde{\exp}(t\mathbf{u}) = \tilde{\phi}_t . \quad (94-2)$$

Its computation is practically achieved solving an ordinary differential equation with a numerical method. Here, the exponential map is a bijective correspondence between vector fields and the space of flows of diffeomorphisms, thanks to the Cauchy theorem (or the Picard-Lindelof theorem).

In medical image registration some authors reported that this bijective correspondence does not hold [LP13] even if this is in clear contradiction with the Cauchy theorem. This claim have started after a misreported counterexample by Milnor [Mil84]. It can be noticed that in this specific counterexample the Lie group considered is the group of the one-dimensional circle, where, thanks to the modularity of the parametrisation, the bijective correspondence is not satisfied. This specific counterexample does not relate to  $\mathbb{R}^D$ , as the Lie group of the circle is not flat, is not periodic and does not have a trivial first fundamental group. And more importantly, it is not relevant in medical image registration.

In the next section we introduce the relationship between the Lie exponential and diffeomorphic image registration.

##### 4.4.2 SVF in the diffeomorphic image registration scheme

The prototypical registration scheme for the diffeomorphic algorithm based on SVF is a particular case of the scheme proposed in Figure 84-1. In this instance, proposed in Figure 95-1, the main difference lies in the representation of the transformation with its parametrisation as a stationary velocity field. The optimisation step encodes

the transformation as an element of the Lie algebra  $V(\Omega)$ , or tangent space. In the resampling step the corresponding flow of diffeomorphisms, element of the Lie group  $\text{Diff}(\Omega)$ , is computed through the exponential map.

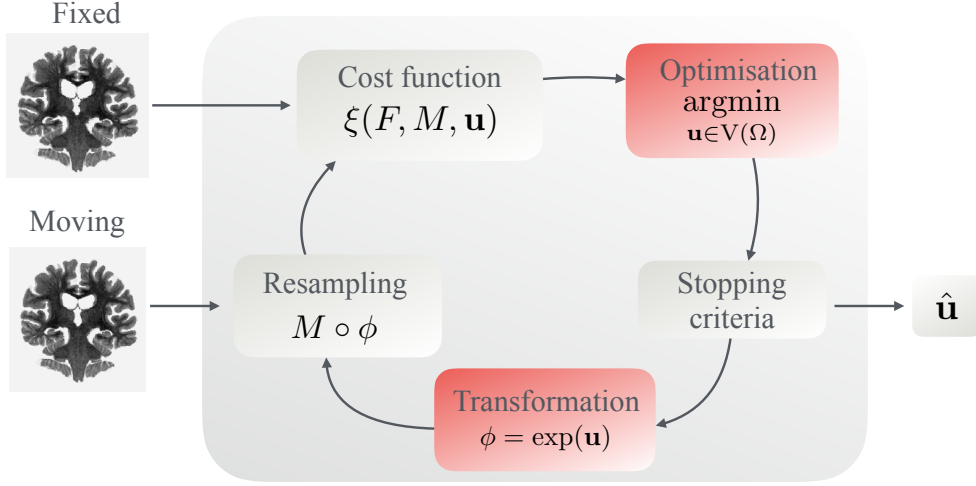


Figure 95-1: **Schematic view of the diffeomorphic registration algorithm.** The archetypal deformable image registration based on diffeomorphisms is made of two inputs (fixed and moving images) an output transformation in the tangent space  $\hat{\mathbf{u}}$  and, as in the more general case, 5 main components: resampling, cost function, optimisation, stopping criteria, and a deformation model. In this case the deformation model of diffeomorphisms parametrised with stationary velocity fields, and the exponential function plays a pivotal role.

A decoupled optimisation scheme, as introduced in Section 4.3.4 can be implemented as well. In this case the cost function  $\xi(F, M, \mathbf{u})$  can be decoupled into three terms:

$$\xi_{F,M}(\mathbf{u}, \mathbf{v}) = \text{Sim}(F, M, \mathbf{u}) + \lambda \text{Dist}(\mathbf{u}, \mathbf{v}) + \text{Reg}(\mathbf{v}) \quad (95-1)$$

where the distance between the two parametrisation of transformation is well defined, as these are elements of an Hilbert space.

If for example the chosen metric is the SSD, then:

$$\text{Sim}(F, M, \mathbf{u}) = \|F - M \circ \exp(\mathbf{u})\| \quad (95-2)$$

$$\text{Dist}(\mathbf{u}, \mathbf{v}) = \|\mathbf{u} - \mathbf{v}\| \quad (95-3)$$

$$\text{Reg}(\mathbf{v}) = \|\mathbf{v}\| . \quad (95-4)$$

In the next section we introduce some of the well established methods for the numerical computation of the Lie exponential, or integration of a stationary velocity

field.

#### 4.4.3 Classical numerical integrators

For the non-linear ODE case, there is no analytical solution to compute the Lie exponential. To address this problem several integrators based on numerical approximations have been proposed. The most commonly utilised are reported in the classical textbook Burden et al. [FB14]. Their improvement in accuracy, stability and computational time is an open field of research that involves medical imaging applications. Bossa et al. [BZO08] presented a comparison of different numerical approaches for the integration of SVFs when applied to diffeomorphic image registration.

A *Lie exponential approximant* is any appropriate numerical integrator of the Lie exponential that deals with small SVFs. We indicate it here with  $\widetilde{\exp}$ . Lie exponential approximants are customarily applied scaling the input tangent vector field to improve the numerical accuracy. Denoting  $\mathbf{u}/N$  with  $\mathbf{v}$ , we can look for the solution of  $\widetilde{\exp}(\mathbf{v})$  and then we can iteratively scale it up to the original size in  $N$  steps.

The most commonly employed exponential approximant, the Euler method, is based on the first order Taylor approximation. Other methods are on the discretisation of the time parameter and on variations of the Taylor expansion of the unknown solution. We refer the reader to the classical reference [FB14] for an exhaustive presentation. In the following equations, and according to the tradition, in the right side of the equations the vector fields are expressed in Lagrangian coordinates.

▷ Classical scaling and squaring:

$$\widetilde{\exp}(\mathbf{v}) = \text{Id} + \mathbf{v} \quad (96-1)$$

▷ Midpoint method:

$$\widetilde{\exp}(\mathbf{v}) = \text{Id} + \mathbf{v} \circ \left( \text{Id} + \frac{1}{2}\mathbf{v} \right) \quad (96-2)$$

▷ Euler modified method:

$$\widetilde{\exp}(\mathbf{v}) = \text{Id} + \frac{1}{2} \left( \mathbf{v} + \mathbf{v} \circ (\text{Id} + \mathbf{v}) \right) \quad (96-3)$$

▷ Heun method:

$$\widetilde{\exp}(\mathbf{v}) = \text{Id} + \frac{1}{4} \left( \mathbf{v} + 3\mathbf{v} \circ \left( \text{Id} + \frac{2}{3}\mathbf{v} \right) \right) \quad (96-4)$$

▷ Heun modified method:

$$\widetilde{\exp}(\mathbf{v}) = \text{Id} + \frac{1}{4} \left( \mathbf{v} + 3\mathbf{v} \circ \left( \text{Id} + \frac{2}{3}\mathbf{v} \circ \left( \text{Id} + \frac{1}{3}\mathbf{v} \right) \right) \right) \quad (96-5)$$

▷ Explicit Runge Kutta 4 method:

$$\widetilde{\exp}(\mathbf{v}) = \text{Id} + \frac{1}{6} (r_1 + r_2 + r_3 + r_4) \quad (97-1)$$

where:

$$r_1 = \mathbf{v} \quad (97-2)$$

$$r_2 = \mathbf{v} \circ \left( \text{Id} + \frac{1}{2}\mathbf{v} \right) \quad (97-3)$$

$$r_3 = \mathbf{v} \circ \left( \text{Id} + \frac{1}{2}\mathbf{v} \circ \left( \text{Id} + \frac{1}{2}\mathbf{v} \right) \right) \quad (97-4)$$

$$r_4 = h\mathbf{v} \circ \left( \text{Id} + \frac{1}{2}\mathbf{v} \circ \left( \text{Id} + \frac{1}{2}\mathbf{v} \circ \left( \text{Id} + \frac{1}{2}\mathbf{v} \right) \right) \right) \quad (97-5)$$

Rather than finding more accurate method to compute the Lie exponential approximant with further elaboration of the Taylor expansion, it is possible to work on the initial scaling of the SVF and on the subsequent composition, exploiting the one parameter subgroup property of diffeomorphisms. This direction led to the scaling and squaring method.

#### 4.4.4 Scaling and squaring method and its generalisation

The scaling and squaring method was introduced in medical imaging by Arsigny et al. [ACPA06], after the paper of Ying, Candes [YC06] where proofs and bounds on the accuracy of these methods are derived. The scaling and squaring method consists of an application of the one-parameter subgroup property, formalised as follows: given the SVF  $\mathbf{u}$  whose integral is  $\phi$  and given  $t, s \in \mathbb{R}$ :

$$\phi_t = \exp(t\mathbf{u}) \quad (97-6)$$

$$\phi_0 = \text{Id} \quad (97-7)$$

$$\phi_s \circ \phi_t = \exp((t+s)\mathbf{u}) = \phi_{s+t} . \quad (97-8)$$

This property translate into physics with the intuitive idea that if we put a particle in a velocity field defined by the SVF  $\mathbf{u}$  for a time  $s$ , and then a second particle for a time  $t$  is left in the same location of the final position of the first one, then the location of the second particle would be the same as the first one if left moving for a time  $s+t$ . Again intuitively we can see that the same idea does not hold for the

time varying velocity fields, and therefore the scaling and squaring methods can not be employed to integrate the non-stationary ordinary differential equations.

To exploit the one parameter subgroup property in the practice of finding numerical approximation of the Lie exponential, we consider the fact that

$$\phi_1 = \exp(\mathbf{u}/N)^N = \underbrace{\exp(\mathbf{u}/N) \circ \cdots \circ \exp(\mathbf{u}/N)}_{N\text{-times}} = \exp(\mathbf{u}) , \quad (98-1)$$

if  $\mathbf{u}$  is small, and for  $t = 1$ , then

$$\exp(\mathbf{u}) \simeq \mathbf{u} . \quad (98-2)$$

and<sup>3</sup> what we obtain is a method with the same approximant of the Euler method, but with a different scaling step and subsequent resampling.

The final iterative composition, right member of the previous expression, can be performed in 3 ways, called *forward composition*, *backward composition* or, when  $N = 2^M$ , *squared composition* (in the nomenclature of Bossa et al. [BZO08] respectively forward Euler, composition method, and scaling and squaring). At the  $k$ -th step, the computations are given by:

▷ Forward composition:

$$\widetilde{\exp}(\mathbf{v})^{k+1} = \widetilde{\exp}(\mathbf{v}) \circ \widetilde{\exp}(\mathbf{v})^k \quad (98-3)$$

▷ Backward composition:

$$\widetilde{\exp}(\mathbf{v})^{k+1} = \widetilde{\exp}(\mathbf{v})^k \circ \widetilde{\exp}(\mathbf{v}) \quad (98-4)$$

▷ Squared composition:

$$\widetilde{\exp}(\mathbf{v})^{2^{k+1}} = \widetilde{\exp}(\mathbf{v})^{2^k} \circ \widetilde{\exp}(\mathbf{v})^{2^k} \quad (98-5)$$

Even if all mathematically equivalent, the squared composition is computationally faster.

After the scaling step, and before the squaring step, the approximation of  $\widetilde{\exp}(\mathbf{v})$  can be computed in several ways. Arsigny et al. [ACAP09] proposed a generalisation of the scaling and squaring framework, where an “adequate” exponential integrator, as for example the Runge-Kutta 4 method is employed. Figure 98-1 represents schematically the general framework.

---

<sup>3</sup>Or  $\exp(\mathbf{u}) \simeq \text{Id} + \mathbf{u}$  if the vector field is considered in Lagrangian coordinates on the right side of the equation.

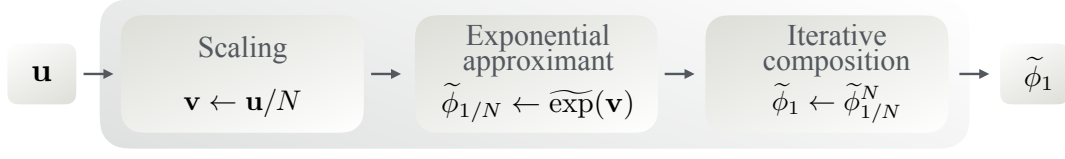


Figure 98-1: **Scaling and composing scheme, as a generalisation of the scaling and squaring.** The input stationary velocity field  $\mathbf{u}$  is scaled by a factor of  $N$ . Then a selected numerical integrator is applied, and its result, indicated with  $\widetilde{\exp}(\mathbf{u}/N)$ , is iteratively composed by itself  $N$ -times. When  $\widetilde{\exp}(\mathbf{u}/N)$  is approximated with  $\text{Id} + \mathbf{u}/N$  and the iterative composition is computed with the squared composition, then the algorithm is the classical scaling and squaring proposed by Arsigny et al. [ACPA06]. When the iterative composition is performed sequentially backward, it is equivalent to the Euler method.

The generalisation of the scaling and squaring method, jointly considered with a class of numerical integrators called *exponential integrators* is part of the contribution, presented in section 4.4.6.

Before going into its details, we need one last theoretical parenthesis about the composition of SVF, that we have been indicated so far with  $\circ$  with no further details about its implementation.

#### 4.4.5 The composition of stationary velocity fields

This section opens a parenthesis whose implications affects the validation and comparison of the methods proposed in the benchmarking part, from Section 4.5.

The composition of stationary velocity fields employed in the scaling and squaring step is not the same mathematical operation as the composition between a stationary velocity field and a diffeomorphism employed in the classical methods, such as Euler or Midpoint. They are mathematically different objects and this fact has an impact on the final error analysis.

The *natural* composition  $\mathbf{u} \circ \phi$  between a stationary velocity field  $\mathbf{u} \in V(\Omega)$  and a diffeomorphism  $\phi \in \text{Diff}(\Omega)$  when resampled on the same grid, requires  $\mathbf{u}$  to be in Lagrangian coordinates and  $\phi$  to be in Eulerian coordinates. In fact the Eulerian representation of  $\phi$  embeds the coordinate systems respect to the origin where  $\mathbf{u}$  is evaluated.

We remind the reader that a vector field is said to be in Lagrangian if each vector has its tail on the spatial element that it intends to move. Therefore the identity vector field in Lagrangian coordinates is the vector field everywhere zero:  $\mathbf{0}(\mathbf{x}) = \mathbf{0}$  for all  $\mathbf{x} \in \Omega$ . A vector field is said to be in Eulerian coordinates if the new position after its application is computed respect to the origin of the frame of reference. The identity in Eulerian coordinates is therefore identity map  $\text{Id}(\mathbf{x}) = \mathbf{x}$ , and the passage

between Eulerian and Lagrangian coordinates is therefore:

$$\underbrace{\phi}_{\text{Lagrangian}} \longmapsto \underbrace{\phi + \text{Id}}_{\text{Eulerian}} \quad (99-1)$$

To dive into the differences between the *natural* composition  $\mathbf{u} \circ \phi$  and the composition between vector fields used in the scaling and squaring algorithm, written with abuse of notation as  $\mathbf{u} \circ \mathbf{u}$ , we introduce a new notation. Indicating with  $\circ$  the composition in the continuous space, with  $\star$  the composition operating between discretised elements in the natural coordinate systems,  $\doteq$  the passage between the continuous and the discrete world, and considering all the indicated vector fields representing discretised diffeomorphisms or velocity fields in Lagrangian coordinates, we can write:

$$\mathbf{u} \circ \phi \doteq \mathbf{u} \star (\text{Id} + \phi) . \quad (100-1)$$

Respect to the composition with the identities (left and right), we have:

$$\mathbf{u} \circ \mathbf{0} \doteq \mathbf{u} \star (\text{Id} + \mathbf{0}) = \mathbf{u} \quad (100-2)$$

$$\mathbf{0} \circ \phi \doteq \mathbf{0} \star (\text{Id} + \phi) = \mathbf{0} \quad (100-3)$$

$$\mathbf{0} \circ \mathbf{0} \doteq \mathbf{0} \star (\text{Id} + \mathbf{0}) = \mathbf{0} . \quad (100-4)$$

This resampling is the one employed to compute the *natural* composition, arising in the classical integration methods. We can notice that it is not symmetric, and behaves differently when the identity is on the left or on the right. When dealing with the scaling and squaring methods, we compose small velocity vector field, and we expect the resampling to have the property of being symmetric and associative. Therefore the resampling in this case has a different definition<sup>4</sup>:

$$\mathbf{u} \circ \mathbf{v} \doteq \mathbf{u} \star (\text{Id} + \mathbf{v}) + \mathbf{v} . \quad (100-5)$$

This operation, as can be quickly shown, is in fact symmetric respect to the identity and it is associative. It is therefore a different operation if compared to the natural composition between a velocity field and a diffeomorphism.

$$\mathbf{0} \circ \mathbf{v} \doteq \mathbf{0} \star (\text{Id} + \mathbf{v}) + \mathbf{v} = \mathbf{v} \quad (100-6)$$

$$\mathbf{u} \circ \mathbf{0} \doteq \mathbf{u} \star (\text{Id} + \mathbf{0}) + \mathbf{0} = \mathbf{u} \quad (100-7)$$

$$(100-8)$$

---

<sup>4</sup>And it should have a different notation too. We kept the same notation for both resampling as its meaning is clear from the nature of the second member.

$$\mathbf{u} \circ (\mathbf{v} \circ \mathbf{w}) \doteq \mathbf{u} \circ (\mathbf{v} \star (\text{Id} + \mathbf{w}) + \mathbf{w}) = \quad (100-9)$$

$$= \mathbf{u} \star (\text{Id} + \mathbf{v} \star (\text{Id} + \mathbf{w}) + \mathbf{w}) + \mathbf{v} \star (\text{Id} + \mathbf{w}) + \mathbf{w} \quad (100-10)$$

$$(\mathbf{u} \circ \mathbf{v}) \circ \mathbf{w} \doteq \mathbf{u} \circ \mathbf{v} \star (\text{Id} + \mathbf{w}) + \mathbf{w} \quad (100-11)$$

$$= \mathbf{u} \circ (\mathbf{v} \circ \mathbf{w}) \quad (100-12)$$

The second kind of resampling introduced, when it is applied to larger vectors produces an increase of the numerical error respect to the classical methods based on the *natural* composition.

After this section about the resampling, in the next one we combine the generalised scaling and squaring method with another class of integrators that have been recently proposed and that are called *exponential integrators*. The resulting algorithms will be called *scaling and squaring based on exponential integrators* and are the main contribution of this thesis.

#### 4.4.6 Combining generalised scaling and squaring and exponential integrators

*Exponential integrators* are a class of numerical integrators. They were introduced in 1958 to solve some particular stiff ODEs for which the numerical integrators based on the Taylor expansion have not provided reasonable results. They originate from the strategy of separating the linear part and the non-linear part of the tangent vector field, and to exploit the closed form of the integration of the linear part to obtain an approximation. A survey about exponential integrators is proposed by Hochbruck et al. in [HO10].

The scaling step, as the first step of the scaling and squaring algorithm, appears to be particularly convenient when dealing with large deformations between images. Once the SVF is reduced in scale, it is possible to integrate it after separating the linear from the non-linear part, following the exponential integrator methodology as explained below. In order to make the explanation formal and self contained we will pay the price of repeating some of the concepts already introduced.

**Thesis:** Let  $\Omega \subset \mathbb{R}^D$  be an image's domain ( $D = 2, 3$  for bi and tri-dimensional images),  $\phi : \Omega \rightarrow \Omega$  a diffeomorphism and  $\mathbf{v}$  its tangent vector field that defines the transformation's velocities and directions at each point of  $\Omega$ .

The relationship between  $\mathbf{v}$  and  $\phi$  is given by the stationary ODE

$$\left. \frac{d\phi_t(\mathbf{x})}{dt} \right|_{t=1} = \mathbf{v}(\phi_1(\mathbf{x})), \quad \phi_0 = \text{Id}, \quad \mathbf{x} \in \Omega, \quad (101-1)$$

where  $\phi_0$  coincides with the identity function  $\text{Id}$  defined on  $\Omega$ , and the solution at the time point  $t = 1$  coincides with the diffeomorphism  $\phi$ . We want to show that the approximation given by:

$$\phi_1(\mathbf{x}) \simeq \mathbf{x} + \mathbf{v}(\mathbf{x}) + \frac{1}{2} \mathbf{J}_{\mathbf{v}(\mathbf{x})} \mathbf{v}(\mathbf{x}) \quad \mathbf{x} \in \Omega \quad (102-1)$$

holds.

**ODE tools:** At the core of the ODE (101-1) there is the concept of *flow of diffeomorphisms*. It is defined as the family of diffeomorphisms  $\{\phi_t\}_{t \in \mathbf{R}}$  continuously parametrised by a time-parameter  $t$ , such that  $\phi_0$  equals the identity  $\text{Id}$  and that satisfy the one-parameter subgroup property  $\phi_t \circ \phi_s = \phi_{t+s}$ .

When the one-parameter subgroup is applied to a point  $\mathbf{x}$  in  $\Omega$ , the new point  $\phi_t(\mathbf{x})$  can be *denoted* with  $\mathbf{x}(t)$  and its time derivative with  $\dot{\mathbf{x}}(t)$ . Equation (101-1), when considered for one particular point, can be rewritten as

$$\dot{\mathbf{x}}(t) = \mathbf{v}(\mathbf{x}(t)) \quad \mathbf{x}(0) = \mathbf{x}. \quad (102-2)$$

**Linear ODE tools:** From the theory of linear ODE, for any real  $d \times d$  matrix  $A$  and any  $d$ -dimensional column vector  $\mathbf{b}$ , it holds

$$\dot{\mathbf{x}}(t) = A\mathbf{x}(t), \quad \mathbf{x}(0) = \mathbf{b} \quad \implies \quad \mathbf{x}(t) = \epsilon_0(tA)\mathbf{b} \quad \forall t \in \mathbf{R}. \quad (102-3)$$

$$\dot{\mathbf{x}}(t) = A\mathbf{x}(t) + \mathbf{b}, \quad \mathbf{x}(0) = \mathbf{0} \quad \implies \quad \mathbf{x}(t) = t\epsilon_1(tA)\mathbf{b} \quad \forall t \in \mathbf{R}. \quad (102-4)$$

Where  $\epsilon_0(Z)$  is the matrix exponential of  $e^Z = \sum_{j=0}^{\infty} \frac{Z^j}{j!}$ , whose numerical computation is performed with `expm`, and  $\epsilon_1(Z)$  is the shifted Taylor expansion given by  $(\epsilon_0(Z) - I)Z^{-1} = \sum_{j=0}^{\infty} \frac{Z^j}{(j+1)!}$  [HL13]. For a positive integer  $k$ ,  $\epsilon_k(Z) = \sum_{j=0}^{\infty} \frac{Z^j}{(j+k)!}$ .

The solution of this linear case uses the matrix exponential: at time  $t$  the analytic solution is provided by  $\mathbf{x}(t) = \epsilon_0(tA)\mathbf{x}_0$  where  $\epsilon_0(tL) = \sum_{j=0}^{\infty} (tL)^j / j!$  is the matrix exponential function.

**Proving Equation 102-1:** Without any loss of generality it is always possible to *translate the coordinate frame* so that the initial position of  $\mathbf{x}(0)$  coincides with the origin of the axis  $\mathbf{0}$ . The translation is given by  $\mathbf{y}(t) := \mathbf{x}(t) - \mathbf{x}(0)$ , and in this new

frame we have  $\mathbf{y}(0) = \mathbf{0}$ ,  $\mathbf{x}(t) = \mathbf{y}(t) + \mathbf{x}(0)$ , and Equation 102-2 can be written as:

$$\dot{\mathbf{y}}(t) = \mathbf{v}(\mathbf{y}(t) + \mathbf{x}(0)) \quad \mathbf{y}(0) = \mathbf{0} . \quad (102-5)$$

The Taylor expansion of the SVF  $\mathbf{v}$  around  $\mathbf{x}(0)$  computed at  $\mathbf{y}(t) + \mathbf{x}(0)$  for any real  $t$  provides<sup>5</sup>

$$\dot{\mathbf{y}}(t) = \mathbf{v}(\mathbf{y}(t) + \mathbf{x}(0)) = \mathbf{v}(\mathbf{x}(0)) + \mathbf{J}_{\mathbf{v}(\mathbf{x}(0))}\mathbf{y}(t) + \mathcal{O}(\mathbf{y}(t)^2) .$$

This last expansion, gives us the hint to follow the *exponential integrators approach* [HIO10]. It consists of the strategy of separating the linear part (whose integration is provided by the exponential map  $\expm$ ) and the non-linear part of the SVF. Equation 102-5 can be written as

$$\dot{\mathbf{y}}(t) = \mathbf{v}_0 + \mathbf{J}_{\mathbf{v}_0}\mathbf{y}(t) + \mathcal{N}_{\mathbf{v}}(\mathbf{y}(t)) , \quad \mathbf{y}(0) = \mathbf{0} , \quad (103-1)$$

where  $\mathbf{v}(\mathbf{x}(0))$  is indicated with  $\mathbf{v}_0$  for notation convenience and  $\mathbf{J}_{\mathbf{v}_0}$  is the  $d \times d$  spatial Jacobian of  $\mathbf{v}_0$ . The non-linear part of the SVF, indicated with  $\mathcal{N}_{\mathbf{v}}(\mathbf{y}(t))$ , can be seen as an operator on the space of the SVF over  $\Omega$ , that subtract the linear part of  $\mathbf{v}$  computed with the Taylor expansion of  $\mathbf{v}$  in  $\mathbf{x}(t)$  around  $\mathbf{x}(0)$ . For a fixed  $\mathbf{x} = \mathbf{x}(0) \in \Omega$ , on which is acting a one-parameter subgroup of diffeomorphisms, it is defined by:

$$\begin{aligned} \mathcal{N}_{\mathbf{v}}(\mathbf{y}(t)) &= \mathbf{v}(\mathbf{y}(t) + \mathbf{x}(0)) - (\mathbf{v}_0 + \mathbf{J}_{\mathbf{v}_0}\mathbf{y}(t)) \\ &= \mathbf{v}(\mathbf{x}(t)) - \mathbf{v}(\mathbf{x}(0)) - \mathbf{J}_{\mathbf{v}(\mathbf{x}(0))}(\mathbf{x}(t) - \mathbf{x}(0)) . \end{aligned}$$

It follows easily that  $\mathcal{N}_{\mathbf{v}}(\mathbf{y}(0)) = \mathbf{0}$  and  $\mathcal{N}_{\mathbf{v}}(\mathbf{y}(t)) \in \mathcal{O}((\mathbf{x}(t) - \mathbf{x}(0))^2)$  when  $\mathbf{x}(t) \rightarrow \mathbf{x}(0)$ .

When the time-parameter  $t$  is in a small neighbour of the origin (as it happens when scaling the SVF by an appropriate factor in the generalised scaling and squaring framework), the non linear part is small, and at the initial ODE problem we can associate a linearised version:

$$\dot{\mathbf{y}}(t) = \mathbf{v}_0 + \mathbf{J}_{\mathbf{v}_0}\mathbf{y}(t) , \quad \mathbf{y}(0) = \mathbf{0} . \quad (103-2)$$

Since  $\mathcal{N}_{\mathbf{v}}(\mathbf{y}(t)) \in \mathcal{O}(\mathbf{y}(t)^2)$ , the solution of the linearised problem 103-2 approximates the solution of the initial problem (102-5).

---

<sup>5</sup>Given  $f$ ,  $g$  and  $h$ , vector valued function in an Euclidean space, with the notation  $f(x) = g(x) + \mathcal{O}(h(x))$  for  $x \rightarrow x_0$  we mean that exists a real positive  $M$  and a  $\delta$  such that  $\|f(x) - g(x)\| < M\|h(x)\|$  when  $\|x - x_0\| < \delta$ .

Passing in *homogeneous coordinates*, Equation 103-2 can be written as

$$\begin{bmatrix} \dot{\mathbf{y}} \\ 0 \end{bmatrix} = \begin{bmatrix} \mathbf{J}_{\mathbf{v}_0} & \mathbf{v}_0 \\ 0 & 0 \end{bmatrix} \begin{bmatrix} \mathbf{y}(t) \\ 1 \end{bmatrix} .$$

And using the implication (102-3), we obtain the solution, written again in homogeneous coordinates:

$$\begin{bmatrix} \mathbf{y}(t) \\ 1 \end{bmatrix} = \epsilon_0 \left( t \begin{bmatrix} \mathbf{J}_{\mathbf{v}_0} & \mathbf{v}_0 \\ 0 & 0 \end{bmatrix} \right) \begin{bmatrix} \mathbf{0} \\ 1 \end{bmatrix} , \quad (104-1)$$

back in the original coordinate system, it becomes

$$\begin{bmatrix} \mathbf{x}(t) \\ 1 \end{bmatrix} = \epsilon_0 \left( t \begin{bmatrix} \mathbf{J}_{\mathbf{v}_0} & \mathbf{v}_0 \\ 0 & 0 \end{bmatrix} \right) \begin{bmatrix} \mathbf{0} \\ 1 \end{bmatrix} - \begin{bmatrix} \mathbf{x}(0) \\ 1 \end{bmatrix} . \quad (104-2)$$

which is the exact solution of the linearised ODE, that approximates the sought solution for any time parameter  $t$  close enough to 0.

In order to avoid the computational cost of the exponential of a matrix, and to have an approach that can be easily vectorized, we can apply (102-4) to the linearised problem (103-2) to obtain the following solution:

$$\mathbf{y}(t) = t\epsilon_1(t\mathbf{J}_{\mathbf{v}_0})\mathbf{v}_0 .$$

and, by translating the coordinate frame to the initial one with  $\mathbf{y}(t) = \mathbf{x}(t) - \mathbf{x}(0)$ , it follows:

$$\mathbf{x}(t) = \mathbf{x}(0) + t\epsilon_1(t\mathbf{J}_{\mathbf{v}_0})\mathbf{v}_0 , \quad \mathbf{x}(1) = \mathbf{x}(0) + \epsilon_1(\mathbf{J}_{\mathbf{v}_0})\mathbf{v}_0 ,$$

that is the solution of the linearised ODE associated to (101-1) at the point  $\mathbf{x}$ .

For its *numerical computation*, we can approximate  $\epsilon_1$  truncating it at its second order:

$$\begin{aligned} \mathbf{x}(t) &= \mathbf{x} + t\epsilon_1(t\mathbf{J}_{\mathbf{v}_0})\mathbf{v}_0 \\ &= \mathbf{x} + t \left( \mathbf{I} + \frac{t\mathbf{J}_{\mathbf{v}_0}}{2} + \frac{t^2\mathbf{J}_{\mathbf{v}_0}^2}{6} + \dots \right) \mathbf{v}_0 \\ &= \mathbf{x} + t\mathbf{v}_0 + \frac{t^2}{2}\mathbf{J}_{\mathbf{v}_0}\mathbf{v}_0 + \mathcal{O}(t^3\mathbf{J}_{\mathbf{v}_0}^2\mathbf{v}_0) . \end{aligned}$$

for  $t \rightarrow 0$ . Therefore the solution to the ODE 101-1 can be written as

$$\phi_t(\mathbf{x}) = \mathbf{x} + t\mathbf{v}_0 + \frac{t^2}{2}\mathbf{J}_{\mathbf{v}_0}\mathbf{v}_0 + \mathcal{O}(t^3\mathbf{J}_{\mathbf{v}_0}^2\mathbf{v}_0) + \mathcal{O}((\mathbf{x}(t) - \mathbf{x}(0))^2) , \quad (104-3)$$

where the first asymptotic error limit is a consequence of having truncated  $\epsilon_1$ , and the second as a consequence of having linearised the problem.

#### 4.4.7 Resulting algorithms

The equation just derived can be applied to the SVF  $\mathbf{w}$ , after having it reduced by a multiplicative factor of  $2^N$  in the scaling and squaring framework. The final algorithm that improves the currently used scaling and squaring is given by the following steps:

1. Scaling of  $\mathbf{u}$  by a factor of  $2^N$ :  $\mathbf{v} = \mathbf{u}/2^N$ .
2. The approximation of the Lie exponential, indicated with  $\widetilde{\exp}(\mathbf{v})$  si computed as

$$\widetilde{\exp}(\mathbf{v}) = \mathbf{x}_0 + \mathbf{v}(\mathbf{x}) + \frac{1}{2}\mathbf{J}_{\mathbf{v}(\mathbf{x})}\mathbf{v}(\mathbf{x}) . \quad (105-1)$$

3. The result  $\widetilde{\exp}(\mathbf{v})$  is pair-wise composed by itself  $2^N$ -times.

According to the choice of the exponential approximant  $\widetilde{\exp}$ , to the truncation of  $\epsilon_1$  and to the iterative composition of  $\epsilon_{1/N}$   $N$  times, the method proposed can be implemented with a range of options:

1. *Scaling and squaring based on exponential integrators (gss\_ei)*:  $\widetilde{\exp}$  is computed approximating the exponential of the matrix  $[\mathbf{J}_{\mathbf{v}_0}, \mathbf{v}_0; 0, 0]$  (Equation 104-2) and the composition is computed by squaring.
2. *Scaling and squaring based on approximated exponential integrators (gss\_aei)*:  $\widetilde{\exp}$  is computed by truncating  $\epsilon_1$  (Equation 105-1, with  $t = 1$ ) and the composition is computed by squaring.
3. *Scaling and composing based on approximated exponential integrators (euler\_aei)*:  $\widetilde{\exp}$  is computed by truncating  $\epsilon_1$  (Equation 105-1, with  $t = 1$ ) and the composition is computed with forward integrations.
4. *Scaling and squaring on approximated exponential integrators with Runge Kutta 4 (euler\_rk4)*:  $\widetilde{\exp}$  is computed with a Runge Kutta 4 method and the composition is performed with the squaring scheme.

If compared to other approximants provided in section 4.4.3, in terms of number of summations and resampling, it can be seen why the one proposed in `ss_aei` may be a promising choice as approximant in the scaling and squaring algorithm.

We can therefore add it with the same notation used for the list proposed in Section 4.4.3, after Equation 96-1:

▷ `ss_aei`:

$$\widetilde{\exp}(\mathbf{v}) = \text{Id} + \mathbf{v} + \frac{\mathbf{J}_{\mathbf{v}}\mathbf{v}}{2} \quad (106-1)$$

Not involving resampling in the exponential approximant, scaling and squaring and the proposed `ss_aei` are faster and more accurate than the other options. Scaling and squaring is faster than `ss_aei`, but the additional term approximating the linear part improves its accuracy.

At this point, and under the strong assumption that there is any one left, the reader may correctly observe that the Equation 106-1 is simply a second order Taylor approximation and that the whole digression regarding the exponential integrators could have been omitted. As the subsequent terms of the series constituting Equation 106-1 are powers of Jacobians and not Hessians, this is only partially true. Moreover, the digression allowed to produce two additional algorithms (`ss_ei` and `euler_aei`) and a new methodology whose more sophisticated methods are still awaiting to be explored (such as the ETDRK4, evolving the exponential integrators in the direction of the Runge Kutta 4 methods) [HO10].

In the next section we analyse the three new algorithms and we benchmark them on a range of synthetic and real data.

## 4.5 Benchmarking

To compare the proposed methods with the state of the art, we selected 6 different datasets, 4 synthetic and 2 real. Each dataset and corresponding results are presented below. Experiments are performed on a Mac book pro 2014 16Gb 1600 MHz DDR3, and the results are reproducible with the open source code proposed in the GitHub repository `CaLie` (Crazy about Lie).

### 4.5.1 Rigid body transformations

The first dataset consists of 50 linear velocity fields, sampled on a  $50 \times 50$  grid and generated from the special Euclidean group  $\text{SE}(2)$  of the rigid body transformation (see for example [HSSE09], pages 191 and 214).

This case provides a particularly interesting benchmarking: the ground truth can be computed with a closed form formula.

Studying these linear ODEs is particularly relevant: a closed form of the analytic solution  $\phi = \exp(\mathbf{v})$  is available, therefore results obtained from numerical integrators can be compared with a ground truth.

Considering the dimension of the domain as  $D = 2$  for simplicity, when  $A$  is an element of the group of the rigid body transformations  $SE(2)$  it can be represented in homogeneous coordinates as

$$A = \begin{bmatrix} \cos(\theta) & -\sin(\theta) & t_1 \\ \sin(\theta) & \cos(\theta) & t_2 \\ 0 & 0 & 1 \end{bmatrix}$$

where  $\theta$  is the rotational part and  $t_1, t_2$  are the translational parts.

The corresponding element in the Lie algebra  $\mathfrak{se}(s)$  is given by

$$dA = \begin{bmatrix} 0 & -\theta & \frac{\theta}{2} \left( \frac{\sin(\theta)}{1-\cos(\theta)} t_1 + t_2 \right) \\ \theta & 0 & \frac{\theta}{2} \left( -t_1 + \frac{\sin(\theta)}{1-\cos(\theta)} t_2 \right) \\ 0 & 0 & 0 \end{bmatrix}.$$

When applied to each point of the domain, it generate the tangent vector field, in the following ODE:

$$\begin{bmatrix} \dot{x}_1(t) \\ \dot{x}_2(t) \\ 0 \end{bmatrix} = dA \begin{bmatrix} x_1(t) \\ x_2(t) \\ 1 \end{bmatrix}.$$

The analytical solution is given by the rotation matrix  $A$ , in the relationship  $A = \exp(dA)$  and  $dA = \log(A)$ , where  $\log$  and  $\exp$  are the matrix Lie logarithm and Lie exponential [Hal15].

The real parts of the eigenvalues of  $\mathbf{a}$  are zeros and the integral curves are circles in the  $D$ -dimensional space around the fixed point of the transformation.

The 50 linear velocity fields sampled with  $\theta \in (-\pi/8, +\pi/8)$  and with the centre randomly selected inside the field of view have been integrated with scaling and squaring (**ss**), midpoint method (**midpoint**), Euler method (**Euler**), Runge Kutta 4 (**rk4**) and the proposed generalised scaling and squaring with exponential integrators **gss\_ei**, with approximated exponential integrators (**gss\_aei**), Euelr with approximated exponential integrators (**Euler\_aei**) and generalised scaling and squaring based on Runge Kutta 4 (**gss\_rk4**).

Results are shown in Figure 108-1. Many interesting things are going on in this figure. The first one is the different asymptotic behaviour of the scaling and squaring based methods (**ss**, **gss\_ei**, **gss\_aei**, **gss\_rk4**) compared to the other methods, based

on the classical composition (`midpoint`, `Euler`, `Euler_aei`, `rk4`). The reason for this difference is after the different nature of the composition, as detailed in Section 4.4.5.

The proposed `gss_ei` has the most interesting behaviour. It has the lowest error for only one step, as with one step the method is equivalent to the computation of the matrix exponential against the analytical ground truth. In this case the matrix exponential is computed with the Pade approximation method provided with the python library Scipy. For the subsequent steps the error grows as at each increase in the number of step, as it is burdened by the resampling, that would be unnecessarily to solve this simplest possible case. Its computational time remains overall stable as the bottleneck of the method is the single computation of the matrix exponential between the scaling and the squaring steps.

The widely utilised `euler` has the worst performance and it is not reaching convergence after 40 steps. Embedding the `aei` formula in the scaling and composing Euler scheme outperforms the `euler` itself and the other widely utilised `midpoint` method. The `rk4`, an overkill for a linear problem, is the fastest to reach convergence but the slowest in term of computational time. Almost as slow, is the proposed `gss_rk4`, that pays having being embedded in a scaling and squaring method with the higher resampling error. The proposed method `gss_ei` outperforms every other methods for the first three steps, to raise up to the higher asymptotic error after hitting the resampling error of the scaling and squaring scheme.

#### 4.5.2 General linear group

The previous example addresses one specific linear case ODE, for which an analytical solution can be easily found. In the general linear case, that generalises the previous example, a solution based on the matrix exponential provides a ground truth for the error of the integration of the SVF generated with the given transformation.

The general linear algebra is considered with the translation of the origin in homogeneous coordinates. The general linear algebra, element  $g \in \mathfrak{gl}(2)$ , is embedded with the translational part  $t \in \mathbb{R}^2$  in the matrix  $dA$  that generates the SVF:

$$dA = \left[ \begin{array}{c|c} g & t \\ \hline 0 & 0 \end{array} \right] \quad \left[ \begin{array}{c} \dot{\mathbf{x}} \\ 0 \end{array} \right] = dA \left[ \begin{array}{c} \mathbf{x} \\ 1 \end{array} \right] .$$

In this experiment, we classify  $dA$  according to its eigenvalues in 6 different kinds:

Kind 1: real eigenvalues with the same positive signs (unstable node).

Kind 2: real eigenvalues with the same negative signs (stable node).

Kind 3: real eigenvalues with opposite signs (saddle).

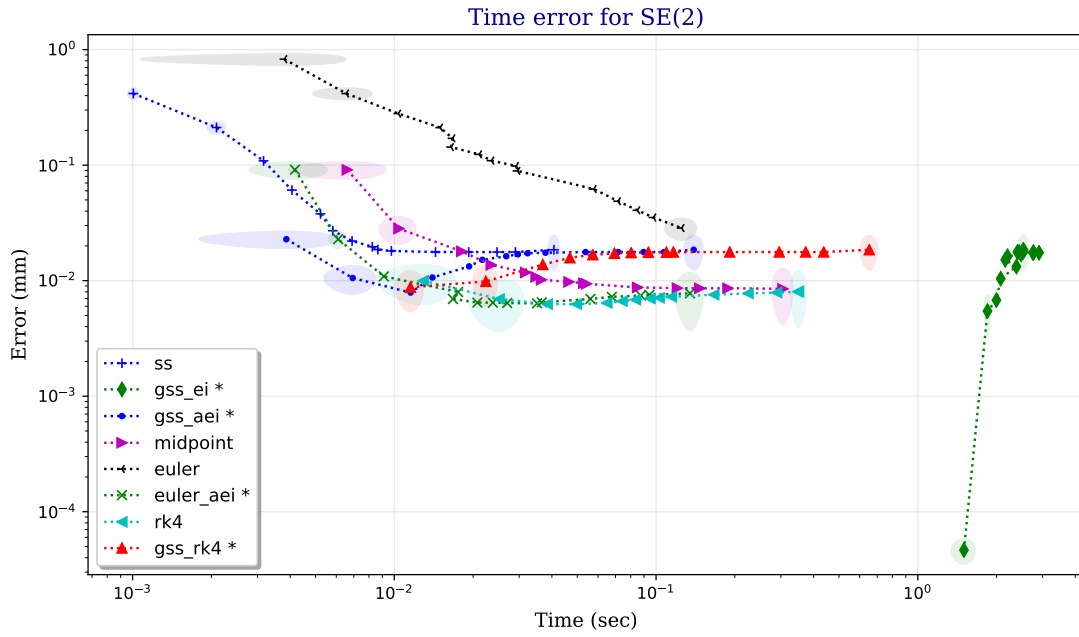


Figure 108-1: **Computational time versus error for 50 SVF generated by rotations.** The proposed methods are indicated with \* and are compared with a selection of the classical methods. Methods are compared for different steps (or discretisation of the interval  $[0, 1]$ ). Each point represents a different number of steps in the list  $[1, 2, 3, 4, 5, 6, 7, 8, 9, 10, 15, 20, 25, 30, 40]$ .

Kind 4: complex (conjugates) eigenvalues with positive real part (unstable spiral).

Kind 5: complex eigenvalues with negative real part (stable spiral).

Kind 6: complex eigenvalues with zero real part (circles). These are elements of  $\mathfrak{se}(2)$  introduced and utilised in the previous section.

In Figure 110-1 we show a representative for each kind of SVF. In the experiment here proposed we selected 50 SVF generated by elements of the general linear algebra of kind ranging from 1 to 5, excluding taste 6 to avoid overlap with the previous experiment.

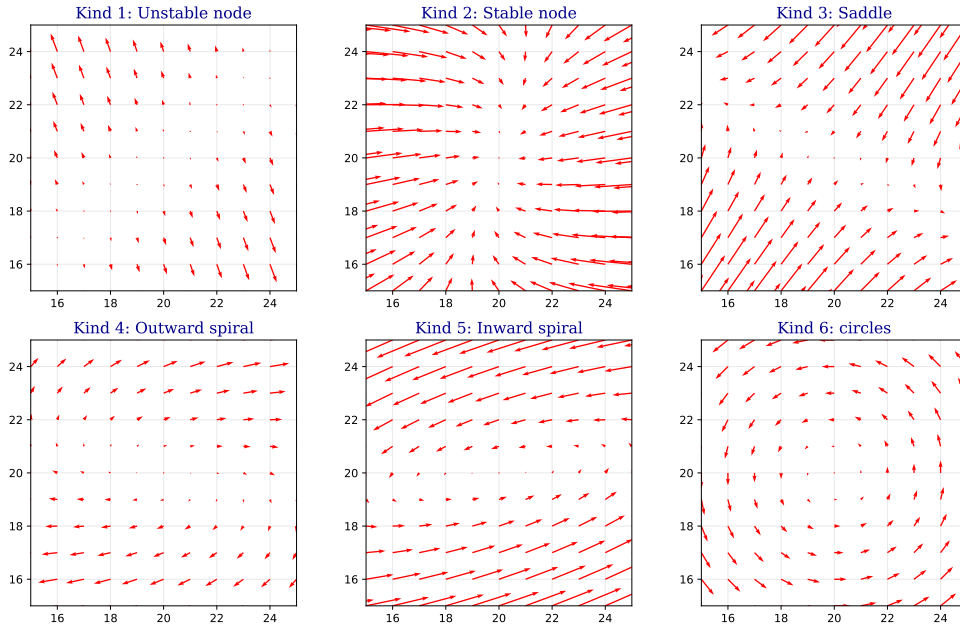


Figure 110-1: **Possible classification of the elements of the general linear group.** From left to right, top to bottom: unstable node, stable node, saddle, unstable spiral, stable spiral and circles.

The randomly chosen parameters of the matrix satisfies the constraint of having the centre of the transformation with the centre of the field of view. The same graph proposed for the previous experiment is shown for this particular case in Figure 110-2.

This case has similarities with the previous one. Again the integration methods are grouped in two, according to the asymptotic behaviour that reflects the chosen scaling method. The ground truth flow field of the SVF generated by  $dA$  is the field generated by its matrix exponential  $A = \expm(dA)$ . The numerical method to compute  $\expm$  is the one provided with Python Scipy and based on the Pade approximation. Moreover the standard deviation are higher, and for some methods it peaks to zero.

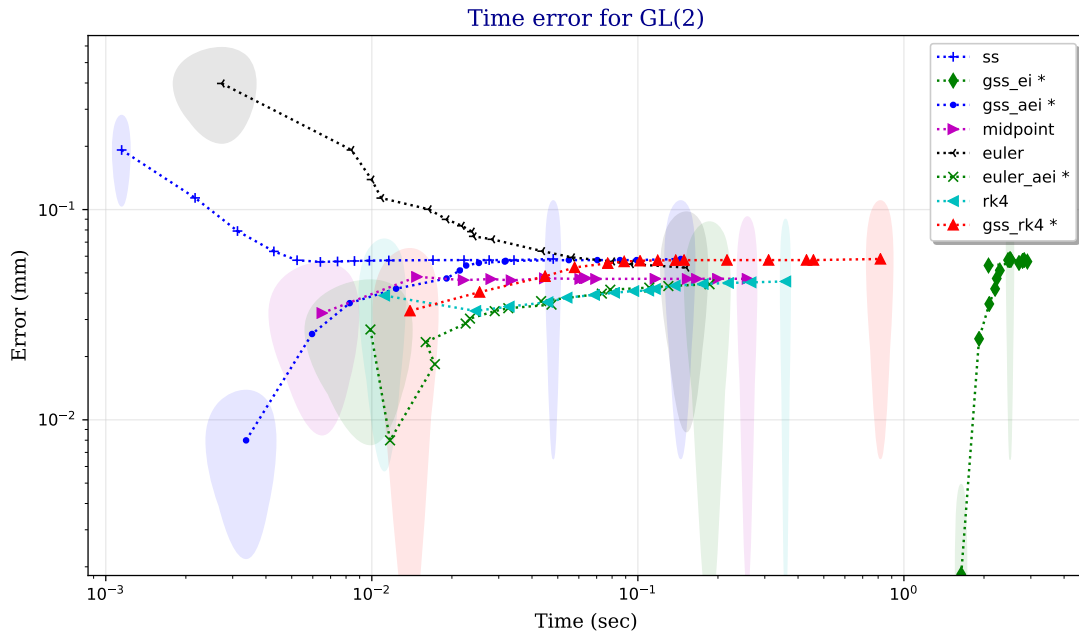


Figure 110-2: **Computational time versus error for 50 SVF generated by linear transformations.** As Figure 108-1 with SVF generated by elements of the general linear algebra. For this dataset, the difference between the two asymptotes is less prominent than the previous case.

As in the previous case the best performance is given by the proposed `gss_ei` for one step, as it is based on the Lie exponential of the linear part. After the first step, as before, the method suffers from the resampling error. The other proposed methods, as being based on the matrix exponential of the linear part tends to follow a similar trend, with the best performance at the first or at the second step.

The validation for a linear dataset is overall biased by the fact that the proposed method is exact on the linear part of the ODE. A more interesting validation is for SVF that are non-linear. It is not simple to find a class of non-linear SVF with a known ground truth. The next section is a step towards this direction.

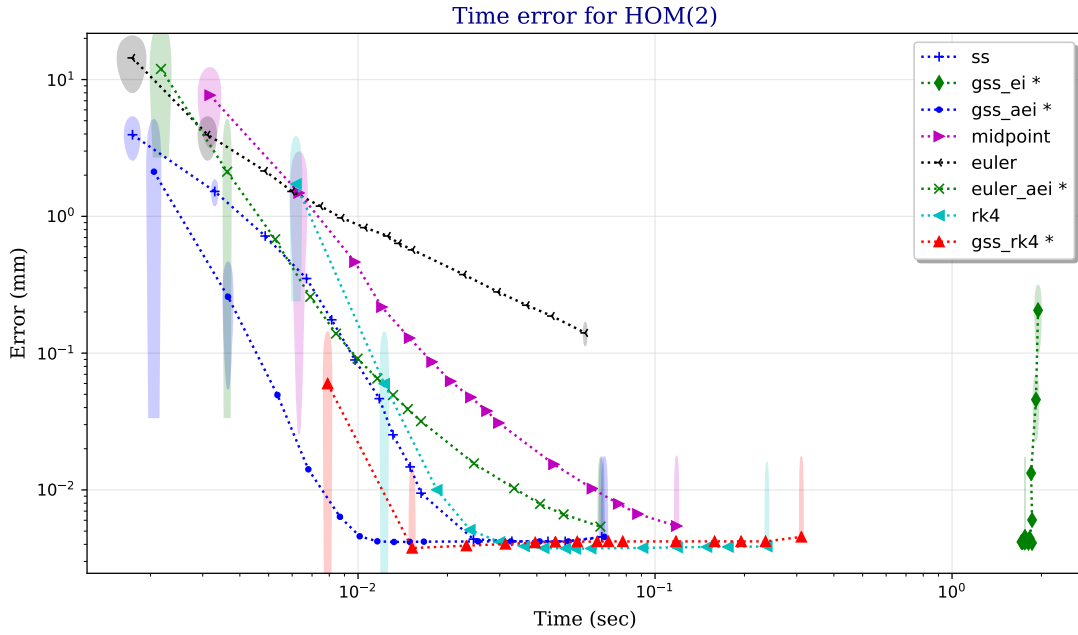


Figure 112-1: **Computational time versus error for 50 SVF generated by homographies.** As Figure 110-2 with SVF generated by elements of the homography algebra. In this non-linear case, the proposed methods beats the state of the art and the two asymptotes in the convergence are almost overlapping

### 4.5.3 Homographies

In this experiment, 50 SVFs are sampled on a regular grid of size  $50 \times 50$  and are generated by homographies in the projective linear group.

This is the first non-linear dataset where the methods are tested. The homographies allows to have a non-linear example where a ground truth can be obtained with a Pade approximation of the matrix exponential. This is the ideal setting to benchmark numerical methods to exponentiate the corresponding vector fields.

Each homography  $H$  is a  $(d + 1) \times (d + 1)$  random matrix. To avoid foldings, degenerate cases and to avoid the exponential matrix to have complex entries, two additional constraints are added: the matrix logarithm of  $H$  must have real entries and each row of  $H$  when multiplied by any of its columns always provides a positive number.

To show how to obtain the ground truth, we introduce some notations. Indicating with  $\mathbf{X}(t)$  the  $(D + 1)$ -dimensional vector  $\mathbf{x}(t)$  in projective coordinates, where all the components depends on time, and with  $H$  an element of the projective general linear algebra  $\mathbf{pgl}(D)$  ( $(D + 1) \times (D + 1)$  matrices defined up to a scaling factor), the ODE in homogeneous coordinates  $\dot{\mathbf{x}}(t) = \mathbf{v}(\mathbf{x}(t))$  becomes  $\dot{\mathbf{X}}(t) = H\mathbf{X}(t)$ .

For  $D = 2$  it corresponds to:

$$\begin{bmatrix} \dot{X}_1(t) \\ \dot{X}_2(t) \\ \dot{X}_3(t) \end{bmatrix} = H \begin{bmatrix} X_1(t) \\ X_2(t) \\ X_3(t) \end{bmatrix}.$$

whose exponential is an element in the group of homographies  $\epsilon_0(H)$ . Passing in homogeneous coordinates with  $(x_1(t), x_2(t)) = (X_1(t)/X_3(t), X_2(t)/X_3(t))$  and taking the derivative of the change of coordinates we obtain the ODE

$$\begin{cases} \dot{x}_1(t) = \frac{\dot{X}_1(t)X_3(t) - X_1(t)\dot{X}_3(t)}{X_3(t)^2} \\ \dot{x}_2(t) = \frac{\dot{X}_2(t)X_3(t) - X_2(t)\dot{X}_3(t)}{X_3(t)^2} \end{cases}$$

which corresponds, for  $X_3(0) = 1$ , to the non-linear system

$$\begin{cases} \dot{x}_1(t) = h_{11}x_1 + h_{12}x_2 + h_{13} - x_1(h_{31}x_1 + h_{32}x_2 + h_{33}) \\ \dot{x}_2(t) = h_{21}x_1 + h_{22}x_2 + h_{23} - x_2(h_{31}x_1 + h_{32}x_2 + h_{33}) \end{cases}$$

where  $h_{ij}$  are the components of  $H$ .

The solution of the last non-linear system is linked with the homogeneous solution

$$S = \epsilon_0(H)\mathbf{X}(0) \quad \mathbf{X}(0) = [\mathbf{x}(0), 1]^T$$

by normalising for the scaling factor, i.e.  $\mathbf{x}(1) = S[1 : 2]/S[3]$ , that still has an analytic formulation.

The outcome of these experiments are shown in Figure 112-1. On this non-linear case we can see that the proposed methods `gss_rk4` and `gss_aei` works better than the classical Euler and the state-of-the-art scaling and squaring.

Interestingly the tow asymptote of the scaling and squaring based method and the forward composition methods are almost overlapping. This can be explained by the fact that for large and non-linear deformation, as the considered homographies, the

different nature in the resampling of the two families of methods<sup>6</sup> is less prominent than the error given by the numerical method for the approximation of the flow of diffeomorphisms.

The proposed method `gss_aei` is again the slowest one, although the main burden of its computations is always the same for any chosen step, as it is given by the exponentiation of the linear part.

### 4.5.4 Gaussian velocity vector fields

In this experiment we used purely synthetic random generated vector fields, smoothed with a Gaussian filter. This is the experiment with the highest non-linearity, where although a ground truth is not provided. Again 50 stationary velocity fields are directly generated on a grid of size  $50 \times 5060$  with values from a normal distribution with  $\sigma_{\text{init}} = 5$  and smoothed with a Gaussian filter with  $\sigma_{\text{gf}} = 2$ . The numerical benchmark for the ground truth comparison is chosen to be the `rk4`.

As for the previous experiments, results are shown a graph with computational time versus error in Figure 114-1. Interestingly, the proposed method `gss_aei` reaches convergence on the scaling and squaring based method asymptote before the other methods respect to the chosen benchmark. The other proposed method `euler_aei` does not seem to reach convergence even after 30 steps. This method could potentially reach the same error of the selected benchmark `rk4`, therefore its minimum is at zero.

The `gss_ei` is again the slowest method, although being more accurate for each step it reaches convergence for 3 steps. In this experiment, the midpoint method is omitted, being too close to the benchmark in terms of performance.

### 4.5.5 BrainWeb dataset

The dataset considered in this experiment consists of 19 SVF created aligning 19 subjects with a selected target using the BrainWeb simulated MR images<sup>7</sup>. The non-linear SVF are generated after affine alingment with the non-rigid diffeomorphic registration method of NiftyReg.

To make the example comparable with the ones previously proposed, we considered only a 2D slice of the obtained SVF passing trough the middle of the brain. As in the previous case, we do not have any ground truth to compare the numerical methods, so again we selected the Runge Kutta 4 with 7 steps as benchmark.

The results are shown in Figure 114-2. It is interesting to notice that in this case as in the previous one, where the SVFs had been generated with Gaussian filters, the standard error is very low. The similar nature that originates the real-case SVFs

---

<sup>6</sup>See section 4.4.5.

<sup>7</sup><http://brainweb.bic.mni.mcgill.ca/brainweb/> last access March 23, 2019.

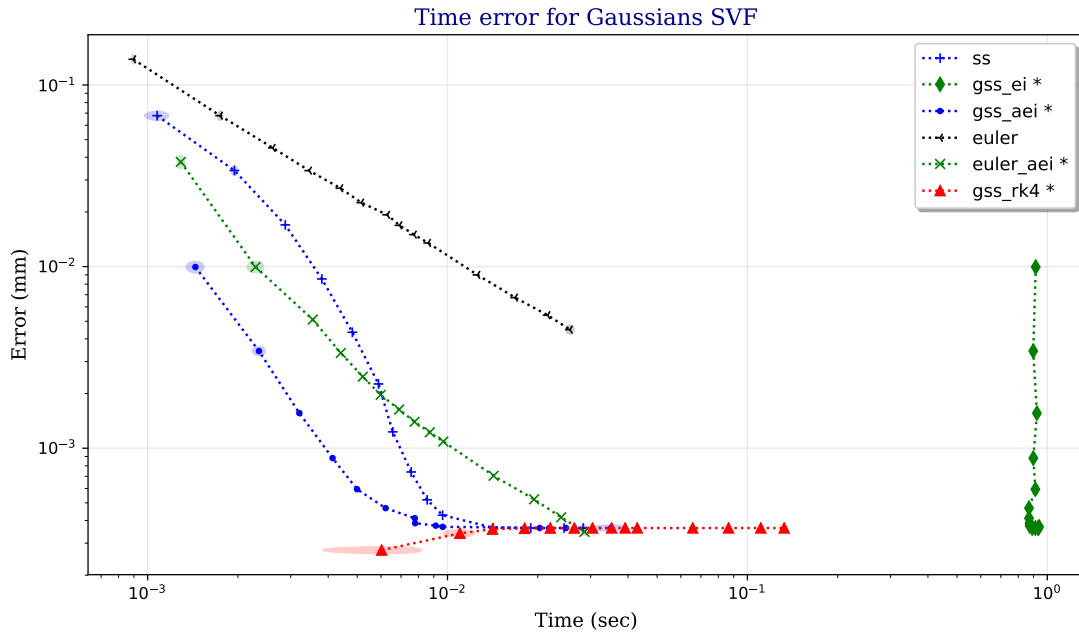


Figure 114-1: **Computational time versus error for 50 randomly generated SVF smoothed with a Gaussian filter.** This is the most non-linear dataset of the one selected. Unlike the previous cases, it is not possible to estimate a ground truth, therefore the *rk4* method for 7 steps is chosen as benchmark. As before, the proposed method *gss\_aei* has the best comparative performance. The other proposed method *euler\_aei* does not seem to reach convergence, even after 30 steps.

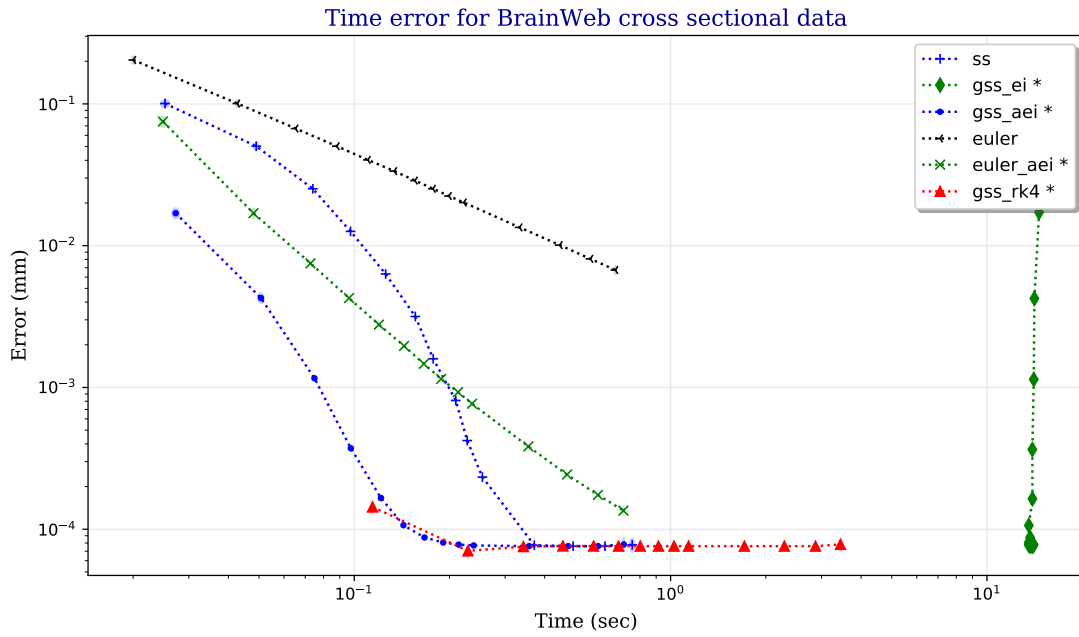


Figure 114-2: **Computational time versus error for 19 SVFs generated with a cross-sectional experiment with the BrainWeb dataset.** This case is very similar to the one previously proposed, where the SVFs had been generated with Gaussian filter smoothing random vector fields. The proposed `gss_ei` improve the scaling and squaring at each step, if compared to the selected benchmarking method.

have less variability than the synthetic data generated by groups of transformations and homographies.

Here again the proposed method have better performance than the state of the art, considering the limitation of the fact that there is no ground truth and that methods differences are compared to another numerical method.

#### 4.5.6 ADNI dataset

The previous experiment was based on a cross-sectional design. In the cross-sectional design the use of diffeomorphisms is not entirely justified as the topological genus may change across subject and the constraint imposed by the deformation model may be too strict to reflect an accurate transformation.

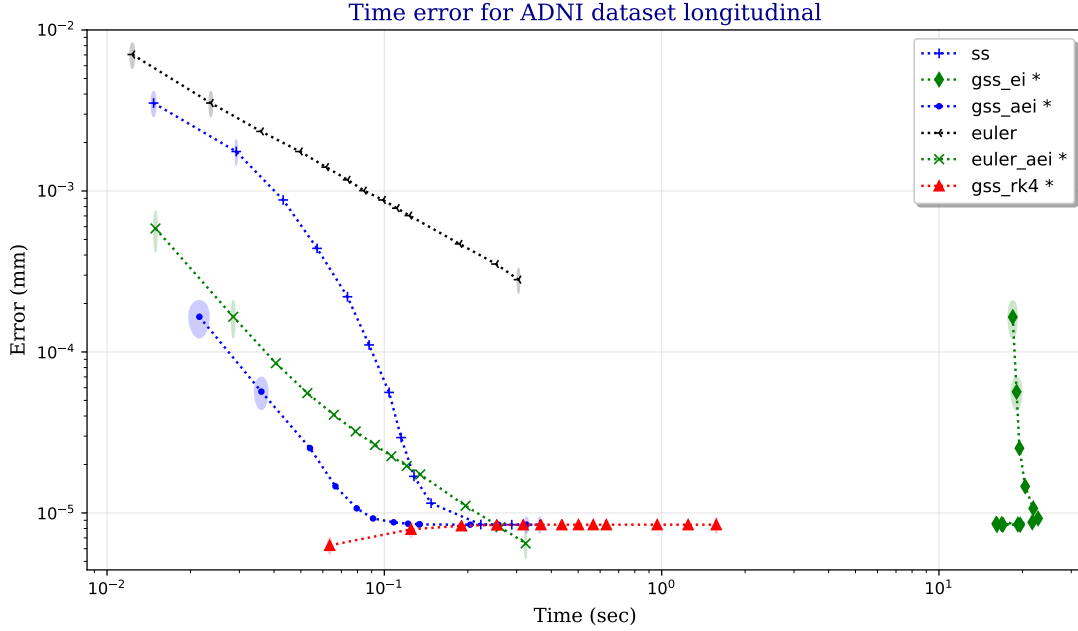


Figure 117-1: **Computational time versus error for 10 SVFs generated with a longitudinal experiment with the ADNI dataset.** This case is very similar to the previous ones, where the proposed methods are improving the state-of-the-art methods, and showing that the findings are consistent across different datasets.

For this reason in the experiment of this section the considered SVF dataset is obtained from real subjects from a longitudinal study. We selected 2 consecutive scans from 10 subjects collected in the ADNI dataset<sup>8</sup>, namely [4039-01, 4172-01, 4195-01, 4379-01, 4501-01, 4526-01, 4625-01, 4657-01, 4672-01, 4676-01] for the first

<sup>8</sup><http://adni.loni.usc.edu/>, last access March 23, 2019.

time point, and [4039-05, 4172-05, 4195-05, 4379-04, 4501-05, 4526-05, 4625-05, 4657-05, 4672-04, 4676-05] for the second time point. After an initial affine alignment, we obtained 10 diffeomorphic transformations between the paired scans and we used them to benchmark the algorithms. As for the previous example, the ground truth employed is the Runge-Kutta method of order 4 with 7 steps.

In Figure 117-1 the proposed `gss_aei` reaches the highest accuracy before the other methods respect the selected benchmark given by the `rk4`. The choice of this benchmark biases the result of the `gss_rk4`, that has the lowest error with the first step, to grow up to the convergence asymptote with the other scaling and squaring based methods.

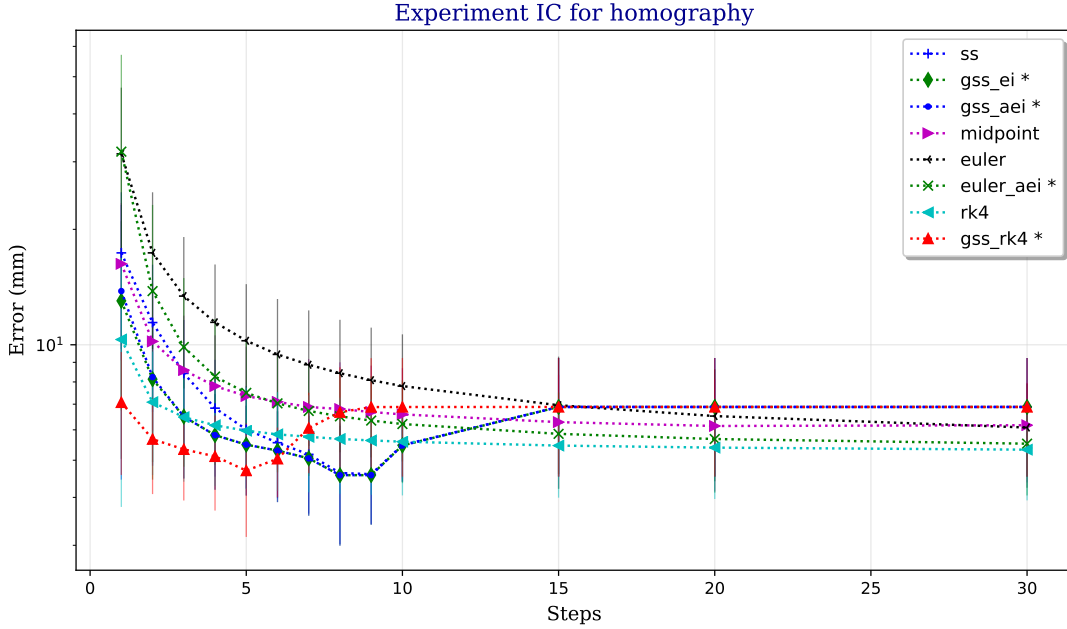


Figure 118-1: **Inverse consistency for the ADNI generated SVF.** For an high enough number of steps the inverse consistency is almost the same for all methods in log-scale. The proposed methods beats the state of the art for a number of steps between 5 and 10.

#### 4.5.7 Inverse consistency

An important requirement for a registration algorithm is the inverse consistency IC. We want to be sure that the transformation registering the image  $A$  with image  $B$  is the inverse of the transformation registering  $B$  with  $A$ .

For our case, given a tangent vector field  $\mathbf{u}$  the IC of the exponential numerical

method  $\widetilde{\text{exp}}_j$  performed in  $j$  steps to compute the Lie exponential  $\text{exp}$  is defined as:

$$\text{IC}_j(\mathbf{u}) = \frac{1}{2} \left( \|\widetilde{\text{exp}}_j(\mathbf{u}) \circ \widetilde{\text{exp}}_j(-\mathbf{u}) - \text{Id}\| + \|\widetilde{\text{exp}}_j(-\mathbf{u}) \circ \widetilde{\text{exp}}_j(\mathbf{u}) - \text{Id}\| \right)$$

where the two orderings in the composition are averaged together, as numerically  $\widetilde{\text{exp}}_j(-\mathbf{u}) \circ \widetilde{\text{exp}}_j(\mathbf{u})$  is not equivalent to  $\widetilde{\text{exp}}_j(\mathbf{u}) \circ \widetilde{\text{exp}}_j(-\mathbf{u})$ .

Inverse consistency results are shown in Figure 118-1. For an high enough number of steps all the methods stabilised around 5 mm for the whole SVF. Interestingly, the Runge Kutta 4 based methods are the ones showing the best results both for small and high number of steps. In the range of steps between 5 and 10, where the algorithms are usually tuned, the second best methods are the proposed `gss_ei` and the `gss_aei` with almost overlapping performance.

#### 4.5.8 Benchmarking with NiftyReg

Despite improving the state-of-the-art integration method, when implemented in an image registration framework, the proposed method showed negligible improvements.

This section is devoted to a comparison between the results obtained with the default NiftyReg algorithm, the diffeomorphic version based on the classical scaling and squaring method, and the diffeomorphic version whose integrations are performed with the approximated exponential integrators.

Comparing the performances of an algorithms involving numerous steps where only a single component had been modified is in general a challenging task. There are many factors that may make the algorithm works better or worst, and in the absence of a ground truth it is not possible to have an unbiased evaluation. The selected algorithm would perform better or worst in the comparison, simply tuning the selected dataset for the benchmarking, and the specific performance would not provide a generalisable answer in selecting a preferred method.

In the specific case, the main bottleneck of the algorithm is the numerical method for the cost function optimisation that is consuming most of the computational resources and whose ill-posedness of any non-convex optimisation makes impossible to predict the extent of the impact of small variations in the input on the overall performance.

What can be done is a comparison between the computational time and the measure of convergence in the most simple situation. We selected three different parametrisation to compare the influence of the overall effect of the exponential integrators:

1 ▷ Non-rigid parameters: `-omp 8 -ln 1 -maxit 400`

2 ▷ Diffeomorphic parameters: `-omp 8 -ln 1 -maxit 400 -vel`

Subject	Default	Diffeomorphic	Diffeomorphic aei
4039	148.335205	1690.162977	1947.620126
4172	164.817128	1756.238949	1310.604626*
4195	154.910263	1688.909095	1954.279128
4379	152.305266	1544.522478*	1917.201186
4501	68.707419*	1278.150236*	1231.295753*
4526	156.516203*	683.571080*	1929.246615
4625	152.959689	707.470090*	1920.410448*
4657	50.776208*	938.789816*	1895.011683
4672	74.945618*	1563.031968*	1075.729488*
4676	58.577132*	1001.179477*	1943.440577

Table 120-1: **Computational time in seconds of standard, diffeomorphic and diffeomorphic with approximated exponential integrators.** The same ADNI dataset presented in the previous section is employed to benchmark the non-rigid (Default) parametrisation, the Diffeomorphic and the diffeomorphic with Approximated Exponential Integrators (Diffeomorphic aei) in NiftyReg. Blue colours is employed when the proposed diffeomorphic aei is faster than the diffeomorphic method. The \* indicate the cases when convergence occurred before the maximum number of 400 iterations.

3 ▷ Diffeomorphic with AEI: `-omp 8 -ln 1 -maxit 400 -vel -aei`

The flag `-omp 8` requires the algorithm to run in parallel on 8 cores, `-ln 1` imposes only one pyramidal level, `-maxit 400` requires the algorithm to stop either for lazy convergence or after 400 steps. `-vel` uses diffeomorphisms parametrised with stationary velocity fields and the custom flag `-aei` requires the algorithm to perform the integration of SVF with the proposed approximated exponential integrators method instead of the classical scaling and squaring.

We impose only one level of the pyramid with max 400 steps of iteration, as more levels would have included additional bias in the algorithms comparison caused by the different starting point of the optimisation for each new level. With a single level all the methods are running from the same starting point, up to the same ending point (400 iterations or earlier) for the whole algorithm execution.

The computational time is not favourable in the use of approximated exponential integrators. The computation of the Jacobian at each step has a weight that is not compensated by a faster convergence, as lazy convergence had been obtained only in N cases.

In the Table 120-1 below, we compared the computational time in seconds to reach convergence for the 10 subjects obtained with the ADNI dataset for the three proposed parametrisations of NiftyReg.

As expected, the parametrisation 1 reported in the second column in the table,

has the best performance for an average factor of 980%. The use of the proposed methods based on approximated exponential integrators improved the computational times in these cases where the convergence had been reached before the maximum limit of iterations. In the other cases, as the same number of iterations had been employed for both methods and the the proposed method includes an extra sum and an extra computation of the Jacobian at each step, the proposed method is slower.

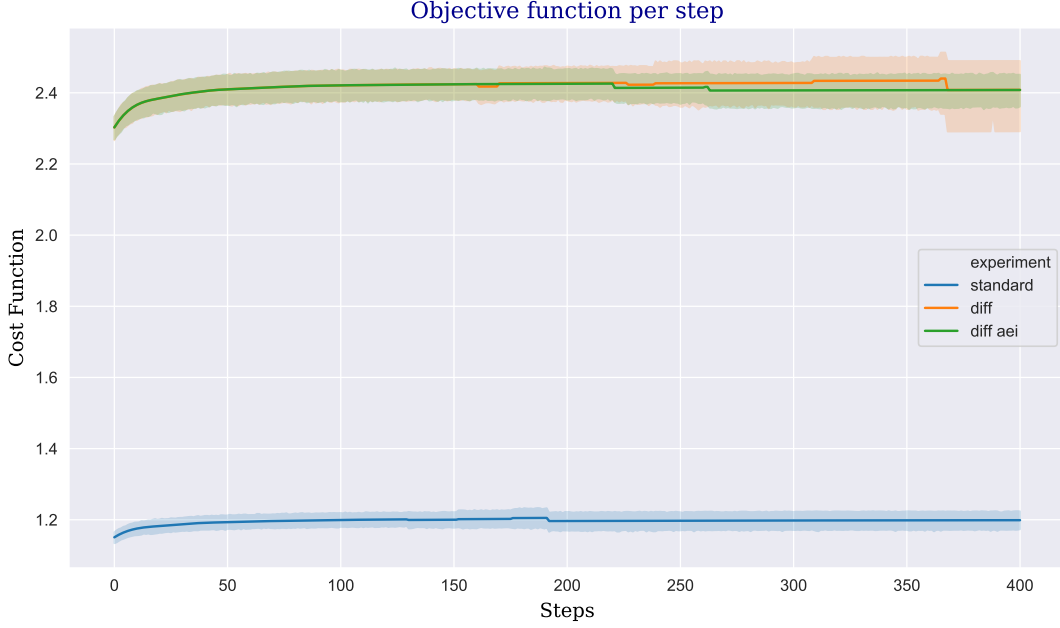


Figure 121-1: **Steps versus Cost function value.** With three parametrisation of NiftyReg applied to the 10 subjects from the ADNI dataset presented in the previous section, this graph compares the cost function values respect to the timepoints. The diffeomorphic registration methods reaches an higher value for the function to be maximised from the first step. The slope is higher as well for the first 50 steps. The proposed method does not differ significantly respect to the state-of-the-art, in particular for the initial range of steps.

Figure 121-1 shows the value of the cost function per iteration for the three selected algorithms. The first increase in the computational time seen in the previous table is compensated by an higher accuracy in the cost function maximisation. The value on the y-axis it the value that must be maximised. Even more interestingly the increase in slope for the diffeomorphic methods is higher in the first 20 steps if compared with the default method. As for the difference between the diffeomorphic method and the diffeomorphic method with approximated exponential integrators, the two situations are virtually indistinguishable for the first 250 time-points, where the standard deviation of the diffeomorphic method becomes larger than the proposed

method based on approximated exponential integrators.

## 4.6 Open-source software: calie

In support of the publication [FLD<sup>+</sup>16], we open-sourced on [github.com](https://github.com/SebastianoF/calie) the code to create the benchmarking. The repository consists of a Python package for the numerical computation of local operations between Lie algebra of stationary velocity fields and its Lie group. It can be used to reproduce the results proposed in the paper and it provides a framework to test a wider range of methods to solve Equation 101-1. This can be found at the URL <https://github.com/SebastianoF/calie>.

## 4.7 Conclusions and limitations

The main challenge faced in this chapter, which arises in almost all methodological endeavours in medical imaging studies, had been to validate a method in absence of a ground truth. To address the problem, we first validate the proposed methods on a range of simple examples, where a ground truth can be attained with analytical formulation or with a more precise numerical method. Afterwards we moved towards a wider range of examples from real medical imaging.

Despite the introduced algorithms had been successful in addressing the problem of the integration of stationary velocity fields, the results obtained when the method is embedded into a registration algorithm are disappointing. This is a consequence of the fact that the integration of SVF is not the main bottleneck of the algorithm, and before addressing this particular problem, the more critical issue of the cost function optimisation should have been considered.

Another interesting findings that can be inferred from the last set of experiments is the ill-posedness of the medical image registration problem when defined as an optimisation problem. As highly non-convex, a small variation in the initial condition would lead to different results and consequent numerical outcome.

This chapter had been also the opportunity to introduce the diffeomorphic image registration. This tool is applied as well in Chapter 5 (see in particular Figure 142-2) as part of a segmentation propagation and label fusion algorithm to produce an automatic method for the segmentation of the neonatal rabbit brain.

## Chapter bibliography

- [ACAP09] Vincent Arsigny, Olivier Commowick, Nicholas Ayache, and Xavier Pennec. A fast and log-euclidean polyaffine framework for locally

- linear registration. *Journal of Mathematical Imaging and Vision*, 33(2):222–238, 2009.
- [ACPA06] Vincent Arsigny, Olivier Commowick, Xavier Pennec, and Nicholas Ayache. A log-euclidean framework for statistics on diffeomorphisms. In *Medical Image Computing and Computer-Assisted Intervention—MICCAI 2006*, pages 924–931. Springer, 2006.
- [AF11] John Ashburner and Karl J Friston. Diffeomorphic registration using geodesic shooting and gauss-newton optimisation. *NeuroImage*, 55(3):954–967, 2011.
- [AHB87] K Somani Arun, Thomas S Huang, and Steven D Blostein. Least-squares fitting of two 3-d point sets. *IEEE Transactions on Pattern Analysis & Machine Intelligence*, 1987.
- [Arn66] Vladimir Arnold. Sur la géométrie différentielle des groupes de lie de dimension infinie et ses applications à l’hydrodynamique des fluides parfaits. In *Annales de l’institut Fourier*, volume 16, pages 319–361. Institut Fourier, 1966.
- [Arn06] Vladimir Arnold. Ordinary differential equations. translated from the russian by roger cooke. second printing of the 1992 edition. universi-text, 2006.
- [Arn13] Vladimir Igorevich Arnol’d. *Mathematical methods of classical mechanics*, volume 60. Springer Science & Business Media, 2013.
- [Ash07] John Ashburner. A fast diffeomorphic image registration algorithm. *NeuroImage*, 38(1):95–113, 2007.
- [BLR<sup>+</sup>17] Alexandre Bône, Maxime Louis, Alexandre Routier, Jorge Samper, Michael Bacci, Benjamin Charlier, Olivier Colliot, Stanley Durrleman, Alzheimer’s Disease Neuroimaging Initiative, et al. Prediction of the progression of subcortical brain structures in alzheimer’s disease from baseline. In *Graphs in Biomedical Image Analysis, Computational Anatomy and Imaging Genetics*, pages 101–113. Springer, 2017.
- [BM92] Paul J Besl and Neil D McKay. Method for registration of 3-d shapes. In *Sensor Fusion IV: Control Paradigms and Data Structures*, volume 1611, pages 586–607. International Society for Optics and Photonics, 1992.

- [BMTY05] M Faisal Beg, Michael I Miller, Alain Trouvé, and Laurent Younes. Computing large deformation metric mappings via geodesic flows of diffeomorphisms. *International journal of computer vision*, 61(2):139–157, 2005.
- [Bro81] Chaim Broit. *Optimal Registration of Deformed Images*. PhD thesis, University of Pennsylvania, Philadelphia, PA, USA, 1981. AAI8207933.
- [BS15] Akanksha Bali and Shailendra Narayan Singh. A review on the strategies and techniques of image segmentation. In *Advanced Computing & Communication Technologies (ACCT), 2015 Fifth International Conference on*, pages 113–120. IEEE, 2015.
- [BZO08] Matias Bossa, Ernesto Zacur, and Salvador Olmos. Algorithms for computing the group exponential of diffeomorphisms: Performance evaluation. In *Computer Vision and Pattern Recognition Workshops, 2008. CVPRW'08. IEEE Computer Society Conference on*, pages 1–8. IEEE, 2008.
- [Car92] M. Do Carmo. *Riemannian geometry*. Birkhauser, Boston, USA, 1992.
- [CLM<sup>+</sup>13] M Jorge Cardoso, Kelvin Leung, Marc Modat, Shiva Keihaninejad, David Cash, Josephine Barnes, Nick C Fox, Sebastien Ourselin, Alzheimer’s Disease Neuroimaging Initiative, et al. STEPS: Similarity and Truth Estimation for Propagated Segmentations and its application to hippocampal segmentation and brain parcellation. *Medical image analysis*, 17(6):671–684, 2013.
- [CRJ<sup>+</sup>04] William R Crum, Daniel Rueckert, Mark Jenkinson, David Kennedy, and Stephen M Smith. A framework for detailed objective comparison of non-rigid registration algorithms in neuroimaging. In *International Conference on Medical Image Computing and Computer-Assisted Intervention*, pages 679–686. Springer, 2004.
- [CRM96] Gary E Christensen, Richard D Rabbitt, and Michael I Miller. Deformable templates using large deformation kinematics. *Image Processing, IEEE Transactions on*, 5(10):1435–1447, 1996.
- [DGM98a] Paul Dupuis, Ulf Grenander, and Michael I. Miller. Variational problems on flows of diffeomorphisms for image matching, 1998.

- [DGM98b] Paul Dupuis, Ulf Grenander, and Michael I Miller. Variational problems on flows of diffeomorphisms for image matching. *Quarterly of applied mathematics*, 56(3):587, 1998.
- [EM70] David G Ebin and Jerrold Marsden. Groups of diffeomorphisms and the motion of an incompressible fluid. *Annals of Mathematics*, pages 102–163, 1970.
- [FB14] Burden Richard J. Faires and Annette Burden. Numerical analysis, 2014. 9th edition Nelson Education 2015.
- [FLD<sup>+</sup>16] Sebastiano Ferraris, Marco Lorenzi, Pankaj Daga, Marc Modat, and Tom Vercauteren. Accurate small deformation exponential approximant to integrate large velocity fields: Application to image registration. In *Proceedings of the IEEE Conference on Computer Vision and Pattern Recognition Workshops*, pages 17–24, 2016.
- [FSFM14] Francesca Pizzorni Ferrarese, Flavio Simonetti, Roberto Israel Foroni, and Gloria Menegaz. A framework for the objective assessment of registration accuracy. *Journal of Biomedical Imaging*, 2014:2, 2014.
- [GLS<sup>+</sup>18] Eli Gibson, Wenqi Li, Carole Sudre, Lucas Fidon, Dzoshkun Shakir, Guotai Wang, Zach Eaton-Rosen, Robert Gray, Tom Doel, Yipeng Hu, Tom Whyntie, Parashkev Nachev, Marc Modat, Dean C. Barratt, Sebastien Ourselin, M. Jorge Cardoso, and Tom Vercauteren. NiftyNet: a deep-learning platform for medical imaging. volume 158, pages 113–122, 2018.
- [GM98] Ulf Grenander and Michael I Miller. Computational anatomy: An emerging discipline. *Quarterly of applied mathematics*, pages 617–694, 1998.
- [GSST03] Ardeshir Goshtasby, Lawrence Staib, Colin Studholme, and Demetri Terzopoulos. Nonrigid image registration: guest editors’ introduction. *Computer vision and image understanding*, 89(2-3):109–113, 2003.
- [Hal15] Brian Hall. *Lie groups, Lie algebras, and representations: an elementary introduction*, volume 222. Springer, 2015.
- [HBO07] Monica Hernandez, Matias N Bossa, and Salvador Olmos. Registration of anatomical images using geodesic paths of diffeomorphisms parameterized with stationary vector fields. In *Computer Vision, 2007. ICCV 2007. IEEE 11th International Conference on*, pages 1–8. IEEE, 2007.

- [Her17] Monica Hernandez. Primal-dual convex optimization in large deformation diffeomorphic metric mapping: Lddmm meets robust regularizers. *Physics in Medicine & Biology*, 62(23):9067, 2017.
- [HH01] Joseph V Hajnal and Derek LG Hill. *Medical image registration*. CRC press, 2001.
- [HL13] Nicholas J Higham and Lin Lijing. Matrix functions: A short course, 2013.
- [HO10] Marlis Hochbruck and Alexander Ostermann. Exponential integrators. *Acta Numer*, 19:209–286, 2010.
- [HPOG09] Monica Hernandez, Xavier Pennec, and Salvador Olmos Gassó. Comparing algorithms for diffeomorphic registration: Stationary lddmm and diffeomorphic demons. Technical report, 2009.
- [HSJ<sup>+</sup>13] Mattias P Heinrich, Ivor JA Simpson, Mark Jenkinson, Michael Brady, and Julia A Schnabel. Uncertainty estimates for improved accuracy of registration-based segmentation propagation using discrete optimisation. In *MICCAI Challenge Workshop on Segmentation: Algorithms, Theory and Applications*, 2013.
- [HSSE09] Darryl D Holm, Tanya Schmah, Cristina Stoica, and David CP Ellis. *Geometric mechanics and symmetry: from finite to infinite dimensions*. Oxford University Press London, 2009.
- [HZTA04] Steven Haker, Lei Zhu, Allen Tannenbaum, and Sigurd Angenent. Optimal mass transport for registration and warping. *International Journal of computer vision*, 60(3):225–240, 2004.
- [ISNC03] Luis Ibanez, William Schroeder, Lydia Ng, and Josh Cates. The itk software guide. *Online*, 2003.
- [JBF<sup>+</sup>08] Clifford R Jack, Matt A Bernstein, Nick C Fox, Paul Thompson, Gene Alexander, Danielle Harvey, Bret Borowski, Paula J Britson, Jennifer L Whitwell, Chadwick Ward, et al. The alzheimer’s disease neuroimaging initiative (adni): Mri methods. *Journal of Magnetic Resonance Imaging*, 27(4):685–691, 2008.
- [JD94] Michael Johnson and Christopher NG Dampney. On the value of commutative diagrams in information modelling. In *Algebraic Methodology and Software Technology (AMAST’93)*, pages 45–58. Springer, 1994.

- [KW08] Boris Khesin and Robert Wendt. *The geometry of infinite-dimensional groups*, volume 51. Springer Science & Business Media, 2008.
- [LAF<sup>+</sup>13] Marco Lorenzi, Nicholas Ayache, Giovanni B Frisoni, Xavier Pennec, and Alzheimer’s Disease Neuroimaging Initiative. LCC-Demons: a robust and accurate symmetric diffeomorphic registration algorithm. *NeuroImage*, 81:470–483, 2013.
- [LBC<sup>+</sup>17] Maxime Louis, Alexandre Bône, Benjamin Charlier, Stanley Durrleman, Alzheimer’s Disease Neuroimaging Initiative, et al. Parallel transport in shape analysis: a scalable numerical scheme. In *International Conference on Geometric Science of Information*, pages 29–37. Springer, 2017.
- [LP13] Marco Lorenzi and Xavier Pennec. Geodesics, Parallel Transport & One-parameter Subgroups for Diffeomorphic Image Registration. *International Journal of Computer Vision*, 105(2):111–127, November 2013.
- [MA70] J Marsden and R Abraham. Hamiltonian mechanics on lie groups and hydrodynamics. *Global Analysis, (eds. SS Chern and S. Smale), Proc. Sympos. Pure Math*, 16:237–244, 1970.
- [MCD<sup>+</sup>14] Marc Modat, David M Cash, Pankaj Daga, Gavin P Winston, John S Duncan, and Sébastien Ourselin. Global image registration using a symmetric block-matching approach. *Journal of Medical Imaging*, 1(2):024003, 2014.
- [Mil84] John Milnor. Remarks on infinite-dimensional lie groups. In *Relativity, groups and topology. 2*. 1984.
- [Mil04] Michael I Miller. Computational anatomy: shape, growth, and atrophy comparison via diffeomorphisms. *NeuroImage*, 23:S19–S33, 2004.
- [Mod04] Jan Modersitzki. *Numerical methods for image registration*. Oxford University Press on Demand, 2004.
- [MRT<sup>+</sup>10] Marc Modat, Gerard R Ridgway, Zeike A Taylor, Manja Lehmann, Josephine Barnes, David J Hawkes, Nick C Fox, and Sébastien Ourselin. Fast free-form deformation using graphics processing units. *Computer methods and programs in biomedicine*, 98(3):278–284, 2010.
- [Mun00] James R Munkres. *Topology*, vol. 2, 2000.

- [MV98] JB Antoine Maintz and Max A Viergever. A survey of medical image registration. *Medical image analysis*, 2(1):1–36, 1998.
- [OAB<sup>+</sup>14] Yangming Ou, Hamed Akbari, Michel Bilello, Xiao Da, and Christos Davatzikos. Comparative evaluation of registration algorithms in different brain databases with varying difficulty: results and insights. *IEEE transactions on medical imaging*, 33(10):2039–2065, 2014.
- [OT14] Francisco PM Oliveira and João Manuel RS Tavares. Medical image registration: a review. *Computer methods in biomechanics and biomedical engineering*, 17(2):73–93, 2014.
- [RAH<sup>+</sup>06] Daniel Rueckert, Paul Aljabar, Rolf A Heckemann, Joseph V Hajnal, and Alexander Hammers. Diffeomorphic registration using b-splines. In *International Conference on Medical Image Computing and Computer-Assisted Intervention*, pages 702–709. Springer, 2006.
- [Roh12] Torsten Rohlfing. Image similarity and tissue overlaps as surrogates for image registration accuracy: widely used but unreliable. *IEEE transactions on medical imaging*, 31(2):153–163, 2012.
- [SDP13a] A. Sotiras, C. Davatzikos, and N. Paragios. Deformable medical image registration: A survey. *Medical Imaging, IEEE Transactions on*, 32(7):1153–1190, July 2013.
- [SDP13b] Aristeidis Sotiras, Christos Davatzikos, and Nikos Paragios. Deformable medical image registration: A survey. *IEEE transactions on medical imaging*, 32(7):1153–1190, 2013.
- [SRNM16] Andre Santos-Ribeiro, David J Nutt, and John McGonigle. Inertial demons: a momentum-based diffeomorphic registration framework. In *International Conference on Medical Image Computing and Computer-Assisted Intervention*, pages 37–45. Springer, 2016.
- [STCS<sup>+</sup>03] Julia A Schnabel, Christine Tanner, Andy D Castellano-Smith, Andreas Degenhard, Martin O Leach, D Rodney Hose, Derek LG Hill, and David J Hawkes. Validation of nonrigid image registration using finite-element methods: application to breast mr images. *IEEE transactions on medical imaging*, 22(2):238–247, 2003.
- [SWA<sup>+</sup>13] Ivor JA Simpson, Mark W Woolrich, JesperL R Andersson, Adrian R Groves, and JuliaA Schnabel. Ensemble learning incorporating uncertain registration. *IEEE transactions on medical imaging*, 32(4):748–756, 2013.

- [T<sup>+</sup>42] Darcy Wentworth Thompson et al. On growth and form. *On growth and form.*, 1942.
- [Thi98] J-P Thirion. Image matching as a diffusion process: an analogy with maxwell’s demons. *Medical image analysis*, 2(3):243–260, 1998.
- [TQ18] Mingzhen Tan and Anqi Qiu. Multiscale frame-based kernels for large deformation diffeomorphic metric mapping. *IEEE Transactions on Medical Imaging*, 2018.
- [TRU98] Philippe Thevenaz, Urs E Ruttimann, and Michael Unser. A pyramid approach to subpixel registration based on intensity. *IEEE transactions on image processing*, 7(1):27–41, 1998.
- [TVVSFAF08] Antonio Tristán-Vega, Gonzalo Vegas-Sánchez-Ferrero, and Santiago Aja-Fernández. Local similarity measures for demons-like registration algorithms. In *Biomedical Imaging: From Nano to Macro, 2008. ISBI 2008. 5th IEEE International Symposium on*, pages 1087–1090. IEEE, 2008.
- [TW16] Xiaoying Tang and Jiong Wu. Principal component analysis of the shape deformations of the hippocampus in alzheimer’s disease. In *Engineering in Medicine and Biology Society (EMBC), 2016 IEEE 38th Annual International Conference of the*, pages 4013–4016. IEEE, 2016.
- [VMK<sup>+</sup>16] Max A Viergever, JB Antoine Maintz, Stefan Klein, Keelin Murphy, Marius Staring, and Josien PW Pluim. A survey of medical image registration. *Medical image analysis*, 33:140–144, 2016.
- [VPPA07] Tom Vercauteren, Xavier Pennec, Aymeric Perchant, and Nicholas Ayache. Non-parametric diffeomorphic image registration with the demons algorithm. In *Medical Image Computing and Computer-Assisted Intervention–MICCAI 2007*, pages 319–326. Springer, 2007.
- [VPPA08] Tom Vercauteren, Xavier Pennec, Aymeric Perchant, and Nicholas Ayache. Symmetric log-domain diffeomorphic registration: A demons-based approach. In Dimitris N. Metaxas, Leon Axel, Gabor Fichtinger, and Gábor Székely, editors, *Medical Image Computing and Computer-Assisted Intervention - MICCAI 2008, 11th International Conference, New York, NY, USA, September 6-10, 2008, Proceedings, Part I*, volume 5241 of *Lecture Notes in Computer Science*, pages 754–761. Springer, 2008.

- [VPPA09] Tom Vercauteren, Xavier Pennec, Aymeric Perchant, and Nicholas Ayache. Diffeomorphic demons: Efficient non-parametric image registration. *NeuroImage*, 45(1):S61–S72, 2009.
- [WM97] David H Wolpert and William G Macready. No free lunch theorems for optimization. *IEEE transactions on evolutionary computation*, 1(1):67–82, 1997.
- [WZW04] Simon K Warfield, Kelly H Zou, and William M Wells. Simultaneous truth and performance level estimation (staple): an algorithm for the validation of image segmentation. *IEEE transactions on medical imaging*, 23(7):903–921, 2004.
- [YC06] Lexing Ying and Emmanuel J Candès. The phase flow method. *Journal of Computational Physics*, 220(1):184–215, 2006.

## Chapter 5

# A multi-atlas for the neonatal rabbit brain

### Contents

---

<b>5.1</b>	<b>MR imaging as biomarker . . . . .</b>	<b>132</b>
5.1.1	MRI readouts . . . . .	132
5.1.2	Image segmentation challenge . . . . .	133
<b>5.2</b>	<b>Image segmentation method for the newborn rabbit . .</b>	<b>134</b>
5.2.1	Currently available rabbit atlases . . . . .	135
<b>5.3</b>	<b>Multi-atlas for the neonatal rabbit brain . . . . .</b>	<b>136</b>
5.3.1	Materials and methods . . . . .	137
5.3.2	Segmentation pipeline and proposed stereotaxic orientation	138
5.3.3	Manual segmentation and taxonomy . . . . .	142
5.3.4	Automatic segmentation algorithm . . . . .	146
5.3.5	Probabilistic atlas creation . . . . .	147
5.3.6	Results . . . . .	147
5.3.7	Validation . . . . .	149
5.3.8	<i>In vivo</i> experiments . . . . .	153
<b>5.4</b>	<b>Parameters benchmarking: multi-modal versus uni-modal</b>	<b>155</b>
<b>5.5</b>	<b>Conclusions . . . . .</b>	<b>156</b>
<b>5.6</b>	<b>Appendix: Newborn Rabbit Brain Taxonomy . . . . .</b>	<b>157</b>

---

Magnetic resonance imaging is a valuable diagnostic tools providing both a 3D map of the tissue architecture and the fibre microstructure. Moreover it can be performed noninvasively *in vivo* and *ex vivo*. The measured dephasing of protons in presence of a varying magnetic field provides a range of biomarkers. According to

the selected sequence, there are several possible numerical quantifications that can be computed from the signal.

To analyse the signal at each spatial location of the brain sample, the first step is often the identification of the regions of interest, according to a standardised taxonomy. In going back to the main pre-clinical study, having established the protocol that is believed to be optimal in studying the effects of antenatal corticosteroids administration on a newborn rabbit animal model, the next step is to choose the best computational tools for the biomarkers quantification and the subsequent statistical analysis.

The goal of this chapter is to present how we obtained an automatic method to produce a segmentation of the region of interest of the newborn rabbit brain. We introduce the first MR multi-atlas for the neonatal rabbit that will be utilised in Chapter 6 for the automatic segmentation of the newborn rabbit brain through a segmentation propagation and label fusion algorithm based on diffeomorphic image registration.

### 5.1 MR imaging as biomarker

In Chapter 3, where we presented the study design, MRI was introduced as one of the three methodologies considered to tackle the investigation of the effects of corticosteroids administration, alongside with neurobehavioural assessment and histological staining.

The established acquisition protocol, provided a high resolution T1, a 64 directions times 3 shells diffusions and the T2-MSME. Resulting dataset allows for the application of the state-of-the-art biomarkers computations, such as neurite orientation dispersion and density imaging (NODDI), proposed by Zhang et al. [ZSWKA12], diffusion tractography, by Tournier et al. [TCC12], NOS-network and g-ratio network, Mancini et al. [MGD<sup>+</sup>17] and g-ratio estimation by Melbourne et al. [MERDV<sup>+</sup>14].

In this initial phase of the study, and given the focus of this work on the development of an automatic segmentation pipeline, customary measurements were used for the initial analysis. The use of more advanced biomarkers derived from DWI and T2-MSME will be left as future work until completion of the acquisition.

#### 5.1.1 MRI readouts

After preliminary investigation involving measuring brain weight and volume, the MRI volume readout was considered the first relevant biomarker in respect to the preterm birth.

From the DWI modality the first two main readouts are scalar measures obtained

from the diffusion tensor fitting: Fractional anisotropy (FA) and mean diffusivity (MD). See for example Hashemi et al. [HBL12] and Sener [Sen01]. FA is a normalised measure of the degree of anisotropy of the water diffusion. The higher value, the more the diffusion is restricted in a single direction. It reflects the measure of coherence of the fibres at a given voxel. MD measures the magnitude of diffusion (of water molecules) within tissue averaging the eigenvalues at each voxel. A more robust version of the MD is the radial diffusivity (RD), where only the first two eigenvalues are averaged. Even simpler measure is the axial diffusivity (AD), corresponding to the first eigenvalue of the diffusion tensor image.

All these measure require to be calculated within specific region of interest. The following sub-sections addresses in further details the problem of obtaining a segmentation and the related problem of estimating the intra cranial volume of each acquisition.

### 5.1.2 Image segmentation challenge

The main challenge in image segmentation is the lack of bias-free accuracy assessment, consequence of the lack of a ground truth. Moreover, the segmentation quality heavily influences the the biomarkers quantification. A varying segmentation quality may bend the subsequent statistic analysis towards the appraisal of the segmentation quality itself rather than the estimation of the underpinning studied biological phenomenon.

Given an MR image, the most direct approach to obtain a segmentation is through manual delineation, optionally based on multiple MR modalities mutually aligned. This choice allows for visual control of the results quality while comparing multiple structures, yet, it is intrinsically biased. Different raters may provide different delineation of the same region, even if following the same protocol. Even the same rater if asked to segment the same region twice may produce two different results. Moreover this approach is very time consuming, and can be even unfeasible for large studies.

To limit the caveats of manual segmentation, many automatic segmentation approaches have been proposed. These are unbiased, reproducible and faster than the human segmentation approach. An automatic segmentation method purely based on intensities is made sub-optimal by MR signal inhomogeneities, or bias field. In a framework initially proposed by Wells et al. [WGKJ96], the correction of the bias field can be performed alongside with a simultaneous intensity labelling within the same algorithm.

The mutual position of the labels representing the tissue type was further considered to improve the automatic method. A Bayesian model correcting for bias field, while segmenting the image based on intensities and taking into account the spatial

prior was proposed by Van Lemput et al. [VLMVS99] and by Ashburner and Friston [AF05]. The proposed *unified segmentation* method is a generative model alternating between an Expectation Maximisation algorithm to optimise the intensities parameters modelled by a Mixture of Gaussian, and a Levenberg-Marquardt (LM) algorithm to estimate the registration and bias field parameters. The decoupled approach was developed after the impossibility of correcting for the bias field in the same step of the MoG parameters. Unified segmentation requires the availability of a probabilistic atlas of the intended segmentation, that can be obtained averaging a manually segmented dataset.

When a comprehensive MR atlas or a probabilistic atlas (obtained by co-registering and averaging together several atlases) is available, it can be transposed over the image awaiting to be parcellated, with a segmentation propagation method [XP00].

Rather than considering a single atlas or probabilistic atlas, a different approach takes into account a multi-atlas, i.e. a dataset of manually segmented images of the considered anatomy. In this method each atlas is propagated over the anatomy to be segmented and the resulting stack of segmentations are *fused* together with a chosen algorithm to provide the sought segmentation. This approach was proposed by Heckemann et al. [HHA<sup>+</sup>06] and further improved by Alijabar et al. [AHH<sup>+</sup>09], Sabuncu et al. [SYVL<sup>+</sup>10] and by Koch et al. [KRB<sup>+</sup>17]. Iglesias et al. in the survey [IS15] confirmed the increase of performance of the multi-atlas approach respect to the single atlas one. In fact the propagation and fusion from multiple atlases can better span the inter-subject variability.

After the segmentation propagation, three common label fusion techniques are *Majority Voting* (MV), *Simultaneous Truth And Performance Level Estimation* (STAPLE) [WZW04] and *Similarity and Truth Estimation for Propagated Segmentations* (STEPS) [CLM<sup>+</sup>13] already introduced in Section 4.1.1.

More recently, with the development of Deep Learning classifiers, latest automatic segmentation approaches based on neural network have further pushed the performance limits. Litjens et al. [LKB<sup>+</sup>17] recently proposed a survey on the topic, and Gibson, Li et al. [GLS<sup>+</sup>18] proposed an open source software for the deep learning based automatic segmentation specific for MR images. The deep learning approach is however highly dependent on the quantity and quality of the data used in the initial learning step. As it is prone to overfitting, it may require a very large amount of training data to estimate the weight of the neural network.

## 5.2 Image segmentation method for the newborn rabbit

We employed the proposed method for the ICV estimation only at the early stage of the study, to compare few manually segmented regions. Throughout the study, the

manual segmentation of few regions turns out to be unsatisfactory. This is because of time limitation and the lack of reproducibility in manual segmentation. Moreover the selection of the regions that are mainly affected by preterm birth and corticosteroids administration was only a working hypothesis, to be verified analysing all the regions. To address these issues we created a multi-atlas for the new-born rabbit brain, for the automatic segmentation of the full brain of the newborn rabbit, presented in the next sections.

### 5.2.1 Currently available rabbit atlases

For the neonatal rabbit, before the proposed contributions, manual segmentation had been the preferred strategy [EBI<sup>+</sup>12, DDL<sup>+</sup>12, LTC<sup>+</sup>15]. The best approximation of a newborn rabbit brain atlas was the adult rabbit brain atlas proposed by Munoz-Moreno et al. [MMAPB<sup>+</sup>13], called here *Barcelona atlas*. This is based on 10 multi-modal scans acquired at 3 Tesla with anisotropic resolution (0.15mm, 0.15mm, 0.7mm) and it provides 60 anatomical regions, whose borders were identified by overlaying structural and diffusion weighted imaging (DWI). It was not possible to adapt the Barcelona atlas to the Newborn anatomy without manual intervention, not only due to its lower resolution and anisotropic acquisition, but also due to the geometrically non-linear growth between newborn and adult. This can be seen in particular comparing Figure 195-2 with Figures 59-2 and 59-3.

The Barcelona atlas was employed by Brusini et al. [BCW<sup>+</sup>18] in a study analysing brain changes between wild and domestic adult rabbits. Also in this case, only due to the lower resolution, manual intervention on the propagated segmentation was required. Another adult rabbit atlas, proposed by Mullhaupt et al. [MAS<sup>+</sup>15] consists of an anatomical delineations of the coronal slices, however, these segmentations are currently not available in digital format.

The lack of a digital atlas prevents from applying the state-of-the-art automatic methods mentioned in Section 5.1.2. This is critical when considering the growing range of studies involving neonatal rabbits, especially in the investigation of pre-term birth related perinatal brain injury [LRM<sup>+</sup>17], cerebral palsy [TDJ<sup>+</sup>05, DDJT07, DQ17] and intrauterine growth restriction [BMMAP<sup>+</sup>14, SMMC<sup>+</sup>15].

To be able to move forward in our study, as well as to provide a multi-atlas for segmentation propagation to the community working with the same animal model, we selected 17 subjects to undergo manual segmentation. The results of this part of the study are presented in Section 5.3.

Before presenting this contribution, we introduce a method for the intracranial volume estimation that was employed in an intermediate stage of the analysis, when a multi-atlas was not available. This method is still relevant for the cases when a multi-

atlas is not available, the regions of interest have been manually delineated, and a subject-dependent normalisation factor, proportional to the intra cranial volume (ICV) must be established.

### 5.3 Multi-atlas for the neonatal rabbit brain

In this section we present the first micro-MR multi-modal multi-atlas for the neonatal rabbit brain, published in [FvdMVDV<sup>+</sup>18]. It provides 12 high resolution multi modal acquisitions segmented in 89 areas with a taxonomy established for the Neonatal brain. The segmentation propagation method to segment new acquisitions and for the validation, is proposed alongside, as open source software.

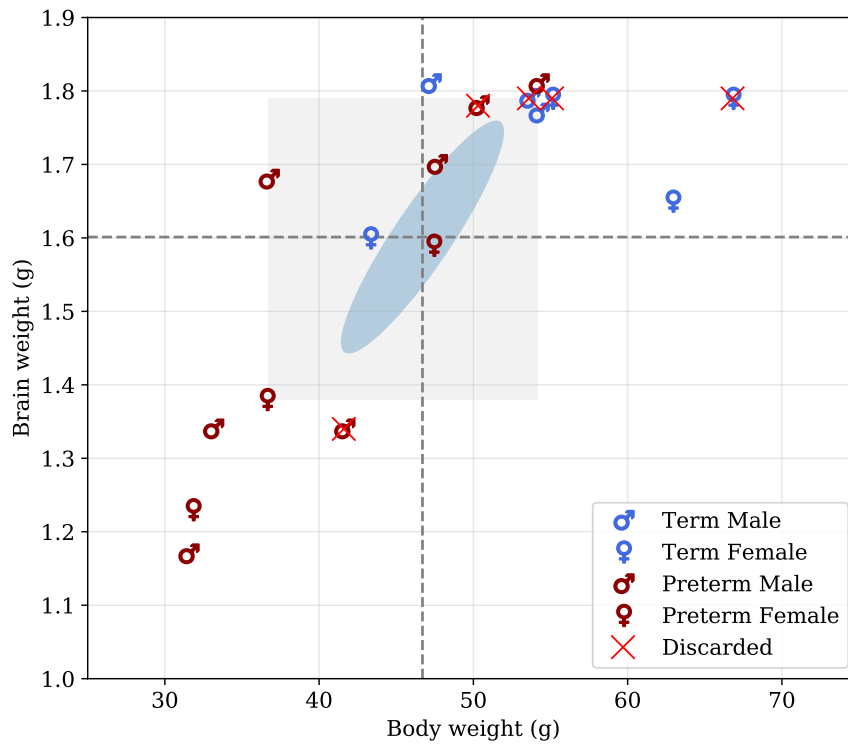


Figure 136-1: **Sample selection and distribution.** Brain and body weight of all subjects prepared for the study: 8 pre-term (7 males / 3 females) and 4 term (3 males / 4 females). Of the initial 17 subjects (10 pre-term, 7 term), 5 have been discarded due to image artefacts. Cross-hair shows the mean, blue ellipsoids the covariance and gray rectangle shows the 25<sup>th</sup> and 75<sup>th</sup> percentiles.

### 5.3.1 Materials and methods

#### Sample collection

Initially, 17 subjects, both born either term (gestation 31 days) or pre-term (gestation 28 days) and represented in Figure 136-1, were prepared according to the following protocol:

1. Time-mated pregnant does (hybrid of New Zealand White and Dendermonde) were obtained from the *Animalium* of the Biomedical Sciences group at the KU Leuven, Belgium. Animals were treated according to current guidelines for animal well-being, and all experiments were approved by the Ethics committee for Animal Experimentation of the Faculty of Medicine (P062/2016). Does were housed in separate cages before delivery, with free access to water and chow and a light-dark cycle of 12h. The does underwent a cesarean section on either 28 (pre-term) or 31 (term) days of gestation. Thereafter, newborn rabbits were nursed in an incubator with twice daily gavage feeding until harvesting on post-conceptual age of 32 days. This established an equivalent time-point at harvesting for both term (gestation 31 days + 1 day postnatal) and pre-term (gestation 28 days + 4 days postnatal).
2. Neonatal rabbits were actively perfused with a mixture of formalin and gadolinium to increase MRI signal to noise ratio while preserving the tissue [JCF<sup>+</sup>02]. Kits were anesthetized with intramuscular ketamine (35 mg/kg, ketamine 1000 CEVA; CEVA Santé Animal, Brussels, Belgium) and xylazin (6 mg/kg, Vexylan; CEVA Santé Animal) and transcardially perfused with 0.9% saline and heparin (100u/mL) followed by perfusion fixation with 4% paraformaldehyde in 0.1 mol/L phosphate buffer (pH 7.4) containing dimeglumine gadopentetate 0.5 mmol/mL (Magnevist<sup>®</sup>, Dimeglumine Gadopentetate 0.5 mmol/mL, Bayer HealthCare Pharmaceuticals, Germany).
3. The head with the brain *in situ* was then immersed in this solution for another 48h followed by a rehydration phase in a 1:200 solution of Magnevist<sup>®</sup>/PBS for 48-72 h. The head was trimmed and placed in a sample holder, surrounded by proton-free perfluoropolyether solution (Fomblin<sup>®</sup>, Solvay Solexis) that minimises susceptibility artefacts at the interface.

Of the initial 17 subjects, 5 have been discarded due to image artefacts: presence of enlarged perivascular spaces ( $n = 1$ ), most likely caused by the perfusion technique, ghosting artefacts ( $n = 3$ ) and wrong input scanner settings ( $n = 1$ ). See Appendix 3.5 for a summary of image artefacts we had to face during the acquisition of newborn rabbit MRI.

### 5.3.2 Segmentation pipeline and proposed stereotaxic orientation

Image acquisitions were performed following the protocol introduced in Section 3.4.

Acquired data were converted from Bruker ParaVision format to Nifti-1 format using our contribution *bruker2nifti* image converter [FSM<sup>+</sup>17]. Despite being customary for rats, the bicommissural orientation (where the anatomical plane passing through the anterior and posterior commissure is parallel to the horizontal plane) is not adequate for rabbits.

Comparing the anatomies of skeletons in Figure 138-1, skulls in Figure 138-2 and brains in Figure 138-3, a difference in the position and anatomies of the skull respect to the body and the lack of a flat superior side in the rabbit brain can be noticed. The choice of orienting the bicommissural plane with the horizontal plane for rat, makes the coronal section compatible with the histological sectioning. Same thing can not be said for the rabbit.

To attain a coronal plane comparable to histological atlases, we propose a stereotaxic orientation where the bicommissural plane forms a constant angle of  $45^\circ$  with the plane parallel to the horizontal plane (represented in Figure 138-4 with full and dashed lines respectively).

This is as well an ideal orientation to compare the growth of the developing brain, as it can be seen in Figure 195-2, where the proposed stereotaxic orientation is adopted.

After subjective visual evaluation of bias field and artefacts, the best acquisition underwent manual alignment in stereotaxic orientation. Thereafter, brain and skull coarse region of interest manual delineation was performed by alternating Gaussian smoothing and symmetrisation with respect to the mid-sagittal plane employing *ITK-SNAP* and *NiftySeg* [YPH<sup>+</sup>06, CCMO12].

The binary mask isolating the region of interest was then automatically propagated on the T1 modality of the remaining 11 acquisitions with an affine segmentation propagation performed with *NiftyReg* [MCD<sup>+</sup>14]. After the initial orientation and the coarse brain and skull extraction for all of the subjects, the *N4ITK* bias field correction [TAC<sup>+</sup>10] was applied. An additional mask was created by thresholding the outliers intensities while manually selecting the threshold percentile. This was subsequently employed to mitigate the impact of image artefacts during the spatial alignment. Both masks were propagated to the B0 weighted image before eddy current correction and tensor fitting, performed with *FSL* (default parameters) version 5.0.9 [JBB<sup>+</sup>12].

Fractional anisotropy map (FA), mean diffusivity map (MD) and RGB encoded direction of the main eigenvalue map (V1) were resampled in the T1 weighted image space to overlay structural information. Due to sample as well as frequency drifting

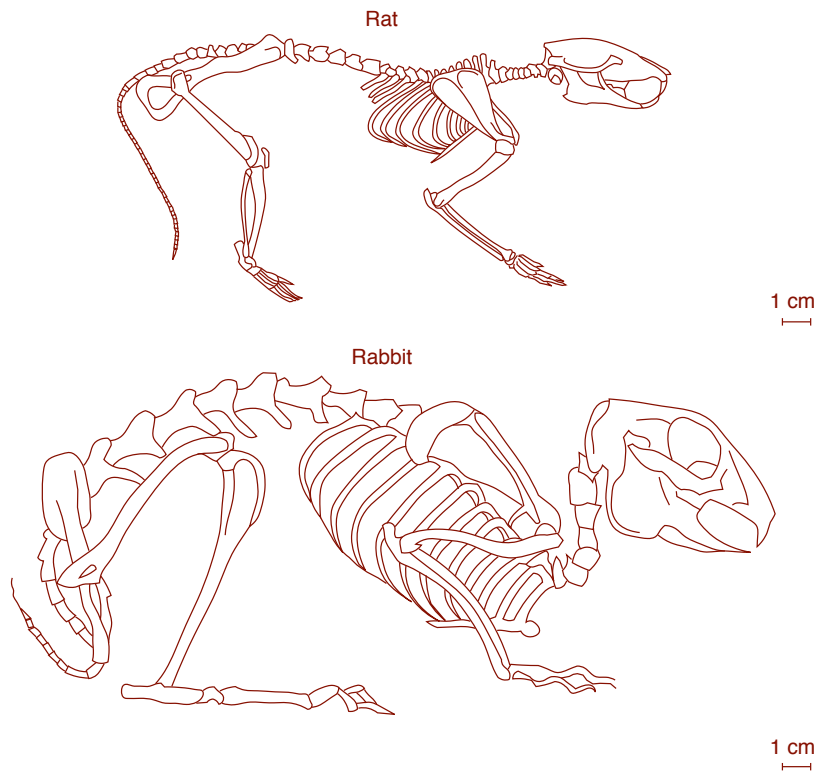


Figure 138-1: **Comparison between adult rat and rabbit skeletons and skulls.** Comparison between the adult rat and rabbit skeletons. Note the difference in latent posture and head position resulting in skull attitude differentiation. Inspired by <https://www.behance.net/> and <http://bcrb.bio.umass.edu/>. Last access March 23, 2019.

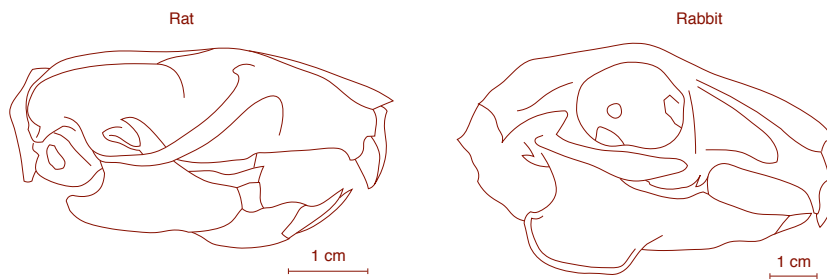


Figure 138-2: **Comparison between adult rat and rabbit skulls.** Comparison between the adult rat and rabbit skull. Note the shape difference of the frontal and parietal skull shape. Inspired by <http://www.skullsite.co.uk/>.

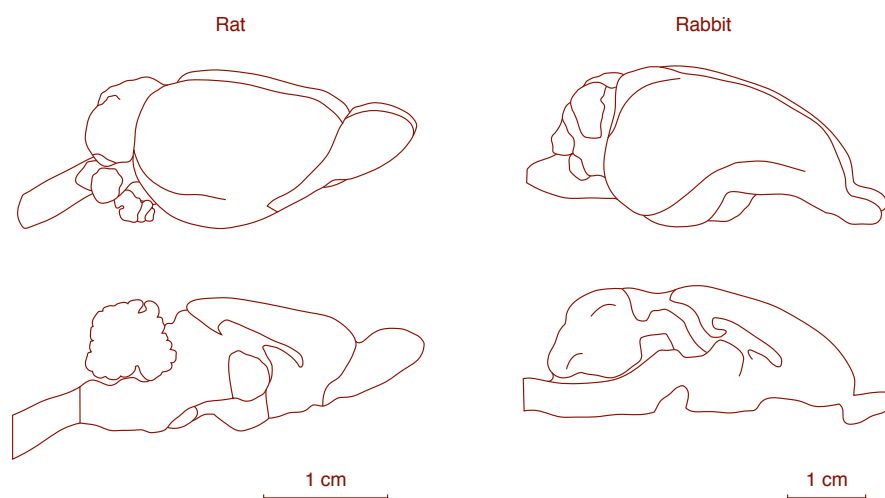


Figure 138-3: **Rat and rabbit brain compared.** Representation of the newborn rat and rabbit brain. 3D representative sketches (top) and mid-sagittal section (bottom). Inspired by <http://www.medicinafetalbarcelona.org/rabbitbrainatlas/> and <http://www.skullsite.co.uk/Rat/comrat.htm>.

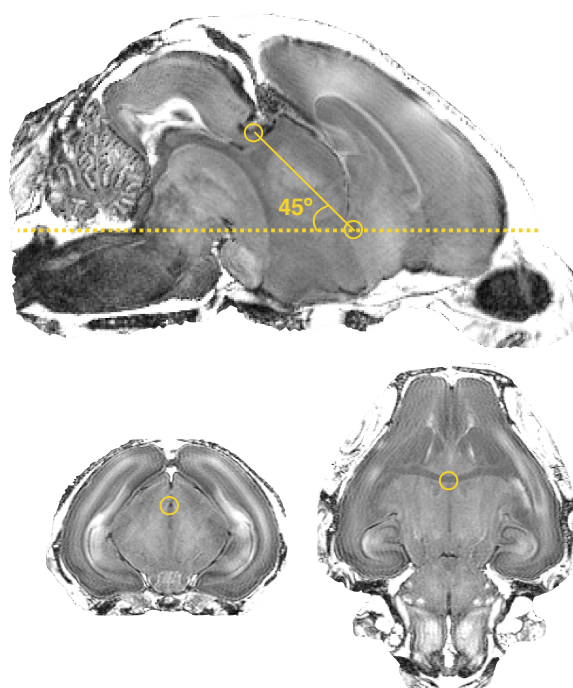


Figure 138-4: **Proposed stereotaxic orientation for the MR imaged newborn rabbit brain.** In the mid-sagittal section, the bicommissural plane forms a  $45^\circ$  angle with the horizontal plane. The full line represents the bicommissural plane and the dashed line the horizontal plane. Centers of the anterior and posterior commissure are highlighted in the coronal and the axial sections.

Level	Region	abbreviation	Label
1.1	Frontal Area	FrA	7, 8
	Medial Prefrontal	PFrA	5, 6
	Occipital Area	OA	9, 10
	Parietal Area	PtA	11, 12
	Temporal	TeA	13, 14
	Cingulate	Cg	15, 16
	Retrosplenium	RS	17, 18
	Insular	Ins	19, 20
1.2	Olfactory lobe	OB	25, 26
	Piriform	Pir	27, 28
1.3	Hippocampus	HA	31, 32
	Subiculum	S	43, 44
	Entorhinal	Ent	45, 46
1.4	Clastrum	CL	53, 54
	Amygdala	Am	55, 56
1.5	Caudate nucleus	CA CN	69, 70
	Putamen	Pu	71, 72
	Globus Pallidus	GP	75, 76
	Basal forebrain	BF	77
	Septum	SA	78
2.1	Thalamus	THA	83, 84
	Hypothalamus	HYP	109, 110
	Mammillary body	MAM	121
2.2	Midbrain	MB	127
	Pretectal	PRT	129, 130
	Superior colliculus	SC	133, 134
	Inferior colliculus	IC	135, 136
	Substantia nigra	SN	139, 140
	Periaqueductal gray	PAG	141, 142
2.3	Pons	PO	151
	Medulla oblongata	MY	153
3.1	Cerebellar vermis	VERM	161
3.2	Cerebellar hemisphere	HEM	179, 180
4	Ventricular system	VS	201
	Lateral ventricles	LV	203, 204
	Periventricular area	PV	211, 212
5.1	Optic tract and optic chiasm	OT	215
5.2	Corpus callosum	cc	218
	External capsule	ec	219, 220
	Internal capsule	int	223, 224
	Corona radiata	cr	225, 226
	Cerebral peduncle	cp	227, 228
	Subcortical white matter	swm	229, 230
5.3	Anterior commissure	ac	233
	Hippocampal commissure	hc	237
	Fimbria of hippocampus	fi	239, 240
	Columns of the fornix	fx	241, 242
	Stria terminalis	st	243, 244
5.4	Mammillothalamic tract	mt	247, 248
	Fasciculus retroflexus	fr	251, 252
	Posterior commissure	pc	253

Table 138-1: **Delineated regions in the proposed new-born rabbit brain taxonomy.** For symmetric structures, we follow- 141 -ed the convention left/right odd/even. An extended hierarchical taxonomy is provided in the supplementary material B of our paper [FvdMVDV<sup>+</sup>18].

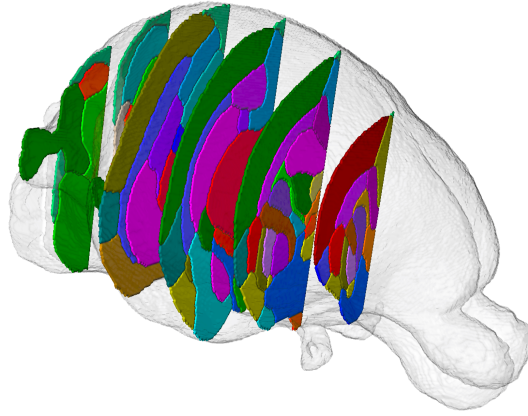


Figure 138-5: **3D brain surface rendering.** Segmentation of 6 selected coronal slices of the right hemisphere are shown with the remaining labels in transparency. Corresponding slices are delineated over the T1 modality with the corresponding nomenclature in Figure 138-6.

occurred during the acquisition, anatomies resulting from different sequences were not perfectly spatially aligned. Therefore the B0 was rigidly aligned using NiftyReg [MCD<sup>+</sup>14] with the T1 (Normalized Mutual Information as measure of similarity) and the same transformation was applied to the remaining DW modalities.

### 5.3.3 Manual segmentation and taxonomy

The available adult atlas [MMAPB<sup>+</sup>13] could not be satisfactory propagated onto the neonatal rabbit anatomy, mainly due to the geometrically non-linear growth between newborn and adult. After a manual landmark based non-rigid registration with 3D Slicer [KPV14], the adult atlas was roughly deformed over the newborn anatomy, and considered as a starting point. The subsequent manual adjustment had to compensate for the anatomical differences and for the ringing artefacts caused by resampling (adult grid spacing:  $0.15 \times 0.15 \times 0.7$  mm, newborn grid spacing:  $0.078 \times 0.078 \times 0.078$  mm).

To reduce the complexity of the manual segmentation, one hemisphere was refined and subsequently registered on the contralateral side [REC<sup>+</sup>17] providing a starting point for further adjustment. Manual refinement was performed by Johannes van der Merwe using *ITK-SNAP* v2.2.0 [YPH<sup>+</sup>06], overlaying the T1, FA, MD and V1 modalities. The neuroanatomical nomenclature selected was adapted from a standard adult rabbit histological atlas [SWW86] and from two standard rat brain atlases [PG07, Swa04], incorporating 89 labels (Table 138-1 and Figures 138-5 and 138-6). Areas requiring histological criteria for identification were not detailed in the atlas.

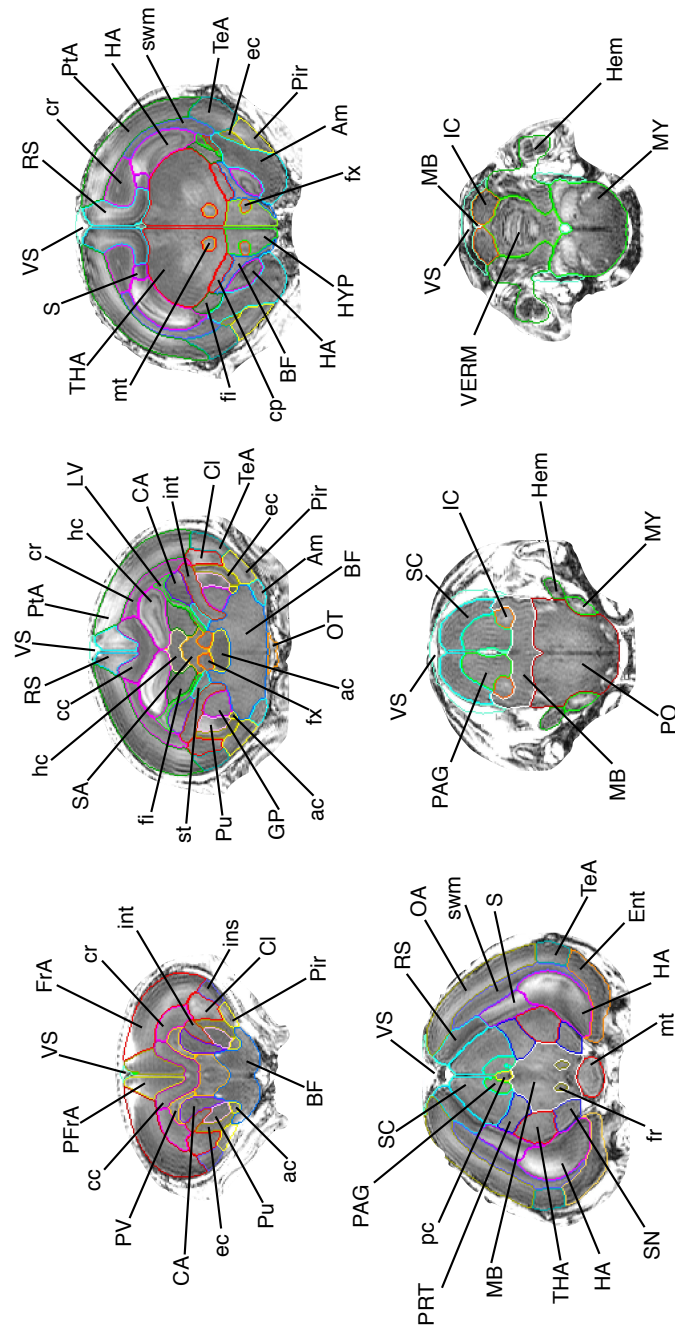


Figure 138-6: **Delineation of anatomical regions over the T1 modality.** Progressive coronal sections, anterior to posterior. Only the segmentation outline is delineated for visualization purposes. Region of interest surrounding the brain is visible in the image, to show the border delineation between the brain and the skull. See Table 138-1 for the abbreviation and nomenclatures. Detailed taxonomy table is proposed in the additional material.

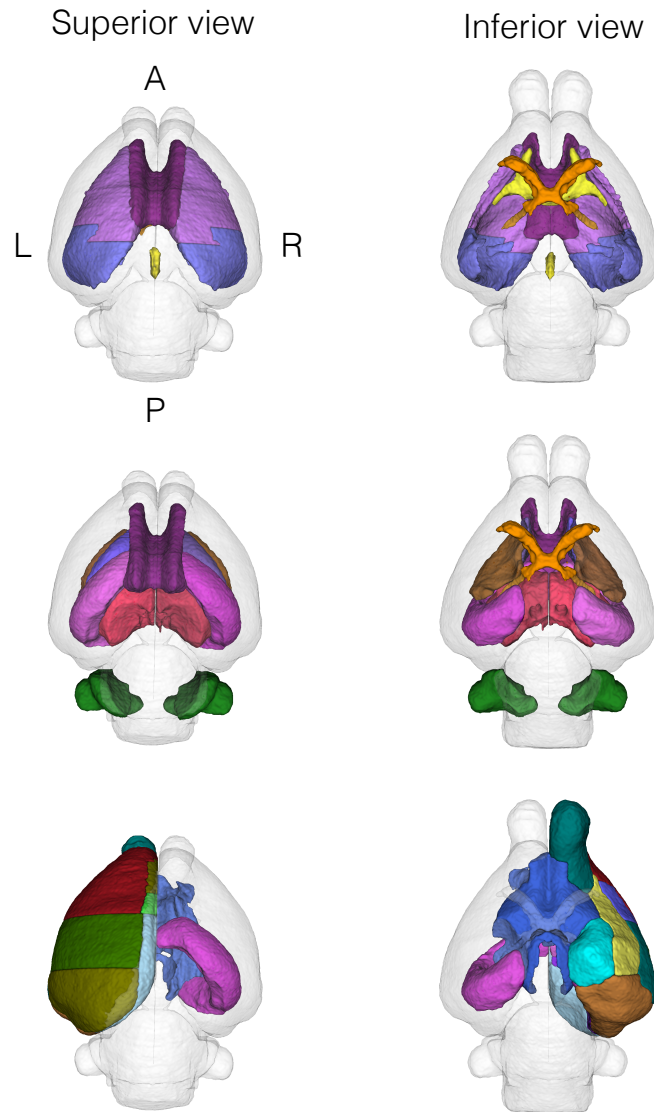


Figure 142-1: **3D brain surface rendering.** The first row emphasises a selection of subcortical regions (corona radiata in pink, corpus callosum in purple and subcortical white matter in blue) and of fibertracts (anterior and posterior commissure in yellow, and optic tracts in orange). The second row highlights the regions that are believed to be affected by pre-term birth. Superior view: corpus callosum (purple), hippocampus left and right (pink), thalami (red), caudate nuclei (blue) and cerebellar hemispheres (green). Inferior view: optic tracts (orange), internal capsula left and right (brown). The third row points out the right hemisphere cortex. Superior view: olfactory bulb (aquamarine blue), anterior (red), frontal (green) and occipital (khaki). Inferior view: piriform (yellow), enthorinal (brown) and amigdala (turquoise), the hippocampi (left and right in pink) and the basal forebrain (blue).

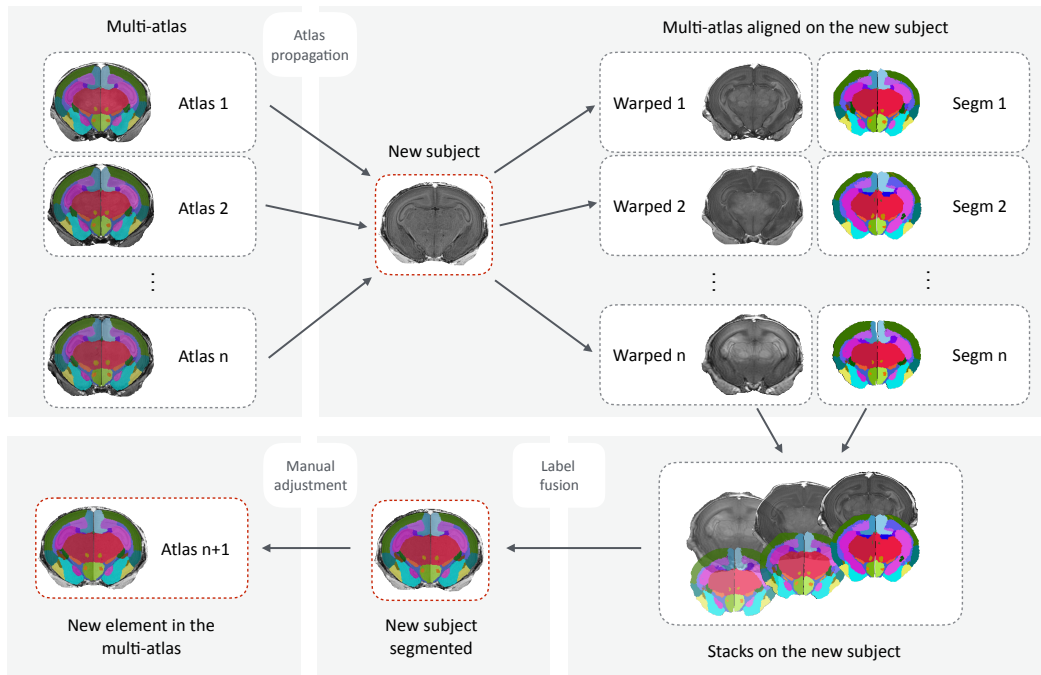


Figure 142-2: **Software scheme.** Visualisation of the segmentation procedure, involving atlas propagation, label fusion and elective manual adjustments. For the creation of our multi-atlas the whole procedure with the manual adjustments had been performed three times.

A hierarchical taxonomy inclusive of the areas appearing in the histology and the produced manual protocol are provided in the Appendix of the chapter, as well as in the supplementary material of our paper [FvdMVDV<sup>+</sup>18].

Delineations covered the whole brain up to the medulla oblongata posterior, partly incorporating some of the ventricular system while excluding the proximal spine and skull.

Regions were classified into cortical regions, cortical subplate, basal ganglia, brain-stem, cerebellum, fibertracts and ventricular system:

- ▷ Cortical and cortical subplate delineation was based upon T1 and V1 intensities, and were defined by their surrounding fibertracts and manually corrected for by neuroanatomical landmarks.
- ▷ The delineation of the basal ganglia was based on T1 weighted and FA, MD intensities while the brainstem with less distinctive T1 definition was based upon the combination of all modalities equally.
- ▷ The fibertracts delineation was mainly based on the T1 and FA intensities, and only secondarily on the V1.

- ▷ Finally, cerebellar hemispheres and vermis were almost completely segmented based on only T1 weighted characteristics.

After completing the manual refinement of the first subject, this was propagated to the next one via affine and non-rigid registration. Non-linear spatial correspondences were estimated through diffeomorphic registration of the bias field corrected T1 images [MRT<sup>+</sup>10]. Subsequent to manual refinement, both segmentations were propagated to the third subject. Through visual assessment, the most suitable of the two propagations was subsequently manually refined. Thereafter, the diffeomorphic segmentation propagation of each of the three refined subjects on the new one to be segmented, was followed by the application of four label fusions methods. This was performed both on the T1 modality alone, or on the T1 and FA combined, in a multi-modal approach. *Majority voting*, *Simultaneous Truth And Performance Level Estimation (STAPLE)* [WZW04] and *Similarity and Truth Estimation for Propagated Segmentations (STEPS)* [CLM<sup>+</sup>13], with a range of parametrisations selected through visual assessment, were applied to provide 8 mono-modal and 8 multi-modal starting points for a further manual refinement.

With the proposed iterative method, schematically represented in figure 142-2, each new subject included to the multi-atlas improved the accuracy of the segmentation propagation and label fusion applied to the next one. To address the bias introduced when selecting an initial subject and to gradually improve the overall quality, the iterative method was applied again twice over the already segmented subjects.

The time of the manual adjustment has decreased significantly, from a time range between 20 to 25 hours for the first subject to a time range between two to six hours, depending on the quality of the image and the initial propagation

#### 5.3.4 Automatic segmentation algorithm

The same procedure developed to initialise the segmentations for the manual adjustment can be extended to approximate the segmentation on a new subject, constituting an automatic segmentation algorithm. The first step consists in the diffeomorphic registration of the region of interest (brain and skull) mask with the subsequent propagation of the labels from each element of the multi-atlas to the new subject.

Among the several label fusion methods employed to produce the resulting parcellation from the stack of the aligned elements of the multi-atlas, the multi-modal Majority Voting provided the best result, both scored with visual assessment and leave-one-out cross validation. Accordingly, this is the proposed choice for the automatic segmentation method.

Label	Region	Grouped sub-labels
1	Corticospinal Tract	223, 224, 225, 226, 227, 228, 229, 230
2	Corpus Call. Area	218, 219, 220
3	Other Fibretracts	215, 233, 237, 239, 240, 241, 242, 243, 244, 247, 248, 251, 252, 253
4	Cerebellar Vermis	161
5	Ventricular System	201, 203, 204, 211, 212
6	Cerebellar Hems.	179, 180
7	Hypothalamus	109, 110, 121
8	Rombocephalon	151, 153
9	Mesencephalon	127, 129, 130, 133, 134, 135, 136, 139, 140, 141, 142
10	Thalamus	83, 84
11	Allocortex	25, 26, 27, 28
12	Hippocampal Area	31, 32, 43, 44, 45, 46
13	Deep Cortex	53, 54, 55, 56
14	Basal Ganglia	69, 70, 71, 72, 75, 76
15	Septum, Basal Forebrain	77, 78
16	Isocortex	5, 6, 7, 8, 9, 10, 11, 12, 13, 14, 15, 16, 17, 18, 19, 20

Table 146-1: **Macro-regions grouping.** For validation purposes, the 89 regions were grouped in to 16 macro-regions. The proposed grouping was constructed by keeping regions of similar importance or anatomy or quality together, in this order of preference.

### 5.3.5 Probabilistic atlas creation

A probabilistic atlas can provide a suitable representation of the average newborn rabbit brain as well as a reference for future studies [MTE<sup>+</sup>95]. Figure 147-1 shows an axial section of the neonatal rabbit brain created with an unbiased group-wise registration applied to the skull stripped T1 acquisitions with *NiftyReg* [MDC<sup>+</sup>12]. The deformation model consists of diffeomorphisms parameterized with stationary velocity fields [ACPA06, VPPA07].

### 5.3.6 Results

Of the initial seventeen subjects to be segmented, visualised in Figure 136-1, five had to be discarded due to the presence of enlarged perivascular spaces ( $n = 1$ ), most likely caused by the perfusion technique, ghosting artefacts ( $n = 3$ ) and wrong input scanner settings ( $n = 1$ ).

In a procedure involving automatic and manual steps, the remaining 12 subjects

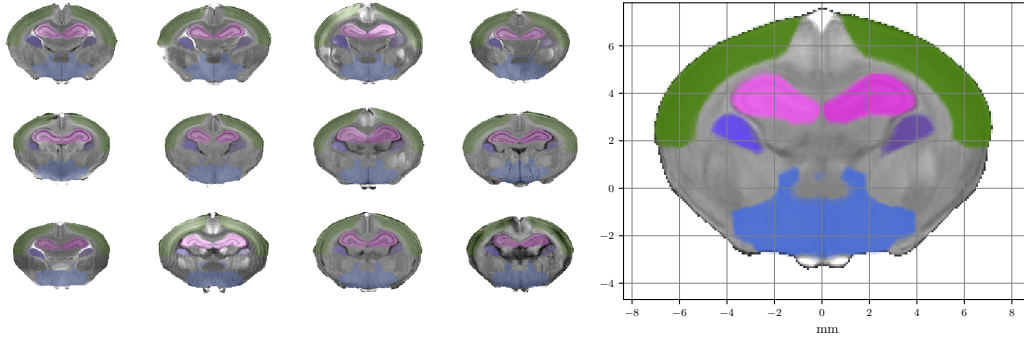


Figure 147-1: **Probabilistic atlas and probabilistic segmentation of 4 selected regions.** Coronal sections at the origin of the coordinate system for each of the 12 subject of the multi-atlas. Each subject is shown with the manual segmentation of parietal cortex (green), hippocampi (pink), caudate nuclei (purple) and basal forebrain (blue). On the right side, the probabilistic atlas as average of the 12 subjects on the left, with the voxel-wise probabilistic labels shown in the space of the atlas for each of the mentioned regions.

were parcellated into the 89 regions listed in Table 138-1. Illustrative views of one subject of the resulting multi-atlas can be visualised in Figures 138-5 and 138-6, where selected coronal sections are shown in 3D and annotated in the orthogonal 2D view. Superior and inferior views of the 3D rendering are proposed in Figure 142-1, emphasising a selection of regions. The resulting software schematic employed to create the multi-atlas is illustrated in Figure 142-2.

Computational time varies according to the computer architecture and the choice of the algorithm parameters. When the pipeline runs on a 2.5 GHz Intel Core i7 processor with SSD hard drive 16 GB 1600 MHz DDR3 and the affine and non-rigid registration steps are parallelised with OpenMP on 8 cores, the computational time for each automatic segmentation involving all the 12 subjects of the multi-atlas is approximately 2h10, including the full range of label fusion methods, as described in Section 5.3.3.

An approximation of the “ideal” average newborn rabbit brain in the proposed stereotaxic orientation is achieved with multimodal group-wise diffeomorphic registration. Its axial section passing through the origin of the coordinate system is shown in Figure 147-1 besides the same slice for each of the 12 subjects of the multi-atlas. With the probabilistic atlas, it is possible to quantify the likelihood of the presence of a determined tissue type at a given voxel.

As called for by Mazziotta et al. [MTE<sup>+</sup>95], the neonatal multi-atlas here proposed is intended as a starting point for a *maintained* digital atlas (<https://github.com/gift-surg/SPOT-A-NeonatalRabbit>). It is open to further improvements and to evolve according to future needs of structural and functional investigations. In analogy with what is currently employed in software development,

possible further upgrades will be tracked in the hosting repository with a version control system.

### 5.3.7 Validation

When the same protocol is applied, the manual segmentation variability between and within operators can be significant, even when segmenting a single region. Taking into account this known limitation, to assess the validity and robustness of an automatic method respect to the manual counterpart we performed five experiments:

1. Inter-operator variability assessment and comparison with the automatic method via hippocampi segmentation.
2. Visual scoring of unlabeled segmentations of the same subject.
3. Intra-operator consistency assessment for the manual adjustment of the automatic initialization via test-retest.
4. Fully automated segmentation assessment via cross validation.

The comparison of their outcomes provides an assessment of the coherence between the manual and the automatic approach. Before detailing them, we briefly recall the definitions of a range of measures to compare two segmentations [TH15, HCOB05]. These were selected before starting the investigation.

#### Selected measures of similarity

The four selected measurements are aimed at obtaining a range of complementary quantifications.

*Dice's score*: it measures the number of overlapping voxels of two regions, over the mean of the voxels. It is defined as

$$\text{Dice}(A_1, A_2) = \frac{2|A_1 \cap A_2|}{|A_1| + |A_2|},$$

where  $|A_j|$  corresponds to the cardinality of the voxels of the region  $A_j$ .

*Covariance distance*: the segmented regions are considered as clouds of points, whose covariance matrices are compared. It provides an idea of how well the relevant features of the distributions are aligned when orthogonally translated onto the same centre, and it is defined as:

$$\text{CovDist}(A_1, A_2) = \alpha \left( 1 - \frac{\text{Tr}(c(A_1)c(A_2))}{\|c(A_1)\| + \|c(A_2)\|} \right),$$

where  $c(A_j)$  is the covariance matrix of the voxel distribution of the label  $j$  in the 3D space,  $\text{Tr}$  is the matrix trace, or the sum of the diagonal elements,  $\|\cdot\|$  is the Frobenius norm and  $\alpha$  is a multiplicative factor corresponding to the maximal possible dissimilarity (here  $\alpha = 10$ ).

*Symmetric Hausdorff distance:* it provides the maximal distance between the contour of one segmentation and the other one. It is defined as

$$\text{HD}(A_1, A_2) = \max(\{H(A_1, A_2), H(A_2, A_1)\}) ,$$

for

$$H(A_i, A_j) = \max_{a_i \in \partial A_i} d(a_i, \partial A_j) ,$$

where  $d(a_i, \partial A_j)$  is the value of the minimal euclidean distance between the contour of  $A_j$ , indicated with  $\partial A_j$ , and the point  $a_i$  belonging to  $A_i$ . The contour considered in this case is the layer of voxels delineating region shape  $A_j$ , still belonging to the region (internal contour).

*Normalised symmetric contour distance:* is a robust symmetric average of the mean of the minimal distances between the two segmentations for each voxel of the contour. It is defined as:

$$\text{NSCD}(A_1, A_2) = \frac{S(A_1, A_2) + S(A_2, A_1)}{|\partial A_1| + |\partial A_2|} ,$$

for

$$S(A_i, A_j) = \sum_{a_i \in \partial A_i} d(a_i, \partial A_j) ,$$

with the same notations as defined above.

### Hippocampi manual segmentation comparison

A randomly selected and unlabeled subject was selected to undergo manual segmentation of the left hippocampus. This was performed by rater<sub>1</sub> (author of our paper [FvdMVDV<sup>+</sup>18] Johannes van der Merwe) and rater<sub>2</sub> (author Lennart Van Der Veen), following the same protocol established during this study. Rater<sub>1</sub> performed the manual adjustments during each phase of the multi-atlas creation.

Differences between the three regions are quantified with the four selected measures and reported in Table 150-1. A visual assessment of the differences is proposed in Figure 150-1.

	Dice	CovDist	HD	NSCD
rater <sub>1</sub> vs rater <sub>2</sub>	0.75	0.301	0.865	0.183
rater <sub>1</sub> vs auto	0.94	0.004	0.441	0.041
rater <sub>2</sub> vs auto	0.73	0.238	0.991	0.214

Table 150-1: **Quantification of the inter-rater variability and automatic method in the segmentation of left hippocampus.** Rater<sub>1</sub> (expert) and rater<sub>2</sub> (non expert) manually segmented the left hippocampus of an unlabeled and randomly selected subject. Resulting segmentations are compared with the automatic one. Differences are assessed with Dice’s score, covariance distance (CovDist), symmetric Hausdorff distance (HD) and normalized symmetric contour distance (NSCD).

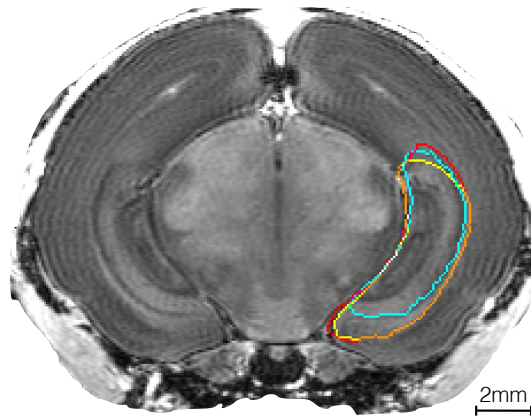


Figure 150-1: **Visual comparison of the inter-rater variability and automatic method in the segmentation of the left hippocampus.** Comparison between automatic method in red, rater<sub>1</sub> in yellow (expert) and rater<sub>2</sub> in turquoise (non expert) for the segmentation of hippocampi, in an axial slice. Regions of intersection between borders are rater<sub>1</sub> ∩ auto in orange, rater<sub>2</sub> ∩ auto in purple, rater<sub>1</sub> ∩ rater<sub>2</sub> in green and rater<sub>1</sub> ∩ rater<sub>2</sub> ∩ auto in white.

### Blinded segmentation scoring

The aim of this test was to compare the quality of the progressive manual refinements and secondarily to quantify the comparison between automatic and manual adjustment. A randomly selected and anonymised subject was considered with the three progressive rounds of manually refined segmentations (round<sub>1</sub>, round<sub>2</sub>, round<sub>3</sub>) and with the outcome of the automatic segmentation based on the remaining 11 subjects (auto). These four segmentations were relabelled, randomly re-ordered and provided to rater<sub>1</sub> for visual scoring. Visual scoring criteria to evaluate the goodness of a segmentation are subjective and based on the compatibility of the borders with the anatomical structures and on the overall smoothness.

The first of the manual adjustments, round<sub>1</sub>, was scored as the worst one in term of quality and the latest manual adjustment, round<sub>3</sub>, was scored as the best one. In between, round<sub>2</sub> and auto were considered equivalent in term of quality based only

on blinded visual assessment.

### Consistency in the manual adjustment of the automatic parcellation assessment

To produce the multi-atlas, each subject underwent a series of three segmentation propagations and manual adjustments. In order to assess the accuracy of the automatic method and at the same time to measure intra-rater variability in the manual adjustment, a randomly selected and anonymized subject was automatically segmented using the remaining 11 subjects, and subsequently underwent manual adjustment twice, in a test-retest experiment.

In this experiment, the rater did not consider necessarily to adjust every region: the macro regions 1, 2, 4, 6, 8, 11 and 12 required no manual intervention after the automatic segmentation. Figure 152-1 shows the differences measured with the selected metrics for all the regions that required manual intervention, comparing the automatic segmentation (*auto*) and the two manual adjustments (*adj1* and *adj2*) in three different boxplot.

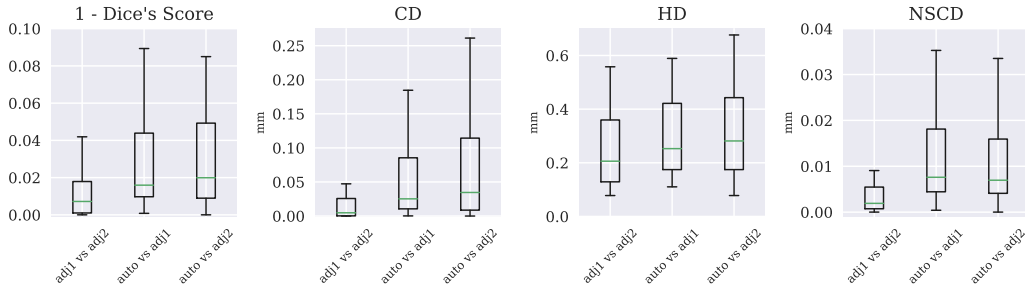


Figure 152-1: **Intra-rater test-retest.** Box plot comparing two different manual adjustments of the same initial segmentation (*adj1*, *adj2*) and the automatic initialization (*auto*) measured with inverted Dice's score (1 - Dice's score), covariance distance (CovDist), symmetric Hausdorff distance (HD) and normalized symmetric contour distance (NSCD). Only the regions with 1 - Dice's score smaller than 1 have been considered (48 regions out of 89). The very low inverted Dice's scores (or very high Dice's score) proves that few manual interventions were required to obtain a visually optimal results, and that consecutive manual interventions on the same subject were performed consistently.

### Automatic segmentation assessment via cross validation

In a leave-one-out cross validation [K<sup>+</sup>95], each subject underwent again automatic segmentation based on the remaining 11 atlases. For each subject, the obtained automatic segmentation was then compared with the available manual one.

To simplify the representation, the delineated regions were grouped into a set of 16 macro-regions, proposed in Table 146-1. The difference between the manual ad-

justment and the segmentation obtained with the remaining 11 subjects were scored with the four proposed metrics. Results are shown in the box plots in Figure 153-1 for the macro-regions.

The boxes show the interquartile interval, whiskers the minimum and the maximum. The central bar shows the median. Macro regions that were better aligned, according to all the selected metrics, were regions 1, 2, 4, 6, 8, 11 and 12.

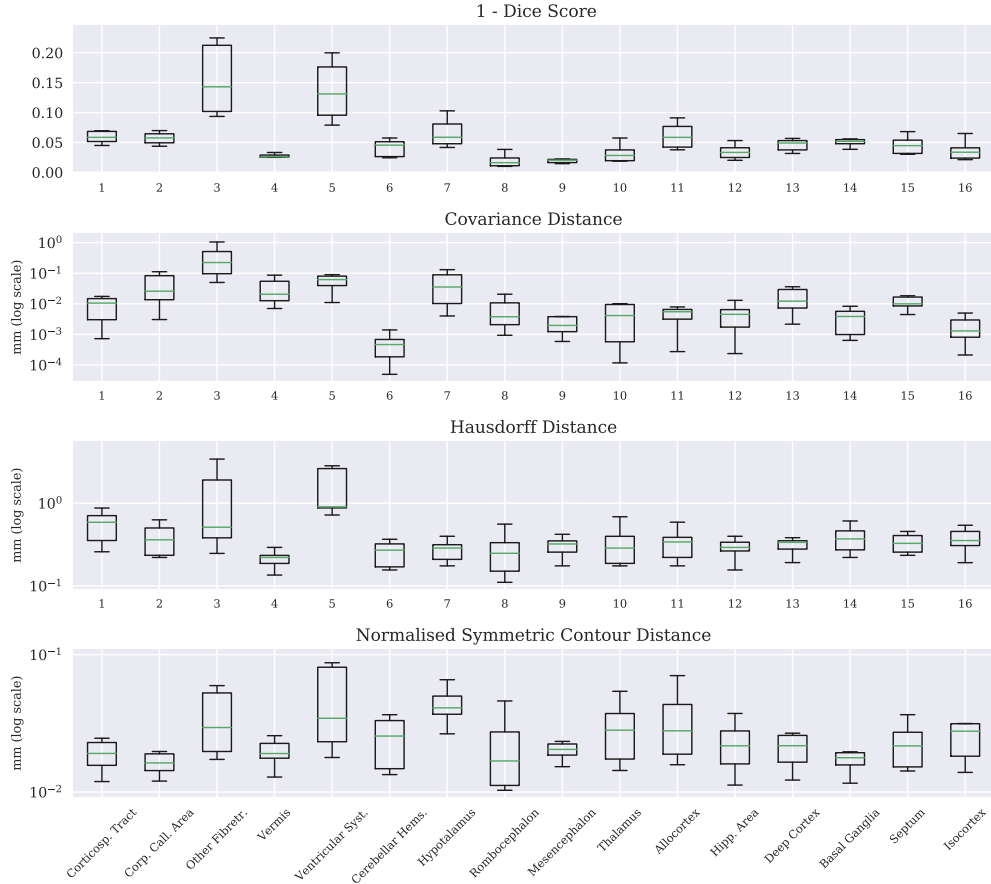


Figure 153-1: **Leave one out cross validation for the selected macro-regions.** Each point in the boxplot corresponds to the error at the given macro-region and for the given scoring system between the manual ground truth and the propagation of one of remaining 11 subjects. Differences between segmentations are scored with 1 - Dice score, covariance distance, Hausdorff distance and normalized symmetric contour distance, and the last three measures are plotted in log-scale. The correspondence between the x-axis and the macro-regions labels is reported in Table 146-1.

### 5.3.8 *In vivo* experiments

To provide an assessment of the quality of the proposed automatic method and to validate the feasibility on a different dataset further *in vivo* acquisitions were planned. Four neonatal rabbits underwent high resolution MRI with the protocol proposed in

## Chapter 3:

## ▷ Structural T1 weighted image acquisition:

MRI was performed on living animals under isoflurane anaesthesia using a Bruker Biospec 9.4 Tesla small animal MR scanner (Bruker Biospin, Ettlingen, Germany; horizontal bore, 20 cm) equipped with actively shielded gradients (600 mT/m) utilising a rat brain surface receiver decoupled to a volume quadrature transmit coil (internal diameter of 72mm). Field homogeneity was corrected using fieldmap correction (MAPSHIM protocol, Bruker Paravision 5.1). Anatomical reference was obtained through a 3D T2 weighted RARE sequences (TR/TE: 42/1000ms; RARE factor: 8; FOV:  $24 \times 30 \times 30$  mm; matrix for the first subject  $128 \times 128 \times 128$ . matrix for the remaining subjects:  $160 \times 192 \times 192$ ; acquisition time 19 min).

## ▷ Diffusion-weighted image acquisition:

Diffusion-weighted images (DWI) were acquired using a spin-echo version of the echo-planar imaging (SE-EPI) sequence with 4 segments; TE/TR: 27/5000ms; 2 averages; FOV:  $30 \times 30$  mm; matrix first subject:  $128 \times 128$ ; matrix remaining subjects:  $192 \times 192$ ; 20 axial slices of 1mm thickness with a 0.2mm gap; 6 directions and 4 B values (100, 500, 1000, 1500 s/mm<sup>2</sup>); acquisition time: 16 min.

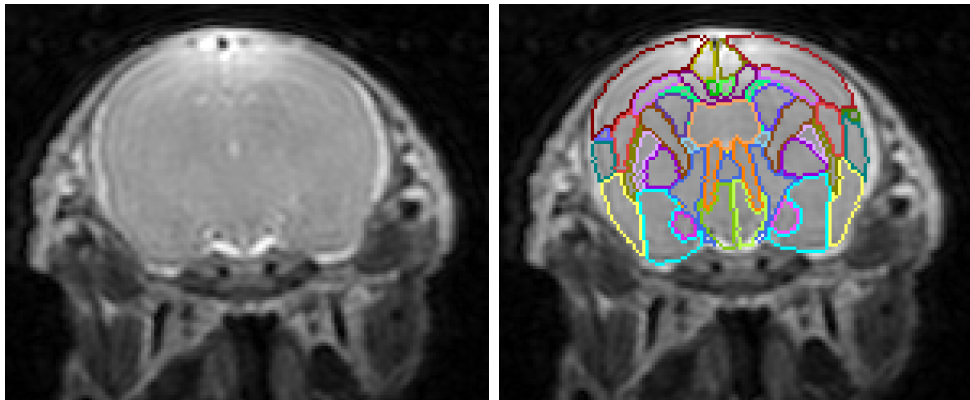


Figure 154-1: **In vivo experiment.** The result of the automatic algorithm tested on an *in vivo* acquisition. The subject, left in the original orientation, is provided with a visually good segmentation. In this setting, the multi-modal approach was not feasible due to the too low resolution of the diffusion weighted image.

As the resolution of the DWI resulted too low compared to the T1, it was not possible to obtain satisfactory results with the multi-modal approach described for the *ex vivo* example. The propagation was therefore based only on the T1 modalities. Moreover, the non-rigid bending energy parameter was increased from 0.5 of the *ex*

*in vivo* setting to 0.8 for the *in vivo*. The low resolution of the DWI made also difficult to quantify the quality of the segmentation alongside the borders that are visible only in the DWI-based modalities (FA, MD and V1).

Results are shown in coronal section in Figure 154-1 for one subject.. As no manual segmentation is available for this dataset, this experiment does not provide a numerical validation of the proposed method. Nonetheless, these preliminary segmentation may provide a valuable initialisation.

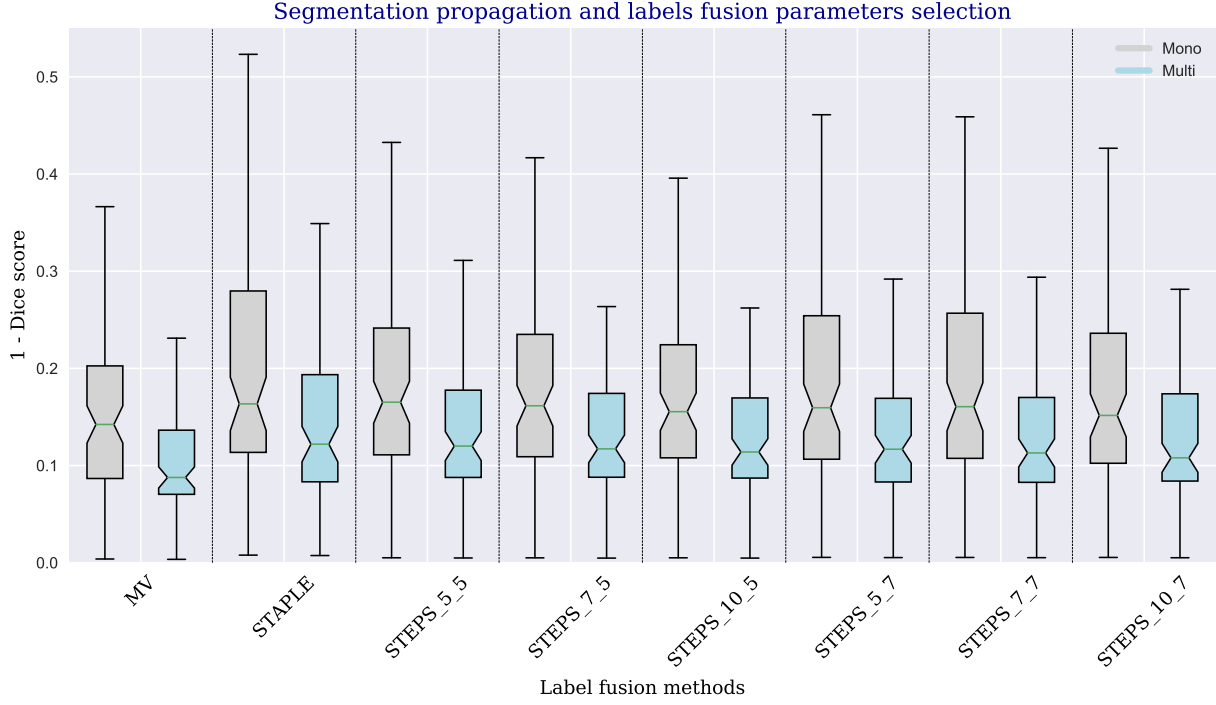


Figure 155-1: **Leave-one-out parametrisation benchmarking.** Comparison between majority voting (MV), STAPLE and STEPS with a range of parametrisations. STEPS\_K\_N represents the STEPS method for  $K = 5, 7, 10$  size of the kernel and  $N = 5, 7$  number of layers.

## 5.4 Parameters benchmarking: multi-modal versus uni-modal

The choice of alternating between manual adjustments and automatic segmentation propagations had revealed to be optimal to reduce the overall amount of manual work while keeping the segmentations quality under control.

During the multi atlas creation, a range of parameters for the registration and the label fusion had been tried and selected through visual scoring. In almost all cases the preferred label fusion method had been the majority voting for all three rounds,

with a multi-modal segmentation propagation and label fusion method, based on T1 and FA maps.

After the creation of the multi atlas, we eventually have a ground truth where to try new experiments on a wider range of parametrisation, as well as to challenge the real impact of the mono-modal and multi-modal registration.

In a leave-one-out experiment design for a randomly selected subject (subject 1702), we compare the automatic registration method using MV, STAPLE and STEPS, with a range of parametrisations (size of the kernel  $k = 5, 7, 10$  and number of layers  $n = 5, 7$ ) and for a segmentation propagation method with mono-modal registration (only the T1 map is considered) or multi-modal (the T1 and the the FA maps are considered).

Figure 155-1 reports in a boxplot the most relevant results of a series of experiments. Each box reports the inverted Dice score for all the 87 regions segmented. The lowest the values, the more accurate the segmentation respect to the ground truth. The variation of parameters within STEPS method had not provided visual improvements, also when considered with a wider range of parameters, not shown here for brevity. STAPLE has the worst performance, and MV the best one. In all cases the multi-modal overperforms the mono-modal.

The improvements in using the multi-modal approach, is a consequence of the fact that the manual adjustments had been performed comparing the overlay of a range of modalities. The fact that the majority voting is as well not surprising, as during the multi-atlas creation the MV had been the method that had consistently provided the best visual scoring, and had been chosen as starting points for each of the three iterative rounds.

## 5.5 Conclusions

In this chapter we addressed the problem of obtaining a reliable measurements of the images acquired with the protocol we established and presented in Chapter 3.

The first contribution is a novel method to compute the intra cranial volume of a dataset through a Bayesian model and a connected graph connecting the acquisitions weighted with the determinants of the affine registrations, presented in [IFM<sup>+</sup>17].

The second contribution is the introduction of the first multi-modal multi-atlas for the neonatal rabbit brain. The method is employed in analysing the produced dataset and will be employed for the acquisition planned at the moment of writing this thesis.

Preliminary results of the data analysis are provided in the next chapter.

## 5.6 Appendix: Newborn Rabbit Brain Taxonomy

Hierarchy	region	Abbreviation	Number
0	Brain [encephalon]	BR	
1	Cerebrum [cerebral hemispheres, endbrain, telencephalon]	CH / Tel	1
1.1	Cerebral cortex	Cx	2
1.1.1	Cortical Plate	Cxpl	3
1.1.1.1	Isocortex/neocortex		4
1.1.1.1.1	Prefrontal area	PFrA	5, 6
1.1.1.1.2	Frontal area	FrA	7, 8
1.1.1.1.3	Occipital area	OA	9, 10
1.1.1.1.4	Parietal area	PtA	11, 12
1.1.1.1.5	Temporal area	TeA	13, 14
1.1.1.1.6	Cingulate area	Cg	15, 16
1.1.1.1.7	Retrosplenial area	RS	17, 18
1.1.1.1.8	Insular area	Ins	19, 20
1.1.1.1.9	Ectorhinal area	Ect	21, 22
1.1.1.2	Allocortex		23
1.1.1.2.1.1	Olfactory lobe	OB	25, 26
1.1.1.2.1.2	Piriform	Pir	27, 28
1.1.1.3	Hippocampal formation	HF	29
1.1.1.3.1	Hippocampal area	HA	31, 32
1.1.1.3.1.1	Ammon's horn CA1 area	CA1	33, 34
1.1.1.3.1.2	Ammon's horn CA2 area	CA2	35, 36
1.1.1.3.1.3	Ammon's horn CA3 area	CA2	37, 38
1.1.1.3.1.4	Dentate Gyrus	DG	39, 40
1.1.1.3.2	Parahippocampal area	PHA	41, 42
1.1.1.3.2.1	Subiculum	S	43, 44
1.1.1.3.2.2	Entorhinal area	Ent	45, 46
1.1.1.3.2.3	Perirhinal area	PRh	47, 48
1.1.2	Cortical subplate, deep cortex	Cxsp	51
1.1.2.1	Clastrum	Cl	53, 54
1.1.2.2	Amygdala	Am	55, 56
1.2	Cerebral nuclei / basal ganglia	BG	65
1.2.1	Striatum	Str	67, 68
1.2.1.1	Caudate nucleus	CA CN	69, 70
1.2.1.2	Putamen	Pu	71, 72
1.2.2	Pallidum	Pa	73, 74

## 5.6. APPENDIX: NEWBORN RABBIT BRAIN TAXONOMY

1.2.2.1	Globus Pallidus	GP	75, 76
1.2.3	Basal forebrain	BF	77
1.2.4	Septum Area	SA	78
2	Brainstem		80
2.1	Interbrain [diencephalon]	IB / D	81
2.1.1	Thalamus	THA	83, 84
2.1.1.1	Epithalamus	EPI	85, 86
2.1.1.1.1	Pineal body	Pi	87, 88
2.1.1.1	Dorsal thalamus	DOR	89, 90
2.1.1.1.1	Anterior thalamic nuclei	AD	91, 92
2.1.1.1.2	Geniculate nuclei	GEN	93, 94
2.1.1.1.3	Intralaminar nuclei	ILM	95, 96
2.1.1.1.4	Lateral thalamic nuclei	LAT	97, 98
2.1.1.1.5	Medial thalamic nuclei	AM	99, 100
2.1.1.1.6	Midline thalamic nuclei	MID/MTN	101, 102
2.1.1.1.7	Ventral thalamic nuclei	VENT	103, 104
2.1.1.2	Ventral thalamus	VNT (VT)	105, 106
2.1.1.2.1	(Ventral lateral) Geniculate nuclei	LGv /GEN	107, 108
2.1.1.2.2	Reticular nuclei	RT	
2.1.2	Hypothalamus	HYP	109, 110
2.1.2.1	Periventricular zone	PVZ	111, 112
2.1.2.2	medial zone	MEZ	113, 114
2.1.2.2.1	Preoptic level	PRO	115, 116
2.1.2.2.2	Anterior level	ANT	117, 118
2.1.2.2.3	Tuberal level	TUB	119, 120
2.1.2.2.4	Mammillary body	MAM	121
2.1.2.3	Lateral zone	LZ	123, 124
2.2	Midbrain [mesencephalon]	MB	127
2.2.1	Pretectal region	PRT	129, 130
2.2.2	Tectum	TC	131, 132
2.2.2.1	Superior colliculus	SC	133, 134
2.2.2.2	Inferior colliculus	IC	135, 136
2.2.3	Tegmentum	TG	137, 138
2.2.3.1	Substantia nigra	SN	139, 140
2.2.3.2	Periaqueductal gray	PAG	141, 142
2.2.3.3	Ventral tegmental area	VTA	143, 144
2.2.3.4	Red nucleus	RN	145, 146
2.2.3.5	Reticular formation		147, 148

2.3	Hindbrain [rhombencephalon]	HB	149
2.3.1	Pons [metencephalon]	PO	151
2.3.2	Medulla [myelencephalon]	MY	153
3	Cerebellum (parencephalon)	Cb	158
3.1	Cerebellar cortex	Cbx	159, 160
3.1.1	Vermal Regions	VERM	161
3.1.1.1	Lingula	LING	163, 164
3.1.1.2	Central lobe	CENT	165, 166
3.1.1.3	Culmen	CUL	167, 168
3.1.1.4	Declive	DEC	169, 170
3.1.1.5	Folium-tuber vermis	FOTU	171, 172
3.1.1.6	Pyramus	PYR	173, 174
3.1.1.7	Uvula	UVU	175, 176
3.1.1.8	Nodulus	NOD	177, 178
3.1.2	Hemispheric Regions	HEM	179, 180
3.1.2.1	Simple lobe	SIM	181, 182
3.1.2.2	Ansiform lobe	AN	183, 184
3.1.1.1	Paramedian lobe	PRM	185, 186
3.1.1.2	Copula pyramidis	COPY	187, 188
3.1.1.3	Paraflocculus	PFL	189, 190
3.1.1.4	Flocculus	FL	191, 192
3.2	Cerebellar nuclei	CBN	193, 194
3.2.1.1	Fastigial nucleus	FN	195, 196
3.2.1.2	Interposed nucleus	IP	197, 198
3.2.1.3	Dentate nucleus	DN	199, 200
4	Ventricular system	VS	201
4.1	Interventricular foramen	IVF	202
4.2	Lateral ventricle	LV	203, 204
4.3	Third ventricle	3V	205
4.4	Cerebral aqueduct	Aq	206
4.5	Fourth ventricle	4V	207
4.6	Central canal	CC	208
4.7	Choroid plexus	chp	209
4.8	Velum interpositum / superior medullary velum	VIP/SMV	210
4.9	Periventricular area	PV	211, 212
5	Fiber tracts:		213
5.1	Cranial nerves		214
5.1.1	Optic tract and optic chiasm	OT	215

5.1.2	Lateral olfactory tract	lo	216
5.2	Lateral forebrain bundle system		217
5.2.1	Corpus callosum	cc	218
5.2.2	External capsule	ec	219, 220
5.2.3	Corticospinal tract		221, 222
5.2.3.1	Internal capsule	int	223, 224
5.2.3.2	Corona radiata	cr	225, 226
5.2.3.3	Cerebral peduncle	cp	227, 228
5.2.3.4	Subcortical white matter	swm	229, 230
5.3	Medial forebrain bundle system		231
5.3.1	Anterior commissure	ac	233
5.3.2	Fornix system	fxs	235, 236
5.3.2.1	Hippocampal commissure	hc	237
5.3.2.2	Fimbria of hippocampus	fi	239, 240
5.3.2.3	Columns of the fornix	fx	241, 242
5.3.3	Stria terminals	st	243, 244
5.4	Hypothalamus related		245
5.4.1	Mammillothalamic tract	mt	247, 248
5.4.2	Stria medullaris	sm	249, 250
5.4.3	Fasciculus tetroflexus	fr	251, 252
5.4.4	Posterior commissure	pc	253

Table 159-0: **Newborn rabbit brain hierarchical taxonomy**, with abbreviation and numbering including the 89 regions proposed in the multi-atlas.

## Chapter bibliography

- [ACPA06] Vincent Arsigny, Olivier Commowick, Xavier Pennec, and Nicholas Ayache. A log-euclidean framework for statistics on diffeomorphisms. In *Medical Image Computing and Computer-Assisted Intervention–MICCAI 2006*, pages 924–931. Springer, 2006.
- [AF05] John Ashburner and Karl J Friston. Unified segmentation. *Neuroimage*, 26(3):839–851, 2005.
- [AHH<sup>+</sup>09] Paul Aljabar, Rolf A Heckemann, Alexander Hammers, Joseph V Hajnal, and Daniel Rueckert. Multi-atlas based segmentation of brain images: atlas selection and its effect on accuracy. *Neuroimage*, 46(3):726–738, 2009.

- [BCW<sup>+</sup>18] Irene Brusini, Miguel Carneiro, Chunliang Wang, Carl-Johan Rubin, Henrik Ring, Sandra Afonso, José A Blanco-Aguilar, Nuno Ferland, Nima Rafati, Rafael Villafuerte, et al. Changes in brain architecture are consistent with altered fear processing in domestic rabbits. *Proceedings of the National Academy of Sciences*, page 201801024, 2018.
- [BMMAP<sup>+</sup>14] Dafnis Batalle, Emma Muñoz-Moreno, Ariadna Arbat-Plana, Miriam Illa, Francesc Figueras, Elisenda Eixarch, and Eduard Gratacos. Long-term reorganization of structural brain networks in a rabbit model of intrauterine growth restriction. *Neuroimage*, 100:24–38, 2014.
- [CCMO12] MJ Cardoso, MJ Clarkson, M Modat, and S Ourselin. Niftyseg: open-source software for medical image segmentation, label fusion and cortical thickness estimation. In *IEEE International Symposium on Biomedical Imaging, Barcelona, Spain*, 2012.
- [CLM<sup>+</sup>13] M Jorge Cardoso, Kelvin Leung, Marc Modat, Shiva Keihaninejad, David Cash, Josephine Barnes, Nick C Fox, Sebastien Ourselin, Alzheimer’s Disease Neuroimaging Initiative, et al. STEPS: Similarity and Truth Estimation for Propagated Segmentations and its application to hippocampal segmentation and brain parcellation. *Medical image analysis*, 17(6):671–684, 2013.
- [DDJT07] Matthew Derrick, Alexander Drobyshevsky, Xinhai Ji, and Sidhartha Tan. A model of cerebral palsy from fetal hypoxia-ischemia. *Stroke*, 38(2):731–735, 2007.
- [DDL<sup>+</sup>12] Alexander Drobyshevsky, Matthew Derrick, Kehuan Luo, Li-Qun Zhang, Yi-Ning Wu, Silvia Honda Takada, Lei Yu, and Sidhartha Tan. Near-Term Fetal Hypoxia-Ischemia in Rabbits. *Stroke*, 43(10):2757–2763, 2012.
- [DQ17] Alexander Drobyshevsky and Katharina A Quinlan. Spinal cord injury in hypertonic newborns after antenatal hypoxia-ischemia in a rabbit model of cerebral palsy. *Experimental neurology*, 293:13–26, 2017.
- [EBI<sup>+</sup>12] Elisenda Eixarch, Dafnis Batalle, Miriam Illa, Emma Muñoz-Moreno, Ariadna Arbat-Plana, Ivan Amat-Roldan, Francesc

Figueras, and Eduard Gratacos. Neonatal neurobehavior and diffusion mri changes in brain reorganization due to intrauterine growth restriction in a rabbit model. *PLoS One*, 7(2):e31497, 2012.

- [FSM<sup>+</sup>17] Sebastiano Ferraris, Dzhoshkun Ismail Shakir, Johannes Van Der Merwe, Willy Gsell, Jan Deprest, and Tom Vercauteren. Bruker2nifti: Magnetic Resonance Images converter from Bruker ParaVision to Nifti format. *The Journal of Open Source Software*, 2(16), Aug 2017.
- [FvdMVDV<sup>+</sup>18] Sebastiano Ferraris, Johannes van der Merwe, Lennart Van Der Veeken, Ferran Prados, Juan-Eugenio Iglesias, Andrew Melbourne, Marco Lorenzi, Marc Modat, Willy Gsell, Jan Deprest, and Tom Vercauteren. A magnetic resonance multi-atlas for the neonatal rabbit brain. *NeuroImage*, 2018.
- [GLS<sup>+</sup>18] Eli Gibson, Wenqi Li, Carole Sudre, Lucas Fidon, Dzhoshkun I Shakir, Guotai Wang, Zach Eaton-Rosen, Robert Gray, Tom Doel, Yipeng Hu, et al. Niftynet: a deep-learning platform for medical imaging. *Computer methods and programs in biomedicine*, 158:113–122, 2018.
- [HBL12] Ray Hashman Hashemi, William G Bradley, and Christopher J Lisanti. *MRI: The Basics: The Basics*. Lippincott Williams & Wilkins, 2012.
- [HCOB05] Markus Herdin, Nicolai Czink, Hüseyin Ozcelik, and Ernst Bonek. Correlation matrix distance, a meaningful measure for evaluation of non-stationary mimo channels. In *Vehicular Technology Conference, 2005. VTC 2005-Spring. 2005 IEEE 61st*, volume 1, pages 136–140. IEEE, 2005.
- [HHA<sup>+</sup>06] Rolf A Heckemann, Joseph V Hajnal, Paul Aljabar, Daniel Rueckert, and Alexander Hammers. Automatic anatomical brain mri segmentation combining label propagation and decision fusion. *NeuroImage*, 33(1):115–126, 2006.
- [IFM<sup>+</sup>17] Juan Eugenio Iglesias, Sebastiano Ferraris, Marc Modat, Willy Gsell, Jan Deprest, Johannes L van der Merwe, and Tom Vercauteren. Template-free estimation of intracranial volume: A preterm birth animal model study. In *Fetal, Infant and Ophthalmic Medical Image Analysis*, pages 3–13. Springer, 2017.

- [IS15] Juan Eugenio Iglesias and Mert R Sabuncu. Multi-atlas segmentation of biomedical images: a survey. *Medical image analysis*, 24(1):205–219, 2015.
- [JBB<sup>+</sup>12] Mark Jenkinson, Christian F Beckmann, Timothy EJ Behrens, Mark W Woolrich, and Stephen M Smith. Fsl. *Neuroimage*, 62(2):782–790, 2012.
- [JCF<sup>+</sup>02] G Allan Johnson, Gary P Cofer, Boma Fubara, Sally L Gewalt, Laurence W Hedlund, and Robert R Maronpot. Magnetic resonance histology for morphologic phenotyping. *Journal of Magnetic Resonance Imaging*, 16(4):423–429, 2002.
- [K<sup>+</sup>95] Ron Kohavi et al. A study of cross-validation and bootstrap for accuracy estimation and model selection. In *Ijcai*, volume 14-2, pages 1137–1145. Stanford, CA, 1995.
- [KPV14] Ron Kikinis, Steve D Pieper, and Kirby G Vosburgh. 3d slicer: a platform for subject-specific image analysis, visualization, and clinical support. In *Intraoperative imaging and image-guided therapy*, pages 277–289. Springer, 2014.
- [KRB<sup>+</sup>17] Lisa M Koch, Martin Rajchl, Wenjia Bai, Christian F Baumgartner, Tong Tong, Jonathan Passerat-Palmbach, Paul Aljabar, and Daniel Rueckert. Multi-atlas segmentation using partially annotated data: Methods and annotation strategies. *IEEE Transactions on Pattern Analysis and Machine Intelligence*, 2017.
- [LKB<sup>+</sup>17] Geert Litjens, Thijs Kooi, Babak Ehteshami Bejnordi, Arnaud Arindra Adiyoso Setio, Francesco Ciompi, Mohsen Ghafoorian, Jeroen AWM van der Laak, Bram Van Ginneken, and Clara I Sánchez. A survey on deep learning in medical image analysis. *Medical image analysis*, 42:60–88, 2017.
- [LRM<sup>+</sup>17] Jun Lei, Jason M Rosenzweig, Manoj K Mishra, Wael Alshehri, Flavia Brancusi, Mike McLane, Ahmad Almalki, Rudhab Bahabry, Hattan Arif, Rayyan Rozzah, et al. Maternal dendrimer-based therapy for inflammation-induced preterm birth and perinatal brain injury. *Scientific Reports*, 7(1):6106, 2017.
- [LTC<sup>+</sup>15] Seong Yong Lim, Yeu-Sheng Tyan, Yi-Ping Chao, Fang-Yu Nien, and Jun-Cheng Weng. New insights into the developing rabbit brain

- using diffusion tensor tractography and generalized q-sampling mri. *PloS one*, 10(3):e0119932, 2015.
- [MAS<sup>+</sup>15] Désirée Müllhaupt, Heinz Augsburger, Andrea Schwarz, Gregor Fischer, Patrick Kircher, Jean-Michel Hatt, and Stefanie Ohlerth. Magnetic resonance imaging anatomy of the rabbit brain at 3 t. *Acta Veterinaria Scandinavica*, 57(1):1, 2015.
- [MCD<sup>+</sup>14] Marc Modat, David M Cash, Pankaj Daga, Gavin P Winston, John S Duncan, and Sébastien Ourselin. Global image registration using a symmetric block-matching approach. *Journal of Medical Imaging*, 1(2):024003, 2014.
- [MDC<sup>+</sup>12] Marc Modat, Pankaj Daga, M Jorge Cardoso, Sebastien Ourselin, Gerard R Ridgway, and John Ashburner. Parametric non-rigid registration using a stationary velocity field. In *Mathematical Methods in Biomedical Image Analysis (MMBIA), 2012 IEEE Workshop on*, pages 145–150. IEEE, 2012.
- [MERDV<sup>+</sup>14] Andrew Melbourne, Zach Eaton-Rosen, Enrico De Vita, Alan Bainbridge, Manuel Jorge Cardoso, David Price, Ernest Cady, Giles S Kendall, Nicola J Robertson, Neil Marlow, et al. Multi-modal measurement of the myelin-to-axon diameter g-ratio in preterm-born neonates and adult controls. In *International Conference on Medical Image Computing and Computer-Assisted Intervention*, pages 268–275. Springer, 2014.
- [MGD<sup>+</sup>17] Matteo Mancini, Giovanni Giulietti, Nicholas Dowell, Barbara Spanò, Neil Harrison, Marco Bozzali, and Mara Cercignani. Introducing axonal myelination in connectomics: A preliminary analysis of g-ratio distribution in healthy subjects. *NeuroImage*, 2017.
- [MMAPB<sup>+</sup>13] Emma Muñoz-Moreno, Ariadna Arbat-Plana, Dafnis Batalle, Guadalupe Soria, Miriam Illa, Alberto Prats-Galino, Elisenda Eixarch, and Eduard Gratacos. A magnetic resonance image based atlas of the rabbit brain for automatic parcellation. *PloS one*, 8(7):e67418, 2013.
- [MRT<sup>+</sup>10] Marc Modat, Gerard R Ridgway, Zeike A Taylor, Manja Lehmann, Josephine Barnes, David J Hawkes, Nick C Fox, and Sébastien Ourselin. Fast free-form deformation using graphics processing units. *Computer methods and programs in biomedicine*, 98(3):278–284, 2010.

- [MTE<sup>+</sup>95] John C Mazziotta, Arthur W Toga, Alan Evans, Peter Fox, and Jack Lancaster. A probabilistic atlas of the human brain: Theory and rationale for its development: The international consortium for brain mapping (icbm). *Neuroimage*, 2(2):89–101, 1995.
- [PG07] Watson Charles Paxinos George. Paxinos & Watson the Rat Brain in Stereotaxic Coordinates. *Elsevier*, 2007.
- [PXP00] Dzung L Pham, Chenyang Xu, and Jerry L Prince. Current methods in medical image segmentation. *Annual review of biomedical engineering*, 2(1):315–337, 2000.
- [REC<sup>+</sup>17] M.B.M. Ranzini, M. Ebner, M.J. Cardoso, Fotiadou A., T. Vercauteren, J. Henckel, A. Hart, S. Ourselin, and M. Modat. Joint Multimodal Segmentation of Clinical CT and MR from Hip Arthroplasty Patients. In B. Glocker, J. Yao, T. Vrtovec, A.F. Frangi, and G. Zheng, editors, *MICCAI workshop on Computational Methods and Clinical Applications in Musculoskeletal Imaging (MSKI 2017)*, pages 69–81, 2017.
- [Sen01] RN Sener. Diffusion mri: apparent diffusion coefficient (adc) values in the normal brain and a classification of brain disorders based on adc values. *Computerized medical imaging and graphics*, 25(4):299–326, 2001.
- [SMMC<sup>+</sup>15] Rui V Simões, Emma Muñoz-Moreno, Rodrigo J Carbajo, Anna González-Tendero, Miriam Illa, Magdalena Sanz-Cortés, Antonio Pineda-Lucena, and Eduard Gratacós. In vivo detection of perinatal brain metabolite changes in a rabbit model of intrauterine growth restriction (iugr). *PloS one*, 10(7):e0131310, 2015.
- [Swa04] Larry W Swanson. *Brain maps III: structure of the rat brain: an atlas with printed and electronic templates for data, models, and schematics*. Gulf Professional Publishing, 2004.
- [SWW86] Judy W Shek, Guang Y Wen, and Henryk M Wisniewski. *Atlas of the rabbit brain and spinal cord*. S Karger Pub, 1986.
- [SYVL<sup>+</sup>10] Mert R Sabuncu, BT Thomas Yeo, Koen Van Leemput, Bruce Fischl, and Polina Golland. A generative model for image segmentation based on label fusion. *IEEE transactions on medical imaging*, 29(10):1714–1729, 2010.

- [TAC<sup>+</sup>10] Nicholas J Tustison, Brian B Avants, Philip A Cook, Yuanjie Zheng, Alexander Egan, Paul A Yushkevich, and James C Gee. N4itk: improved n3 bias correction. *IEEE transactions on medical imaging*, 29(6):1310–1320, 2010.
- [TCC12] J-Donald Tournier, Fernando Calamante, and Alan Connelly. Mr-trix: diffusion tractography in crossing fiber regions. *International Journal of Imaging Systems and Technology*, 22(1):53–66, 2012.
- [TDJ<sup>+</sup>05] Sidhartha Tan, Alexander Drobyshevsky, Tamas Jilling, Xinhai Ji, Lauren M Ullman, Ila Englof, and Matthew Derrick. Model of cerebral palsy in the perinatal rabbit. *Journal of child neurology*, 20(12):972–979, 2005.
- [TH15] Abdel Aziz Taha and Allan Hanbury. Metrics for evaluating 3d medical image segmentation: analysis, selection, and tool. *BMC medical imaging*, 15(1):29, 2015.
- [VLMVS99] Koen Van Leemput, Frederik Maes, Dirk Vandermeulen, and Paul Suetens. Automated model-based tissue classification of mr images of the brain. *IEEE transactions on medical imaging*, 18(10):897–908, 1999.
- [VPPA07] Tom Vercauteren, Xavier Pennec, Aymeric Perchant, and Nicholas Ayache. Non-parametric diffeomorphic image registration with the demons algorithm. In *Medical Image Computing and Computer-Assisted Intervention–MICCAI 2007*, pages 319–326. Springer, 2007.
- [WGKJ96] William M Wells, W Eric L Grimson, Ron Kikinis, and Ferenc A Jolesz. Adaptive segmentation of mri data. *IEEE transactions on medical imaging*, 15(4):429–442, 1996.
- [WZW04] Simon K Warfield, Kelly H Zou, and William M Wells. Simultaneous truth and performance level estimation (staple): an algorithm for the validation of image segmentation. *IEEE transactions on medical imaging*, 23(7):903–921, 2004.
- [YPH<sup>+</sup>06] Paul A Yushkevich, Joseph Piven, Heather Cody Hazlett, Rachel Gimpel Smith, Sean Ho, James C Gee, and Guido Gerig. User-guided 3d active contour segmentation of anatomical structures: significantly improved efficiency and reliability. *Neuroimage*, 31(3):1116–1128, 2006.

- [ZSWKA12] Hui Zhang, Torben Schneider, Claudia A Wheeler-Kingshott, and Daniel C Alexander. Noddi: practical in vivo neurite orientation dispersion and density imaging of the human brain. *Neuroimage*, 61(4):1000–1016, 2012.



## Chapter 6

# Newborn rabbit brain data analysis

### Contents

---

<b>6.1</b>	<b>Pre-clinical trial data analysis aims . . . . .</b>	<b>169</b>
<b>6.2</b>	<b>Bruker2nifti and NiLabels . . . . .</b>	<b>170</b>
<b>6.3</b>	<b>Data collection pipeline . . . . .</b>	<b>173</b>
<b>6.4</b>	<b>Exploratory Data analysis . . . . .</b>	<b>175</b>
6.4.1	Statistical model: from theory to practice . . . . .	175
6.4.2	Full brain volume differences: are the results due to chance? . . . . .	177
6.4.3	Region-wise volume outcome . . . . .	180
6.4.4	Region-wise fractional anisotropy . . . . .	181
6.4.5	Region-wise mean diffusivity . . . . .	181
<b>6.5</b>	<b>Conclusions . . . . .</b>	<b>183</b>

---

### 6.1 Pre-clinical trial data analysis aims

In this chapter we introduce the initial results of the customary MRI biomarkers: Volume, FA and MD for the subjects acquired at the moment of writing the thesis, and automatically segmented with the method proposed in Chapter 5 for the pre-clinical study introduced in Chapter 3, to address the clinical question presented in Chapter 2.

Before detailing the results, both as methodology and as code documentation, in the next section we present two open source Python software packages. With the automatic method for segmentation propagation they constitute the building blocks of the pipeline developed for the data analysis, presented in Section 6.3.

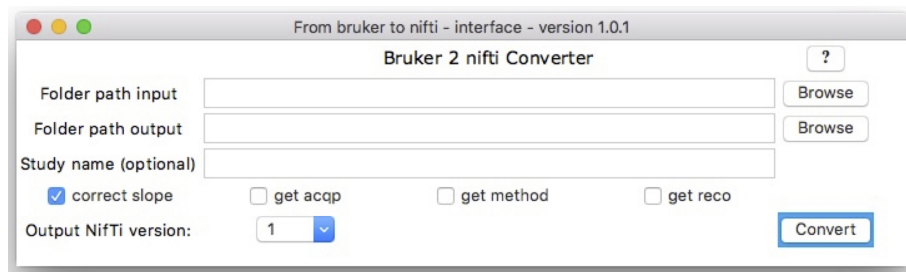


Figure 169-1: **Bruker2nifti converter interface.** Code documentation can be found at the git-hub page provided in the publication [FSM<sup>+</sup>17].

## 6.2 Bruker2nifti and NiLabels

Erickson et al. concluded their paper *Imaging in clinical trials* [EB07] advocating for a standardisation of format acquisitions. The DICOM format is considered one of the standards to connect the clinical and the research world [MEM02]. DICOM is meant to be a flexible format, able to cope with the wide range of needs arising in practice, the increasing tools clinicians are offered by private companies and the variety of imaging modality not only including MR but also CT and other X-Ray scanners.

The consequence of the need for flexibility within a standardised format is that there are several DICOM standards. Most of the time the tools developed to cope with the DICOM format provided by a producer have poor outcomes if applied to DICOM format produced by another one.

For example the *mrconvert* converter from the software package *mrtrix* [TCC12] has optimal performance with DICOM-Siemens, but can not cope with DICOM produced by Bruker scanner that we are interested to analyse.

Moreover, all available converters from Bruker format have been developed to convert data acquired with ParaVision version 5. During the study, the update to ParaVision version 6 made these converter unusable for our scope.

For this reason, and to gain a tool to parse and convert the native Bruker format, part of the project was to develop a converter from the Bruker format to Nifti, the standard format for neuroimaing research [Cox04], bypassing any conversion to the DICOM format.

The resulting converter, called *bruker2nifti*, is equipped with a command line interface and a graphical user interface, shown in Figure 169-1. The access to the GUI interface does not require any programming knowledge, making the converter a tool for any user. It was open-sourced and published on the Journal of Open Source Software [FSM<sup>+</sup>17]. The software can be further customised to access other structure of the Bruker file structure, such as the FID file, where the  $k$ -space information is stored, as well as to convert the results in other formats than Nifti.

The second open source contribution, *NiLabels*, is a collection of tools to automatise simple manipulations and measurements of medical images and segmentations in Nifti format. It is mainly based on the python package Numpy and Nibabel and it is based on a facade design pattern to access the core methods.

The need of adding another software tool, is that to apply a developed algorithm to a set of images is a very common task usually involving this sequence of operations:

1. Loading the image with nibabel.
2. Extract the header or the data.
3. Apply the selected algorithm.
4. Create a new instance of the modified nifti image.
5. Save it to file.

*NiLabels* is aimed at reducing these steps in a single command, allowing to have as input and output directly the path to the input and output image. The facade access the underpinning algorithm providing directly the path to the input image, and the unit-testing are implemented for the underpinning algorithm.

*NiLabels* (version 0.0.2) can:

- ▷ Check if there are missing labels in a segmentation and returns a report with the number of connected components per label.
- ▷ Get the stacks of 4d images so that they are predisposed for label fusion algorithms (using for example *niftySeg* for the label fusion).
- ▷ Quickly manipulate the components of the header, applying rotations respect to the center of the image or the origin, change the datatype or the translational part.
- ▷ Normalise the intensities of an image given the values below a list of labels of a segmentation, getting the contour of a segmentation, and produce graftings between segmentations.
- ▷ Relabel a segmentation given the list of old and the corresponding new labels, permute labels according to a given permutation, keep only one label and assign all the others the same value, get the probabilistic prior from a stack of segmentations.
- ▷ Clean a segmentation leaving only a pre-defined number of connected components for each label and merges the extra components with the closest label.

- ▷ Compute volumes per label of a segmentations.
- ▷ Compute distances between segmentations, such as the dice score, covariance distance, Hausdorff distance and normalised symmetric contour distance.
- ▷ Get all the voxel values below a specified label of a segmentation from the underpinning anatomical image (FA, MD...).
- ▷ Manipulate the shape of the volume of an image, extending a slice an new dimension, splitting the labels in a 4d image and merge it back, and cut each slice of a 4d volume for a given 3d binary compatible segmentation.
- ▷ Symmetrize a segmentation with respect to a plane (with and without rigid registration based on an underpinning anatomy).

Bruker2nifti and NiLabels are components of the pipeline presented below, aimed at processing and analysing the data.

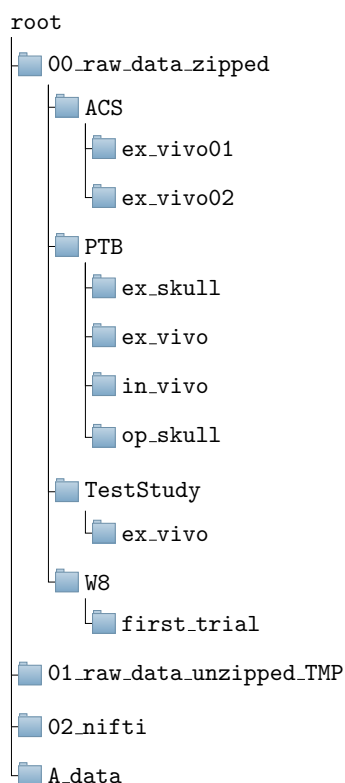


Figure 172-1: **Data folder structure.** From the root folder, each subfolder group is named *phase* (00\_raw\_data\_zipped, 01\_raw\_data\_unzipped\_TMP ...), *study* (ACS, PTB ...) and *category* (ex\_vivo01, ex\_skull ...). Nomenclatures for *study* and *category* are the same for each *phase*.

### 6.3 Data collection pipeline

Figure 173-1 provides an overview of the image analysis pipeline. The pipeline is open-sourced and can be found at <https://github.com/gift-surg/RabbitBrainAnalysis>. It is used to provide the clinicians the readouts of the selected biomarkers, and it constitutes the starting point for the research of future biomarkers, as introduced in Chapter 5. Moreover it will be utilised for the analysis of the upcoming acquisitions.

The folder structure on the Network Attached Storage (NAS) where the files are stored, are is divided in 4 subfolders, as shown in Figure 172-1:

- ▷ **00\_raw\_data\_zipped**: contains the zipped Bruker raw data, divided by *study*: ACS, PTB, W8 (temporary name for the recent 8 weeks acquisitions) and **TestStudy** for the test acquisitions and *category*: **ex\_vivo01** for the 0.1 mg ACS administration and **ex\_vivo01** for the 0.2 mg, **ex\_skull** for the acquisitions of samples outside the skulls, **op\_skull** for the acquisitions with the transcranial perfusion or open skull. Each other folder in the root has the same substructure folder. Each sample has a unique identifier number associated to a database entry, specifying the study and category of belonging, amongs other parameters.
- ▷ **01\_raw\_data\_unzipped\_TMP**: temporary folder where the raw Bruker files are unzipped before the nifti conversion. The unzipped files are systematically erased after the conversion.
- ▷ **02\_nifti**: folder storing the files converted into the nifti format. No other pre-processing than the conversion is performed.
- ▷ **A\_data**: folder with the elaboration of the samples retrieved from **02\_nifti**. Here samples undergo most of the image processing and biomarker extraction. After the processing each subject folder contains a folder called **report** with the outcomes of the biomarker extractions.

Throughout the structure, temporary files created for intermediate steps are stored into folders with **z\_** as suffix.

Steps involved in the pipeline are:

1. Store the downloaded file (e.g. **HVDM\_\_13111\_31052018\_1\_1.zip**) of the latest acquisition in zip format on the NAS, in the correct folder of the folder structure, and renaming it to **13111.zip**.
2. Update the text-file **data\_received\_2018.txt** with the original filename, date of download and laboratory notes received within the file.

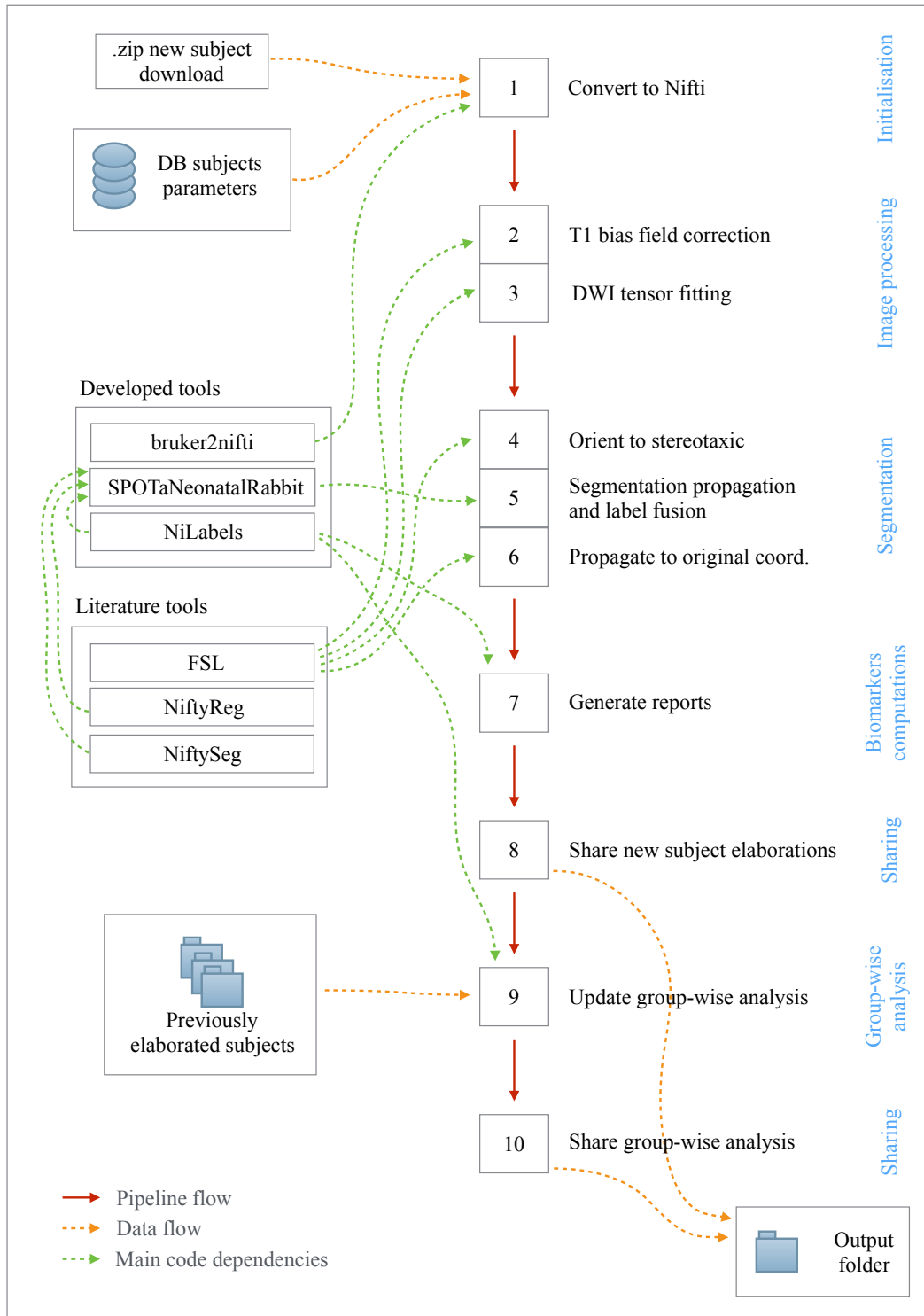


Figure 173-1: **Schematic representation of the full data analysis pipeline.** Pipeline is divided in 10 phases. Developed and open sourced underpinning tools are *bruker2nifti*, *NiLabels* and *SpotANeonatalRabbit*. The central column represents the stages of the pipeline, named in blue on the right, the left column the data input and software and the lower right object the output location.

3. Update the database with the parameters with the new subjects and with the default parameters related to its *study* and *category*.
4. Run the conversion step and visually assess the results stored in `02_nifti`. If required update manually the parameters of the entry database. There parameters may occasionally require further manual adjustments, although this is seldom required. As the study is moving forwards and the outcome of the scanning section is reaching standard uniformity in the quality, the default parameters produces good final results.
5. Run the second part of the pipeline, involving image processing, automatic segmentation and biomarker extraction. This part of the pipeline sends automatically the processed data (oriented, bias field corrected and segmented T1, MSME-T2 and DTI-based modalities, outcome of the statistical analysis) to a Dropbox shared folder with the other members of the study.

## 6.4 Exploratory Data analysis

In this section we provide the preliminary results of the MRI analysis. Subjects involved in the study are the ones acquired at the moment of writing the thesis. We also provide only the outcomes of the MRI study, leaving to [vdMvdVF<sup>+</sup>19] the outcomes of neurobehavioural assessments and histology and its comparison with the MRI data analysis.

As reported in Figure 57-1, we examine the outcomes of the 4 datasets presented in Section 3.2: Term or control (T), pre-term (PT), late pre-term (LPT) and late pre term with administration of antenatal corticosteroids (LPT+).

At the moment of writing this thesis, we collected 11 Term subjects, 14 pre-term subjects, 6 late pre-term and 11 late pre-term with steroids. The number of samples for each dataset provides the input for a preliminary investigation for future studies.

In the next sections we introduce the selected statistical model, and the subsequent data analysis for the volume, the fractional anisotropy (FA) and the mean diffusivity (MD)

### 6.4.1 Statistical model: from theory to practice

To provide a level of statistical significance as unbiased as possible, every study should integrate the statistical analysis as part of the experiment design before starting the acquisition. Reasonable controversies can arise from studies whose statistical analysis had been chosen after looking at the data, as the choice can be biased by the results one wants to obtain.

Three factors among the four *sample size*, *level of significance*, *effect size* and *statistical power* should be established in advance, and the fourth one obtained from the first three and from the selected statistical model. During the data acquisitions, the study should rigorously be bounded by the selected factors, and the consequent conclusions should be limited only to the initially established statistics.

This ideal setting is often not practical in reality. The study presented in this thesis had been the first MRI study performed on newborn rabbit brains, therefore the effect size, as well as the brain location of the possible damage and the biomarkers had to be considered as part of a wider exploratory study rather than as a single statistical hypothesis. As for the level of significance, strictly related to the sample size and the statistical power, could not be established in advance due to the mortality rate (see Figure 136-1) invalidating artefacts (see Appendix 3.5) and general impossibility of selecting a statistical model due to lack of preliminary information about the distribution of any of the involved biomarkers.

Manually discarding the faulty acquisitions while establishing the protocol, as performed in the presented study, it may not be acceptable during a controlled statistical trial. Nonetheless the data obtained from the viable acquisitions had provided important insights that would provide a qualitative starting point for future studies, as well as supportive evidence for the hypothesis testing performed in the concomitant neurobehavioural assessment and the histological analysis.

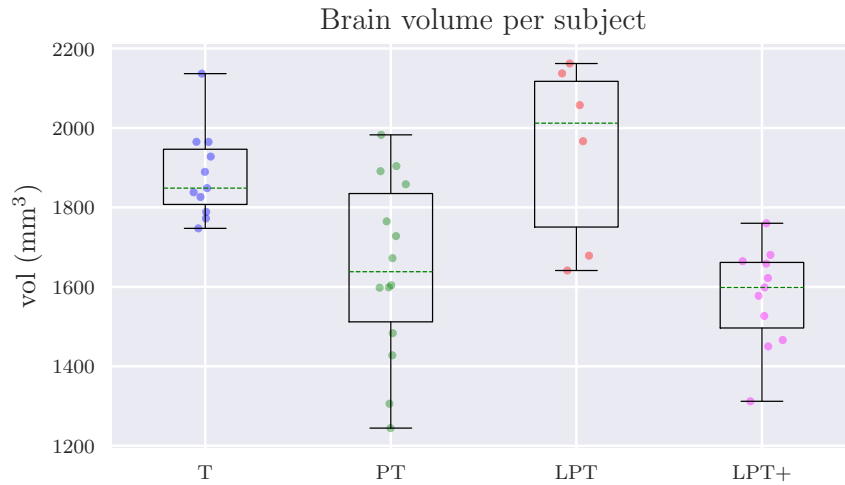


Figure 176-1: **Brain volume per subject.** Preliminary results for the on-going study shows different distributions in the brain volumes for term (T), pre-term (PT), late pre-term (LPT) and late pre-term with administration of corticosteroids (LPT+). Numbers are not providing statistically significant conclusions, although visually the group with the lowest brain volume appears to be the one of the fourth group.

To investigate the data obtained with the pipeline presented in the previous sec-

tions, we employed a bootstrapping critical value method based on the Pearson correlation coefficient. The bootstrapping critical value method is particularly suited when comparing different groups of small datasets, and is preferred to the traditional statistical methods when computational power is available. Among others, this method had been advocated by Horowitz et al. [Hor94], Hall et al. [HH96] and Hongyi et al. [HLM96].

#### 6.4.2 Full brain volume differences: are the results due to chance?

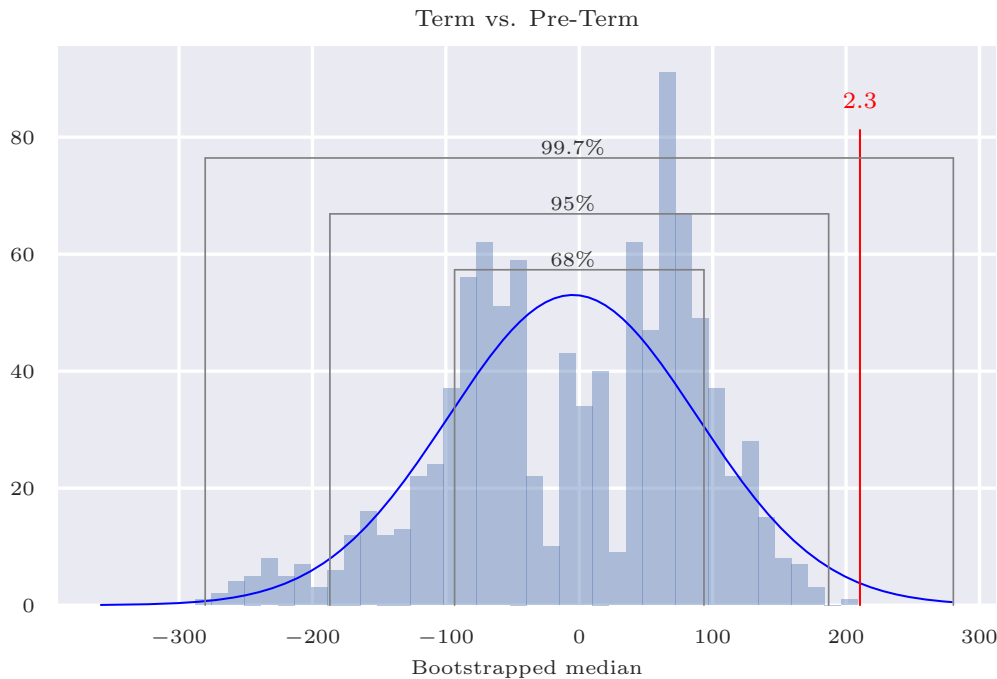


Figure 177-1: **Chance model for the median volume to compare the rabbit full brain volume of term and pre-term.** The difference of the median between group T and group PT observed in Figure 176-1 is significant respect to the chance model of median of the bootstrapped volumes, for a Pearson correlation coefficient of 2.3.

The boxplots of the full brain volume per subjects divided by groups is shown in Figure 176-1. The first thing to be noticed from this figure is the brain volume variability, that appears to be consistent with the human brain volume variability. From Figure 136-1, we know that the newborn rabbit body weight ranges between 30 to 55 grams for the pre-term and from 45 to 65 grams for the control. This is consistent with the variability in newborn humans, ranging from 2.5 to 5 kilograms in the healthy population, as reported by Ray et al. [RSM<sup>+</sup>12].

Only from the boxplot, it is possible to notice a visual difference between the median of the four groups, although we want to know to what extent this difference

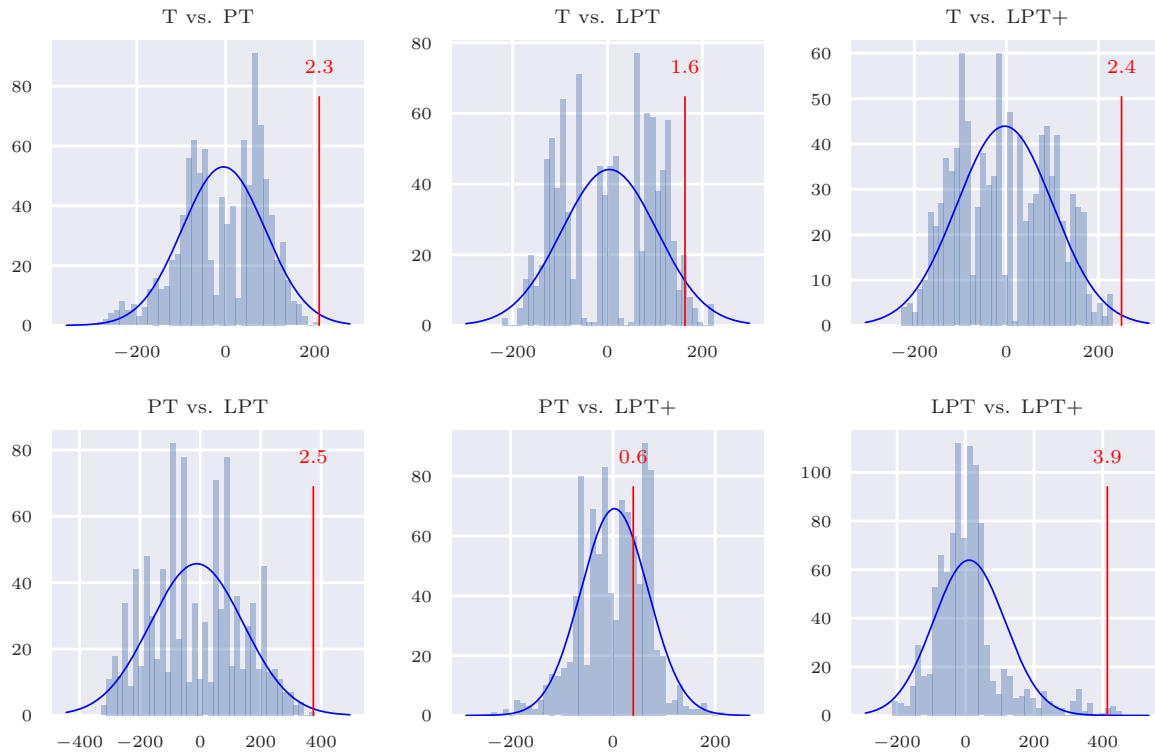


Figure 177-2: **Chance models for the median volume for the four selected groups.** Figure 177-1 was providing only one of the possible six comparisons between the boxplots shown in Figure 176-1. In this figure all the possible six models comparisons are shown. The highest difference is reported for late pre-term (LPT) and late pre-term with steroids (LPT+) with a Pearson index of 3.9. The median of the volumes for the pre-term and late pre-term with steroids are not statistically different, with a Pearson index of 0.6.

is due to chance or if the difference is statistically significant.

In this and in the following sections, the probability that the obtained results are significant, for any readouts (volume, FA, MD), is investigated considering the mean of each group respect to a *chance model*. Each median of the four groups (term, pre-term, late pre-term and late pre-term with steroids) is therefore compared with the median of each one of the other group individually, respect to the bootstrapped distribution of the means of the two groups.

As initial case, to compute the statistical significance of the difference between the full brain volume of the term (T, 11 subjects) and pre-term (PT, 14 subjects) acquisitions, we considered the dataset of the two sets combined, with 25 elements, and we randomly bootstrapped from it two subsets of 11 and 14 data points. The distribution of the difference of their medians is, thanks to the Central Limit Theorem is normally distributed<sup>1</sup>, and provides the reference chance model. The distribution

<sup>1</sup>This is theoretically true, even if the source of the distribution is not normally distributed, and

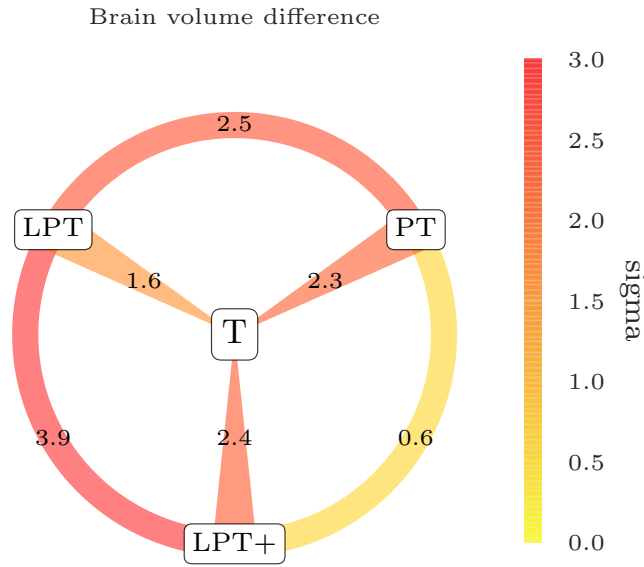


Figure 177-3: **Brain volumes Pearson correlation coefficients for the four selected groups.** Pearson correlation coefficients reported in Figure 177-2 are summarised in this graph. This representation will turn out to be relevant to compare the sub-volumes of the analysed rabbit brains.

can be fitted with a Gaussian with mean  $\mu_{\text{model}}$  and variance  $\sigma_{\text{model}}$ . The Pearson

$$P(x; \mu_{\text{model}}, \sigma_{\text{model}}) = \frac{|\mu_{\text{model}} - x|}{\sigma_{\text{model}}}$$

where  $x$  is the observed difference between the means of the Term and Pre-Term groups.

Figure 177-1 shows the outcome of this specific example, with the histogram of the bootstrapped medians and the fitted Gaussian model. We observe that the Central Limit Theorem fails to provide a Gaussian histogram. This is mainly a consequence of a small sample size compared to the distribution range.

For a Pearson index equals to 1, or one time the standard deviation of the bootstrapped model, the proposed method is equivalent to pass a Student t-test with  $\alpha = 11\%$ . When equal to two times the sigma, it corresponds to  $\alpha = 2.5\%$  and when equals to three times sigma, it corresponds to  $\alpha = 1.5\%$  [BB17].

The mutual comparison between the four region with the respective bootstrapped median histogram and the fitted normal distributions is shown in Figure 177-2

Since the relevant data to compare the four groups is the Pearson correlation coefficient, the graph proposed in Figure 177-3 quickly shows in colorscale the differences between the four groups. This device will be saving space and will make

---

for a large enough sample size.

the comparison between Pearson correlation coefficient easier, when in the following sections we will perform a region-wise analysis.

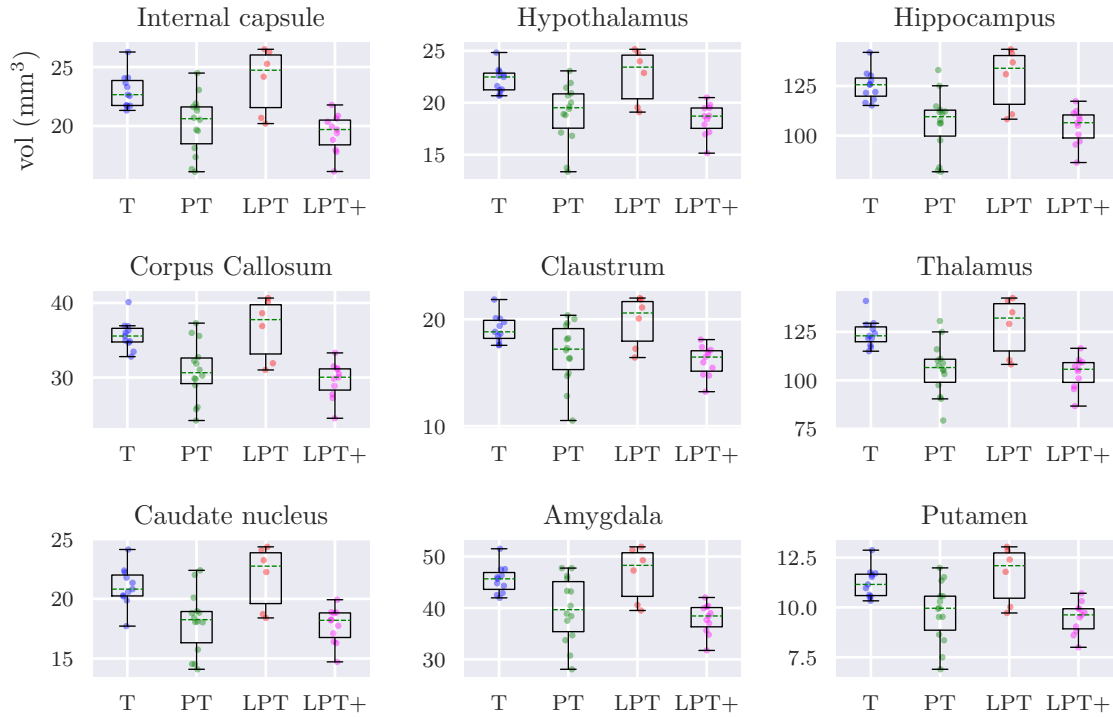


Figure 180-1: **Brain volumes per subjects per regions.** As Figure 176-1, here we show the volumes of the regions that are believed to be affected by gestational age.

### 6.4.3 Region-wise volume outcome

In the previous sections we introduced the tools for the exploratory data analysis relevant for our experiment and the comparison graph to provide the significance of the outcomes shown in the boxplot. In this section we consider 9 brain sub-regions that are believed to be affected by the encephalopathy induced by prematurity.

The medians of the volumes of the selected regions are shown in Figure 180-1 as boxplots. The related Pearson coefficients, expressed in the proposed graphs, are shown in Figure 180-2.

We can see that the results are coherent with the full volume, for a non statistically significant difference between pre-term and late pre-term with steroids. The highest significant difference is between late pre-term and late pre-term with steroids, in particular in the hippocampi, Amygdala, Corpi Callosi and Caudate Nuclei.

This result is particularly interesting as it shows that administering steroids on a late pre-term, from the volume point of view, has a comparable effect of a pre-term

birth. This seems to indicate that the steroids have a negative effect on the brain.

#### 6.4.4 Region-wise fractional anisotropy

The same figures presented in the previous section are produced here for the FA readout. The same 9 brain sub-regions that are believed to be affected by the encephalopathy induced by prematurity are considered for the degree of diffusivity in the brain.

The medians of the FAs are shown in Figure 181-1 as boxplots, and as before, the related Pearson coefficients, are shown in Figure 181-2.

If compared to the volume study, the level of significance is here drastically reduced. the thalamus seems to have a consistent FA across the four groups when mutually compared. For the Internal Capsule, only the comparison between the Term and the late-preterm with steroids appears to be slightly significant, with a Pearson coefficient of 1.0, equivalent to an  $\alpha$  of 11% in an equivalent Student's t-test.

Hypothalamus, Corpus Callosum, Caudate Nucleus and Putamen have an higher level of significance, but the Pearson index is never above 2.0, reaching this value only for differentiating term and pre-term.

The evidence of an effect of the three treatments considered respect to the term (control) and respect to each others is weak for the FA. Further studies are required to investigate if the difference is given by a real effect, or if possible artefacts may have influenced in the variability of the outcome more than the effects of the treatments.

#### 6.4.5 Region-wise mean diffusivity

As in the previous section, we provide a boxplot and the Pearson's graphs for the FA readout in Figure 181-3 and in Figure 181-4 respectively, for the 9 selected regions.

If the FA analysis provided a weak information to distinguish the differences between regions, the MD did not provide any significant readout for most of the regions. The difference between the pre-term and the late-preterm, in contrast to what have happened for the volumes and the FA, appears in this case to be significant for the Corpus Callosum, less significant for the Caudate Nucleus and the Putamen, and not significant for every other regions.

Even if at an exploratory phase, the reliability of these results are debatable. Even more than in the previous case, where the FA had been investigated, for the MD, there seems to be no statistical difference between the groups, apart from the Corpus Callosum, that shines as an outlier.

The presence of this outlier opens the question: the lack of an observed difference is the consequence of lack of a measurable effect in the treatment or the measurements had been undergone to a regression to mean after an undetected DWI artefacts?

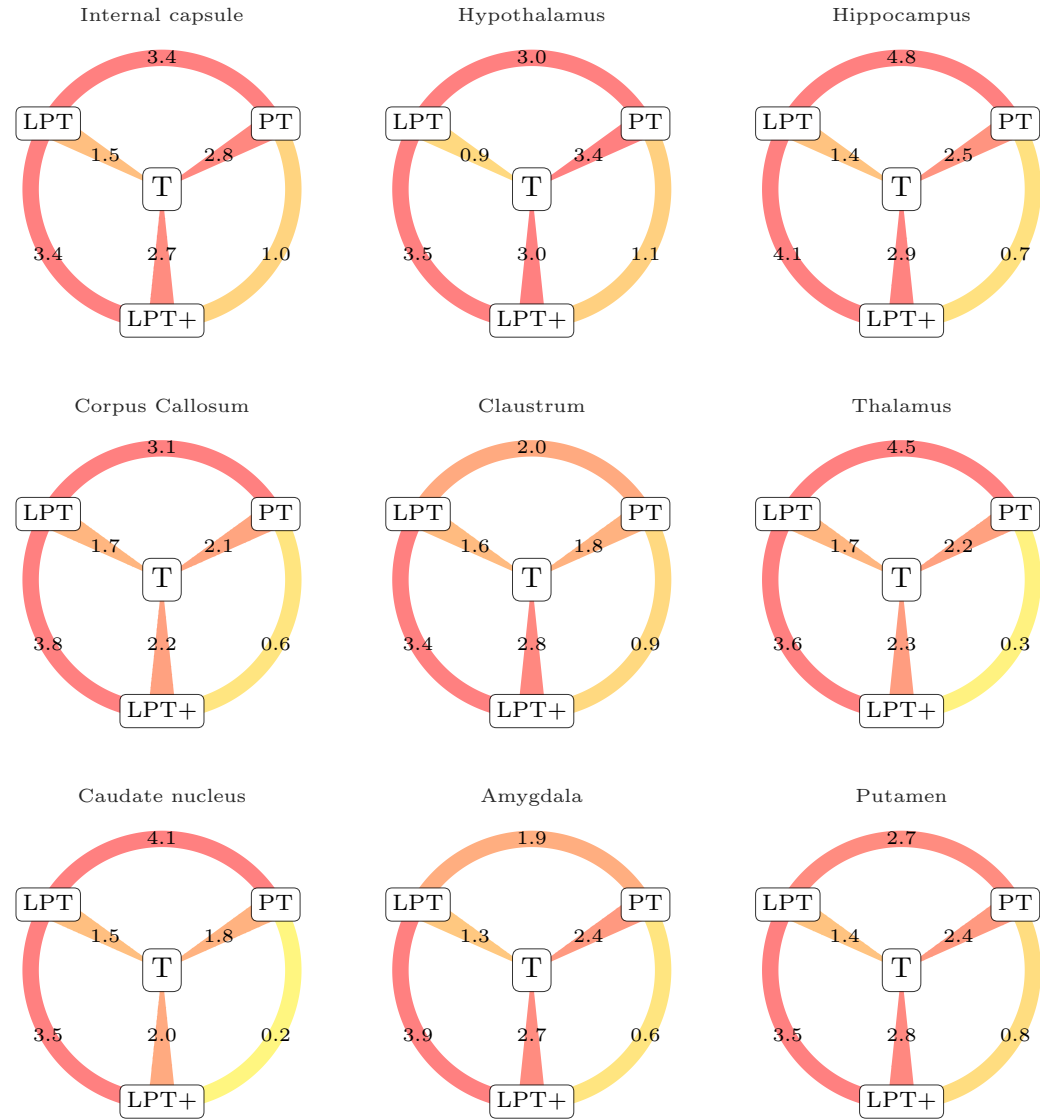


Figure 180-2: **Region-wise brain volumes Pearson correlation coefficients for the four selected groups.** Pearson correlation coefficients for the volumes of 9 selected regions. This graph provides a quick overview of the significance of the differences between the boxes of the boxplots for the region volumes shown in Figure 180-1.

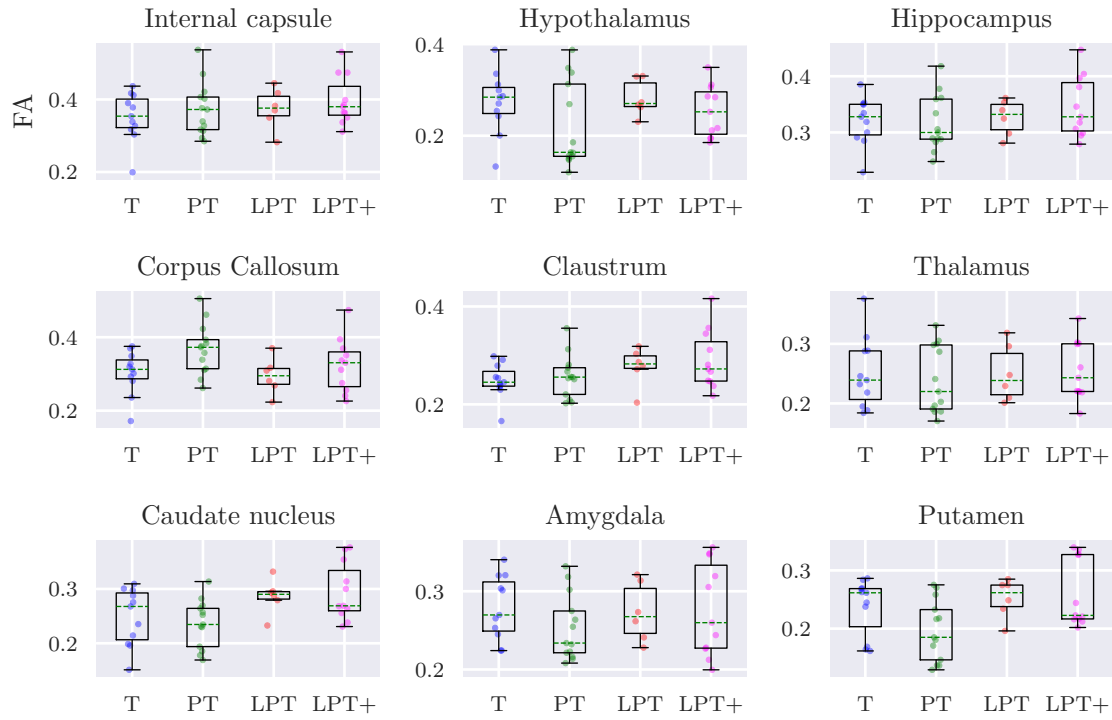


Figure 181-1: **Fractional anisotropy (FA) for the 9 selected regions.** From this preliminary investigation, no sharp visual difference can be visually identified between the boxes of each region.

A possible answer is proposed in the conclusions.

## 6.5 Conclusions

After providing an overview of the aims, and introducing the tools and the data collection pipeline, we proposed an exploratory data analysis of the results.

The main focus of the thesis had been developing and making available computational tools to clinicians and researchers for MRI analysis, in particular for the newborn rabbit. The main tools provided are the full data analysis pipeline, going from the native scanner images format to the final data analysis, with no manual intervention. The same pipeline can be adapted to other animals and studies of different nature with few parameters adjustments.

Due to the exploratory nature of this study, the statistical results do not provide any definitive answer. Nonetheless the volume analysis may indicate some hints towards the future directions. From the volumes alone, in fact, it seems that the intervention of corticosteroids hinders the development of the brain volume, as shown in Figure 176-1 and Figure 180-1.

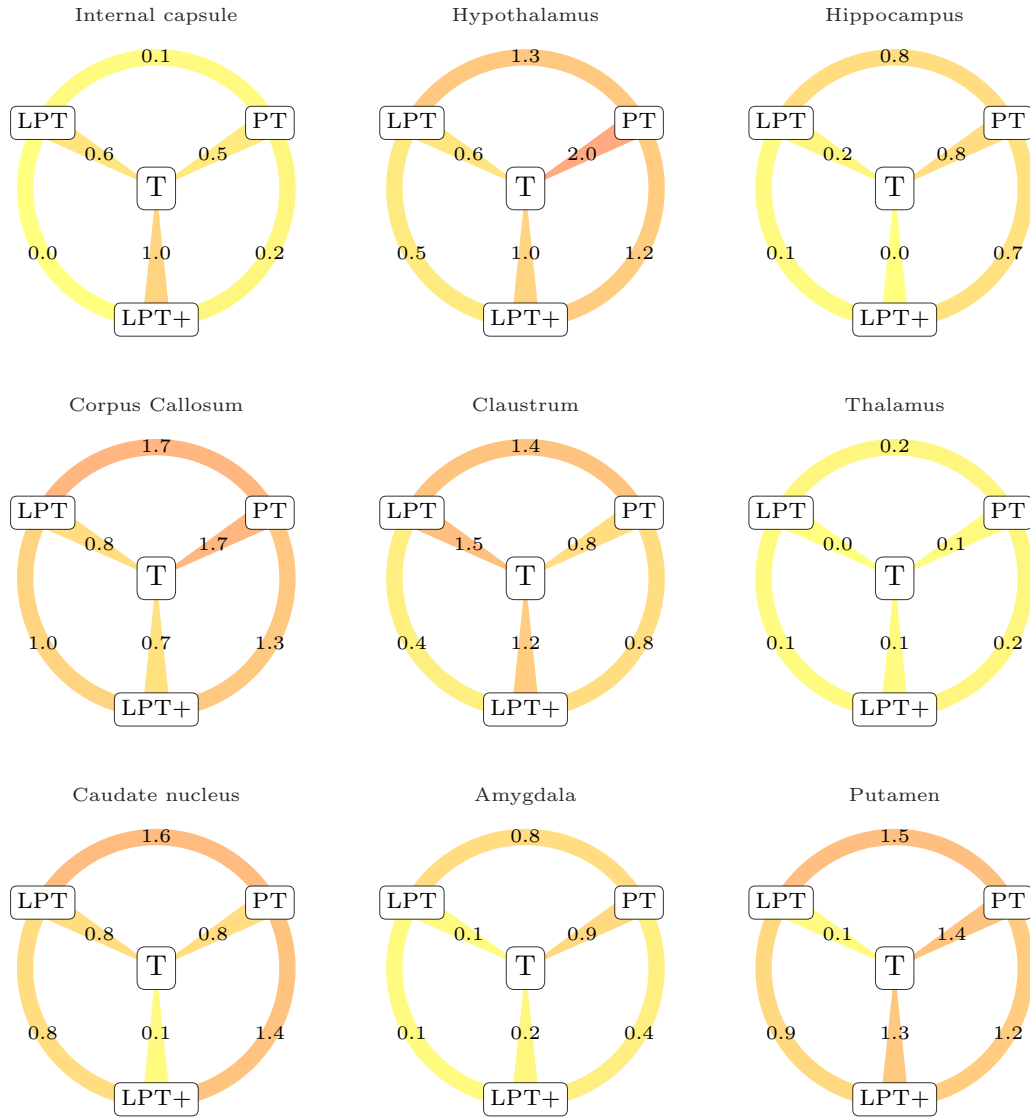


Figure 181-2: **Region-wise Fractional Anisotropy Pearson correlation coefficients for the four selected groups.** Pearson correlation coefficients for the volumes of 9 selected regions. This graph provides a quick overview of the significance of the differences between the boxes of the boxplots shown in Figure 181-1.

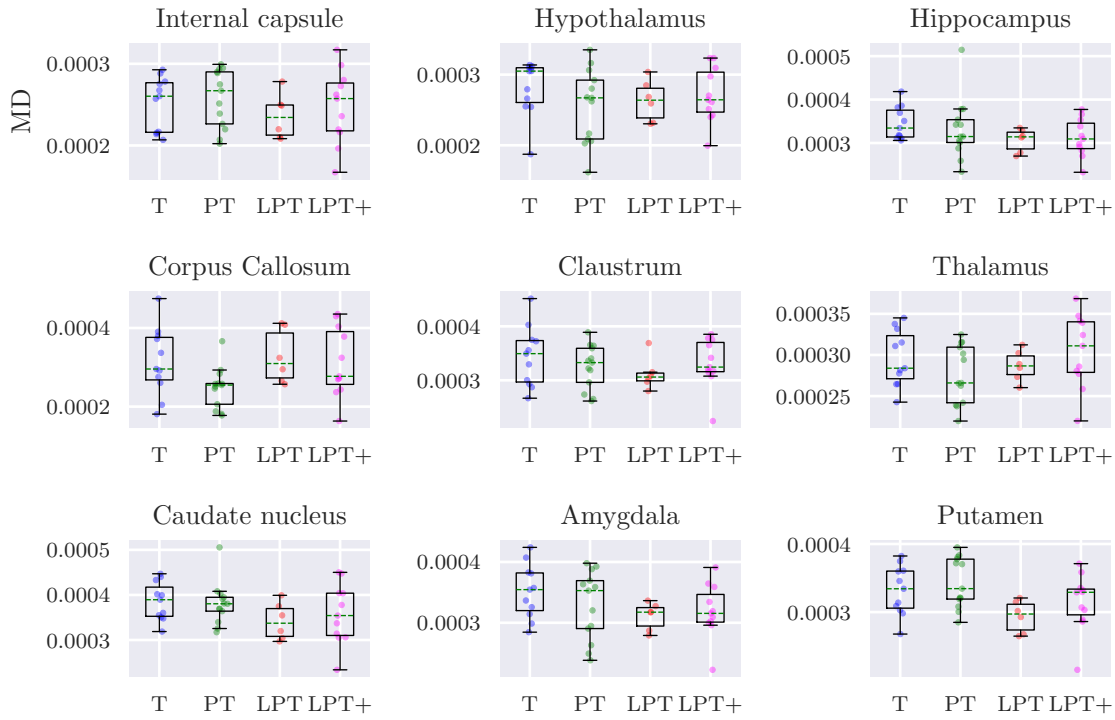


Figure 181-3: **Mean diffusivity (MD) for selected 9 regions.** In contrast to what happens for the volume, and on a similar trend of the fractional anisotropy, MD does not appear to differentiate between groups.

The DWI-based modalities had not provided any significant differences between the considered datasets, in particular for the fractional anisotropy (FA) and the mean diffusivity (MD) shown in Figure 181-2 and Figure 181-4 respectively.

The lack of statistically significant difference in the FA and MD and not in the volume can be explained considering concomitant informations coming from the histological studies. During a phase of the research where we tried to estimate the g-ratio both from MRI, using the method presented by Melbourne et al [MERB<sup>+</sup>13], and histological staining, Johannes van der Merwe could not obtain any significant read-outs. Further histological investigations had shown that early traces of myelination are visible only after the 7<sup>th</sup> day of life of a rabbit.

The late myelination of the rabbit may suggest that a DWI-based investigation at day 1 is not the best modality to obtain significant biomarkers. As reported by Peterson [Pet03], on humans pre-term birth affects the myelination development. It is therefore reasonable to carry an investigation on the four proposed datasets, after myelination have occurred. At the moment of writing the thesis, the study is moving towards the DWI analysis of a 8 weeks old rabbit model (see Section 7.2.4 for future work).

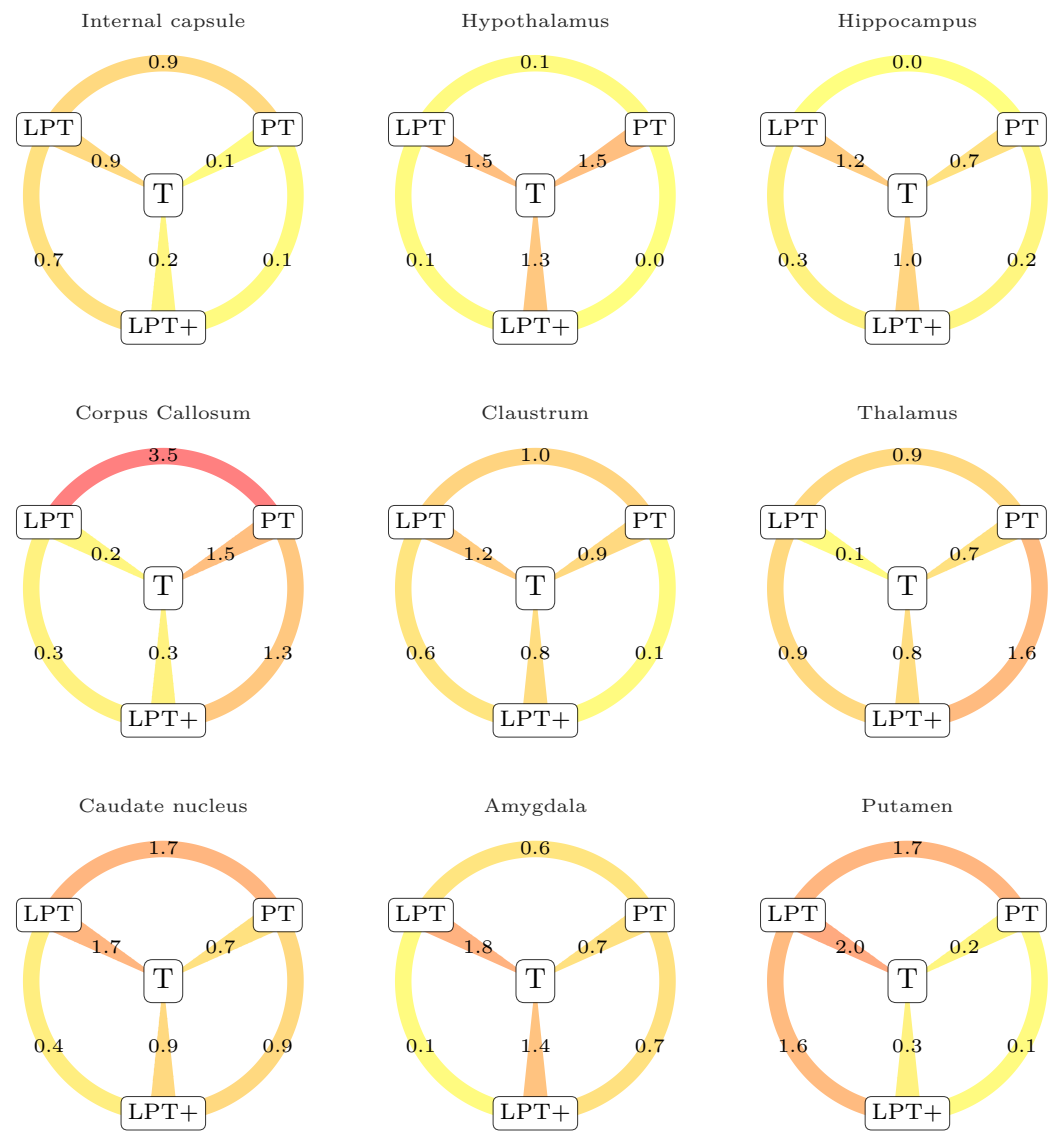


Figure 181-4: **Region-wise Mean Diffusivity Pearson correlation coefficients for the four selected groups.** Pearson correlation coefficients for the volumes of 9 selected regions. This graph provides a quick overview of the significance of the differences between the boxes of the boxplots shown in Figure 181-3.

What presented in this chapter provides a starting point for future studies. Once an higher number of subjects, in the Week 8 study will be obtained, and once the sex difference is taken into account as confounding factor, the clinical question will have an answer. Other than the sex differences, further studies should also differentiate between samples from the same mother, as we may expect a lower variability among them, and should be taking into account a parallel biochemical analysis investigating cortisol levels, blood pressure and immune/inflammatory markers, to compensate for the different baseline of each sample.

## Chapter bibliography

- [BB17] Peter Bruce and Andrew Bruce. *Practical statistics for data scientists: 50 essential concepts*. " O'Reilly Media, Inc.", 2017.
- [Cox04] Cox, Robert W and Ashburner, John and Breman, Hester and Fissell, Kate and Haselgrove, Christian and Holmes, Colin J and Lancaster, Jack L and Rex, David E and Smith, Stephen M and Woodward, Jeffrey B and others. A (sort of) new image data format standard: Nifti-1. *Neuroimage*, 22:e1440, 2004.
- [EB07] Bradley J Erickson and Jan C Buckner. Imaging in clinical trials. *Cancer informatics*, 4:13, 2007.
- [FSM<sup>+</sup>17] Sebastiano Ferraris, Dzhoshkun Ismail Shakir, Johannes Van Der Merwe, Willy Gsell, Jan Deprest, and Tom Vercauteren. Bruker2nifti: Magnetic Resonance Images converter from Bruker ParaVision to Nifti format. *The Journal of Open Source Software*, 2(16), Aug 2017.
- [FvdMVDV<sup>+</sup>18] Sebastiano Ferraris, Johannes van der Merwe, Lennart Van Der Veeken, Ferran Prados, Juan-Eugenio Iglesias, Andrew Melbourne, Marco Lorenzi, Marc Modat, Willy Gsell, Jan Deprest, and Tom Vercauteren. A magnetic resonance multi-atlas for the neonatal rabbit brain. *NeuroImage*, 2018.
- [HH96] Peter Hall and Joel L Horowitz. Bootstrap critical values for tests based on generalized-method-of-moments estimators. *Econometrica: Journal of the Econometric Society*, pages 891–916, 1996.
- [HLM96] GS Hongyi Li and Maddala. Bootstrapping time series models. *Econometric reviews*, 15(2):115–158, 1996.

- [Hor94] Joel L Horowitz. Bootstrap-based critical values for the information matrix test. *Journal of Econometrics*, 61(2):395–411, 1994.
- [MEM02] Peter Mildenerger, Marco Eichelberg, and Eric Martin. Introduction to the dicom standard. *European Radiology*, 12(4):920–927, Apr 2002.
- [MERB<sup>+</sup>13] Andrew Melbourne, Zach Eaton-Rosen, Alan Bainbridge, Giles S Kendall, Manuel Jorge Cardoso, Nicola J Robertson, Neil Marlow, and Sebastien Ourselin. Measurement of myelin in the preterm brain: multi-compartment diffusion imaging and multi-component t2 relaxometry. In *International Conference on Medical Image Computing and Computer-Assisted Intervention*, pages 336–344. Springer, 2013.
- [Pet03] Bradley S Peterson. Brain imaging studies of the anatomical and functional consequences of preterm birth for human brain development. *Annals of the New York Academy of Sciences*, 1008(1):219–237, 2003.
- [RSM<sup>+</sup>12] Joel G Ray, Michael Sgro, Muhammad M Mamdani, Richard H Glazier, Alan Bocking, Robert Hilliard, and Marcelo L Urquia. Birth weight curves tailored to maternal world region. *Journal of Obstetrics and Gynaecology Canada*, 34(2):159–171, 2012.
- [TCC12] J-Donald Tournier, Fernando Calamante, and Alan Connelly. Mr-trix: diffusion tractography in crossing fiber regions. *International Journal of Imaging Systems and Technology*, 22(1):53–66, 2012.
- [vdMvdVF<sup>+</sup>19] Johannes van der Merwe, Lennart van der Veen, Sebastiano Ferraris, Willy Gsell, Uwe Himmelreich, Jaan Toelen, Sebastien Ourselin, Andrew Melbourne, Tom Vercauteren, and Jan De-prest. early neuropathological and neurobehavioral consequences of preterm birth in a rabbit model. *Scientific reports*, 9(1):3506, 2019.

# Chapter 7

## Conclusions and future work

### Contents

---

<b>7.1</b>	<b>Contributions . . . . .</b>	<b>190</b>
7.1.1	Pre-clinical contributions . . . . .	190
7.1.2	Methodological contributions and limitations . . . . .	190
7.1.3	Open source software contributions and limitations . . . . .	191
<b>7.2</b>	<b>Future work . . . . .</b>	<b>191</b>
7.2.1	Further methods on the exponential integrators . . . . .	191
7.2.2	Open source code maintenance and improvements . . . . .	192
7.2.3	A NiLearn-inspired investigation for the fMRI rabbit brain analysis . . . . .	194
7.2.4	Longitudinal design . . . . .	194
7.2.5	4D multi-modal multi-atlas for the rabbit brain . . . . .	195
7.2.6	Extending the range of biomarkers . . . . .	197
7.2.7	Histology-MRI multi atlas for the rabbit brain . . . . .	197
7.2.8	A rabbit tracker for automatic unbiased neurobehavioural assessment . . . . .	198

---

The aim of this PhD project is the development of the computational tools for MRI data analysis in diffeomorphic image registration and within the project *encephalopathy of prematurity in a rabbit animal model*. Previous chapters of this thesis introduced the results and contributions while providing an overview of the related existing computational methods and state-of-the-art.

In this final chapter we summarise the results and contributions, discussing their limitations, and subsequently introducing a wide range of possible improvements as future work.

## 7.1 Contributions

We divide the contributions according to their relevance with respect to the clinical or pre-clinical contributions, methodological contributions and open source software contributions.

### 7.1.1 Pre-clinical contributions

The main result of the PhD project in the pre-clinical contribution is the creation of the first multi-atlas for the newborn brain rabbit, presented in Chapter 5 and [FvdMVDV<sup>+</sup>18]. The automatic segmentation method here proposed within combines existing as well as newly created software and algorithms. The underpinning methodology is developed to work optimally with the manually segmented subjects. These are too few to attempt any deep learning-based automatic segmentation, therefore the proposed diffeomorphic segmentation propagation and label fusion (MV, STEPS and STAPLE) represents the state-of-the-art automatic segmentation for the newborn rabbit.

The multi-modal multi-atlas presented has to be considered as a starting point for the clinical research on the brain of the newborn rabbit. Further developments and customisations are simplified thanks to the fact that both the segmentation propagation code and the multi-atlas are open-sourced and proposed in a versioned controlled repository.

The customary volume, FA and MD data analysis, combined with the histological examination and the neurobehavioural assessment provided the basis for the paper under review *Premature birth neurobehavioral consequence in a non-infective and non-ischemic rabbit model*, and will be at the core of future MRI data mining, on the current and future acquisitions.

### 7.1.2 Methodological contributions and limitations

The methodological contribution of this research is the application of the exponential integrators for the numerical approximation of the Lie exponential presented in Chapter 4 and in [FLD<sup>+</sup>16].

Since the Lie exponentiation represents a component in the diffeomorphic image registration method, and not its main bottleneck, its improvement in accuracy and computational time have resulted in an improvement of small magnitude in the whole registration algorithm. Nonetheless, with the advancements in tackling narrower bottlenecks, such as the optimisation method, the proposed *ss\_aei* may provide to be a valuable tool.

### 7.1.3 Open source software contributions and limitations

The first problem we had to tackle had been the conversion from the Bruker ParaVision format to the nifti format. The proposed software was presented in Chapter 6 as the first component for the rabbit brain analysis.

The pipeline providing the automatic segmentation propagation, presented in Chapter 5 and in [FvdMVDV<sup>+</sup>18] is the second software contribution. It provides a versatile and easy to customise segmentation propagation pipeline, whose parameters are tuned for the proposed multi-atlas dataset. The same pipeline can be nonetheless easily adapted to work for the segmentation of any other anatomy, provided a relative mono-modal or multi-modal atlas.

## 7.2 Future work

In the research carried forward in the last three years, the main goal had been the creation and improvements of computational tools to automate data processing and analysis. The main driving problem was the creation of an automatic segmentation method for the newborn rabbit brain. This has to be considered as a starting point for new research. Some possible directions are delineated in the next sections.

### 7.2.1 Further methods on the exponential integrators

The algorithms introduced in Chapter 4 and in [FLD<sup>+</sup>16] represents the simplest among the range of the *exponential integrators methods* available in literature. More advanced exponential integrators-based methods should be further exploited in diffeomorphic image registration. For example the ETDRK4, proposed by Cox and Matthews [CM02], constitutes the starting point for future explorations in this domain.

A particularly interesting option is given by the implicit trapezoid method, for which we produced promising, yet unpublished results. Following Darkner et al. [DPLS18], where the trapezoidal method is employed in the integration of SVF within the proposed collocations for diffeomorphic deformation (CDD) model, the same integration method can be embedded in the generalised scaling and squaring proposed in our paper [FLD<sup>+</sup>16]. In the trapezoid method the approximation of the exponential of the SVF  $\mathbf{v}$ , at the step  $j$  with step-size  $h$ , indicated by  $\phi_j$  is given by:

$$\phi_j = \phi_{j-1} + \frac{h}{2}(\mathbf{v} \circ \phi_{j-1} + \mathbf{v} \circ \phi_j) \quad (191-1)$$

where the integral flow  $\phi_j$  at the second member can be approximated with a fixed point algorithm, or with a nested iterative method, such as the Euler or midpoint.

Indicating the approximation with to  $\tilde{\varphi}_j$ , this approach results in employing  $\tilde{\varphi}_j = \phi_{j-1} + \mathbf{v} \circ \phi_{j-1}$  (Euler) or  $\tilde{\varphi}_j = \phi_{j-1} + \mathbf{v} \circ (\phi_{j-1} + \frac{1}{2}\mathbf{v} \circ \phi_{j-1})$  (Midpoint) as core approximation of the scaling and squaring algorithm.

After the limitations exposed in Section 7.1.2, another possible field of application for the exponential integrators is their combination in the numerical computation of the log-composition. Given two stationary velocity fields  $\mathbf{u}$  and  $\mathbf{v}$ , their log-composition is defined as:

$$\mathbf{u} \oplus \mathbf{v} = \log(\exp(\mathbf{u}) \circ \exp(\mathbf{v})) , \quad (192-1)$$

where  $\exp$  and  $\log$  are the Lie exponential and Lie logarithm. As the exponential integrators in the generalised scaling and squaring are approximating  $\exp(\mathbf{u})$  separating the linear and the non-linear part, the composition between exponentiated vector fields can be performed after the scaling step, with a subsequent composition step including the subsequent application of the logarithm, and so to make the vector fields being recomposed in the tangent space rather than in the Lie group.

Future work in addressing the improvements of the computational tools related to the Log-Euclidean framework can be developed considering the accelerating convergence series (ACS) applied to the computation of the Lie logarithm as proposed by Bossa et al. [BO08]. ACS are a mathematical method developed to improve the convergence of numerical series and therefore to increase the speed of convergence of series arising from numerical methods (see for example Smith et al. [SF79]).

### 7.2.2 Open source code maintenance and improvements

Other than the already deployed `bruker2nifti` software converter (see Section 6.2), which underwent peer-review with the Journal of Open Source Software (JOSS), several other packages have been developed in support of the PhD project and open-sourced on `github`:

- ▷ `RabbitBrainAnalysis`: pipeline for the data analysis of the newborn rabbit brain. The code brings the output of the Bruker scanner and returns the elaborated modalities oriented in stereotaxic coordinates, automatically segmented and provided with subject-wise and comparative data analysis.
- ▷ `NiLabels`: a Python package providing a set of tools to automatise simple manipulations and measurements of medical images and segmentations in `nifti` format.
- ▷ `calie`: a Python package for the numerical computation of local operations between Lie algebra of stationary velocity fields and its Lie group.

- ▷ `matrix_expmv` Matlab scripts aimed at comparing a range of methods for the computation of  $\expm(A)*v$  without necessarily computing the exponential of the matrix  $A$  directly.
- ▷ `intra-cranial-volume-estimation`: a Python package for the template-free ICV estimation, as proposed in [IFM<sup>+</sup>17].
- ▷ `SPOT-A-NeonatalRabbit`: Segmentation Propagation on Target (...as a Neonatal Rabbit), a Python package to automatise segmentation propagation and label fusion. Utilised to produce results in [FvdMVDV<sup>+</sup>18].
- ▷ `MRImultiAtlasForNeonatalRabbitBrain` Python code for the benchmarking and validation of the Neonatal Rabbit brain Multi-Atlas. Utilised to produce the graphs and tables of [FvdMVDV<sup>+</sup>18].
- ▷ `RunPythonOnCluster`: simple skeleton to interface Python pipelines and the UCL main cluster. Used to run the main pipeline for the brain rabbit data analysis.
- ▷ `BrainWebRawToNifti`: simple Python script to manipulate the downloaded raw data from the BrainWeb dataset and to convert them to the nifti image format. Brainweb dataset was utilised for benchmarking of `intra-cranial-volume-estimation`.
- ▷ `DummyForMRI` simple dummy phantom of synthetic MRI non-realistic data for pipeline segmentation propagation and label fusion algorithms testing. Utilised for benchmarking of `intra-cranial-volume-estimation`.
- ▷ `LaTeXCommenter`: a very simple Python script to add and remove annotations between subsequent versions of a LaTeX document. It was utilised for the submission of [FvdMVDV<sup>+</sup>18].
- ▷ `counting_sub_multisets` a Python package for the computation of constrained  $k$ -resolutions of  $n$ , in enumerative combinatorics. The proposed method is available as a pre-print on [arxiv.org/abs/1511.06142](https://arxiv.org/abs/1511.06142).

In general, research outcomes that are strictly dependent upon code other than being published, require to undergo periodic maintenance. For most of the repository this is an ongoing process, according to the interest the research community have shown and according to the issue raised.

Started in May 2016, the JOSS initiative is a developer oriented peer-reviewed open-access scientific journal covering open-source software. This appears to be a promising option to have the code peer-reviewed by experts other than citable as

a publication. Given their generalisability and possible interest from other research groups, NiLabels (presented in section 6.2) and calie (presented in section 4.6) appears to be best candidate to undergo a peer-review process and are potential candidates for publication.

NiLabels in particular is intended to be integrated in the `nipy` project. This is a collection of tools developed by the active community of Python developers working in neuroimaging and neuroscience.

### 7.2.3 A NiLearn-inspired investigation for the fMRI rabbit brain analysis

Within the `nipy` ecosystem, one can find the NiLearn [APE<sup>+</sup>14] package. This is a statistical neuroimaging toolkit for neuroimaging data, oriented in particular towards functional MRI (fMRI). It enables to compute statistical maps of the brain with the latest machine learning and statistical learning tools and to plot them on brain surfaces and 3D volume with an appealing visualisation.

The reasons why `nilearn` is particularly appealing are:

1. Open source.
2. Versatile and open to contributions and customisation.
3. Well documented and therefore easy to use and compatible with the wide Python ecosystem.
4. Supported by a wide community.
5. Covering a wide range of applications.

The reasons why a software equivalent to NiLearn has never been done for the neonatal and adult rabbit (or for any animal) are the lack of interest in the specie and lack of a template availability. The multi-atlas proposed in the thesis and the increasing interest in the rabbit as a translational specie would make the adaptation of NiLearn for the rabbit brain a possibly high impact endeavour.

The produced tool for the fMRI analysis on the *in vivo* newborn rabbit, would open a new range of biomarker for the proposed investigation and for similar ones.

### 7.2.4 Longitudinal design

After the *in vivo* feasibility study presented in Section 3.3.1, we concentrated the attention on the *ex vivo* acquisition throughout the project. This does not exclude a further study with a longitudinal investigation.

In this setting each subject could be scanned three times, *in vivo* at day 1 and day 7, and *ex vivo* again at day 7. This would provide a prior for the possibility of reconstructing the high resolution at the first time-point and therefore to propagate the parcellation from the second time-point *ex vivo* to the first time-point *in vivo*.

The work proposed by Ongie and Jacob [OJ15], extends the recently developed theory of sampling signals of finite rate of innovation to increase the image resolution exploiting the  $k$ -space signal. In this approach, the super-resolved image is obtained estimating from a resolution-independent mask prior obtained from the  $k$ -space. In the proposed setting, the method can be enhanced combining in a probabilistic model the prior obtained from the  $k$ -space of the first time-point and the prior obtained from the propagated high resolution time-point.

Another approach to bring the *in vivo* at the first time-point to the high resolution level could be generalising the work proposed by Demirel et al. [DA10] for the satellite image enhancement to three dimensions. The proposed method is based on the interpolation of the high-frequency sub-band. Again, it could be enhanced using the prior knowledge of the high resolution scan at the second time-point.

At the moment of writing this thesis an investigation on the 8 weeks old *ex vivo* rabbit model is in progress in Leuven. Preliminary results comparing the 1d and the 8W models can be seen in Figure 195-1 and Figure 195-2. Particularly interesting is the shape evolution of the cerebellum, visible in the posterior side of the sagittal view. This part, related to motor control and coordination undergoes major growth. It is also interesting to notice that, due to myelination, the intensities of the adult rabbit are sharper and the anatomical structures are better delineated in the MRI.

This will provide a fruitful starting point for the future steps of the study.

### 7.2.5 4D multi-modal multi-atlas for the rabbit brain

With the planned *ex vivo* day 7 and the week 8 acquisition moving forward at the moment of writing this thesis, it will be possible to create the first 4D probabilistic atlas of the developing brain for the newborn rabbit. The analogous for humans had been developed by Kuklisova-Murgasova et al. [KMAS<sup>+</sup>11].

This would provide a prior knowledge of the probability of the location of each segmented regions to apply methods such as unified segmentation [AF05] for the automatic segmentation at any time-point. The main challenges of this future work would be dealing with the inversion of the contrast due to the myelination process, and would at the same time provides important insights into the anatomical and physiological development of this process.

The comparison between the human and rabbit 4D probabilistic developing brain atlas would provide as well insights in the validity of the rabbit as a translational

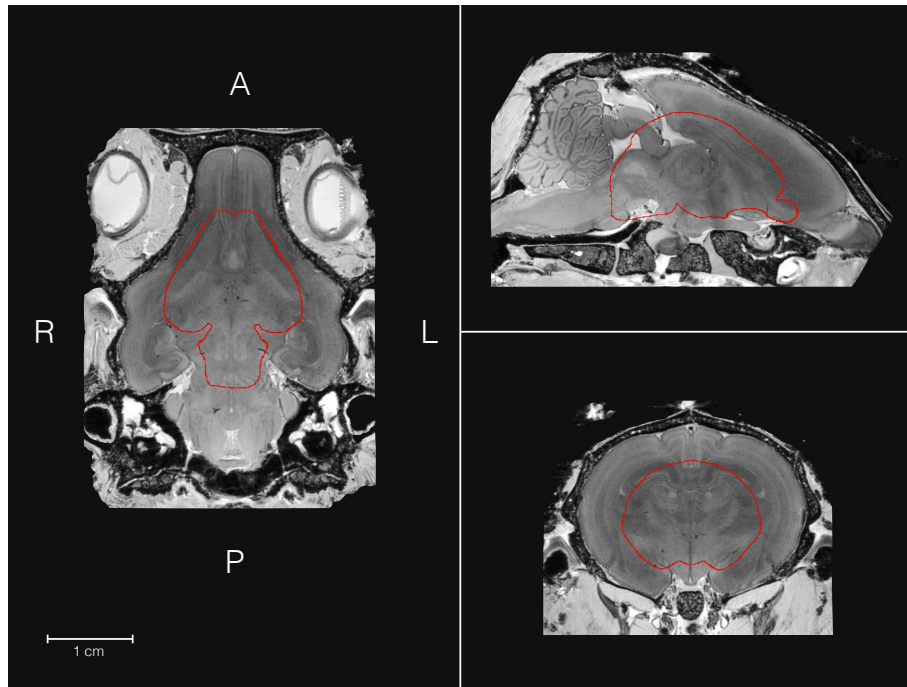


Figure 195-1: **Comparison between an 8 weeks old rabbit (subject 12503) and 1 day old rabbit (subject 1305) acquired with *ex vivo* protocol.** Newborn rabbit is shown as contour of the brain segmentation. Both subjects are oriented in stereotaxic coordinates (see Section 5.3.2 for details).

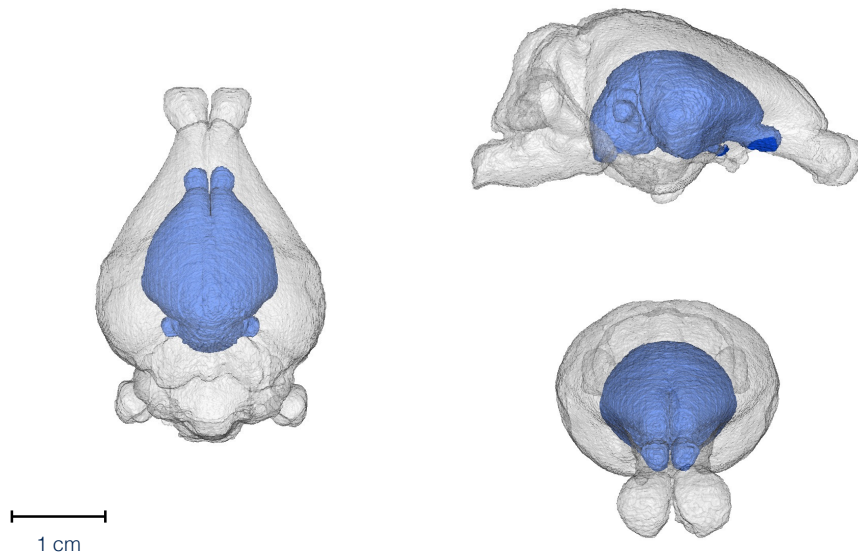


Figure 195-2: **3D rendering of the newborn (1d) and adult (8w) brain tissue segmentation.** Subjects and orientation are the same as in Figure 195-1. Left: superior view. Top right: lateral view. Bottom right: frontal view.

animal model.

### 7.2.6 Extending the range of biomarkers

The protocol introduced in Section 3.4 allows for the study of more sophisticated biomarkers than the initial ones proposed in this phase of the study. In exploring the biological effects of a condition and a drug, the methodological and the clinical insights can not be considered independently. As it is not possible to know in advance what are the regions that are mainly affected by PTB and ACS, it is reasonable to consider an as wide as possible range, to then examine their statistical relevance, isolating them from the confounding factors. This would provide further insights in the understanding of the rabbit developing brain one one side, and would provide further insight of the biomarker itself on the other.

Therefore, the first next step would be to explore the neurite orientation dispersion and density imaging (NODDI), proposed by Zhang et al. [ZSWKA12].

A second investigation would be to go beyond the diffusion tensor and to consider the state-of-the-art spherical harmonic decomposition based tractography, as proposed by Tournier et al. and made publicly available in the open source software MRTrix [TCC12].

Another investigation would involve the morphology of the cortex. Cortical thickness is a widely used imaging biomarker. Lerch et al. [LCD<sup>+</sup>08] provided an algorithm for automatically measuring cortical thickness across the entire cortex for the fixed mouse brain. The method is then applied to investigate the effects of Huntington’s Disease. Affected mouse showed an increase in cortical thickness also seen in human foregoing Huntington’s Disease.

### 7.2.7 Histology-MRI multi atlas for the rabbit brain

Histology has a higher resolution than the micro-MRI but does not allow for 3D representation. Pichat et al. [PIY<sup>+</sup>18] reviewed the latest results in reconstructing 3D volumes from the histological studies. One of the preferred and most promising approach is to rely on the 3D MRI volume to correct for the shearing, tears, debris, and fractures produced during the sample sectioning and staining.

With the multi-atlas proposed in Chapter 5 and [FvdMVDV<sup>+</sup>18] we provided as well a standardised taxonomical table 156-1. This extended taxonomy is meant to help in the process of 3D reconstruction, as the 52 regions delineated in each subject of the multi-atlas are considered in a hierarchy with other 80 regions whose delineation is visible only at histological level.

The histology and MRI data are still in the process of being acquired. Their integration can be converted into a result similar to the Allen mouse histological

## 7.2. FUTURE WORK

atlas. A screenshot of this atlas is shown in figure 198-1. This would provide the first digital publicly available newborn rabbit histological atlas.

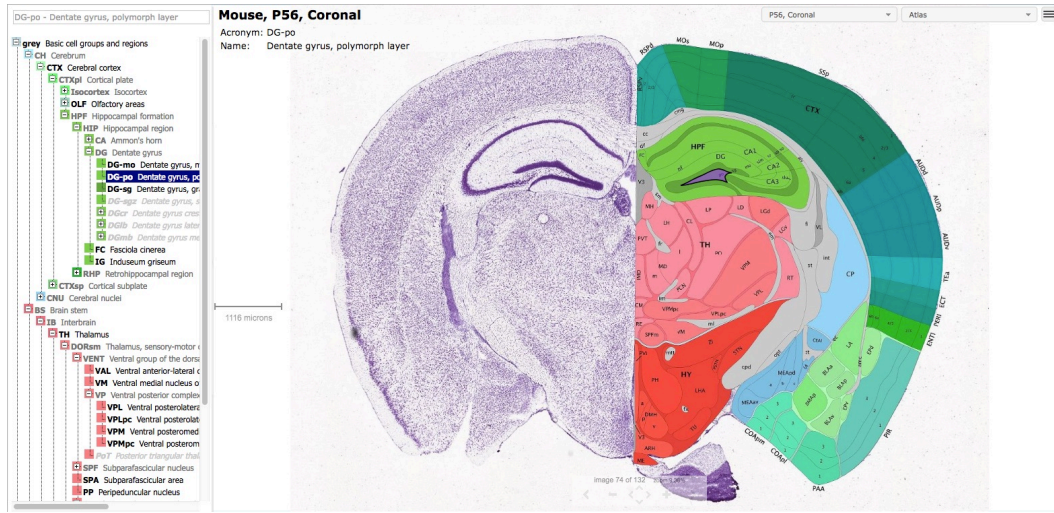


Figure 198-1: **Allen mouse atlas, coronal section.** A screenshot of a coronal section from the online Allen, [LHA<sup>+</sup>07] mouse histological atlas. This result was achieved annotating the histological sections of a mouse, and made quickly available in an interactive web interface. Combining the 3D MRI annotation, as shown in Figure 138-6 and the histological data acquired in this project, would produce a 3D atlas with histological resolution. Researches in this direction are presented in [PIY<sup>+</sup>18].

### 7.2.8 A rabbit tracker for automatic unbiased neurobehavioural assessment

Significant results on the effects of corticosteroids administration on the newborn rabbit had been obtained in the phase of the study involving the neurobehavioural assessment.

This was performed in double blind by human rating at videos of the rabbits behaviours under determined circumstance. More than one rater with diverse degree of experience had been involved.

Visual assessment had been the only option available due to lack of resources to buy, develop or adapt an existing automatic tracking system, such as the widely utilised EthoVision [NST01] by Noldus, AnyMaze by Stoelting or the open source motr utilised in [BRB<sup>+</sup>09].

An algorithm for the gait classifying, would provide an ideal benchmarking for the development of an automatic behavioural assessment software for the particular case of the newborn, pre-adolescent, adolescent and adult rabbit. Accurate tracking would as well provide a numerical data readout and could open new possibilities in the behavioural analysis and further understanding in the corticosteroid administration.

It is interesting to underline that almost no steps had been carried forward in this direction, when the whole research project could have been exclusively based on automatising the neurobehavioural assessment rather than based on the analysis of the MRI or histology outcomes.

## Chapter bibliography

- [AF05] John Ashburner and Karl J Friston. Unified segmentation. *Neuroimage*, 26(3):839–851, 2005.
- [APE<sup>+</sup>14] Alexandre Abraham, Fabian Pedregosa, Michael Eickenberg, Philippe Gervais, Andreas Mueller, Jean Kossaifi, Alexandre Gramfort, Bertrand Thirion, and Gaël Varoquaux. Machine learning for neuroimaging with scikit-learn. *Frontiers in neuroinformatics*, 8:14, 2014.
- [BO08] Matias Bossa and Salvador Olmos. A new algorithm for the computation of the group logarithm of diffeomorphisms. In *2nd MICCAI Workshop on Mathematical Foundations of Computational Anatomy*, 2008.
- [BRB<sup>+</sup>09] Kristin Branson, Alice A Robie, John Bender, Pietro Perona, and Michael H Dickinson. High-throughput ethomics in large groups of drosophila. *Nature methods*, 6(6):451, 2009.
- [CM02] Steven M Cox and Paul C Matthews. Exponential time differencing for stiff systems. *Journal of Computational Physics*, 176(2):430–455, 2002.
- [DA10] Hasan Demirel and Gholamreza Anbarjafari. Satellite image resolution enhancement using complex wavelet transform. *IEEE geoscience and remote sensing letters*, 7(1):123–126, 2010.
- [DPLS18] Sune Darkner, Akshay Pai, Matthew G Liptrot, and Jon Sporring. Collocation for diffeomorphic deformations in medical image registration. *IEEE transactions on pattern analysis and machine intelligence*, 40(7):1570–1583, 2018.
- [FLD<sup>+</sup>16] Sebastiano Ferraris, Marco Lorenzi, Pankaj Daga, Marc Modat, and Tom Vercauteren. Accurate small deformation exponential approximant to integrate large velocity fields: Application to image registration. In *Proceedings of the IEEE Conference on Computer Vision and Pattern Recognition Workshops*, pages 17–24, 2016.

- [FvdMVDV<sup>+</sup>18] Sebastiano Ferraris, Johannes van der Merwe, Lennart Van Der Veeken, Ferran Prados, Juan-Eugenio Iglesias, Andrew Melbourne, Marco Lorenzi, Marc Modat, Willy Gsell, Jan Deprest, and Tom Vercauteren. A magnetic resonance multi-atlas for the neonatal rabbit brain. *NeuroImage*, 2018.
- [IFM<sup>+</sup>17] Juan Eugenio Iglesias, Sebastiano Ferraris, Marc Modat, Willy Gsell, Jan Deprest, Johannes L van der Merwe, and Tom Vercauteren. Template-free estimation of intracranial volume: A preterm birth animal model study. In *Fetal, Infant and Ophthalmic Medical Image Analysis*, pages 3–13. Springer, 2017.
- [KMAS<sup>+</sup>11] Maria Kuklisova-Murgasova, Paul Aljabar, Latha Srinivasan, Serena J Counsell, Valentina Doria, Ahmed Serag, Ioannis S Gousias, James P Boardman, Mary A Rutherford, A David Edwards, et al. A dynamic 4d probabilistic atlas of the developing brain. *NeuroImage*, 54(4):2750–2763, 2011.
- [LCD<sup>+</sup>08] Jason P Lerch, Jeffrey B Carroll, Adrienne Dorr, Shoshana Spring, Alan C Evans, Michael R Hayden, John G Sled, and R Mark Henkelman. Cortical thickness measured from mri in the yac128 mouse model of huntington’s disease. *Neuroimage*, 41(2):243–251, 2008.
- [LHA<sup>+</sup>07] Ed S Lein, Michael J Hawrylycz, Nancy Ao, Mikael Ayres, Amy Bensinger, Amy Bernard, Andrew F Boe, Mark S Boguski, Kevin S Brockway, Emi J Byrnes, et al. Genome-wide atlas of gene expression in the adult mouse brain. *Nature*, 445(7124):168–176, 2007.
- [NST01] Lucas PJJ Noldus, Andrew J Spink, and Ruud AJ Tegelenbosch. Ethovision: a versatile video tracking system for automation of behavioral experiments. *Behavior Research Methods, Instruments, & Computers*, 33(3):398–414, 2001.
- [OJ15] Greg Ongie and Mathews Jacob. Super-resolution mri using finite rate of innovation curves. In *Biomedical Imaging (ISBI), 2015 IEEE 12th International Symposium on*, pages 1248–1251. IEEE, 2015.
- [PIY<sup>+</sup>18] Jonas Pichat, Juan Eugenio Iglesias, Tarek Yousry, Sébastien Ourselin, and Marc Modat. A survey of methods for 3d histology reconstruction. *Medical image analysis*, 46:73–105, 2018.
- [SF79] David A Smith and William F Ford. Acceleration of linear and

logarithmic convergence. *SIAM Journal on Numerical Analysis*, 16(2):223–240, 1979.

- [TCC12] J-Donald Tournier, Fernando Calamante, and Alan Connelly. Mrtrix: diffusion tractography in crossing fiber regions. *International Journal of Imaging Systems and Technology*, 22(1):53–66, 2012.
- [ZSWKA12] Hui Zhang, Torben Schneider, Claudia A Wheeler-Kingshott, and Daniel C Alexander. Noddi: practical in vivo neurite orientation dispersion and density imaging of the human brain. *Neuroimage*, 61(4):1000–1016, 2012.